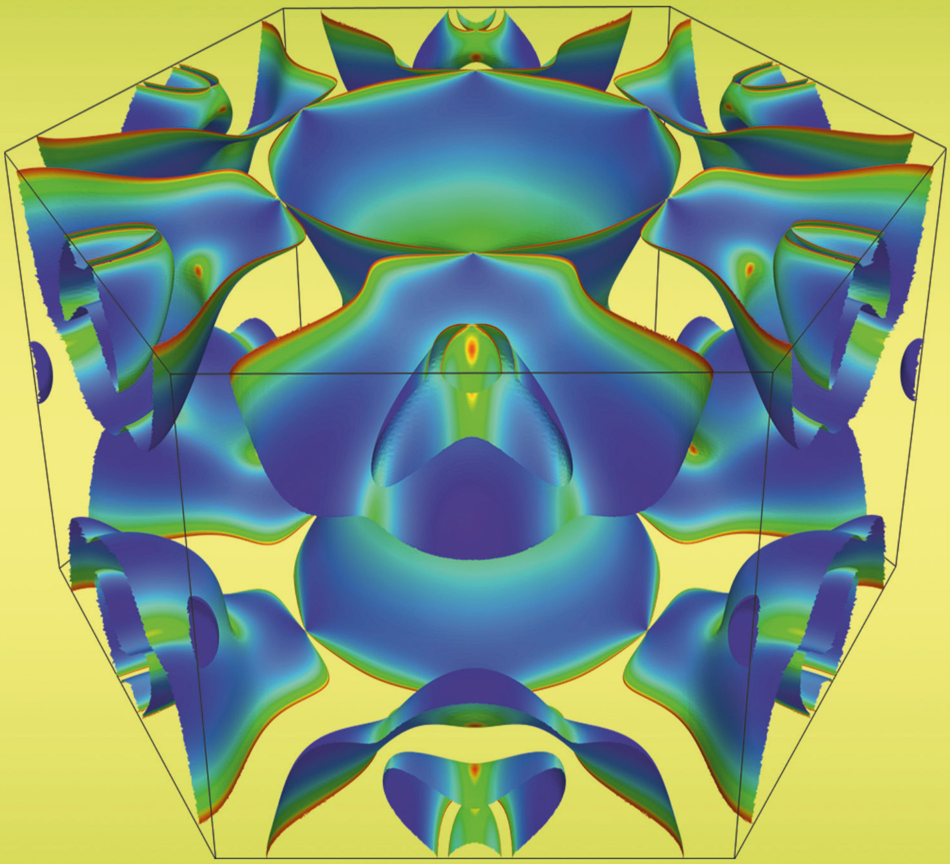

Ab initio description of transverse transport due to impurity scattering in transition-metals

Bernd Zimmermann

JÜLICH
FORSCHUNGSZENTRUM

Member of the Helmholtz Association

Schriften des Forschungszentrums Jülich
Reihe Schlüsseltechnologien / Key Technologies Band / Volume 89

Forschungszentrum Jülich GmbH
Peter Grünberg Institut (PGI)
Quanten-Theorie der Materialien (PGI-1/IAS-1)

Ab initio description of transverse transport due to impurity scattering in transition-metals

Bernd Zimmermann

Schriften des Forschungszentrums Jülich
Reihe Schlüsseltechnologien / Key Technologies Band / Volume 89

ISSN 1866-1807 ISBN 978-3-89336-985-0

Bibliographic information published by the Deutsche Nationalbibliothek.
The Deutsche Nationalbibliothek lists this publication in the Deutsche
Nationalbibliografie; detailed bibliographic data are available in the
Internet at http://dnb.d-nb.de.

Publisher and Distributor: Forschungszentrum Jülich GmbH
Zentralbibliothek
52425 Jülich
Tel: +49 2461 61-5368
Fax: +49 2461 61-6103
Email: zb-publikation@fz-juelich.de
www.fz-juelich.de/zb

Cover Design: Grafische Medien, Forschungszentrum Jülich GmbH

Printer: Grafische Medien, Forschungszentrum Jülich GmbH

Schriften des Forschungszentrums Jülich
Reihe Schlüsseltechnologien / Key Technologies, Band / Volume 89

D 82 (Diss. RWTH Aachen University, 2014)

ISSN 1866-1807
ISBN 978-3-89336-985-0

Abstract

This thesis attempts to shed light on various spin-orbit driven transport phenomena in materials, as a crucial for the further development of the field of spintronics. In particular, we address the skew-scattering mechanism in dilute alloys, which gives rise to the anomalous and spin Hall effect, as well as spin-relaxation processes.

We create the tools to access these quantities from *ab initio* calculations in the framework of the full-potential all-electron Korringa-Kohn-Rostoker Green-function method, by (a) developing and implementing a new tetrahedron method for the calculation of complicated, multi-sheeted Fermi surfaces even of complex transition-metal compounds, and (b) developing an efficiently parallelized and thus highly scalable computer program (up to thousands of processors) for the precise calculation of scattering properties.

In a first application of the new tetrahedron method, we calculate the Elliott-Yafet spin-mixing parameter on the Fermi surfaces of $5d$ and $6sp$ metals, and discover a yet unexplored dependence on the electron's spin-polarization direction. As we show, this anisotropy can reach gigantic values in uniaxial hcp crystals due to the emergence of large spin-flip hot-areas or hot-loops on the Fermi surface, supported by the low symmetry of the hcp crystal. A simple model is able to reveal an interesting interplay between the orbital character of the states at special points, lines or areas in the Brillouin zone and the matrix-elements of the spin-flip part of the spin-orbit coupling operator.

We further calculate the skew-scattering contribution to the anomalous Hall effect (AHE) in dilute alloys based on a ferromagnetic host for the first time. A systematic study of $3d$ impurities in bcc Fe, as well as the non-magnetic hosts Pd, Pt and Au, allows us to identify trends across the periodic table. In all our calculations, we also observe a strong correlation between the spin Hall effect and anomalous Hall effect in these materials, which is of interest for the creation and detection of strongly spin-polarized currents. A Fermi-surface analysis of the contributions to the AHE reveals a non-trivial, peaked behavior at small hot-spots around spin-orbit lifted degeneracies. We then proceed to the more complicated $L1_0$-ordered alloy FePt and address different kinds of disorder. We showcase the power of our method by treating the very complicated compounds $\mathrm{Fe}_x\mathrm{Mn}_{1-x}\mathrm{Si}$ and $\mathrm{MnSi}_{1-x}\mathrm{Ge}_x$, based on the non-Fermi liquid manganese silicide (MnSi). Finally, we also calculate the pure spin Hall effect for $4d/5sp$ and $5d/6sp$ impurities in fcc Ir and hcp Re hosts. For the latter, we discover a strong dependence on the electron's spin-polarization direction.

Contents

Conventions and Abbreviations

In this thesis, we try to stick to the following conventions in mathematical expressions:

Symbol		Explanation
$\vec{r}$	arrow head	3-dimensional vector (containing Cartesian components)
$\hat{r}$	hat	normalized 3-dimensional vector
$\overleftrightarrow{\sigma}$	double arrow head	3×3-dimensional tensor
$\underline{c}$	underline	general vector
$\underline{\underline{M}}$	double underline	general matrix
$\mathcal{S}$	calligraphic symbol	operator (in basis-independent form)

The following abbreviations are used:

Abbr.	Meaning
AHA	anomalous Hall angle
AHC	anomalous Hall conductivity
AHE	anomalous Hall effect
AMR	anisotropic magneto-resistance
ASA	atomic sphere approximation
B-field	Zeeman-like exchange field
bcc	body-centered cubic
BZ	Brillouin zone
CPU	central processing unit
DFT	density functional theory
DOS	density of states
fcc	face-centered cubic
FLAPW	full potential linearized augmented plane-wave (method)
FP	full potential
FS	Fermi surface
GF	Green function
hcp	hexagonal close-packed
IBZ	irreducible part of the BZ
ISHE	inverse spin Hall effect
IT	information technology
KKR	Korringa-Kohn-Rostoker
LDA	local density approzimation
MCA	magneto-crystalline anisotropy
SHA	spin Hall angle
SHC	spin Hall conductivity
SHE	spin Hall effect
SOC	spin-orbit coupling
SQA	spin-quantization axis
SRA	scalar-relativistic approximation
XC	exchange-correlation (functional)

1

Introduction

The past advances in information technology (IT) have been mostly achieved through the miniaturization of electric elements, which led to a steady increase of computational power. This road of progress, however, soon leads to an end, because the device-sizes approach the atomic scale, and fundamental problems arise. One of these problems is waste heat, which accompanies a charge current and eventually leads to the destruction of a nano-scale device. On the other hand, the ever growing number of electrical devices — which seem indispensable in our IT-craving society — creates an unmistakable demand for low-power devices; the so-called ***green IT***. A technological revolution is necessary to overcome these challenges. The electron's spin-degree of freedom plays a vital role in this development, leading to the emergence of the field of *spintronics*. As formulated by Žutić *et al.* [1], three key challenges must be mastered from an application point of view: (i) the efficient generation of a spin-current, (ii) the loss-free transport of information encoded in the spin across a device and (iii) the detection of spin-currents. Although methods exist for all three challenges, their up-to-date low efficiency hinders the realization of practically applicable spin-based electronic devices.

The solution lies in the specific design of new materials aimed at creating or enhancing a desired functionality, which pushes applications beyond current limitations. The physical effects, which are at the heart of spintronics, are essentially based on the coupling of the electron's spin and orbital degrees of freedom (spin-orbit coupling, or abbreviated as SOC). SOC effects can be tuned or amplified by microscopic means, *e.g.* by introducing surfaces or interfaces, forming quantum wells, through the interplay with magnetism, through doping with impurities or introducing other kinds of disorder.

This opens the way to many fascinating phenomena and plays the central role in various fields of current research. Among them are the magneto-crystalline anisotropy energy [2, 3] or the Dzyaloshinskii-Moriya interaction [4], which lead to the emergence of non-collinear and non-trivial magnetic structures, such as skyrmions [5–7]. Topological insulators are a recently established field in solid-state physics, where SOC forms non-trivial electronic states on the surface of an insulator, which are extremely robust against external perturbations and lead to dissipationless edge-currents [8]. Closely related are the quantum-spin Hall effect [9–12] and quantum-anomalous Hall effect [13, 14]. The Rashba effect [15, 16] is an example where SOC leads to a spin-polarization of electronic states. The interplay between magnetization and spin-currents is used in spin transfer torques [17–20]. Furthermore, the topological Hall effect is a result of the interplay between SOC, charge currents and non-collinear magnetism [21–23]. The combination of spin-orbit coupling with temperature gradients and heat currents gives rise to many interesting effects in the field of spin-caloritronics [24].

In order to tailor the specific properties of a material, a detailed understanding of the underlying processes on a microscopic level is of utmost importance. Theoretical investigations, in combination with numerical simulations, present a powerful tool to identify the important aspects of a physical effect. In contrast to an experimental situation, theoreticians can work under idealized conditions and include or neglect certain aspects, thus unambiguously linking the effect to a cause. On the other hand, the inclusion of all relevant contributions and their proper treatment in a numerical simulation have to be achieved if an effect is to be described in a correct quantitative manner. This is especially true for SOC effects, since the spin-orbit coupling strength is relatively weak compared to other interactions in solids. Only *ab initio* methods have the desired accuracy to reach predictive power and help to accelerate material development towards applications.

In recent years, the prediction [25–28] and experimental verification [29] of the spin Hall effect (SHE) in non-magnetic materials have opened new paths in spintronics. It enables the generation of pure spin currents in the transverse direction to an applied external electric field. Two main microscopic processes can be distinguished: an intrinsic (band-structure) effect and an extrinsic (disorder-driven) contribution. While the former is closely tied to topological properties and thus leads to dissipationless currents, the extrinsic skew-scattering process is caused by a spin-orbit induced scattering-asymmetry between spin-up and spin-down electrons. Due to the vast number of possible combinations between host materials and dopants, the skew-scattering contribution serves as versatile tool in tailoring material properties.

Through vivid research already conducted on the SHE, the much longer known anomalous Hall effect (AHE) in ferromagnets [30, 31] has regained much attention due to its intimate relation with the SHE. Here, the very similar mechanisms generate both, a transverse charge and spin current, leading to a finite Hall voltage between the two sides of the sample. This makes the AHE, in contrast to the SHE, easier to access from an experimental point of view. Moreover, insights into the mechanisms behind the AHE ultimately lead to a better understanding of the SHE, and vice versa. However, from a theoretical point of view, the AHE presents a greater challenge for two main reasons: First, the absence of time-reversal symmetry leads to an increased number of degrees of freedom. Second, the subtle interplay between the magnetism mediated by d-electrons and spin-orbit coupling effects push state-of-the-art computational methods to their limits.

The SHE and AHE, together with the inverse spin Hall effect (ISHE) in non-magnetic [32] and ferromagnetic [33] materials, display an ideal way for the creation and detection of pure spin currents or spin-polarized charge currents, and thus address two key challenges outlined in the beginning of this introduction. The third key challenge listed by Žutić *et al.* requires the control of spin-relaxation processes [1], which occur through various SOC-mediated mechanisms [34–36].

This thesis attempts to explore the field of the impurity and spin-orbit driven skew-scattering mechanism behind the SHE and AHE, as well as spin-relaxation processes in dilute alloys by theoretical investigations based on the *ab initio* Korringa-Kohn-Rostoker Green-function method. The Fermi surface — which is a unique fingerprint of a metal — is of crucial importance for the determination of transport properties.

In order to go beyond previous attempts, which were mostly based on noble metal hosts [37–41], the study of complex transition-metal compounds is pursued in this work. Therefore, a robust algorithm for the correct and precise determination of complicated, multi-sheeted Fermi surfaces of two-dimensional film systems, as well as three-dimensional bulk materials, was implemented in the beginning of this work. The algorithm is based on a tetrahedron method, allowing for an unambiguous determination of (spin-orbit induced) avoided band crossings. Beyond this rather general tool which enables the evaluation of many material properties beyond the scope of this thesis, a method for calculating the scattering properties of transition metal compounds has been implemented in the same stand-alone program. Our approach to investigate the transport properties is based on a linearized Boltzmann equation, which is, in comparison with other approaches more transparent. This transparency is gained by a clear physical interpretation of the of the quantities that appear within this approach — such as scattering rates, mean-free paths and electron lifetimes. It is efficiently parallelized to scale up to thousands of processors and thus allows for the high accuracy desired to study the AHE and SHE. The high efficiency needed to try a vast number of host-impurity combinations, in order to identify chemical trends and spot promising new materials, is evident.

As a first application of the Fermi-surface part of the newly developed program, the Elliott-Yafet (spin-mixing) parameter of heavy $5d$ transition metal compounds was calculated. The Elliott-Yafet parameter displays the host-crystal contribution to impurity or phonon-triggered spin-relaxation processes. Special focus was laid on a yet unexplored anisotropy of the Elliott-Yafet parameter with respect to the direction of the spin-polarization of electrons, which was proven for the first time to be able to reach gigantic values. The formation of broad spin-flip hot-areas and hot-loops on the Fermi surface, which emerge due to a peculiar character of the electronic states in uniaxial crystals, could be identified as the origin of the effect. Knowing this anisotropy enables the fine tuning of spin-relaxation times for electrons by external fields, and thus provides an extremely useful tool in the design of new materials for spintronic applications.

As a next step, the calculation of the impurity-driven skew-scattering contribution to the AHE in ferromagnetic hosts — ranging from alloys based on a simple bcc iron host to the very complicated and exotic material manganese silicide — was achieved for the first time. A detailed analysis of the Fermi-surface contributions to the AHE reveals the importance of small spin-orbit induced gaps in the band structure. Additionally, the effect of doping the non-magnetic hosts Pd, Pt and Au with magnetic $3d$ impurities was investigated systematically, in order to extract general trends and to identify the driving forces behind the effect. The results show that the transverse current is strongly spin-polarized for most impurity-host combinations, providing a tool to control the spin-flow through an external magnetic field. Finally, the spin Hall effect in non-magnetic metals doped with $4d$ and $5d$ impurities is investigated. An emphasis on the role of an anisotropy with respect to the spin-polarization direction of the electron in uniaxial hcp crystals is made, and for the first time the size of the skew-scattering induced anisotropy has been calculated, showing larger effects than intrinsic contributions to the anisotropy.

This thesis is structured as follows: *Chapter 2* presents the Korringa-Kohn-Rostoker (KKR) formalism as density-functional theory method on which our investigations are based. The foundations of the method are well described in the existing literature, and as a result this section is kept very short. Instead, special focus is given to a coherent and transparent presentation of the relevant equations for an implementation of the method.

In *Chapter 3*, an introduction to the anomalous and spin Hall effects is given. After a short survey of the history of the AHE, the basic equations for the calculation of the skew-scattering contribution via a semi-classical Boltzmann equation are derived.

Chapter 4 presents the details of the newly implemented tetrahedron method for a precise calculation of the Fermi surface within the framework of the KKR method.

In *Chapter 5*, the results of the calculation of the Elliott-Yafet (spin-mixing) parameter are presented. After analyzing the *ab initio* results in $5d$ and $6sp$ transition metals with special focus on the anisotropy with respect to the direction of electron spin-polarization, we turn to a simple model which is able to capture the basic mechanism behind this anisotropy. Afterwards, predictions made by the simple model are verified through explicit band-structure calculations under an applied B-field.

In *Chapter 6*, we turn to the investigation of the anomalous Hall effect in ferromagnetic hosts. We delve into the effect by means of a microscopic analysis in terms of Fermi-surface contributions for various impurities in bcc Fe. We proceed to more complicated alloys — namely the $L1_0$-ordered FePt alloy — and finally to Fe or Ge-doped manganese silicide (MnSi). The latter presents a major challenge due to the complexity of the system with eight atoms in the unit cell and the breaking of many symmetries, in particular, space-inversion symmetry.

Chapter 7 proceeds with the non-magnetic hosts Pd, Pt and Au. Here, we systematically study doping effects upon inclusion of $3d$ transition metal impurities and aim to link the skew-scattering induced anomalous and spin Hall effects to trends of the impurity *d* states which shift through the Fermi energy while going across the $3d$ series.

Finally, in *Chapter 8*, we turn our attention to the SHE and investigate the influence of a vast number of impurities (*i.e.* the $4d$ and $5sp$ impurities from Y to Cd and the $5d$ and $6sp$ impurities from Lu to Pb) in an fcc Ir and hcp Re host. For the latter, we explicitly address an anisotropy of the SHE as the dependence on the spin-polarization direction.

2 The Korringa-Kohn-Rostoker (KKR) method

2.1. Density functional theory

The aim in solid state physics is to solve the many-body problem of N interacting electrons in an external potential,

$$\mathcal{H}\left|\Psi(\vec{r}_1,\dots,\vec{r}_N)\right\rangle = E_0\left|\Psi(\vec{r}_1,\dots,\vec{r}_N)\right\rangle, \tag{2.1}$$

where the Hamilton operator $\mathcal{H}$ contains the electrostatic potentials of the atomic nuclei (in the Born-Oppenheimer approximation), the kinetic energy of the electrons, the electron-electron interaction and possibly relativistic corrections. However, this task becomes extremely difficult – if not impossible – even on modern supercomputers, due to the enormous amount of memory needed to store the many-body wavefunction Ψ: For a single Fe atom with $N = 26$ electrons, the many-body wavefunction has a dimension of $3 \cdot 26 = 78$. Working on a real-space grid with only 10 grid-points per dimension results in a demand to store 10^{78} numbers, which is close to the total number of atoms in the universe. Thus, any attempt to work with the full many-body wavefunction evidently fails.

However, Hohenberg and Kohn [42] showed by general principles, that any ground state observable can be expressed as functional of the ground-state electron-density $n_0(\vec{r})$ of the system. The density is only dependent on three space-coordinates ($\vec{r} = (x, y, z)^{\mathrm{T}}$), compared to the $3N$ coordinates of Ψ. Moreover, Hohenberg and Kohn stated that the functional determining the total energy of the system becomes minimal for the ground-state density, which yields a 'recipe' for obtaining n_0 out of all possible allowed densities.

Unfortunately, this energy functional is unknown. A clever way of approximating the ground-state density nevertheless is to introduce an auxiliary, fictitious system of *non*-interacting electrons that yields the same density as the interacting electron system [43]. This so-called Kohn-Sham system of non-interacting electrons allows to make reasonable approximations to the energy functional. Most importantly, a big part of the kinetic energy of the electrons is treated exactly [44]. Also the Hartree part of the electron-electron interaction is described exactly. The remaining parts are summed up in an unknown part, the so-called exchange-correlation potential, where more or less sophisticated approximations can be made. All these parts add up to an *effective* Kohn-Sham potential in which the non-interacting electrons move. In these terms, the complexity of the initial problem was reduced enormously and can be solved by numerical simulations with a desired accuracy.

It remains to find a reasonable approximation to the exchange-correlation part to the effective potential. As starting point serves the homogeneous electron gas (HEG), where the exchange-correlation contribution to the energy per particle ϵ_{xc} can be calculated. Then, the contribution of volume $\mathrm{d}\vec{r}$ around a point $\vec{r}$ to the total exchange-correlation energy is approximated by the value if the whole electron gas was homogeneous with density $n(\vec{r})$, *i.e.*

$$E_{\mathrm{xc}} = \int \mathrm{d}\vec{r}\; n(\vec{r})\, \epsilon_{\mathrm{xc}}(n(\vec{r}))\,. \tag{2.2}$$

In fact, the exchange part for the HEG is known exactly by the Fock integral to be $\epsilon_{\mathrm{x}} = A_{\mathrm{x}}\, n^{1/3}$ (with a constant A_{x}) [45] the correlation part can be obtained exact expressions for the high- and low-density limits and augmented by quantum Monte Carlo calculations for densities in between. There exist different parametrizations to the latter, yielding different LDA xc-functionals, *e.g.* [46–48]. In our calculations, we employ the parametrization of Vosko, Wilk and Nusair [46].

2.2. The KKR Green function method

Introduction to Green functions

The concept of Green functions was introduced by the English mathematician George Green. In the field of differential equations, a Green function $G(x, x'; z)$ is the solution of the equation

$$(z - \mathcal{L})\; G(x, x'; z) = \delta(x - x')\ , \tag{2.3}$$

where $\mathcal{L}$ is a given linear differential operator, z is a scalar parameter (normally a real or complex valued number) and $\delta(x - x')$ is the Dirac delta function. Once the Green function is known, a solution $f(x)$ to the differential equation

$$(z - \mathcal{L})\, f(x) = h(x) \tag{2.4}$$

can be found easily for any inhomogeneity $h(x)$ by integration of the Green function,

$$f(x) = f_0(x) + \int \mathrm{d}x'\; G(x, x'; z)\, h(x')\ , \tag{2.5}$$

where $f_0(x)$ is a solution to the differential equation (2.4) without inhomogeneity $(h = 0)$.

Green functions in solid state physics

In the focus of solid state physics is the quantum-mechanical Schrödinger equation (or other differential equations, *e.g.* the Dirac equation), where the differential operator is the Hamiltonian

$$\mathcal{H} = \mathcal{K} \otimes \sigma_0 + \mathcal{V} \tag{2.6}$$

with the kinetic energy operator $\mathcal{K}$, the identity operator in spin-space σ_0 and the potential $\mathcal{V}$, which might be a full matrix in spin-space (*e.g.* if spin-orbit coupling is included in $\mathcal{V}$). Representing this Hamiltonian in real- and spin-space basis, (using atomic Rydberg units) we obtain the well known equation

$$\begin{aligned} \langle \vec{r}, \sigma | \, \mathcal{H} \, | \vec{r}\,', \sigma' \rangle &= \mathcal{H}^{\sigma,\sigma'}(\vec{r}, \vec{r}\,') & (2.7) \\ &= -\left(\frac{\partial^2}{\partial \vec{r}^{\,2}} \, \delta(\vec{r} - \vec{r}\,') \right) \delta_{\sigma,\sigma'} + V^{\sigma,\sigma'}(\vec{r}, \vec{r}\,') \ , & (2.8) \end{aligned}$$

with $\sigma \in \{\uparrow, \downarrow\}$. The definition of the Green function in a basis-independent representation reads

$$(E - \mathcal{H})\mathcal{G}(E) = \mathbb{1} \ , \tag{2.9}$$

where $\mathbb{1}$ is the identity operator and E the energy. Hence, the Green function depends on an energy parameter E and can be formally written as the inverse of the operator $\mathcal{G}(E) = (E - \mathcal{H})^{-1}$.

It is equivalent to search for the wavefunctions $|\, \psi_i \,\rangle$ and eigenenergies ϵ_i of the system on the one hand, or the Green function $\mathcal{G}(E)$ on the other. Both quantities contain all information about the system, as becomes evident when $\mathcal{G}(E)$ is written in the so-called spectral representation,

$$\mathcal{G}^{\pm}(E) = \sum_i \frac{|\, \psi_i \,\rangle \, \langle\, \psi_i \,|}{E - \epsilon_i \pm i\gamma} \ , \tag{2.10}$$

where a small imaginary part ($\gamma \to 0^+$) was added to avoid singularities when $E = \epsilon_i$. Depending on the sign of the imaginary part, one obtains two equivalent but yet different Green functions, which are called *retarded* ($\mathcal{G}^+$) and *advanced* ($\mathcal{G}^-$), respectively. For the rest of this thesis, we work with the retarded Green function and simply write $\mathcal{G}(E)$ omitting the superscript. Note that the sum in Eq. (2.10) runs over all possible eigenstates i in the system. Representing now $\mathcal{G}(E)$ in real- and spin-space, we arrive at

$$G^{\sigma,\sigma'}(\vec{r}, \vec{r}\,'; E) = \langle \vec{r}, \sigma | \, \mathcal{G}(E) \, | \vec{r}\,', \sigma' \rangle = \sum_i \frac{\psi_i^{\sigma}(\vec{r}) \ \left(\psi_i^{\sigma'}(\vec{r}\,')\right)^*}{E - \epsilon_i + i\gamma} \ , \tag{2.11}$$

where the star denotes complex conjugation and transposition in case of spinors. The nominator can be interpreted in terms of wave-packet propagation as an outgoing wave at $\vec{r}$, generated by a source at $\vec{r}\,'$. Therefore, the Green function is also often called a *propagator*. In this interpretation, the difference between retarded and advanced Green functions is, that they describe the propagation of an electron forward and backward in time, respectively.

Due to the spectral representation (2.10) the Green function can be calculated by first obtaining the eigenstates of the system by diagonalization of the Hamiltonian. On the other hand, if the Green function can be obtained first, then the wavefunctions can be calculated by diagonalizing the Green function $G^{\sigma,\sigma'}(\vec{r},\vec{r};E)$.

In our method of choice, the KKR Green function method, the sum in Eq. (2.10) is avoided by solving directly Eq. (2.9) based on a multiple scattering ansatz, as we will see later.

Charge density from the Green function

Any ground-state observable A can be obtained from the Green function via

$$\langle A\rangle = -\frac{1}{\pi}\mathrm{Im}\int_{-\infty}^{E_\mathrm{F}} \mathrm{d}E\ \mathrm{Tr}\left[\mathcal{A}\,\mathcal{G}(E)\right] \tag{2.12}$$

by using the appropriate operator $\mathcal{A}$ and E_F is the Fermi energy. For the central quantity in density functional theory, the charge density $\rho(\vec{r})$, this operator is given by the projection operator $\mathcal{P}_{\vec{r}}$ onto the position $\vec{r}$, which reads (σ_0 is the identity operator in spin space)

$$\mathcal{P}_{\vec{r}} = |\,\vec{r}\,\rangle\,\langle\,\vec{r}\,|\otimes\sigma_0 = \sum_\sigma |\,\vec{r},\sigma\,\rangle\,\langle\,\vec{r},\sigma\,|\ . \tag{2.13}$$

By evaluating the trace over real- and spin-space,

$$\mathrm{Tr}\left[\mathcal{X}\right] = \sum_{\sigma'}\int \mathrm{d}\vec{r}\,'\,\langle\,\vec{r}\,',\sigma'\,|\,\mathcal{X}\,|\,\vec{r}\,',\sigma'\,\rangle\ , \tag{2.14}$$

we arrive at

$$\rho(\vec{r}) = -\frac{1}{\pi}\ \mathrm{Im}\sum_\sigma\ \int_{-\infty}^{E_\mathrm{F}} \mathrm{d}E\ G^{\sigma,\sigma}(\vec{r},\vec{r};E)\ . \tag{2.15}$$

Note that only the diagonal elements of the Green function $\mathcal{G}(E)$ enter this expression. Omitting the energy integration and summation over the spin-index, we obtain the spin- and space-resolved density of states,

$$n^\sigma(\vec{r},E) = -\frac{1}{\pi}\mathrm{Im}G^{\sigma,\sigma}(\vec{r},\vec{r};E)\ . \tag{2.16}$$

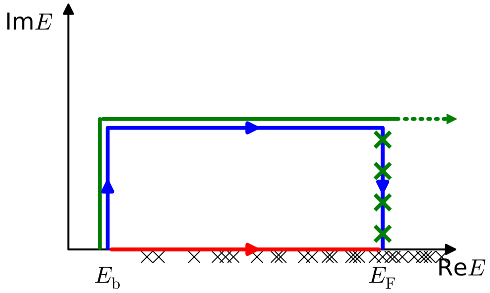

Figure 2.1.: The integration over the valence states in Eq. (2.17) (starting from E_b up to the Fermi energy E_F, red line) is replaced by a contour integral in the complex plane (blue line). By introducing a Fermi function, the contour can formally be extended to infinity (green line), but the residues at the Matsubara energies have to be accounted for (green crosses). The poles of the Green function lie infinitesimally below the real axis (black crosses).

Energy integration

Although we consider mainly general aspects of the Green function in this introductory section, we stress here some aspects of the energy integration in Eq. (2.12). One in practice distinguishes between the states which are very low in energy (core states) on the one hand, and the valence and conduction bands on the other. Because the core states are highly localized, they can be treated separately and are excluded from the integral. Thus, the lower limit of the integral can start below the lowest valence band (but higher than the highest core state),

$$\int_{-\infty}^{E_\mathrm{F}} = \sum_{\text{core states}} + \int_{E_\mathrm{b}}^{E_\mathrm{F}} \tag{2.17}$$

However, even after truncating the energy integration to the valence band region, this remains a numerically very cumbersome task: due to the aforementioned poles of the Green function at the eigenenergies, many sampling points are needed to evaluate the value of the integral correctly. This problem can be overcome by extending the energy integration on the real axis (red line in Fig. 2.1) to a contour integral in the complex-energy plane (blue line), as introduced by Wildberger *et al.* [49]. This is possible due to the analytical behavior of the Green function in the upper half of the complex plane: due to the introduction of the small positive parameter $\gamma \to 0^+$ in Eq. (2.10), all poles of $\mathcal{G}$ actually lie below the real axis. The advantage is, that the pole contribution of the Green function becomes broadened at energies with finite imaginary part, and only a few energy points (usually 40-50) are needed to sample the integral correctly. Additionally, to improve the convergence in a self-consistent calculation and speed up the calculation, the integrand in Eq. (2.12) is weighted by a Fermi function,

$$f_T(E - E_\mathrm{F}) = \frac{1}{1 + \exp\left(\beta\left(E - E_\mathrm{F}\right)\right)} \tag{2.18}$$

where $\beta = 1/(k_\mathrm{B}\,T)$ is the inverse temperature and k_B the Boltzmann constant. In this way the integration is formally extended to infinity (*cf.* green line in Fig. 2.1),

$$\langle A\rangle = -\frac{1}{\pi}\mathrm{Im}\int_{E_\mathrm{b}}^{\infty} \mathrm{d}E\; f_T(E - E_\mathrm{F})\; \mathrm{Tr}\left[\mathcal{A}\,\mathcal{G}(E)\right]\,, \tag{2.19}$$

but in practice it is sufficient to stop a bit above E_F when the Fermi function vanishes. Because the Fermi distribution has poles in the complex plane at $E_\mathrm{F} \pm (2n-1)\pi\,i/\beta$ we also have to account for the residues of the integrand at these so called Matsubara energies (green crosses).

Left- and right solutions

The operator $E - \mathcal{H}$, which defines the Green function, is non-hermitian if the energy E is chosen to be a complex number. This operator has left- and right solutions

$$\begin{aligned} (E-\mathcal{H})\,|\,\omega\,\rangle &= 0\,, && (2.20)\\ \langle\,\bar{\omega}\,|\,(E-\mathcal{H}) &= 0\,, && (2.21) \end{aligned}$$

where we denoted the left solution by a bar. By choosing a different symbol (ω instead of ψ), we highlight that $|\,\omega\,\rangle$ is not a state in the Hilbert space (this would only be true for real energies of the Hamiltonian).

The Green function is both, the left and right inverse of this operator,

$$\begin{aligned} \mathcal{G}(E)\,(E-\mathcal{H}) &= \mathbb{1}\,, && (2.22)\\ (E-\mathcal{H})\,\mathcal{G}(E) &= \mathbb{1}\,. && (2.23) \end{aligned}$$

Later we will use that $\mathcal{G}$ can be written in terms of the solutions (2.20) and (2.21), where we will need both, the left and right hand side solutions.

Dyson equation

Let us now come to the big advantage of the Green function method that enables not only the efficient calculation of the Green function of the crystal *without* knowledge of the wavefunctions, but also the efficient treatment of perturbed systems. Assume that the Hamiltonian $\mathcal{H}$ describing the system of interest can be split into two parts,

$$\mathcal{H} = \mathcal{H}_0 + \Delta\mathcal{V}\,, \tag{2.24}$$

where $\mathcal{H}_0$ is the Hamiltonian of a simpler system to which the Green function $\mathcal{G}_0(E)$ is known and $\Delta\mathcal{V}$ is regarded as perturbation. Then the Green function of interest can be related to $\mathcal{G}_0(E)$ by the Dyson equation,

$$\mathcal{G} = \mathcal{G}_0 + \mathcal{G}_0 \, \Delta\mathcal{V} \, \mathcal{G} \ , \tag{2.25}$$

as can be easily verified by inserting Eq. (2.24) into the definition of $\mathcal{G}$ (Eq. (2.9)) and employing $(E - \mathcal{H}_0) = (\mathcal{G}_0)^{-1}$. The Green function of interest appears on the left and right hand side of Eq. (2.25), which can be solved by repetitively inserting the equation into itself, leading to an expansion in powers of $\Delta\mathcal{V}$,

$$\mathcal{G} = \mathcal{G}_0 + \mathcal{G}_0 \, \Delta\mathcal{V} \, \mathcal{G}_0 + \mathcal{G}_0 \, \Delta\mathcal{V} \, \mathcal{G}_0 \, \Delta\mathcal{V} \, \mathcal{G}_0 + \ldots \ . \tag{2.26}$$

This series expansion, also sometimes called Born series, represents an efficient way to calculate $\mathcal{G}$ if the perturbation $\Delta\mathcal{V}$ is small and the right hand side can be truncated after a few terms. However, if the perturbation is not small, the Dyson equation can be transformed to

$$\mathcal{G} = \left(\mathbb{1} - \mathcal{G}_0 \, \Delta\mathcal{V}\right)^{-1} \mathcal{G}_0 \ , \tag{2.27}$$

which can be directly evaluated. However, due to the inversion operation, this is computationally more demanding.

Lippmann-Schwinger equation

Similarly to the Dyson equation for Green functions, the wavefunctions of an perturbed and unperturbed system,

$$\begin{aligned} \mathcal{H}_0 \, |\, \psi_0 \,\rangle &= E \, |\, \psi_0 \,\rangle && (2.28) \\ (\mathcal{H}_0 + \Delta\mathcal{V}) \, |\, \psi \,\rangle &= E \, |\, \psi \,\rangle && (2.29) \end{aligned}$$

are related to each other by the Lippmann-Schwinger equation

$$|\, \psi \,\rangle = |\, \psi_0 \,\rangle + \underbrace{\mathcal{G}_0(E) \, \Delta\mathcal{V} \, |\, \psi \,\rangle}_{:=|\, \psi_{\mathrm{sc}} \,\rangle} \ . \tag{2.30}$$

The second term on the right hand side is also called *scattered wave*, $|\, \psi_{\mathrm{sc}} \,\rangle$. It can be easily verified by inserting Eq. (2.30) into Eq. (2.29) that the ansatz for $|\, \psi \,\rangle$ indeed fulfills the Schrödinger equation for the perturbed system. The Lippmann-Schwinger equation can again be solved by iteration, which leads to the Born series expansion, or by transforming Eq. (2.30) to

$$\left(\mathbb{1} - \mathcal{G}_0(E) \, \Delta\mathcal{V}\right) |\, \psi \,\rangle = |\, \psi_0 \,\rangle \tag{2.31}$$

and solving it by inversion.

The Lippmann-Schwinger equation can be interpreted in terms of scattering off a perturbing potential. Suppose an incoming electron with wavefunction $|\, \psi_0 \,\rangle$ (before the scattering event) is approaching the scattering region. Without the scattering potential, it would still evolve as described by $|\,\psi_0\,\rangle$ (first term on the r.h.s. of Eq. (2.30)). The scattering potential introduces deviations from this limit as given by the second term. The result is an outgoing wave $|\,\psi\,\rangle$, which is a superposition of eigenstates of the system $\mathcal{H}_0$.

The form of the Lippmann-Schwinger presented in Eq. (2.30) is only valid if the energy E is an eigenenergy to both systems, $\mathcal{H}_0$ and $\mathcal{H}$. If there exists an eigenstate of $\mathcal{H}$ at an energy which is not included in the spectrum of $\mathcal{H}_0$, the first term on the right hand side of Eq. (2.30) vanishes and we obtain

$$|\,\psi\,\rangle = \mathcal{G}_0(E)\,\Delta\mathcal{V}\;|\,\psi\,\rangle \qquad (E \notin \{\epsilon_i^0\}) \;. \tag{2.32}$$

T-matrix

In the spirit of scattering off an impurity, the transition matrix $\mathcal{T}(E)$ is introduced by the definition

$$\Delta\mathcal{V}\,|\,\psi\,\rangle = \mathcal{T}(E)\,|\,\psi_0\,\rangle \;\;, \tag{2.33}$$

which transforms the Lippmann-Schwinger and Dyson equation into

$$|\,\psi\,\rangle = |\,\psi_0\,\rangle + \mathcal{G}_0(E)\,\mathcal{T}(E)\;|\,\psi_0\,\rangle \;\;, \tag{2.34}$$

$$\mathcal{G}(E) = \mathcal{G}_0 + \mathcal{G}_0(E)\,\mathcal{T}(E)\,\mathcal{G}_0 \;. \tag{2.35}$$

This way, the problem of solving the Lippmann-Schwinger and Dyson equation is translated to finding the $\mathcal{T}$-matrix of the system,

$$\mathcal{T}(E) = \Delta\mathcal{V}\,(\mathbb{1} + \mathcal{G}_0(E)\,\mathcal{T}(E)) \;\;. \tag{2.36}$$

Conclusions

Thus, we have a set of equivalent equations of similar complexity, *i.e.* the Dyson equation (2.25), the Lippmann-Schwinger equation (2.30) and the equation to determine the $\mathcal{T}$-matrix (2.36). Only one of them must be solved and the other quantities can be determined successively.

In the code used in this thesis, the solution of the Lippmann-Schwinger equation for the system of interest is pursued. We will also encounter some $\mathcal{T}$-matrices and Dyson-equations in the more detailed description of the method (see the following sections). This is due to the KKR ansatz, *i.e.* the separation into (i) scattering properties of single atoms in a reference system and (ii) the multiple scattering ansatz for the crystal properties.

2.3. Single-site scattering

Free space

In this section we deal with the scattering properties of a single atom in free space, *i.e.* the Hamiltonian of the reference potential is just the kinetic energy operator, $\mathcal{H}_0 = \mathcal{K} \otimes \sigma_0$. Because the spatial part of the Hamiltonian is identical for the two spin-channels, we neglect the spin-degree of freedom for a moment to simplify the notation. The eigenfunctions of $\mathcal{K}$ are just plane waves,

$$\begin{aligned} \langle\, \vec{r}\, |\, \varphi_{\vec{k}}\, \rangle = \varphi_{\vec{k}}(\vec{r}) &= \mathrm{e}^{i\,\vec{k}\cdot\vec{r}} && (2.37)\\ &= \sum_L 4\pi\, i^\ell\, j_\ell(\kappa r)\, Y_L(\hat{r})\, Y_L(\hat{k})\ . && (2.38) \end{aligned}$$

In the second line, the plane wave has been expanded in real spherical harmonics $Y_L(\hat{x})$ and the expansion coefficients are given by spherical Bessel functions $j_\ell(x)$. The angular momentum and magnetic quantum numbers are combined to the multi-index, $L = (\ell, m)$. We further used $\kappa = |\vec{k}| = \sqrt{E}$, $r = |\vec{r}|$ is the magnitude and $\hat{r} = \vec{r}/r$ is the direction of $\hat{r}$.

The Green function for free space (here denoted by the lowercase symbol g instead of $\mathcal{G}$) is also known analytically to be

$$g(\vec{r}, \vec{r}\,'; E) = -\frac{1}{4\pi}\, \frac{\mathrm{e}^{i\,\kappa|\vec{r}-\vec{r}\,'|}}{|\vec{r}-\vec{r}\,'|} \tag{2.39}$$

and can be expanded in a similar way,

$$\begin{aligned} g(\vec{r}, \vec{r}\,'; E) &= \sum_L Y_L(\hat{r})\, \frac{1}{r\, r'}\, g_\ell(r, r'; E)\ Y_L(\hat{r}')\ , \qquad \text{with} && (2.40)\\ g_\ell(r, r'; E) &= \kappa\, r\, r'\ j_\ell(\kappa r_<)\ h_\ell(\kappa r_>)\ , && (2.41) \end{aligned}$$

where $r_{<(>)}$ is the smaller (larger) radius of r and r' and $h_\ell(x) = n_\ell(x) - i\, j_\ell(x)$ is the spherical Hankel function, and $n_\ell(x)$ is the spherical Neumann function (also called spherical Bessel function of second kind)[1].

The spherical Bessel and Hankel functions are two linearly independent solutions to the radial Schrödinger equation of free space. Thus, any linear combination of the two is also a solution to the differential equation. However, only the Bessel function enters Eq. (2.38) and determines the physical solutions, because the Hankel function diverges as $h(x) \sim 1/x^{\ell+1}$ for $x \to 0$ and thus cannot be normalized. However, both solutions enter Eq. (2.41) for the Green function.

---

[1] We use a definition of the Hankel function which is in agreement to Drittler [50], but differs from other works [51–53] by a factor $(-i)$, which modifies some of the equations.

To simplify some equations in the subsequent chapters, the factor $1/(r\,r')$ was introduced in the expansion (2.40), and the expansion factor (2.41) can be conveniently rewritten as

$$g_\ell(r,r';E) = \kappa\ \left[\Theta(r'-r)\ J_L(r;E)\ H_L(r';E) + \Theta(r-r')\ H_L(r;E)\ J_L(r';E)\right]\ ,$$
$$\text{with}\quad J_L(r;E) = r\,j_\ell(\kappa r)\ ,\quad H_L(r;E) = r\,h_\ell(\kappa r)\ ,\quad \kappa = \sqrt{E} \tag{2.42}$$

Taking the spin degree of freedom into account, we have two degenerate, linearly independent eigenfunctions of $\mathcal{H}_0$ at every $\vec{k}$, which we label $|\,\psi^0_{\vec{k},\uparrow}\rangle$ and $|\,\psi^0_{\vec{k},\downarrow}\rangle$. A convenient choice for these eigenfunctions is

$$\begin{aligned}\langle\,\vec{r},\sigma\,|\,\psi^0_{\vec{k},s}\,\rangle &= \varphi^0_{\vec{k}}(\vec{r})\ \delta_{\sigma,s} &(2.43)\\ &= \mathrm{e}^{i\,\vec{k}\cdot\vec{r}}\quad \delta_{\sigma,s}\quad \text{for}\quad s\in\{\uparrow,\downarrow\} &(2.44)\end{aligned}$$

or written as spinors

$$\begin{aligned}\boldsymbol{\Psi}^0_{\vec{k},\uparrow} &= \varphi^0_{\vec{k}}(\vec{r})\ \boldsymbol{\chi}^{\uparrow}\quad\text{and} &(2.45)\\ \boldsymbol{\Psi}^0_{\vec{k},\downarrow} &= \varphi^0_{\vec{k}}(\vec{r})\ \boldsymbol{\chi}^{\downarrow}\ , &(2.46)\end{aligned}$$

i.e. they are chosen to be parallel to the basis vectors of spin space. Any pair of linear combinations of $\boldsymbol{\Psi}^0_{\vec{k},\uparrow}$ and $\boldsymbol{\Psi}^0_{\vec{k},\downarrow}$ such that they form a basis for the degenerate subspace would also be a valid choice.

The green function of free space including spin then simply reads

$$g^{\sigma\sigma'}(\vec{r},\vec{r}\,';E) = \delta_{\sigma,\sigma'}\ \underbrace{g(\vec{r},\vec{r}\,';E)}_{\text{cf. (2.40)}} \tag{2.47}$$

Atomic potential of finite range

Next, we consider a potential of finite range embedded in free space, described by the Hamiltonian $\mathcal{H} = \mathcal{K}\otimes\sigma_0 + \mathcal{V}$. Here, the perturbing potential $\mathcal{V}$ shall be understood as matrix in spin-space with possible off-diagonal terms (as it is the case if spin-orbit coupling is included). In real- and spin-space representation we obtain

$$\begin{aligned}\langle\vec{r},\sigma|\,\mathcal{V}\,|\vec{r}\,',\sigma'\rangle &= V^{\sigma\sigma'}(\vec{r},\vec{r}\,')\quad\text{with} &(2.51)\\ V^{\sigma\sigma'}(\vec{r},\vec{r}\,') &= \begin{cases}\sum\limits_{L,L'}\frac{1}{r^2}\ V^{\sigma\sigma'}_{LL'}(r)\ Y_L(\hat{r})\ Y_{L'}(\hat{r}')\ \delta(r-r') & |\vec{r}|\le R\\ 0 & |\vec{r}|>R\end{cases}\quad\text{for} &(2.52)\end{aligned}$$

In other works, the potential is often denoted as dependent on only one spatial vector, *e.g.* $V^{\sigma\sigma'}(\vec{r})$. However, we need to explicitly consider both spatial arguments

Notation for spinors

Suppose the symbol $|\,\psi_k\,\rangle$ describes the state of a spin-$\frac{1}{2}$-particle. The label k can also be a multi-index. Representing this state in a basis of real- and spin-space yields

$$|\,\psi_k\,\rangle = \sum_{\sigma=\uparrow,\downarrow} \int \mathrm{d}\vec{r}\; \psi_k^{\sigma}(\vec{r})\;\; |\,\vec{r}\,\rangle \otimes |\,\sigma\,\rangle \;\; . \tag{2.48}$$

The basis vectors of spin space are commonly represented by (2×1)-vectors,

$$|\!\uparrow\rangle \equiv \boldsymbol{\chi}^{\uparrow} \equiv \begin{pmatrix} 1 \\ 0 \end{pmatrix} \quad \text{and} \quad |\!\downarrow\rangle \equiv \boldsymbol{\chi}^{\downarrow} \equiv \begin{pmatrix} 0 \\ 1 \end{pmatrix} \;\; , \tag{2.49}$$

leading to the spinor-form of $|\,\psi_k\,\rangle$,

$$\langle\,\vec{r}\,|\,\psi_k\,\rangle \equiv \boldsymbol{\Psi}_k(\vec{r}) \equiv \sum_{\sigma} \psi_k^{\sigma}(\vec{r})\;\boldsymbol{\chi}^{\sigma} \equiv \begin{pmatrix} \psi_k^{\uparrow}(\vec{r}) \\ \psi_k^{\downarrow}(\vec{r}) \end{pmatrix} \;\; . \tag{2.50}$$

Thus, bold symbols are used to indicate a vector in spin-space in our notation.

$\vec{r}$ and $\vec{r}\,'$ if they couple through semi-local or non-local contributions contained in the potential. This is the case for spin-orbit coupling, where the angular momentum operator $\mathcal{L} = \hat{r} \times \hat{p}$ contains a spatial derivative (as can be seen if the momentum operator is expressed in real-space basis), and thus the spin-orbit coupling operator is semi-local in real space.

Lippmann-Schwinger equation

The Lippmann-Schwinger equations for the two linear independent solutions of $\mathcal{H}_0$ in real- and spin-space read

$$\psi^{\sigma}_{\vec{k},\uparrow}(\vec{r}) \;=\; \mathrm{e}^{i\,\vec{k}\cdot\vec{r}}\,\delta_{\sigma,\uparrow} + \sum_{\sigma''} \int \mathrm{d}\vec{r}\,'\,\mathrm{d}\vec{r}\,''\, g(\vec{r},\vec{r}\,')\; V^{\sigma,\sigma''}(\vec{r}\,',\vec{r}\,'')\; \psi^{\sigma''}_{\vec{k},\uparrow}(\vec{r}\,'') \;, \tag{2.53}$$

$$\psi^{\sigma}_{\vec{k},\downarrow}(\vec{r}) \;=\; \mathrm{e}^{i\,\vec{k}\cdot\vec{r}}\,\delta_{\sigma,\downarrow} + \sum_{\sigma''} \int \mathrm{d}\vec{r}\,'\,\mathrm{d}\vec{r}\,''\, g(\vec{r},\vec{r}\,')\; V^{\sigma,\sigma''}(\vec{r}\,',\vec{r}\,'')\; \psi^{\sigma''}_{\vec{k},\downarrow}(\vec{r}\,'') \;. \tag{2.54}$$

This form is derived from Eq. (2.30) by inserting identity operators,

$$\begin{aligned} \langle\,\vec{r},\sigma\,|\,\psi_{\vec{k},s}\,\rangle \;&=\; \langle\,\vec{r},\sigma\,|\,\psi^{0}_{\vec{k},s}\,\rangle \qquad\qquad (2.55)\\ &+\; \sum_{\sigma'\sigma''} \int \mathrm{d}\vec{r}\,'\;\mathrm{d}\vec{r}\,''\;\; \underbrace{\langle\vec{r},\sigma|\,g\,|\vec{r}\,',\sigma'\rangle}_{=g(\vec{r},\vec{r}\,')\,\delta_{\sigma,\sigma'}} \underbrace{\langle\vec{r}\,',\sigma'|\,\mathcal{V}\,|\vec{r}\,'',\sigma''\rangle}_{\text{cf. Eq. (2.51)}} \langle\,\vec{r}\,'',\sigma''\,|\,\psi_{\vec{k},s}\,\rangle \;, \end{aligned}$$

and inserting Eq. (2.44) for the first term on the right hand side, we obtain Eq. (2.53) for $s = \uparrow$ and Eq. (2.54) for $s = \downarrow$.

The Lippmann-Schwinger equations (2.53) and (2.54) each represents a set of two coupled differential equations for every k-point. They can also be cast into a spinor-form [52]

$$\mathbf{\Psi}_{\vec{k},s}(\vec{r}) \;=\; \mathrm{e}^{i\,\vec{k}\cdot\vec{r}}\,\boldsymbol{\chi}^{s} + \int \mathrm{d}\vec{r}\,'\,\mathrm{d}\vec{r}\,''\,g(\vec{r},\vec{r}\,')\;\mathbf{V}(\vec{r}\,',\vec{r}\,'')\;\mathbf{\Psi}_{\vec{k},s}(\vec{r}\,'') \qquad (2.56)$$

with $s \in \{\uparrow,\downarrow\}$ and $\mathbf{V}(\vec{r}\,',\vec{r}\,'')$ is to be understood as a (2×2)-matrix in spin-space.

The first term on the right hand side of Eqs. (2.53) and (2.54) represents the two linear independent eigenstates of the potential-free system $\mathcal{H}_0$, described by the quantum numbers $\vec{k}$ and s. The eigenstate $\mathbf{\Psi}_{\vec{k},s}(\vec{r})$ of the full Hamiltonian $\mathcal{H}$ inherits these numbers as labels, but they are not “good” quantum numbers in the usual sense (*e.g.* “spin” is not a good quantum number if spin-orbit coupling is present).

Next, we expand the eigenfunctions in real spherical harmonics [54],

$$\begin{aligned}
\psi^{\sigma}_{\vec{k},s}(\vec{r}) &= \sum_{L} 4\pi i^{\ell}\; R^{\sigma s}_{L}(\vec{r};E)\;Y_L(\hat{k}) && (2.57)\\
&= \sum_{L,L'} 4\pi i^{\ell}\;\frac{1}{r}\,R^{\sigma s}_{L'L}(r;E)\;Y_L(\hat{k})\;Y_{L'}(\hat{r}) \quad \text{with} && (2.58)\\
R^{\sigma s}_{L}(\vec{r};E) &= \sum_{L'} \frac{1}{r}\;R^{\sigma s}_{L'L}(r;E)\;Y_{L'}(\hat{r})\;. && (2.59)
\end{aligned}$$

First, the expansion of the vector $\vec{k}$ leads to a combined angular momentum index L, then the expansion of $\vec{r}$ leads to the index L'. Note that in our notation, the indices s and L (the latter originating from $\vec{k}$), which are associated with the boundary conditions, are the indices to the right of $R^{\sigma s}_{L'L}$. Inserting the expansion (2.58) into the Lippmann-Schwinger equation (2.53), we arrive after a lengthy calculation (*cf.* appendix A.2 or Ref. [52]) at a reformulated Lippmann-Schwinger equation for the radial part $R^{\sigma s}_{L'L}(r;E)$,

$$R^{\sigma s}_{L'L}(r;E) = J_L(r;E)\;\delta_{L',L}\;\delta_{\sigma,s} + \sum_{\sigma'',L''}\int \mathrm{d}r''\;g_{\ell'}(r,r'';E)\;V^{\sigma\sigma''}_{L'L''}(r'')\;R^{\sigma''s}_{L''L}(r'';E)\;. \qquad (2.60)$$

Similarly to the case of free space, where a regular and irregular solution to the radial Schrödinger equation are found (Bessel and Hankel functions), also a irregular solution to the radial Schrödinger equation with potential can be found. The resulting Lippmann-Schwinger equation for the irregular solution $S^{\sigma s}_{L'L}(r;E)$ reads

$$S^{\sigma s}_{L'L}(r;E) = H_L(r;E)\;\beta^{\sigma s}_{L'L}(E) + \sum_{\sigma'',L''}\int \mathrm{d}r''\;g_{\ell'}(r,r'';E)\;V^{\sigma\sigma''}_{L'L''}(r'')\;S^{\sigma''s}_{L''L}(r'';E)\;, \qquad (2.61)$$

where the factors $\beta^{\sigma s}_{L'L}(E)$ were introduced. It is convenient to chose them such (see next section about the single-site Green function), that the irregular solutions $S^{\sigma s}_{L'L}(r;E)$ coincide with the Hankel functions as irregular solutions of free space outside the scattering region [50],

$$S^{\sigma s}_{L'L}(r;E) = H_L(r;E)\ \delta_{L,L'}\ \delta_{\sigma,s} \quad \text{for } r > R. \tag{2.62}$$

These correct boundary conditions are fulfilled by (for a proof see Drittler [50])

$$\beta^{\sigma s}_{L'L}(E) = \delta_{L',L}\ \delta_{\sigma,s} - \kappa \int \mathrm{d}r'\ J_L(r';E) \sum_{\sigma'',L''} V^{\sigma\sigma''}_{L'L''}(r')\ S^{\sigma'' s}_{L''L}(r';E)\ . \tag{2.63}$$

A possibility to obtain the solution to the radial Lippmann-Schwinger equations (2.60) and (2.61) is to rewrite them as Born series expansion. However, this series is not guaranteed to converge since $g_\ell(r,r')$ and $H_L(r;E) = r\,h_\ell(\kappa r)$ diverge for small arguments. In practice, it turns out that the regular solution converges for most atomic potentials, but the irregular solution does not converge when spin-orbit coupling is included. Therefore, a direct solution of Eqs. (2.60) and (2.61) is pursued by expanding the radial dependency in Chebyshev polynomials $T_n(x)$, *i.e.*

$$f(x) = \sum_{j=0}^{\infty} a_j\ T_j(x)\ . \tag{2.64}$$

In practice it is sufficient to truncate the expansion after N terms. Then, also the integration can be represented as a $(N \times N)$-matrix, and the solutions R and S can be found by matrix-inversion. For details we refer to the work of Bauer [54].

To be more precise, the functions R and S are called the regular and irregular *right* solutions of the radial Lippmann-Schwinger equation. Similarly, the regular and irregular *left* solutions (denoted by an overbar) are defined by [54]

$$\bar{R}^{s\sigma}_{LL'}(r;E) = \delta_{L,L'}\ \delta_{s,\sigma}\ J_{L'}(r;E) + \sum_{\sigma'',L''} \int \mathrm{d}r''\ \bar{R}^{s\sigma''}_{LL''}(r'';E)\ V^{\sigma''\sigma}_{L''L'}(r'')\ g_{\ell'}(r'',r;E) \tag{2.65}$$

and

$$\bar{S}^{s\sigma}_{LL'}(r;E) = \bar{\beta}^{s\sigma}_{LL'}\ H_{L'}(r;E) \quad + \sum_{\sigma'',L''} \int \mathrm{d}r''\ \bar{S}^{s\sigma''}_{LL''}(r'';E)\ V^{\sigma''\sigma}_{L''L'}(r'')\ g_{\ell'}(r'',r;E) \tag{2.66}$$

with

$$\bar{\beta}^{s\sigma}_{LL'}(E) = \delta_{L,L'}\,\delta_{s,\sigma} - \kappa \sum_{\sigma''L''} \int \mathrm{d}r'\ \bar{R}^{s\sigma''}_{LL''}(r';E)\ V^{\sigma''\sigma}_{L''L'}(r')\ H_{L'}(r';E)\ . \tag{2.67}$$

Note that the quantum numbers corresponding to the boundary condition are now written as first index of $\bar{R}^{s\sigma}_{LL'}$ and $\bar{S}^{s\sigma}_{LL'}$.

Single-site Green function

The Green function for the single atom in free space can analogously be expanded in spherical harmonics,

$$\mathring{G}^{\sigma\sigma'}(\vec{r},\vec{r}\,';E) = \sum_{L,L'} Y_L(\hat{r})\;\frac{1}{rr'}\mathring{G}^{\sigma\sigma'}_{L,L'}(r,r';E)\;Y_{L'}(\hat{r}') \; . \tag{2.68}$$

Having the regular and irregular solution of the Lippmann-Schwinger equation at hand, the expansion coefficients are given by [54]

$$\mathring{G}^{\sigma\sigma'}_{LL'}(r,r') = \kappa \sum_{s,L''} \Big[\Theta(r'-r)\; R^{\sigma s}_{LL''}(r)\; \bar{S}^{s\sigma'}_{L''L'}(r') + \Theta(r-r')\; S^{\sigma s}_{LL''}(r)\; \bar{R}^{s\sigma'}_{L''L'}(r')\Big] \; . \tag{2.69}$$

Atomic t-matrix

It is convenient to define the atomic t-matrix as the integral

$$t^{ss'}_{LL'}(E) = \sum_{\sigma\sigma'} \int \mathrm{d}\vec{r}\,\mathrm{d}\vec{r}\,'\; \bar{J}^{s\sigma}_L(\vec{r};E)\; V^{\sigma\sigma'}(\vec{r},\vec{r}\,')\; R^{\sigma s'}_{L'}(\vec{r}\,';E) \; , \tag{2.70}$$

where $\bar{J}^{s\sigma}_L(\vec{r};E)$ is the left regular solution of the reference system. In the case of free space as reference system, this reduces to (*cf.* Eq. (2.42))

$$\begin{aligned} \bar{J}^{s\sigma}_L(\vec{r};E) &= \delta_{s\sigma}\; j_\ell(\kappa r)\; Y_L(\hat{r}) && (2.71)\\ &= \delta_{s\sigma}\; \frac{1}{r} J_L(r;E)\; Y_L(\hat{r}). && (2.72)\end{aligned}$$

Employing the expansions into spherical harmonics, Eqs. (2.52) and (2.59), and integration over the angular parts leads to

$$t^{ss'}_{LL'}(E) = \sum_{\sigma,\sigma'} \sum_{L''} \int_0^{R_{\max}} \mathrm{d}r\;\delta_{s\sigma}\; J_L(r;E)\; V^{\sigma\sigma'}_{L,L''}(r)\; R^{\sigma' s'}_{L''L'}(r;E) \tag{2.73}$$

2.4. Multiple scattering ansatz

Let us next consider a set of identical scatterers at lattice positions $\vec{R}_n$ $(n = 1 \ldots N)$. The generalization to the case of multiple atoms in the unit cell will be done in the next section 2.5. In the following discussion we distinguish between the global Cartesian vector $\vec{x}$ and the cell-centered coordinates $\vec{r}$ around a scattering center,

$$\vec{x} = \vec{R}_n + \vec{r}. \tag{2.74}$$

In this representation, the potential reads

$$V^{\sigma\sigma'}(\vec{R}_n+\vec{r},\vec{R}_{n'}+\vec{r}\,') = \delta_{nn'}\; V^{n,\sigma\sigma'}(\vec{r},\vec{r}\,') \equiv \delta_{nn'}\; V^{\sigma\sigma'}(\vec{r},\vec{r}\,') \tag{2.75}$$

where $V^{n,\sigma\sigma'}(\vec{r},\vec{r}\,')$ is a single scattering potential restricted to the cell n and the second equality holds because all scattering potentials shall be identical. The scattering solutions of the potential $V^{\sigma\sigma'}(\vec{r},\vec{r}\,')$ has been discussed in the previous sections.

The basic idea of the multiple scattering ansatz for finding the eigenfunctions is to regard an incoming wave to a scattering potential at site n as a superposition of the scattered waves from all other sites n'. This matching condition results in the KKR secular equation, that is the central quantity of this section.

Structure constants

Let us again start with the Green function of free space (neglecting the spin degree of freedom for a moment),

$$g(\vec{x},\vec{x}\,';E) = \kappa \sum_L j_L(\vec{x}_>;E)\; h_L(\vec{x}_<;E)\;. \tag{2.76}$$

where we used $j_L(\vec{x};E) = j_\ell(\sqrt{E}x)\; Y_L(\hat{x})$ to denote the product of a spherical Bessel function and real spherical harmonic, and similarly for the Hankel function, $h_L(\vec{x};E) = h_\ell(\sqrt{E}x)\; Y_L(\hat{x})$. These symbols shall not be confused with the previously defined $J_L(r;E) = r\, j_\ell(\sqrt{E}r)$ (analogously for $H_L(r;E)$), denoted by a capital letter. Inserting the cell-centered coordinates according to Eq. (2.74) and shifting the origin to cell n, we can transform Eq. (2.76) into [51]

$$g(\vec{r},\vec{r}\,'+\vec{R}_{n'}-\vec{R}_n;E) = \delta_{nn'}\;\kappa \sum_L j_L(\vec{r}_<;E)\; h_L(\vec{r}_>;E) + \sum_{LL'} j_L(\vec{r};E)\; g^{nn'}_{LL'}(E)\; j_{L'}(\vec{r}\,';E)\;. \tag{2.77}$$

This form is derived by separating the onsite-part (first term) and employing an addition theorem for Hankel functions[2] [51],

$$h_L(\vec{r}\,'+\vec{R}_{n'}-\vec{R}_n;E) = \frac{1}{\kappa}\sum_{L'} g^{nn'}_{LL'}(E)\; j_{L'}(\vec{r}\,';E) \quad \text{for } n\neq n'\;. \tag{2.78}$$

The expansion coefficients in Eq. (2.78) are called structure constants and can be evaluated by

$$g^{nn'}_{LL'}(E) = (1-\delta_{nn'})\; 4\pi\kappa \sum_{L''} i^{\ell-\ell'+\ell''}\; C_{LL'L''}\; h_{L''}(\vec{R}_n-\vec{R}_{n'};E), \tag{2.79}$$

---

[2] We use a definition of the Hankel function which differs from Zeller's definition [51] by a factor $(-i)$, which modifies some of the equations.

with the Gaunt coefficients $C_{LL'L''} = \int \mathrm{d}\Omega\ Y_L(\hat{r})\ Y_{L'}(\hat{r})\ Y_{L''}(\hat{r})$. The structure constants depend solely on the geometry of the set of scatterers and are independent of the individual scattering properties. Because the Gaunt coefficients vanish for $\ell'' > \ell + \ell'$, the sum in Eq. (2.79) is finite and the structure constants can be computed efficiently. However, they decay only slowly as function of the distance $\vec{R}_{n'} - \vec{R}_n$. The generalization to spin-$\frac{1}{2}$-particles is straight forward: to simplify the notation in the next subsection, we introduce another multi-index, namely $\Lambda = (L, \sigma) = (\ell, m, \sigma)$. The structure constants with spin then simply read

$$g^{nn'}_{\Lambda\Lambda'} = g^{nn'}_{LL'}\,\delta_{\sigma\sigma'} \qquad \text{with } \Lambda = (L, \sigma)\ . \tag{2.80}$$

Structural Dyson equation

Let us now consider the Green function $G^{\sigma\sigma'}(\vec{x}, \vec{x}\,'; E)$ for the set of scatterers. Again, by writing the Green function in the cell-centered coordinates, an analogous equation to Eq. (2.77) can be derived [51],

$$G^{\sigma\sigma'}(\vec{r} + \vec{R}_n, \vec{r}\,' + \vec{R}_{n'}; E) = \delta_{nn'}\ \mathring{G}^{\sigma\sigma'}(\vec{r}, \vec{r}\,'; E) + \sum_{\Lambda\Lambda'} R^{\sigma}_{\Lambda}(\vec{r}; E)\ G^{nn'}_{\Lambda\Lambda'}(E)\ \bar{R}^{\sigma'}_{\Lambda'}(\vec{r}\,'; E)\ , \tag{2.81}$$

with the single-site Green function $\mathring{G}$ from Eq. (2.68). Additionally, we introduced the notation $R^{\sigma}_{\Lambda} \equiv R^{\sigma s}_{L}$ with $\Lambda = (L, s)$ (*cf.* Eq. 2.57). Note that all quantities are additionally energy dependent. Here, the coefficients $G^{nn'}_{LL'}$ are called *structural Green functions* and can be determined from the structure constants (of free space) by a Dyson equation,

$$G^{nn'}_{\Lambda\Lambda'}(E) = g^{nn'}_{\Lambda\Lambda'}(E) + \sum_{n''\Lambda'', \Lambda'''} g^{nn''}_{\Lambda\Lambda''}(E)\ t_{\Lambda''\Lambda'''}(E)\ G^{n''n'}_{\Lambda'''\Lambda'}(E) \tag{2.82}$$

where the atomic t-matrix $t_{\Lambda\Lambda'} = t^{ss'}_{LL'}$ from Eq. (2.73) enters (for a derivation, see *e.g.* [52]).

For the description of a crystal structure, the set of scatterers is arranged periodically and the quantities in fact only depend on the relative position $\vec{R}_n - \vec{R}_{n'}$. Therefore, the determination of the structural Green functions is simplified by solving Eq. (2.82) in reciprocal space. A Fourier transformation yields

$$G_{\Lambda\Lambda'}(\vec{k}; E) = g_{\Lambda\Lambda'}(\vec{k}; E) + \sum_{\Lambda'', \Lambda'''} g_{\Lambda\Lambda''}(\vec{k}; E)\ t_{\Lambda''\Lambda'''}(E)\ G_{\Lambda'''\Lambda'}(\vec{k}; E) \tag{2.83}$$

with the transformation relation

$$g_{\Lambda\Lambda'}(\vec{k}; E) = \sum_{n \neq n'} g^{nn'}_{\Lambda\Lambda'}(E)\ \mathrm{e}^{i\,\vec{k}\cdot(\vec{R}_n - \vec{R}_{n'})}. \tag{2.84}$$

Now, the k-dependent structural Green functions can be obtained by matrix inversion,

$$G_{\Lambda\Lambda'}(\vec{k};E) = \left[\left(\underline{\underline{1}} - \underline{\underline{g}}(\vec{k};E)\ \underline{\underline{t}}(E)\right)^{-1} \underline{\underline{g}}(\vec{k};E)\right]_{\Lambda\Lambda'} \tag{2.85}$$

The structural Green function is then calculated by an inverse Fourier transformation,

$$G^{nn'}_{\Lambda\Lambda'}(E) = \frac{1}{V_{\mathrm{BZ}}} \int_{\mathrm{BZ}} \mathrm{d}\vec{k}\ G_{\Lambda\Lambda'}(\vec{k};E)\ \mathrm{e}^{-i\,\vec{k}\cdot(\vec{R}_n - \vec{R}_{n'})}\ , \tag{2.86}$$

where V_{BZ} denotes the volume of the Brillouin zone.

Now we have all ingredients to evaluate the Green function (2.81) of the crystal and can determine the charge density.

KKR secular equation

Next, we derive the KKR secular equation (neglecting the spin-degree for a moment to simplify the notation), from which the band structure of the crystal can be determined. We again employ multiple scattering theory, and assume that a wave has been scattered at a certain site n. The outgoing scattered wave ψ^{sc} can be expanded in Hankel functions,

$$\psi^{\mathrm{sc},\,n}_{\vec{k}}(\vec{r}) = \sum_L b^{\mathrm{sc},\,n}_{\vec{k},L}\ h_L(\vec{r};E)\ . \tag{2.87}$$

This wave can also be interpreted as incoming wave to a different site n',

$$\psi^{\mathrm{in},\,n'}_{\vec{k}}(\vec{r}\,') = \sum_L b^{\mathrm{in},\,n'}_{\vec{k},L}\ j_L(\vec{r}\,';E)\ . \tag{2.88}$$

Employing the transformation for Hankel functions (2.78), the amplitudes for the two waves can be connected by the structure constants,

$$\begin{aligned} b^{\mathrm{in},\,n'}_{\vec{k},L'} &= -\frac{1}{\kappa} \sum_L g^{nn'}_{LL'}(E)\ b^{\mathrm{sc},\,n}_{\vec{k},L} \\ &= -\frac{1}{\kappa} \sum_L g^{nn'}_{LL'}(E)\ \mathrm{e}^{i\,\vec{k}\cdot(\vec{R}_n - \vec{R}_{n'})}\ b^{\mathrm{sc},\,n'}_{\vec{k},L}\ . \end{aligned} \tag{2.89}$$

In the last step, the Bloch theorem was used to link the amplitudes of the scattered waves at site n and n' through multiplication of the Bloch phase factor. This is possible due to the periodicity of the crystal lattice.

Up until now we only considered the evolution of waves between two sites. Next, we consider all scatterers in the crystal, which form the total incoming wave at site n'

(with amplitudes c instead of b). The relation (2.89) then reads

$$c^{\mathrm{in},\,n'}_{\vec{k},L'} = -\frac{1}{\kappa}\sum_{L}\underbrace{\sum_{n\neq n'} g^{nn'}_{LL'}(E)\ \mathrm{e}^{i\,\vec{k}\cdot(\vec{R}_n-\vec{R}_{n'})}}_{g_{LL'}(\vec{k},E)}\ c^{\mathrm{sc},\,n'}_{\vec{k},L} \tag{2.90}$$

$$= -\frac{1}{\kappa}\sum_{L} g_{LL'}(\vec{k},E)\ c^{\mathrm{sc},\,n'}_{\vec{k},L}\ , \tag{2.91}$$

where in the last step the Fourier transform of $g^{nn'}_{LL'}$ has been introduced. The last equation relates the total incoming wave and scattered wave at the same site n' to each other. On the other hand, also the atomic t-matrix relates these two quantities,

$$c^{\mathrm{sc},\,n'}_{\vec{k},L} = \kappa\sum_{L'} t_{LL'}(E)\, c^{\mathrm{in},\,n'}_{\vec{k},L'}\ . \tag{2.92}$$

Combining Eqs. (2.91) and (2.92) and dropping the (arbitrary) superscript n' leads to the KKR secular equation

$$\sum_{L'}\left[\delta_{LL'} - \sum_{L''} g_{LL''}(\vec{k};E)\ t_{L''L'}(E)\right]\ c^{\mathrm{in}}_{\vec{k}L'} = 0\ , \tag{2.93}$$

The last equation can be easily generalized to the case with spin by replacing L with the generalized index $\Lambda = (L,\sigma)$,

$$\sum_{\Lambda'}\left[\delta_{\Lambda\Lambda'} - \sum_{\Lambda''} g_{\Lambda\Lambda''}(\vec{k};E)\ t_{\Lambda''\Lambda'}(E)\right]\ c^{\mathrm{in}}_{\vec{k}\Lambda'} = 0\ , \tag{2.94}$$

which is often written as

$$\det\left(\delta_{\Lambda\Lambda'} - \sum_{\Lambda''} g_{\Lambda\Lambda''}(\vec{k};E)\ t_{\Lambda''\Lambda'}(E)\right) = 0\ . \tag{2.95}$$

Note that $g_{\Lambda\Lambda''}$ is spin-diagonal (*cf.* Eq. (2.80)).

The secular equation is only fulfilled for certain pairs of $\vec{k}$ and E. Thus, for a given k-path in the Brillouin zone, we have to scan all energies for the determination of the band structure $E(\vec{k})$, which is given implicitly by the secular equation. This is in contrast to other methods (*e.g.* plane wave methods), where the band energies are directly calculated by diagonalization of a Hamiltonian for each $\vec{k}$ of interest.

To solve the secular equation in practice, we regard Eq. (2.94) as eigenvalue problem,

$$\underline{\underline{M}}(\vec{k},E)\ \underline{c}_\nu = \lambda_\nu\ \underline{c}_\nu \tag{2.96}$$

The secular equation is fulfilled if at least one of the eigenvalues vanishes, $\lambda_\nu = 0$, for a given pair $(\vec{k},E)$. The term inside the brackets of Eq. (2.94) is also referred to as *KKR matrix* and is abbreviated by $\underline{\underline{M}}(\vec{k},E)$.

Although the determination of the band structure is cumbersome in the KKR method, the determination of the Fermi surface (where $E = E_{\mathrm{F}}$ is fixed to the Fermi energy) can be done efficiently. Now, the k-vectors have to be scanned, which enter the secular equation only as Fourier transform of the structure constants, while the $R_L(\vec{r}; E)$ are not changing. Details about the method to determine the Fermi surface are described in chapter 4.

2.5. Generalization to multiple atoms in the unit cell

Until now we considered only the case that the potential in all cells are identical, *i.e.* $V^n(\vec{r}, \vec{r}\,') \equiv V(\vec{r}, \vec{r}\,')$ (*cf.* Eq. (2.75)). This is equivalent to a periodic lattice with only one atom in the unit cell. If the unit cell comprises different atom types, which can be different elements or the same elements but at inequivalent positions (and consequently differently shaped cells, as it is the case for *e.g.* the hexagonal close-packed crystal structure), we expand the potential around the cell centers as

$$V^{\sigma\sigma'}(\vec{R}_n + \vec{\chi}_\mu + \vec{r}, \vec{R}_{n'} + \vec{\chi}_{\mu'} + \vec{r}\,') = \delta_{nn'}\delta_{\mu\mu'}\; V^{\mu,\sigma\sigma'}(\vec{r}, \vec{r}\,') \; . \tag{2.97}$$

Thus, the cell centers are located at positions $\vec{R}_n + \vec{\chi}_\mu$, where n labels the lattice sites and $\mu = 1 \ldots N_{\mathrm{at}}$ the atoms in the unit cell, $\vec{\chi}_\mu$ being the respective basis vector. Then we have to solve the single-site problem for each potential in the unit cell, $V^{\mu,\sigma\sigma'}(\vec{r}, \vec{r}\,')$, yielding μ-dependent regular and irregular single-site right solutions $R^\mu_{\Lambda'\Lambda}(r; E)$ and $H^\mu_{\Lambda'\Lambda}(r; E)$ (as well as corresponding left-solutions) and atomic t-matrices $t^\mu_{\Lambda\Lambda'}(E)$. All indices n in the previous section have to be replaced by the pair $(n\mu)$, but the Fourier transforms in Eqs. (2.84) and (2.86) are only performed with respect to n, yielding

$$g^{\mu\mu'}_{\Lambda\Lambda'}(\vec{k}; E) = \sum_{n \neq n'} g^{n\mu n'\mu'}_{\Lambda\Lambda'}(E)\; \mathrm{e}^{i\,\vec{k}\cdot(\vec{R}_n - \vec{R}_{n'})} \tag{2.98}$$

and

$$G^{n\mu n'\mu'}_{\Lambda\Lambda'}(E) = \int_{\mathrm{BZ}} \mathrm{d}\vec{k}\; G^{\mu\mu'}_{\Lambda\Lambda'}(\vec{k}; E)\; \mathrm{e}^{-i\,\vec{k}\cdot(\vec{R}_n - \vec{R}_{n'})} \; , \tag{2.99}$$

respectively. The KKR secular equation (2.94) turns into

$$\sum_{\Lambda',\mu'} \left[\delta_{\Lambda\Lambda'}\; \delta_{\mu\mu'} - \sum_{\Lambda''} g^{\mu\mu'}_{\Lambda\Lambda''}(\vec{k}; E)\; t^{\mu'}_{\Lambda''\Lambda'}(E) \right]\; c^{\mathrm{in},\,\mu'}_{\vec{k}\Lambda'} = 0 \; , \tag{2.100}$$

i.e. the dimension of the coefficient vector and KKR matrix is multiplied by a factor N_{at}.

2.6. KKR wavefunctions

Let us now turn to the expression to calculate the wavefunctions within the KKR method. The regular solutions $R_L^{\sigma s,\mu}(\vec{r};E)$ span the solution space of physical (*i.e.* normalizable) wavefunctions to a given energy E in a cell around $\vec{\chi}_\mu$, where $\mu \in \{1,\dots,N_{\text{at}}\}$ labels the atoms in the unit cell. Thus, we can make the ansatz

$$\psi^\sigma_{\vec{k}}(\vec{r}+\vec{\chi}_\mu) = \sum_\Lambda a^\mu_{\vec{k}\Lambda}\; R_L^{\sigma s,\mu}(\vec{r};E) \qquad \text{for } E(\vec{k}) = E\ , \quad \Lambda = (L,s) \tag{2.101}$$

The expansion coefficients $a^\mu_{\vec{k}\Lambda}$ have to be chosen such, that the matching condition at the cell boundary, determined by multiple scattering theory, is fulfilled.

To derive an expression for the expansion coefficients $a^\mu_{\vec{k}\Lambda}$, we consider the total wavefunction in the interstitial region ($|\vec{r}| > R^\mu_{\text{max}}$). According to the Lippmann-Schwinger equation (2.30), the total wavefunction is a superposition of the incident and scattered wave,

$$\begin{aligned}
\psi^\sigma_{\vec{k}}(\vec{r}+\vec{\chi}_\mu) &= \psi^{\text{in},\sigma}_{\vec{k}}(\vec{r}+\vec{\chi}_\mu) + \psi^{\text{sc},\sigma}_{\vec{k}}(\vec{r}+\vec{\chi}_\mu) && (2.102)\\
&= \sum_L c^{\text{in}}_{\vec{k}L} j_L(\vec{r};E) + \sum_L c^{\text{sc}}_{\vec{k}L} h_L(\vec{r};E) && (2.103)\\
&= \sum_{L'} \underbrace{\left\{ \sum_L j_L(\vec{r};E)\,\delta_{LL'} + \kappa\, h_L(\vec{r};E)\; t_{LL'} \right\}}_{\equiv R_{L'}(\vec{r};E) \text{ for } |\vec{r}|>R^{\text{max}}} c^{\text{in}}_{\vec{k}L'} && (2.104)
\end{aligned}$$

From the first to the second line, the results from the previous section have been inserted and from the second to the third line, the relation $c^{\text{sc}}_{\vec{k}\Lambda} = \kappa\ \sum_{\Lambda'} t_{\Lambda\Lambda'}\ c^{\text{in}}_{\vec{k}\Lambda}$ was used. The term appearing in the bracket can be identified as the radial solution for $\vec{r}$ lying outside the scattering region.

Because of the continuity at the cell boundary of both, the radial solution and the wavefunction, the coefficients must be identical, hence

$$\psi^\sigma_{\vec{k}}(\vec{r}+\vec{\chi}_\mu) = \sum_\Lambda c^\mu_{\vec{k}\Lambda}\; R_L^{\sigma s,\mu}(\vec{r};E) \quad \text{and} \quad \sum_{\Lambda'} M^{\mu\mu'}_{\Lambda\Lambda'}(\vec{k},E)\; c^{\mu'}_{\vec{k}\Lambda'} = 0\ . \tag{2.105}$$

The expansion coefficients for the wavefunctions $a^\mu_{\vec{k}\Lambda}$ in Eq. (2.101) are therefore identical to the eigenvectors of the KKR matrix $c^\mu_{\vec{k}\Lambda}$ when the corresponding eigenvalue vanishes.

Normalization of the wavefunction

To calculate physical quantities, the wavefunctions must be normalized according to

$$\langle\, \psi_{\vec{k}} \,|\, \psi_{\vec{k}} \,\rangle = 1 \tag{2.106}$$

However, the eigenvectors $\tilde{c}_L^{s\mu}$ returned by a numerical eigenvalue routine are usually not normalized in such a way. Here, we denote the unnormalized coefficients by a tilde. Inserting the expansion (2.105) into the left hand side of Eq. (2.106) yields

$$\begin{aligned} \langle\, \psi_{\vec{k}} \,|\, \psi_{\vec{k}} \,\rangle &= \sum_\sigma \sum_\mu \int_{V^\mu} \mathrm{d}\vec{r}\; |\psi^\sigma(\vec{r}+\vec{\chi}_\mu)|^2 && (2.107) \\ &= \sum_\sigma \sum_\mu \int \mathrm{d}\vec{r}\; \Theta^\mu(\vec{r})\; \psi^{\sigma *}(\vec{r}+\vec{\chi}_\mu)\, \psi^\sigma(\vec{r}+\vec{\chi}_\mu) && (2.108) \end{aligned}$$

where V^μ is the volume of the atomic site μ. By introducing the shape functions $\Theta^\mu(\vec{r})$, the integration was extended to full space.[3] Together with the expansion of the shape functions into real spherical harmonics, $\Theta^\mu(\vec{r}) = \sum_L \Theta_L(r)\, Y_L(\hat{r})$, and the expansion of the wavefunctions,

$$\begin{aligned} \psi^\sigma_{\vec{k}}(\vec{r}+\vec{\chi}_\mu) &= \sum_{L,s} R_L^{\sigma s,\mu}(\vec{r};E)\, c^{s\mu}_{\vec{k}L} && (2.109) \\ &= \sum_{L'} Y_{L'}(\hat{r}) \sum_{L,s} \frac{1}{r}\, R^{\sigma s,\mu}_{L'L}(r;E)\, c^{s\mu}_{\vec{k}L}\ , && (2.110) \end{aligned}$$

Equation (2.108) can be written in the form [52]

$$\begin{aligned} \langle\, \psi_{\vec{k}} \,|\, \psi_{\vec{k}} \,\rangle &= \sum_\mu \sum_{ss'} \sum_{LL'} c^{s,\mu *}_{\vec{k}L}\, \rho^{ss',\mu}_{LL'}\, c^{s',\mu}_{\vec{k}L'} \qquad \text{with} && (2.111) \\ \rho^{ss',\mu}_{LL'}(E) &= \sum_{L_1,L_2,L_3} C_{L_1,L_2,L_3} \int \mathrm{d}r\; \Theta_{L_1}(r) \sum_\sigma \left[R^{\sigma s,\mu}_{L_2 L}(r;E)\right]^*\; R^{\sigma s',\mu}_{L_3 L'}(r;E) \end{aligned}$$

Hence, the integration has to be performed only once per energy and the $\vec{k}$-independent matrix $\underline{\underline{\rho}}$, which is a matrix in (L,s,μ)-space, is obtained. The norm of a state $|\, \psi_{\vec{k}} \,\rangle$ can then be calculated by a vector-matrix-vector product. Then the correctly normalized coefficients are given by

$$\begin{aligned} c^{s,\mu}_{\vec{k}L} &= \frac{1}{\sqrt{P}}\, \tilde{c}^{s,\mu}_{\vec{k}L} \qquad \text{with} && (2.112) \\ P &= \sum_\mu \sum_{ss'} \sum_{LL'} \tilde{c}^{s,\mu *}_{\vec{k}L}\, \rho^{ss',\mu}_{LL'}\, \tilde{c}^{s',\mu}_{\vec{k}L'} = \left(\underline{\tilde{c}}_{\vec{k}}\right)^\dagger\; \underline{\underline{\rho}}\;\; \underline{\tilde{c}}_{\vec{k}}. \end{aligned}$$

In the last equation, the symbol $\underline{\tilde{c}}_{\vec{k}}$ is a vector in (s,μ,L)-space.

---

[3]

$$\Theta^\mu(\vec{r}) = \begin{cases} 1 & \text{for} \quad \vec{r} \text{ in cell } \mu \\ 0 & \phantom{\text{for}} \quad \text{otherwise} \end{cases}$$

Spin expectation-value of the wavefunction

The ith component of the spin expectation-value is given by

$$S_{i,\vec{k}} = \frac{1}{2} \langle \psi_{\vec{k}} | \, \sigma_i^{\mathrm{P}} \, | \psi_{\vec{k}} \rangle \qquad (\text{with } \hbar = 1) \tag{2.113}$$

with the Pauli matrices

$$\sigma_x^{\mathrm{P}} = \begin{pmatrix} 0 & 1 \\ 1 & 0 \end{pmatrix} \; , \quad \sigma_y^{\mathrm{P}} = \begin{pmatrix} 0 & -i \\ i & 0 \end{pmatrix} \; , \quad \sigma_z^{\mathrm{P}} = \begin{pmatrix} 1 & 0 \\ 0 & -1 \end{pmatrix} \; . \tag{2.114}$$

Inserting the expansion (2.105) for the wavefunctions and performing similar manipulations as in the previous subsection, equation (2.113) can be transformed into [52]

$$S_{i,\vec{k}} = \frac{1}{2} \sum_{\mu} \sum_{LL'} \sum_{ss'} \left[c_{\vec{k}L}^{s,\mu} \right]^* \; \Sigma_{LL',i}^{ss',\mu}(E) \; c_{\vec{k}L'}^{s',\mu} \tag{2.115}$$

where the $\underline{\underline{\Sigma}}_i$-matrices are defined by

$$\begin{aligned} \Sigma_{LL',i}^{ss',\mu}(E) &= \sum_{\sigma,\sigma'} \int_{V^\mu} \mathrm{d}\vec{r} \; [R_L^{\sigma s,\mu}(\vec{r};E)]^* \; \left(\sigma_i^{\mathrm{P}}\right)^{\sigma\sigma'} \; R_{L'}^{\sigma' s',\mu}(\vec{r};E) \qquad (2.116) \\ &= \sum_{L_1,L_2,L_3} C_{L_1,L_2,L_3} \int \mathrm{d}r \; \Theta_{L_1}(r) \sum_{\sigma,\sigma'} \left[R_{L_2 L}^{\sigma s,\mu}(r;E) \right]^* \; \left(\sigma_i^{\mathrm{P}}\right)^{\sigma\sigma'} \; R_{L_3 L'}^{\sigma' s',\mu}(r;E) \end{aligned}$$

In analogy to the matrix $\underline{\underline{\rho}}$ from the previous subsection, also the $\underline{\underline{\Sigma}}_i$-matrices are $\vec{k}$-independent and only have to be calculated once per energy. Then, to calculate the spin expectation-value of all states belonging to this energy, only the vector-matrix-vector product represented by (2.115) has to be performed.

Gauge freedom for the case of "conjugation degeneracy"

For non-magnetic solids, each electronic state is two-fold degenerate if the crystal structure is inversion symmetric. This follows from the combination of time-reversal and space-inversion symmetry [55]. Namely, acting with the time reversal operator $\mathcal{K}$ and the space-inversion operator $\mathcal{I}$ (and, following Yafet [55], calling their combined action as "conjugation", $\mathcal{C} = \mathcal{K} \cdot \mathcal{I}$) onto a state $|\, \psi_{\vec{k}}^{(1)} \, \rangle$ will yield a second, linearly independent state $|\, \psi_{\vec{k}}^{(2)} \, \rangle = \mathcal{C} |\, \psi_{\vec{k}}^{(1)} \, \rangle$. In this case, always two eigenvalues of the KKR matrix vanish with corresponding coefficient-eigenvectors $\underline{c}^{(1)}$ and $\underline{c}^{(2)}$, which are linearly independent and can be chosen to be orthogonal to each other (we dropped the index $\vec{k}$ for convenience). Due to the presence of time-reversal and space-inversion symmetry, the spin expectation-value of the two states just differ in sign [52, 56],

$$\begin{aligned} S_i^{(1)} &= -S_i^{(2)} \qquad \text{with} && (2.117)\\ S_i^{(j)} &= \underline{c}^{(j)\dagger}\, \underline{\underline{\Sigma}}_i\, \underline{c}^{(j)}\ , \qquad (j=1,2)\ . && (2.118) \end{aligned}$$

However, the coefficients are not uniquely determined, since any linear combination of $\underline{c}^{(1)}$ and $\underline{c}^{(2)}$ is also a solution to the KKR secular equation. This arbitrariness arises due to the lack of a physically defined spin-quantization axis (SQA), as opposed to magnetic systems. However, a SQA is defined in experiments by means of an external magnetic field, e.g. in conduction electron spin resonance (CESR) experiments, or ferromagnetic leads, e.g. in electron-spin injection experiments [57]. Therefore, we have to fix the gauge by choosing a correct linear combination which resembles the chosen SQA. Two different choices can be considered:

1. either that the spin expectation-value in the direction of the SQA $\hat{s}$ is maximal,
2. or that the spin expectation-value in the perpendicular directions to $\hat{s}$, denoted by $\hat{p}_1$ and $\hat{p}_2$, vanishes.

The three directions $(\hat{p}_1, \hat{p}_2, \hat{s})$ shall be mutually orthogonal to each other and define a right-handed coordinate system.

In the presence of spin-orbit coupling, the two conditions are not equivalent to each other, as shown by Heers [52]. She argues, that the two gauges resemble different experimental setups: the former will be realized in a CESR experiment, where the applied magnetic field will maximize the spin along the direction of the magnetic field. The second condition resembles more the situation in a spin-injection experiment, where the electrons are exactly polarized along the magnetization of an ferromagnetic lead. Both gauges have been used in the literature [56, 58]. Pientka *et al.* [59] analyzed the difference of the two gauges in more detail, and they show that the first one is equivalent to applying an infinitesimal exchange field (consistent with the interpretation given by Heers). They also show, that this gauge is better applicable for the calculation of *e.g.* the Berry curvature, because the latter gauge produces unphysical jumps in the Berry curvature.

A general linear combination of the two wavefunctions, which preserves the norm and orthogonality of $|\,\psi_{\vec{k}}^{(1)}\,\rangle$ and $|\,\psi_{\vec{k}}^{(2)}\,\rangle$, is given by [52]

$$\begin{aligned} \underline{c}^{(+)} &= \cos(\alpha/2)\ \underline{c}^{(1)} + \sin(\alpha/2)\ \mathrm{e}^{i\beta}\ \underline{c}^{(2)}\ , && (2.119)\\ \underline{c}^{(-)} &= -\sin(\alpha/2)\ \underline{c}^{(1)} + \cos(\alpha/2)\ \mathrm{e}^{i\beta}\ \underline{c}^{(2)}\ . && (2.120) \end{aligned}$$

The coefficients α and β have to be chosen such that the desired condition is fulfilled.

Generalizing the approach from Heers [52] to an arbitrary direction of the SQA $\hat{s}$, we require for the first condition (maximal spin expectation-value along the direction $\hat{s}$)

$$\frac{\partial S_{\hat{s}}^{(+)}}{\partial \alpha} = 0 \quad \text{and} \quad \frac{\partial S_{\hat{s}}^{(+)}}{\partial \beta} = 0 \tag{2.121}$$

and for the second condition (vanishing spin expectation-value perpendicular to the direction $\hat{s}$)

$$S_{\hat{p}_1}^{(+)} = 0 \quad \text{and} \quad S_{\hat{p}_2}^{(+)} = 0 \ , \tag{2.122}$$

where

$$S_{\hat{n}}^{(+)} = \underline{c}^{(+)\dagger} \ \left(\underline{\underline{\vec{\Sigma}}} \cdot \hat{n} \right) \ \underline{c}^{(+)} \tag{2.123}$$

is the spin expectation-value along the direction $\hat{n}$ and $\underline{\underline{\vec{\Sigma}}} = \left(\underline{\underline{\Sigma}}_x, \ \underline{\underline{\Sigma}}_y, \ \underline{\underline{\Sigma}}_z \right)^{\mathrm{T}}$ is a vector of the matrices defined in Eq. (2.116).

Inserting the ansatz (2.119) into the conditions (2.121) and (2.122), respectively, we arrive after some algebra at

$$\begin{array}{lll} \beta = \arg\left(S_{\hat{s}}^{12}\right) \ , & \alpha = \ \ \operatorname{atan}\left(\operatorname{Re}\left(\mathrm{e}^{i\beta}\, S_{\hat{s}}^{12}\right) / S_{\hat{s}}^{1}\right) & \text{for condition } 1 \, , \\ \beta = \arg(\xi)/2 \ , & \alpha = -\operatorname{atan}\left(S_{\hat{p}_1}^{1} / \operatorname{Re}\left(\mathrm{e}^{i\beta}\, S_{\hat{p}_1}^{12}\right)\right) & \text{for condition } 2 \, , \end{array} \tag{2.124}$$

where

$$\xi = -\frac{S_{\hat{p}_1}^{1}\, S_{\hat{p}_2}^{12*} - S_{\hat{p}_2}^{1}\, S_{\hat{p}_1}^{12*}}{S_{\hat{p}_1}^{1}\, S_{\hat{p}_2}^{12} - S_{\hat{p}_2}^{1}\, S_{\hat{p}_1}^{12}} \ , \tag{2.125}$$

$$S_{\hat{n}}^{12} = \underline{c}^{(1)\dagger} \left(\underline{\underline{\vec{\Sigma}}} \cdot \hat{n} \right) \underline{c}^{(2)} \ , \tag{2.126}$$

$$S_{\hat{n}}^{1} = \underline{c}^{(1)\dagger} \left(\underline{\underline{\vec{\Sigma}}} \cdot \hat{n} \right) \underline{c}^{(1)} \ . \tag{2.127}$$

2.7. Impurity scattering

In contrast to the idealized situation of a perfectly ordered crystal, which was assumed in the previous sections, in real materials also imperfections are present. Examples are dislocations of host atoms, missing atoms or the presence of impurities. Some properties of real materials are influenced drastically by them [60, 61]. For instance, the residual resistivity of a metal is a consequence of the presence of such imperfections [62]. Also the skew-scattering contribution to the anomalous and spin Hall effects, which play a central role in this thesis, is caused by impurities [37].

In this section, we describe the scattering properties of an impurity embedded in an otherwise perfectly ordered periodic host system. The impurity atom shall be located at an atomic site of the host (also called a substitutional impurity). In general, the electronic properties of the atoms surrounding the impurity will also be altered due to hybridization effects with the impurity states. This can lead to *e.g.* charge transfer or spin polarization of the respective atoms. However, these effects typically decay quickly, so that it is reasonable to divide the crystal into two regions: a finite region (also called impurity cluster) around the impurity site and all other atoms (see the work of Bauer [54] for details). We can then assume that the scattering properties of the latter are identical to those of an atom of the perfectly ordered host and Bloch electrons only scatter off atoms in the impurity cluster.

We first introduce our notation: the atoms in the impurity cluster shall be labeled by a combined index $i = (n, \mu)$, where the center of the ith cell is located at

$$\vec{\tau}_i = \vec{R}_n + \vec{\chi}_\mu \ , \tag{2.128}$$

where $\vec{R}_n$ is a lattice vector and $\vec{\chi}_\mu$ a basis vector of the μth atom in the unit cell.

The situation is conceptually similar to the single-site problem of section 2.3, where we considered a potential of finite range in free space. Now we have a perturbing potential $\Delta\mathbf{V}^n(\vec{r}, \vec{r}\,') = \mathbf{V}^{\mathrm{imp},n}(\vec{r}, \vec{r}\,') - \mathbf{V}^{\mathrm{host},n}(\vec{r}, \vec{r}\,')$ in a periodic host, where n labels the atoms in the impurity cluster and bold symbols denote a (2×2)-matrix in spin space.

Impurity radial solutions

Note that in this and the following subsections, we drop the energy dependence to simplify our notation.

Similar to Eq. (2.60) we define the radial solutions for the single-site problem [52], *i.e.*

$$R^{\mathrm{imp},\sigma s}_{L'L}(r) = J_L(r)\ \delta_{L',L}\ \delta_{\sigma,s} + \sum_{\sigma'',L''} \int \mathrm{d}r''\ g_{\ell'}(r, r'')\ V^{\mathrm{imp};\sigma\sigma''}_{L'L''}(r'')\ R^{\sigma'' s}_{L''L}(r'')\ , \tag{2.129}$$

and analogous expressions for the irregular solution $S^{\mathrm{imp},\sigma s}_{L'L}$ and the left-hand side solutions, $\bar{R}^{\mathrm{imp},s\sigma}_{LL'}$ and $\bar{S}^{\mathrm{imp},s\sigma}_{LL'}$. This definition takes the free space as reference system, and this is how the impurity radial solutions are calculated in the code and used to obtain the t^{imp}-matrix (and Δ-matrix, see later) [54].

However, there exist also a relations to the (unperturbed) radial solutions of the host, which are used in some derivations (for simplicity we write them in matrix notation):

$$\underline{\underline{R}}^{\mathrm{imp}}(r) = \underline{\underline{R}}(r) + \int \mathrm{d}r'\, \mathring{\underline{\underline{G}}}(r, r')\ \Delta\underline{\underline{V}}\ \underline{\underline{R}}^{\mathrm{imp}}(r')\,, \tag{2.130}$$

where $\mathring{\underline{\underline{G}}}$ denotes the single-site Green's function for the host potential (*cf.* Eq. 2.68) and $\Delta\underline{\underline{V}} = \underline{\underline{V}}^{\mathrm{imp}} - \underline{\underline{V}}^{\mathrm{host}}$. An analogous formulation is found by regarding the impurity-potential as the reference system and the host-potential as the perturbed one,

$$\underline{\underline{R}}(r) = \underline{\underline{R}}^{\mathrm{imp}}(r) - \int \mathrm{d}r'\, \mathring{\underline{\underline{G}}}^{\mathrm{imp}}(r, r')\ \Delta\underline{\underline{V}}\ \underline{\underline{R}}(r')\,, \tag{2.131}$$

Here, the single-site Green function of the impurity $\mathring{\underline{\underline{G}}}^{\mathrm{imp}}$, is defined analogously to $\mathring{\underline{\underline{G}}}$ in Eq. (2.68), where now the radial solutions to the impurity potential enter.

Impurity Green function

As in the case of the periodic host, the Green function for the host system with embedded impurity is given by two parts, a single-site term and a back-scattering term [52, 54],

$$\underline{\underline{G}}^{\mathrm{imp}}(\vec{r}+\vec{\tau}_i,\vec{r}\,'+\vec{\tau}_{i'}) = \delta_{ii'}\;\underline{\underline{\mathring{G}}}^{\mathrm{imp},i}(\vec{r},\vec{r}\,') + \underline{\underline{R}}^{\mathrm{imp},i}(\vec{r})\;\underline{\underline{G}}^{\mathrm{imp},ii'}\;\underline{\underline{\bar{R}}}^{\mathrm{imp},i'}(\vec{r}\,')\ , \tag{2.132}$$

In the back-scattering term, the structural Greens function $\underline{\underline{G}}^{\mathrm{imp},ii'} = G^{\mathrm{imp},ii'}_{\Lambda\Lambda'}$ enters. It is related to the structural Green function of the perfect crystal by the Dyson equation,

$$\underline{\underline{G}}^{\mathrm{imp}} = \underline{\underline{G}}^{\mathrm{host}} + \underline{\underline{G}}^{\mathrm{host}}\;\Delta\underline{\underline{t}}\;\underline{\underline{G}}^{\mathrm{imp}}\ . \tag{2.133}$$

The matrices read in index notation as $G^{\mathrm{imp},ii'}_{\Lambda\Lambda'}$, $G^{\mathrm{host},ii'}_{\Lambda\Lambda'}$ and $\Delta t^{i}_{\Lambda\Lambda'} = t^{\mathrm{imp},i}_{\Lambda\Lambda'} - t^{\mathrm{host},\mu}_{\Lambda\Lambda'}$, the latter being the difference of the atomic t-matrices. Here, $i=(n,\mu)$ labels the N_{cls} atoms in the impurity cluster and $\Lambda=(L,\sigma)=(\ell,m,\sigma)$ is a multi-index comprised of the orbital and spin quantum numbers. In contrast to the equivalent Eq. (2.82) for the periodic crystal, N_{cls} is finite and the structural Dyson equation can be directly solved in real space by inverting a matrix of size $(2\cdot N_{\mathrm{cls}}\cdot(\ell_{\mathrm{max}}+1)^2)\times(2\cdot N_{\mathrm{cls}}\cdot(\ell_{\mathrm{max}}+1)^2)$ [54],

$$\underline{\underline{G}}^{\mathrm{imp}} = \left[\underline{\underline{1}} - \underline{\underline{G}}^{\mathrm{host}}\;\Delta\underline{\underline{t}}\right]^{-1}\;\underline{\underline{G}}^{\mathrm{host}}\ . \tag{2.134}$$

However, $G^{\mathrm{host},ii'}_{\Lambda\Lambda'}$ is found in reciprocal space and Fourier transformed back to the real-space impurity cluster according to Eq. (2.99). If the chosen impurity cluster is large, the resolution in k-space must be very fine. Typically, in the impurity calculations presented later, a k-mesh with 500 k-points per direction has been used.

Impurity wavefunction

In this section we want to derive the coefficients that yield the wavefunctions of the host system with embedded impurity in terms of the radial solutions of the impurity problem [52], *i.e.*

$$\psi^{\mathrm{imp},\sigma}(\vec{r}) = \frac{1}{r}\sum_{LL'} R^{\mathrm{imp},\sigma s}_{L'L}(r)\;c^{\mathrm{imp},s}_{L}\;Y_{L'}(\hat{r})\ . \tag{2.135}$$

The wavefunction spinors for the real system (*i.e.* with the impurity), $\mathbf{\Psi}^{\mathrm{imp}}_{k} = (\psi^{\mathrm{imp},\uparrow}_{k},\psi^{\mathrm{imp},\downarrow}_{k})^{\mathrm{T}}$, can be related to the ones of the pristine crystal, $\mathbf{\Psi}_{k} = (\psi^{\uparrow}_{k},\psi^{\downarrow}_{k})^{\mathrm{T}}$, by the Lippmann-Schwinger equation (2.30). The index $k=(\vec{k},\nu)$ comprises the Bloch wave vector $\vec{k}$ of the pristine crystal (which is a “good” quantum number in this case) and ν labels additional degeneracies. However, the wave vector is inherited by the impurity wavefunction as labels only, because the translational symmetry is broken.

For the standard form of the Lippmann-Schwinger equation, we obtain in real space representation

$$\psi_k^{\mathrm{imp},\sigma}(\vec{x}) = \psi_k^{\sigma}(\vec{x}) + \sum_{\sigma',\sigma''} \int \mathrm{d}\vec{x}\,'\ \mathrm{d}\vec{x}\,''\ G^{\sigma\sigma'}(\vec{x},\vec{x}\,')\ \Delta V^{\sigma'\sigma''}(\vec{x}\,',\vec{x}\,'')\ \psi_k^{\mathrm{imp},\sigma''}(\vec{x}\,'')\ , \tag{2.136}$$

with $\vec{x} = \vec{r} + \vec{\tau}_i$, $\vec{x}\,' = \vec{r}\,' + \vec{\tau}_{i'}$ etc. However, we choose as starting point another form of the Lippmann-Schwinger equation:

$$\psi_k^{\mathrm{imp},\sigma}(\vec{x}) = \psi_k^{\sigma}(\vec{x}) + \sum_{\sigma',\sigma''} \int \mathrm{d}\vec{x}\,'\ \mathrm{d}\vec{x}\,''\ G^{\mathrm{imp},\sigma\sigma'}(\vec{x},\vec{x}\,')\ \Delta V^{\sigma'\sigma''}(\vec{x}\,',\vec{x}\,'')\ \psi_k^{\sigma''}(\vec{x}\,'') \tag{2.137}$$

This form can be simply derived from Eq. (2.136) by interchanging the role of the perturbed and unperturbed systems. For the rest of this section, we will drop the index k to simplify our notation.

We recall the expansion of the potential according to Eq. (2.52),

$$\begin{aligned} \Delta V^{\sigma\sigma'}(\vec{r}+\vec{\tau}_i, \vec{r}\,'+\vec{\tau}_{i'}) &= \delta_{ii'}\ \Delta V^{i,\sigma\sigma'}(\vec{r},\vec{r}\,') \qquad (2.138) \\ &= \delta_{ii'} \sum_{L,L'} \frac{1}{r^2}\ \Delta V_{LL'}^{i,\sigma\sigma'}(r)\ Y_L(\hat{r})\ Y_{L'}(\hat{r}')\ \delta(r-r'). \end{aligned}$$

as well as the expansion of the host wavefunctions,

$$\psi^{\sigma}(\vec{r}+\vec{\tau}_i) = \sum_{L,L',s} \frac{1}{r}\, R_{L'L}^{\sigma s,i}(r)\ c_{\Lambda}^{i}\ Y_{L'}(\hat{r})\,. \tag{2.139}$$

Inserting these equations together with Eq. (2.132) into the Lippmann-Schwinger equation (2.137), we arrive (after a derivation similar to the one shown in the appendix A.2 or presented in the work of Heers [52]) at

$$\begin{aligned} \sum_{\Lambda'} R_{\Lambda\Lambda'}^{\mathrm{imp},i}(r)\ c_{\Lambda'}^{\mathrm{imp},i} &= \sum_{\Lambda'} \sum_{i'} \Big\{ R_{\Lambda\Lambda'}^{i}(r)\ \delta_{ii'} + \qquad (2.140) \\ &+ \sum_{\Lambda^{(2)},\Lambda^{(3)}} \int \mathrm{d}r'\ \delta_{ii'}\ \mathring{G}_{\Lambda\Lambda^{(2)}}^{\mathrm{imp},i}(r,r')\ \Delta V_{\Lambda^{(2)}\Lambda^{(3)}}^{i}(r')\ R_{\Lambda^{(3)}\Lambda'}^{i}(r') + \\ &+ \sum_{\Lambda^{(2)},\Lambda^{(3)}} R_{\Lambda\Lambda^{(2)}}^{\mathrm{imp},i}(r)\ G_{\Lambda^{(2)}\Lambda^{(3)}}^{\mathrm{imp},ii'} \times \\ &\times \sum_{\Lambda^{(4)},\Lambda^{(5)}} \int \mathrm{d}r'\ \bar{R}_{\Lambda^{(3)}\Lambda^{(4)}}^{\mathrm{imp},i'}(r')\ \Delta V_{\Lambda^{(4)}\Lambda^{(5)}}^{i'}(r')\ R_{\Lambda^{(5)}\Lambda'}^{i'}(r') \Big\}\ c_{\Lambda'}^{i'} \end{aligned}$$

We can identify the second line as the second part on the r.h.s. of Eq. (2.131), and thus it can be rewritten as $\delta_{ii'}\left(R_{\Lambda\Lambda'}^{\mathrm{imp},i}(r) - R_{\Lambda\Lambda'}^{i}(r)\right)$ and partly cancels with the first part on the r.h.s. of Eq. (2.140). Additionally, the fourth line of Eq. (2.140) can be identified with the t-matrix element $\Delta t^{\mathrm{imp},i'}_{\Lambda^{(3)}\Lambda'}$ and the whole equation simplifies to[4]

$$\sum_{\Lambda'} R^{\mathrm{imp},i}_{\Lambda\Lambda^{(2)}}(r)\; c^{\mathrm{imp},i}_{\Lambda^{(2)}} = \sum_{\Lambda',\Lambda^{(2)},i'} R^{\mathrm{imp},i}_{\Lambda\Lambda^{(2)}}(r) \left\{ \delta_{\Lambda^{(2)}\Lambda'}\; \delta_{ii'} + \sum_{\Lambda^{(3)}} G^{\mathrm{imp},ii'}_{\Lambda^{(2)}\Lambda^{(3)}}\; \Delta t^{\mathrm{imp},i'}_{\Lambda^{(3)}\Lambda'} \right\} c^{i'}_{\Lambda'}\,. \tag{2.141}$$

A comparison of the coefficients yields the final result, from which the impurity coefficients can be obtained from the host coefficients,

$$c^{\mathrm{imp},i}_{\Lambda} = \sum_{\Lambda',i'} \left\{ \delta_{\Lambda\Lambda'}\; \delta_{ii'} + \sum_{\Lambda''} G^{\mathrm{imp},ii'}_{\Lambda\Lambda''}\; \Delta t^{\mathrm{imp},i'}_{\Lambda''\Lambda'} \right\} c^{\mu'}_{\Lambda'}\, \mathrm{e}^{\mathrm{i}\,\vec{k}\cdot\vec{R}_{n'}}\,, \tag{2.142}$$

where additionally the equality $c^{i'}_{\Lambda'} = c^{\mu'}_{\Lambda'}\, \mathrm{e}^{\mathrm{i}\,\vec{k}\cdot\vec{R}_{n'}}$ was used. The phase factor results from the Bloch theorem and accounts for the lattice translation contained in $\vec{\tau}_i = \vec{R}_n + \vec{\chi}_\mu$.

The transition matrix and scattering rates

In the following we think of the electrons as states of the pristine crystal, *i.e.* they shall be Bloch electrons, because the impurity region is small with respect to the whole crystal. We would like to know the transition rate to scatter from a state $\boldsymbol{\psi}_k$ into a state $\boldsymbol{\psi}_{k'}$ due to the presence of the impurity. The wavefunction of the initial state (far away from the impurity) shall equal the wavefunction of the unperturbed system. However, this state only serves as a boundary condition, and the true state of the system with impurity is given by the impurity wavefunction $\boldsymbol{\psi}^{\mathrm{imp}}_k$. Therefore, the transition rate is by Fermi's golden rule given as [37, 52]

$$P_{kk'} = 2\pi\, cN\, |T_{kk'}|^2\, \delta(E_k - E_{k'}) \tag{2.143}$$

with the impurity concentration c, the number of atoms in the whole crystal N, and the delta-function restricts the transitions to states with the same energy (being equal to the Fermi energy for electronic transport properties, *cf.* chapter 3). The transition matrix elements are given by

$$T_{k'k} = \int \mathrm{d}\vec{x}\, \mathrm{d}\vec{x}\,'\; \boldsymbol{\psi}^{\dagger}_{k'}(\vec{x})\, \Delta\mathbf{V}(\vec{x},\vec{x}\,')\, \boldsymbol{\psi}^{\mathrm{imp}}_{k}(\vec{x}\,')\ . \tag{2.144}$$

The difference in the potential is only non-vanishing in the impurity cluster, thus truncating the integration to a finite region. Inserting the expansions for the host and

---

[4] In fact, the usual definition reads $\Delta t^{\mathrm{imp},i'}_{\Lambda^{(3)}\Lambda'} = \sum_{\Lambda^{(4)},\Lambda^{(5)}} \int \mathrm{d}r'\; \bar{R}^{i'}_{\Lambda^{(3)}\Lambda^{(4)}}(r')\; \Delta V^{i'}_{\Lambda^{(4)}\Lambda^{(5)}}(r')\; R^{\mathrm{imp},i'}_{\Lambda^{(5)}\Lambda'}(r')$, *i.e.* R^{imp} and R are interchanged. However, the equivalence of the two formulations can be easily shown by inserting the Born series for the Lippmann-Schwinger equation relating R^{imp} to R.

impurity wavefunctions (Eqs. (2.135) and (2.139)) as well as for the potential (2.139) yields after some algebra

$$\begin{aligned} T_{k'k} &= \sum_i \sum_{\substack{\Lambda,\Lambda' \\ \Lambda'',\Lambda'''}} \int \mathrm{d}r \; \left(R^i_{\Lambda''\Lambda}(r)\, c^i_{k',\Lambda} \right)^\dagger \; \Delta V^i_{\Lambda''\Lambda'''}(r) \; R^{\mathrm{imp},i}_{\Lambda'''\Lambda'}(r)\, c^{\mathrm{imp},i}_{k,\Lambda'} && (2.145) \\ &= \sum_i \sum_{\Lambda,\Lambda'} c^{i*}_{k',\Lambda} \Delta^i_{\Lambda\Lambda'} \; c^{\mathrm{imp},i}_{k,\Lambda'} \;, && (2.146) \end{aligned}$$

where from the first to the second line, the Δ-matrix has been defined by [52]

$$\Delta^i_{\Lambda\Lambda'} = \sum_{L'',L'''} \int \mathrm{d}r \; R^{i*}_{\Lambda\Lambda''}(r) \; \Delta V^i_{\Lambda''\Lambda'''}(r) \; R^{\mathrm{imp},i}_{\Lambda'''\Lambda'}(r) \;. \tag{2.147}$$

The Δ-matrix is very similar to the Δt-matrix, $\Delta t^{\mathrm{imp},i}_{\Lambda\Lambda'}$. However, in the Δ-matrix enters the *conjugate transpose of the left* radial solution to the host potential instead of the *right* radial solution. Because the Δ-matrix is independent of the indices k and k', it only has to be computed once (for the Fermi energy, remembering that the radial solutions are in fact energy dependent, what has been dropped from the notation for simplicity).

By inserting Eq. (2.142) for the impurity wavefunction coefficients, we can further modify Eq. (2.146) so that only the coefficients of the host wavefunction enter, *i.e.*

$$T_{k'k} = \sum_{i,i'} \sum_{\Lambda,\Lambda'} c^{i*}_{k',\Lambda} T^{ii'}_{\Lambda\Lambda'} \; c^{i'}_{k,\Lambda'} \;, \tag{2.148}$$

where we introduced the T-matrix as

$$T^{ii'}_{\Lambda\Lambda'} = \sum_{\Lambda''} \Delta^i_{\Lambda\Lambda''} \left(\delta_{ii'}\, \delta_{\Lambda''\Lambda'} + \sum_{\Lambda'''} G^{\mathrm{imp},ii'}_{\Lambda''\Lambda'''} \; \Delta t^{\mathrm{imp},i'}_{\Lambda'''\Lambda'} \right) \;. \tag{2.149}$$

Also the T-matrix needs to be computed only once (per energy), and then it can be used to to obtain $T_{k'k}$ for all pairs of k and k'. Thus the formulation (2.148) is computationally much more efficient than (2.146), both from the computing time perspective and the memory demand, and thus used in the code developed in this thesis.

Optical theorem

A useful relation of the $\mathcal{T}$-matrix - called the optical theorem - is given in a basis-independent form by the following equation (for a derivation, see *e.g.* [63])

$$\frac{1}{2i} \left(\mathcal{T}^\dagger - \mathcal{T} \right) = \pi\, \mathcal{T}^\dagger \, \mathcal{T} \;. \tag{2.150}$$

The optical theorem is very useful to test the validity of the (numerically) calculated Δt-matrices, but also the $T_{kk'}$-matrix. For the latter, the optical theorem reads [52]

$$-\operatorname{Im}T^{\sigma\sigma}_{kk} = \frac{\pi}{V_{\mathrm{BZ}}} \sum_{\sigma'} \int\limits_{\mathrm{FS}} \frac{\mathrm{d}S}{|\vec{v}_{\vec{k}}|} \, |T^{\sigma\sigma'}_{kk'}|^2 \; . \tag{2.151}$$

Usually, the op

Strategy for a massively parallel computation

For the calculation of the anomalous Hall effects, the transition rates $P_{kk'} \sim |T_{kk'}|^2$ usually have to be evaluated on a dense grid representing the Fermi surface (*cf.* chapter 4). Then, the matrix $P_{kk'}$ becomes very large, and the memory required to store it is in the range of a few hundred GByte up to a few TByte. Also, the time to calculate all matrix elements would require several days up to a few weeks on a modern desktop CPU. As example, we give the computational demands for the evaluation of Eq. (2.149) for MnSi (*cf.* section 6.3) on a dense Fermi-surface grid of about half a million k-points ($N_k \approx 500.000$). This requires storing about 2.5×10^{11} floating point numbers (we work with a 8 byte double-precision representation), which yields about 1.8 TByte. To calculate each matrix element according to Eq. (2.148), we have to perform about N floating-point operations, with $N = N_{\mathrm{cls}} \times 2 \times (\ell_{\mathrm{max}} + 1)^2 = 41 \times 2 \times 16 = 1312$ the matrix size of $T^{ii'}_{\Lambda\Lambda'}$. This adds up to about 10^{17} floating point operations for the whole $P_{kk'}$-matrix (not taking into account a factor 8, which comes from averaging $P_{kk'}$ over different impurity positions, *cf.* section 6.3), and would take about 50 days of computation on a single-core CPU.

The need for a massively parallel implementation for the computation of the scattering rates is evident, and the problem is ideally suited for state-of-the-art supercomputer. As example, one midplane (*i.e.* a medium-sized allocation unit) of the supercomputer JUQUEEN contains about 8 TByte of memory and 8192 compute cores, which allows to store the matrix in memory and computation in a reasonable time (for the aforementioned example approximately 1 hour). However, we have to choose an appropriate strategy so split the $P_{kk'}$-matrix and distribute the sub-matrices across the compute cores, because the memory available per compute core is only 1 GByte (in spite the large overall memory).

The most straightforward way to distribute the matrix $P_{kk'}$ across the processors would be to parallelize the outer or the inner loop (see Fig. 2.2a), *i.e.*

```
do k1 in chunk_FSpoints(my_rank,n_ranks=8192)
  do k2 in all_FSpoints
    call calculate_matrixelement(k1,k2)
  end do
end do
```

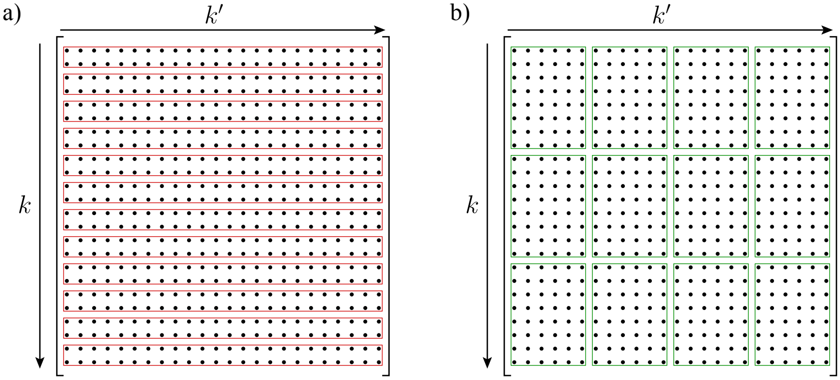

Figure 2.2.: Two strategies for distributing the work for calculating and storing $P_{kk'}$ across the processors. (a) Row-like division corresponding to a parallelized outer loop. (b) Sub-matrix division of (nearly) quadratic shape yields a more efficient handling of memory.

This way, each processor needs the input-data from all k-points (because of the inner loop). The largest data to be read in are the host wavefunction coefficients (in total about 2 GByte for the example of MnSi) and would not fit into the memory for this parallelization strategy. Another, slightly more complicated but much more memory-efficient treatment results from the division in (nearly) quadratic sub-matrices (see Fig. 2.2b):

```
do k1 in chunk_FSpoints(my_rank_rows,n_ranks_rows=128)
  do k2 in chunk_FSpoints(my_rank_cols,n_ranks_cols=64)
    call calculate_matrixelement(k1,k2)
  end do
end do
```

In this way, not all wavefunction coefficients are needed at every core, but only a fraction of $(1/N_{\text{col}}^{\text{ranks}} + 1/N_{\text{row}}^{\text{ranks}})$. For our example, this yields about 50 MByte per core and enough memory is left for the storage of the other input quantities (*e.g.* the $T_{\Lambda\Lambda'}^{ii'}$-matrix) and the output quantities. However, this approach requires more communication across the processors when post-processing the $P_{kk'}$-matrix, *e.g.* when solving the Boltzmann equation (see section 3.5 in the next chapter 3). However, the communication required to solve Boltzmann equation is very limited (one collective call after each iteration step in solution of the Boltzmann equation), and this does not represent a bottleneck. Thus, a very efficient and also highly scalable parallel implementation is achieved.

3 Anomalous and spin Hall effects

3.1. Introduction and short history survey of the AHE

The ordinary Hall effect, discovered by Edwin Hall at the end of the 19th century [64], is familiar to nearly every high-school pupil: a current flowing in y-direction through a material experiences a deviation into the transverse (*i.e.* perpendicular) x-direction if an external magnetic field H is applied along the z-direction. The electrons, which constitute the current, acquire a transverse velocity due to the Lorentz force and consequently, lead to a finite resistivity in the direction perpendicular to the external magnetic and electric field.

Already at this early time in history, Hall also noticed an ‘anomalous’ contribution to the Hall current if the material is ferromagnetic [30], and the following relation has been established experimentally:

$$\rho_{xy} = R_{\mathrm{O}}\, H + 4\pi\, R_{\mathrm{S}}\, M, \tag{3.1}$$

where the first term is the ordinary Hall contribution with the ordinary Hall coefficient R_{O}, proportional to the external magnetic field, and the second term is the anomalous (or spontaneous) contribution, later to be known as anomalous Hall effect (AHE), which is proportional to the magnetization of the sample. For most of the materials, the anomalous contribution is much larger than the ordinary one.

In contrast to the ordinary Hall effect, the microscopic mechanism behind the AHE could not be explained directly. The first successful attempts were made only about 60 years later by Karplus and Luttinger in 1954 [65] and by Smit in 1955 [66], where they related the AHE to the spin-orbit coupling. Spin-orbit coupling is at the heart of the AHE since it acts, roughly speaking, as in internal magnetic field on the electrons and causes an anomalous velocity in the transverse direction.

Much later than the anomalous Hall effect, the closely related *spin Hall effect* (SHE) was predicted [25, 26] and recently also realized experimentally [29]. It is a promising candidate to generate and, via the inverse spin Hall effect, also to detect pure spin currents, which are at the heart of the relatively new field of spintronics. The SHE can be thought of as a special case of the AHE in a non-magnetic material. In this picture, time-reversal symmetry requires that the bands are twofold spin-degenerate, and further that the anomalous velocity acquired by spin-up and spin-down electrons is equal in magnitude but different in sign. As a consequence, the spin-up and spin-down charge currents in the transverse direction exactly cancel each other, leading however to a pure transverse spin-current.

Since the prediction and discovery of the SHE, besides many studies on the SHE [27, 37, 38, 67, 68], also the AHE has regained much interest, because insights into the one effect will contribute to the understanding of the other. Moreover, currently the AHE is better suited to be studied experimentally due to the finite Hall voltage that is associated with it, and it is difficult to detect spin-currents directly. To circumvent this problem in the SHE, the so-called inverse spin Hall effect (ISHE) is used to convert a pure spin current into a transverse charge current or finite Hall voltage.

3.2. Contributions to the anomalous and spin Hall effects — skew scattering

In the early theories, three major distinct mechanisms were established which contribute to the anomalous velocity: an *intrinsic* contribution and two extrinsic ones, named *skew-scattering* and *side-jump.*

The first one was introduced by Karplus and Luttinger [65] and is a pure band-structure effect, therefore it is called *intrinsic.* It originates from the coupling of different Bloch bands under an applied electric field, where the Hamiltonian is perturbed by $\delta\mathcal{H} = \mathcal{E}_x\,\hat{x}$. Karplus and Luttinger derived a scaling law $\rho_{xy}^{\mathrm{intr}} \sim \rho_{xx}^2$ (ρ_{xx} being the longitudinal resistivity), that correctly described many experimental findings. In the modern theories of AHE, the intrinsic contribution to the anomalous velocity is calculated in terms of the Berry curvature.

Another, semiclassical approach was tried by Smit [66, 69], who looked at the evolution of wave packets under the presence of impurities and discovered the *skew-scattering* mechanism. Here, spin-orbit coupling leads to an asymmetry in the scattering rates, *i.e.* the scattering from a state k into a state k' is different from the reversed process. This in turn leads to a preferred scattering into $+y$-direction or $-y$-direction and therefore also to an anomalous velocity. Smit also found a scaling law for the skew-scattering contribution to the resistivity, which is proportional to the longitudinal resistivity, $\rho_{xy}^{\mathrm{sk}} \sim \rho_{xx}$. It therefore scales differently than the intrinsic contribution.

Smit also argued that the electrons exhibit coordinate shifts when hitting an impurity [69], and this mechanism was named *side-jump* by Berger [70–72]. Strangely, it does not depend on the impurity concentration, being a disorder effect. It scales as the intrinsic contribution and it is therefore very difficult to distinguish the two effects experimentally.

In the modern theory [31, 73], two more contributions scaling as the intrinsic and side-jump contribution are distinguished. They are called *intrinsic skew-scattering* and *anomalous distribution contribution*. The former comes from a higher (*i.e.* fourth) order expansion in the strength of the scattering potential. Working in a semi-classical picture, the latter is closely related to the side-jump contribution and accounts for a correction to the distribution function, because the electrons acquire a change in their potential energy upon side-jump scattering. However, these contributions cannot be distinguished experimentally from the intrinsic and side-jump contributions. Therefore, an appropriate name for their sum is *scattering-independent* contribution [74].

The main focus of this work is on the skew-scattering mechanism, which is the dominating one for clean samples and in the dilute limit of impurity concentration. This is because the skew-scattering contribution to the conductivity scales inversely proportional to the impurity concentration c in this limit. Thus it decays with increasing c, and at some break-even point c_0 will be comparable with other contributions. However, our method employing the semi-classical Boltzmann equation (which is described later) is only valid in the clean limit and should be only applied there.

Besides the AHC, also the longitudinal conductivity scales inversely proportional to the impurity concentration, and the anomalous Hall angle (AHA), defined as ratio between the two, is independent of c in this limit. The AHA stands for an efficiency of converting a longitudinal current into a transverse (partly spin-polarized) current. Similarly, also the SHA can be interpreted as an efficiency of converting a (longitudinal) charge current into a pure (transverse) spin current.

3.3. Experimental detection and scaling laws

The anomalous contribution to the transverse resistivity can be relatively easily extracted experimentally: the Hall resistivity is measured in a varying applied magnetic field. The resulting curve shows two regions with different slopes, which stem from a field-dependence of the magnetization: at higher fields, the anomalous contribution is constant, because the magnetization has reached its saturation value. Thus, the slope is solely determined by the ordinary Hall coefficient. At low fields, however, also the magnetization depends on the magnetic field and contributes to the slope. To obtain the anomalous Hall coefficient, R, the high-field data is extrapolated to zero field. This value yields the anomalous Hall resistivity $\rho_{\mathrm{AH}} = 4\pi R_{\mathrm{S}}\, M$.

Beyond the extraction of the total ρ_{AH} it is challenging to separate out the different contributions to the anomalous Hall effect. Commonly, a distinction between the skew-scattering contribution on the one hand and the scattering-independent contribution on the other, is made by referring to their different scaling behavior with the longitudinal resistivity,

$$\rho_{\mathrm{xy}} = a\,\rho_{xx} + b\rho_{xx}^2 \ . \tag{3.2}$$

Both quantities are varied at the same time through the control of another parameter, *e.g.* the impurity concentration [75], the temperature [76] or the film thickness [77, 78]. With the combination of temperature- and thickness-dependent experiments on epitaxial Fe films, more terms can be distinguished, and Tian *et al.* [77] argue that it is presumably the separation of the side-jump contribution, as also confirmed by tight-binding model calculations [79]. However, some assumptions made in their line of thought still have to be verified theoretically.

Alternatively, often the conductivity is considered instead of the resistivity. The two tensor quantities are intimately related to each other, $\overset{\leftrightarrow}{\sigma} = (\overset{\leftrightarrow}{\rho})^{-1}$, which yields the relations

$$\sigma_{xy} = \frac{-\rho_{yx}}{\rho_{xx}^2 + \rho_{xy}^2} \approx \frac{\rho_{xy}}{\rho_{xx}^2} \ , \tag{3.3}$$

$$\sigma_{xx} = \frac{\rho_{xx}}{\rho_{xx}^2 + \rho_{xy}^2} \approx \frac{1}{\rho_{xx}} \ . \tag{3.4}$$

Here, we assumed $\rho_{xx} = \rho_{yy}$ and $\rho_{xy} = -\rho_{yx}$, which is the case for a cubic crystal, or a tetragonal or hexagonal crystal with magnetization along the c-axis. Additionally, the fact that $\rho_{xy} \ll \rho_{xx}$ was employed. With these relations, Eq. (3.2) turns into

$$\sigma_{\mathrm{xy}} = a\,\sigma_{xx} + b \tag{3.5}$$

Commonly, a is also called the skew-scattering anomalous Hall angle α^{c} (*cf.* Eq. (3.25)).

3.4. Theoretical approaches to electron transport

Three major *ab initio* approaches are distinguished when it comes to electron transport.

The first one is the semi-classical approach based on the Boltzmann equation. Its beauty lies in the clear physical interpretation in terms of scattering rates and evolution of wave packets. This approach is used in this work and is explained in more detail in the next section 3.5.

The Kubo formalism goes beyond and — in contrast to the semi-classical Boltzmann approach — treats the problem on a fully quantum mechanical level employing a Green function formalism to calculate transport properties. There exist several levels of approximations within the Kubo formalism, *e.g.* Kubo-Bastin (independent electron approximation at zero frequency), Kubo-Středa (working at zero temperature) or Kubo-Greenwood (neglecting asymmetric parts and unable to treat the AHE or SHE). The advantage over the Boltzmann formalism is the treatment of concentrated alloys [80], which in turn requires the calculation of the Green function of the disordered system. However, it lacks transparency and therefore it is difficult to develop a microscopic understanding of the underlying physical effects.

Finally, the Keldish formalism goes one step beyond the Kubo formalism and uses non-equilibrium Green functions. Thus it becomes possible to go beyond linear response theory, but it is numerically very demanding. However, the Keldish formalism is frequently applied to simple systems, like the electron transport through a quantum dot [81].

3.5. Semi-classical approach to electron transport

The Boltzmann equation determines the non-equilibrium distribution function of semi-classical particles, which are accelerated by external fields and are subject to collisions. In the context of electron transport in a solid, these are Bloch electrons scattering at impurities or phonons. With the term *semi-classical* we mean, that the electrons behave classically in the time span between two scattering events, but the scattering amplitudes are computed from quantum-mechanical equations. The connection between the 'classical' and the 'quantum' world is formed by Fermi's golden rule. Once the distribution function is known, transport properties such as the charge or spin conductivity tensor can be calculated.

In this section, we will derive an equation for calculating the conductivity tensor. First, we will give the basic ansatz for the Boltzmann equation, simplify it under the assumption of a homogeneous weak electric field at low temperatures, and finally obtain a linearized expression reformulated in terms of the vector mean free path. We will show how to solve the resulting equation by an iterative scheme. Finally, we will give the expression for the calculation of the conductivity tensor and transverse transport coefficients.

Simplifying the Boltzmann equation

The Boltzmann equation describes the evolution of a non-equilibrium distribution function $f = f(\vec{r}, \vec{k}, t)$, depending on the position $\vec{r}$, the crystal momentum (or Bloch vector) $\vec{k}$ and time t. The total rate of change in the distribution function is given by

$$\frac{\mathrm{d}f}{\mathrm{d}t} = \frac{\partial f}{\partial t} + \frac{\partial f}{\partial \vec{x}} \cdot \frac{\mathrm{d}\vec{x}}{\mathrm{d}t} + \frac{\partial f}{\partial \vec{k}} \cdot \frac{\mathrm{d}\vec{k}}{\mathrm{d}t} \tag{3.6}$$

The second and third terms on the right hand side of Eq. (3.6) are also called drift and field terms, respectively. The latter can be rewritten as $\frac{1}{\hbar}\frac{\partial f}{\partial \vec{k}} \cdot \vec{F}$, where the external force $\vec{F} = -\mathrm{e}\,\vec{\mathcal{E}}$ acting on the electrons is determined by an external electric field $\vec{\mathcal{E}}$.[1]

In the steady state, the total rate of change must be compensated by the collision term, $\frac{\mathrm{d}f}{\mathrm{d}t} = \left(\frac{\partial f}{\partial t}\right)_{\mathrm{coll}}$. For a time-independent and homogeneous external electric field, only the field term in Eq. (3.6) survives and the Boltzmann equation reads

$$-\frac{\mathrm{e}}{\hbar}\,\frac{\partial f_k}{\partial \vec{k}} \cdot \vec{\mathcal{E}} = \left(\frac{\partial f_k}{\partial t}\right)_{\mathrm{coll}} \;, \tag{3.7}$$

where from here on we explicitly denote the k-dependence of f_k and comprehend the symbol $k = (\vec{k}, \nu)$ as a multi-index, where ν labels additional degeneracies (*e.g.* in systems with time-reversal and space-inversion symmetry each level is at least twofold degenerate).

In the next step, we assume a weak electric field which allows us to linearize Eq. (3.7) in $\vec{\mathcal{E}}$. It is fruitful to separate the full non-equilibrium distribution function into an equilibrium part $f^0(\epsilon_{\vec{k}})$ and a deviation (or a response) due to the external field g_k,

$$f_k = f^0(\epsilon_{\vec{k}}) + g_k \;. \tag{3.8}$$

The equilibrium part is given by the Fermi-Dirac distribution function and only depends implicitly on the Bloch vector via the band energy $\epsilon_{\vec{k}}$. The deviations g_k will be (in lowest order) linear in the electric field, and therefore we can replace f_k by $f^0(\epsilon_{\vec{k}})$ on the left hand side of Eq. (3.7). Making use of the chain rule for the derivative and the definition of the group velocity $v_{\vec{k}} = \partial\epsilon_{\vec{k}}/(\hbar\,\partial\vec{k})$, we arrive at

$$-\,e\,\frac{\partial f^0(\epsilon_{\vec{k}})}{\partial \epsilon_{\vec{k}}}\;\vec{v}_{\vec{k}} \cdot \vec{\mathcal{E}} = \left(\frac{\partial f_k}{\partial t}\right)_{\mathrm{coll}} \;. \tag{3.9}$$

Let us next turn to the collision term on the right hand side of Eq. (3.9). It has been shown by Luttinger and Kohn [82], that it is of the form

$$\left(\frac{\partial f_k}{\partial t}\right)_{\mathrm{coll}} = \sum_{k'} \left(f_{k'}\;P_{k',k} - f_k\;P_{k,k'}\right) \;, \tag{3.10}$$

where $P_{k,k'}$ is the transition rate for scattering from a state $k = (\vec{k}, \nu)$ into a state $k' = (\vec{k}', \nu')$. Thus, the first and second term on the right hand side stand for transitions of occupied states k' to unoccupied states k (scattering-in term) and vice versa (scattering-out term), respectively. We shortly want to comment on the form of Eq. (3.10): some authors present terms proportional to $f_{k'}(1 - f_k)$ instead of $f_{k'}$, which can be intuitively understood by recalling that the electron scatters from an *occupied* state k' into an *empty* state k. However, Luttinger and Kohn argued in their

---

[1] In our notation, the symbol $e > 0$ denotes the elementary charge.

rigorous derivation (*cf.* Appendix F in Ref. [82]), that the collision term (3.10) is of the form presented in Eq. (3.10). Inserting Eq. (3.8) in Eq. (3.10) leads to

$$\left(\frac{\partial f_k}{\partial t}\right)_{\text{coll}} = \sum_{k'} \left(g_{k'}\ P_{k',k} - g_k\ P_{k,k'}\right) \tag{3.11}$$

$$+ \sum_{k'} \left(f^0(\epsilon_{\vec{k}'})\ P_{k',k} - f^0(\epsilon_{\vec{k}})\ P_{k,k'}\right) \tag{3.12}$$

The microscopic reversibility does not hold (*i.e.* $P_{k,k'} \neq P_{k',k}$) due to the presence of spin-orbit coupling in the system and the second term on the right hand side (3.12) does not vanish in a trivial way. In fact, it is this asymmetry that leads to the anomalous and spin Hall effects [37, 83]. However, the total sum in (3.12) vanishes, which can be seen in the limit of vanishing electric field: the left hand side of Eq. (3.9) vanishes and in the collision term (3.10) the distribution function for the equilibrium state enters, which directly proves our statement.

The next step is to linearize also the response of the system in $\vec{\mathcal{E}}$, leading to the ansatz

$$g_k = \mathrm{e}\, \frac{\partial f^0(\epsilon_{\vec{k}})}{\partial \epsilon_{\vec{k}}}\ \vec{\lambda}_k \cdot \vec{\mathcal{E}} \quad \xrightarrow{T\to 0} \quad -\mathrm{e}\ \delta(\epsilon_{\vec{k}} - \epsilon_F)\ \vec{\lambda}_k \cdot \vec{\mathcal{E}}\ . \tag{3.13}$$

By this ansatz we reformulate the Boltzmann equation in terms of the vector mean free path $\vec{\lambda}_k$ instead of the distribution function f_k (or the deviations g_k, respectively). The derivative of the Fermi distribution function in the ansatz is justified by the fact that for weak electric fields, deviations from the equilibrium distribution function will only occur for states whose energy is close to the Fermi energy (*cf.* the field term in Eq. (3.9)). It is peaked around the Fermi energy and turns into a δ-function $\delta(\epsilon_{\vec{k}} - \epsilon_F)$ for infinitesimally small temperatures.

In this low-temperature and low-field limit, excitations like phonons and magnons are frozen out and the scattering is dominated by elastic scattering off impurities and the scattering rate $P_{k,k'} = \tilde{P}_{k,k'}\ \delta(\epsilon_{\vec{k}} - \epsilon_{\vec{k}'})$ is proportional to the Dirac δ-function. This allows us to set $f^0(\epsilon_{\vec{k}}) = f^0(\epsilon_{\vec{k}'})$ when inserting the ansatz (3.13) into Eq. (3.11) and we arrive at

$$\left(\frac{\partial f_k}{\partial t}\right)_{\text{coll}} = \mathrm{e}\frac{\partial f^0(\epsilon_{\vec{k}})}{\partial \epsilon_{\vec{k}}}\ \vec{\mathcal{E}} \cdot \sum_{k'} \left(\vec{\lambda}_{k'}\ P_{k',k} - \vec{\lambda}_k\ P_{k,k'}\right)\ . \tag{3.14}$$

Inserting this result into Eq. (3.9) we arrive at an equation for the vector mean free path,

$$\vec{\lambda}_k = \tau_k \left[\vec{v}_{\vec{k}} + \sum_{k'} P_{\vec{k}',\vec{k}}\ \vec{\lambda}_{k'}\right]\ , \qquad \vec{k} \in \mathrm{FS}\ , \tag{3.15}$$

where we introduced the relaxation time τ_k of a state defined by

$$\tau_k^{-1} = \sum_{k'} P_{k,k'}\ . \tag{3.16}$$

The final form of the Boltzmann equation (3.15) is a self-consistency problem via the sum on the right hand side (corresponding to the scattering-in term in the collision term (3.10)). Possibilities to solve it are discussed *e.g.* in [62]. We focus on an iterative solution (see next sub-section).

It is worth noticing that Eq. (3.15) yields in fact one equation for each Cartesian component of $\vec{\lambda}_k$, which are however decoupled from each other. Then, for an external electric field of arbitrary direction, the mean free path is parallel to the applied electric field and given by $(\vec{\lambda}_k \cdot \hat{n}_{\mathcal{E}})$, where $\hat{n}_{\mathcal{E}} = \vec{\mathcal{E}}/|\mathcal{E}|$.

Because the deviations are only non-vanishing for states at the Fermi energy, the mean free path has to be found only for those states contained in the Fermi surface. This also reduces the computational effort to evaluate the sum on the right hand side of Eq. (3.15). The summation over the multi-index $k' = (\vec{k}', \nu')$ is in fact a summation over the degeneracies and an integration over the Brillouin zone (BZ),

$$\sum_{k'} \rightarrow \sum_{\nu'} \int_{\mathrm{BZ}} \frac{\mathrm{d}^3 k'}{V_{\mathrm{BZ}}} \,, \tag{3.17}$$

where V_{BZ} is the BZ volume. Because the scattering rates contain a δ-function and the Bloch-vector $\vec{k}$ is restricted to the Fermi surface, also the integral in Eq. (3.15) can be restricted to a Fermi-surface integral and we arrive at

$$\vec{\lambda}_k = \tau_k \left[\vec{v}_{\vec{k}} + \frac{1}{V_{\mathrm{BZ}}} \sum_{\nu'} \int_{\mathrm{FS}} \frac{\mathrm{d}S}{\hbar\, |\vec{v}_{\vec{k}}|}\; \tilde{P}_{\vec{k}',\vec{k}}\; \vec{\lambda}_{k'} \right] \,, \qquad \vec{k} \in \mathrm{FS} \,. \tag{3.18}$$

Solution of the Boltzmann equation

A way to solve Eq. (3.15) is achieved by iterating. This means, that in the first step we start from the so-called relaxation time approximation, $\vec{\lambda}_k^{(0)} = \tau_k\, \vec{v}_{\vec{k}}$. This result is inserted into the right hand side of Eq. (3.15) to obtain $\vec{\lambda}_k^{(1)}$. This procedure is iterated until self-consistency is achieved. Usually, the mean free path converges very quickly and only 10-30 iterations are needed to bring the average root-mean-square (RMS) to the order 10^{-9}, defined by

$$\mathrm{RMS}_i = \frac{\sqrt{\sum_k \left(\lambda_{k,i}^{(n+1)} - \lambda_{k,i}^{(n)} \right)^2}}{N_{\vec{k}}\; N_\nu} \,, \qquad i \in \{x, y, z\} \,, \tag{3.19}$$

where $N_{\vec{k}}$ and N_ν is the number of k-points and number of degeneracies, respectively.

As it turns out in our calculations, the iterative solution to the Boltzmann equation does not always converge. It is important to exploit symmetries as much as possible. Especially a condition $\sum_{\vec{k}} \vec{v}_{\vec{k}} = 0$ seems to be crucial for the convergence (*cf.* section 6.3.6).

Calculation of the conductivity tensor

The charge conductivity tensor $\overset{\leftrightarrow}{\sigma}_c$ describes the charge flow of a system under the application of an electric field $\vec{\mathcal{E}}$ in linear response, thus

$$\vec{j}_c = \overset{\leftrightarrow}{\sigma}_c \, \vec{\mathcal{E}} \; , \tag{3.20}$$

where the charge-current density $\vec{j}_c$ is defined by

$$\begin{aligned} \vec{j}_c &= -\frac{\mathrm{e}}{V} \sum_k f_k \, \vec{v}_{\vec{k}} = \sum_k \left[f^0(\epsilon_{\vec{k}}) + g_k \right] \vec{v}_{\vec{k}} \\ &= \frac{\mathrm{e}^2}{V} \sum_k \delta(\epsilon_k - \epsilon_F) \, \vec{v}_{\vec{k}} \left(\vec{\lambda}_k \cdot \vec{\mathcal{E}} \right) \\ &= \frac{\mathrm{e}^2}{\hbar V \, V_{\mathrm{BZ}}} \sum_\nu \int_{\mathrm{FS}} \frac{\mathrm{d}S}{|\vec{v}_{\vec{k}}|} \, \vec{v}_{\vec{k}} \otimes \vec{\lambda}_k \cdot \vec{\mathcal{E}} \; . \end{aligned} \tag{3.21}$$

Here, V is the unit-cell volume and "$\otimes$" denotes the tensor product. From the first to the second line we realized that the sum over the equilibrium distribution function vanishes. This can be again seen easily by setting the electric field $\vec{\mathcal{E}}$ to zero, which also implies that $\vec{j}$ and g_k vanish. By comparing Eq. (3.20) and Eq. (3.21) we obtain

$$\overset{\leftrightarrow}{\sigma}_c = \frac{\mathrm{e}^2}{\hbar} \frac{1}{(2\pi)^3} \sum_\nu \int_{\mathrm{FS}} \frac{\mathrm{d}S}{|\vec{v}_{\vec{k}}|} \, \vec{v}_{\vec{k}} \otimes \vec{\lambda}_k \; . \tag{3.22}$$

Analogously, we define the spin-conductivity

$$\overset{\leftrightarrow}{\sigma}_s = \frac{\mathrm{e}^2}{\hbar} \frac{1}{(2\pi)^3} \sum_\nu \int_{\mathrm{FS}} \frac{\mathrm{d}S}{|\vec{v}_{\vec{k}}|} \, \langle p^{\hat{n}} \rangle_k \, \vec{v}_{\vec{k}} \otimes \vec{\lambda}_k \; , \tag{3.23}$$

where $\langle p^{\hat{n}} \rangle_k$ is the spin-polarization value of state $k = (\vec{k}, \nu)$ with spin-quantization axis along direction $\hat{n}$. The spin-polarization is dimensionless and related to the spin expectation-value by $\langle s^{\hat{n}} \rangle = (\hbar/2) \, \langle p^{\hat{n}} \rangle$. By this choice, charge and spin conductivity have the same unit. To calculate the true flow of angular momentum, we have to compute

$$\vec{j}_{\mathrm{s}} = -\frac{\hbar}{2\mathrm{e}} \overset{\leftrightarrow}{\sigma}_{\mathrm{s}} \cdot \vec{\mathcal{E}} \tag{3.24}$$

The conversion factor accounts for an angular momentum of $\hbar/2$ carried by an electron, which is charged by $(-\mathrm{e})$. Some authors include this factor (sometimes without the minus-sign) in the definition of the spin-conductivity tensor (see [38] for a detailed discussion). However, then also the equations to calculate the spin Hall angle (see below) have to be adapted.

We finally show, that the conductivity tensor scales inversely linear with the impurity concentration c: the impurity concentration enters Eq. (2.143) just as a pre-factor and thus $P_{kk'} \sim c$. This leads to the scaling $\tau_k \sim 1/c$ (*cf.* Eq. (3.16)), and consequently the mean-free path scales as $\vec{\lambda}_k \sim 1/c$ (*cf.* Eq. (3.15)), which proves our statement.

Transverse conductivity

We can now define the anomalous Hall conductivity as the xy-component of the charge conductivity tensor, σ^{c}_{xy}. It means, that the external electric field is applied along the y-direction, and the transverse charge current is measured along the x-direction.

The corresponding anomalous Hall angle is defined by

$$\alpha^{\mathrm{c}} = \frac{\sigma^{\mathrm{c}}_{xy}}{\sigma^{\mathrm{c}}_{yy}} \ . \tag{3.25}$$

However, for a ferromagnet with magnetization along the z-axis and cubic crystal symmetry, the longitudinal conductivities σ^{c}_{xx} and σ^{c}_{yy} will be equal to each other, and thus often the xx-component is entering the denominator in definitions of the AHA. Moreover, in some definitions of the anomalous Hall angle, the other tensor element $\sigma^{\mathrm{c}}_{yx} = -\sigma^{\mathrm{c}}_{xy}$ enters the nominator of the definition and thus differs from Eq. (3.25) by a minus-sign.

Similarly, the spin Hall angle is defined as

$$\alpha^{\mathrm{s}} = \frac{\sigma^{\mathrm{s}}_{xy}}{\sigma^{\mathrm{c}}_{yy}} \ . \tag{3.26}$$

Note that the *charge* conductivity enters the denominator. Care has to be taken when comparing the sign of the spin Hall angles to other works, due to the ambiguities concerning which component (the xy or yx component) to take for the definition, and also whether an additional sign comes from the definition of the spin conductivity.

Momentum- and spin-relaxation times

We finally give equations for the momentum- and spin-relaxation times.

We consider first a paramagnetic host, where each state is two-fold degenerate due to the conjugation-degeneracy (*cf.* section 2.6). Thus, we have $k = (\vec{k}, \sigma)$, with $\sigma \in \{\uparrow, \downarrow\}$ labeling the two degenerate states. The momentum relaxation time τ_{p} and spin-relaxation time T_1 for a paramagnetic host are defined by [52]

$$\tau_{\mathrm{p}} = \frac{2}{\sum_{\vec{k},\vec{k}'} \left(P^{\uparrow\uparrow}_{\vec{k},\vec{k}'} + P^{\downarrow\downarrow}_{\vec{k},\vec{k}'} \right)} \ , \tag{3.27}$$

$$T_1 = \frac{1}{\sum_{\vec{k},\vec{k}'} \left(P^{\uparrow\downarrow}_{\vec{k},\vec{k}'} + P^{\downarrow\uparrow}_{\vec{k},\vec{k}'} \right)} \ . \tag{3.28}$$

For the case of a magnetic host, the degeneracy is absent and we only have a momentum relaxation time, which we define by

$$\tau_{\mathrm{p}} = \frac{2}{\sum_{\vec{k},\vec{k}'} P_{\vec{k},\vec{k}'}} \ . \tag{3.29}$$

4

The Fermi surface

The Fermi surface (FS) is an iso-energy surface in reciprocal space, consisting of all those Bloch vectors $\vec{k}$, whose energy equals the Fermi energy, $\epsilon(\vec{k}) = \epsilon_F$. It is a characteristic property of a metal and some physical effects can already be deduced from its form. For example, when the Fermi surface consists of large parts that are parallel to each other, then the so-called *focusing effect* [84] can occur, where long-ranged Friedel-like charge oscillations around an impurity atom in a perfect crystal *focused* along certain directions occur. Some more important qualitative characteristics of a Fermi surface are whether it crosses the Brillouin zone (BZ) boundary or consists of multiple sheets crossing each other or having avoided crossings (corresponding to degeneracies or lifted degeneracies, respectively).

The form of the Fermi surface can range from relatively simple, sphere-like shapes for the alkali and noble metals to complicated, multi-sheeted forms with many crossings (*cf.* Fig. 4.1). The Fermi surface for simple forms could already be calculated in [52], where the search for Fermi-surface points (FS points) was based on a radial grid and a fixed number of directions in $\vec{k}$-space (*cf.* left panel in Fig. 4.2). However, this method has several disadvantages. For example, in the case of multi-sheeted Fermi surfaces with crossings, this method fails due to the ambiguity of the connection of FS points on neighboring radial rays. More difficulties arise when Fermi-surface parts are parallel to the radial grid, as it is already the case for the so-called *neck* around the L-point in the noble metals Cu, Ag and Au, or when small pockets exist near the BZ boundary and a large number of rays are needed to resolve these regions accurately.

These deficiencies can be overcome by subdividing the reciprocal space into a set of space-filling tetrahedra (*cf.* right panel in Fig. 4.2 for a two-dimensional illustration). Now, the Fermi-surface points are searched for along the edges of the tetrahedra and a Fermi surface piece is created by connecting the points with a straight line, resulting in triangles or quadrangles (*cf.* Fig. 4.3). However, it should be noticed that the definition of tetrahedra breaks the symmetry. This is closely related to the fact that there is an ambiguity in choosing the orientation of the tetrahedra. To resolve this problem, we determine the Fermi surface in the irreducible part of the BZ only and apply the symmetry operations of the crystal afterwards.

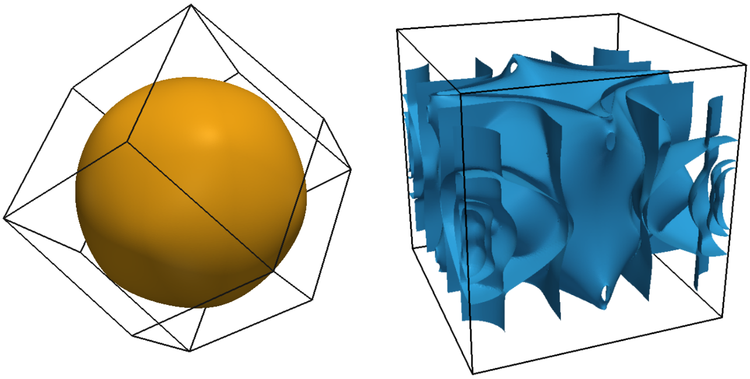

Figure 4.1.: Comparison between a simple Fermi surface for the alkali metal bcc-Rb (left) to a complicated, multi-sheeted Fermi surface of the ordered FePt-alloy in the $L1_0$-structure. Calculations are done with the code developed in this thesis. The figure has been already presented in [85].

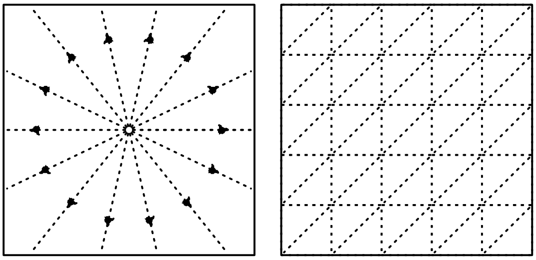

Figure 4.2.: Two-dimensional illustration of the radial method (left) and the tetrahedron method (right) for Fermi-surface calculations. The tetrahedra are shown as triangles in this plot. Dashed lines correspond to paths where intersections with the Fermi surface are searched for.

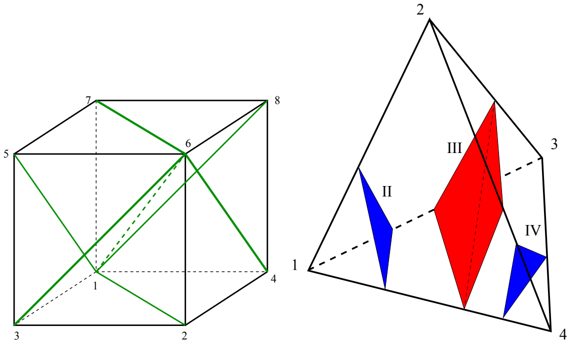

Figure 4.3.: Left: the tetrahedra are constructed from a cubic grid. Each cube is cut into six tetrahedra. Right: resulting shapes when the Fermi surface intersects with the tetrahedron.

A difficulty in combination with the KKR method is the actual search for band-structure points, because an implicit equation has to be solved to obtain the dispersion relation $\epsilon_{\vec{k}}$ via the eigenvalues of the KKR-matrix $\lambda(k, \epsilon)$ (*cf.* Eq. (2.96)). This drawback of the method can however also be used as a strength: it enables us to describe whether two nearby Fermi-surface sheets cross or do not cross (*cf.* section 4.1.2), whereas in most other methods (*e.g.* the Full Potential Linearized Planewave method) always either a crossing or an anti-crossing is assumed.

In this chapter, we first present the implemented tetrahedron method in section 4.1. We shortly list the different steps needed for the calculation of the Fermi surface, and we afterwards describe each step in detail. Additionally, a pre-processing step is described to speed-up calculations. Afterwards, in section 4.2 a simpler tetrahedron method is described, which only works if a very fine grid is chosen and was applied for the calculation of the spin-mixing parameter (presented in chapter 5.2).

4.1. Description of the tetrahedron method

The construction of the tetrahedra is based on a cubic grid, where each cube is divided into six tetrahedra (*cf.* Fig. 4.3 and appendix A.1 for details). For each tetrahedron we perform the following steps:

1. search for band-structure points along each edge of a tetrahedron
2. if multiple bands cross the tetrahedron: group the points according to their band
3. for each band: determine the shape of the FS piece, and truncate it to the interior of the IBZ

In the end, the Fermi surface is represented by a set of triangles.

4.1.1. Step 1: search for band-structure points

The band-structure points are indicated by a vanishing eigenvalue of the KKR matrix (*cf.* Eq. (2.96)). Before going into details, we make some general comments about the KKR-eigenvalues and their connection to the usual band structure in periodic crystals. Because the KKR matrix is in general non-hermitian, the eigenvalues are complex numbers and there exists a left and right eigenvector to a given eigenvalue. A KKR-eigenvalue has no direct physical meaning, except when it vanishes: then the right eigenvector corresponds to the Bloch wavefunction. The KKR-eigenvalues change continuously as a function of $\vec{k}$, therefore one can also speak about an *eigenvalue band*. For the case that a peculiar eigenvalue band is zero for some point $\vec{k}_0$ and a certain energy E_0, then it becomes physical and corresponds to a usual energy band. The eigenvalues of this band around $\vec{k}_0$ are not zero, but will vanish for a different energy close to E_0.

To find the band-structure points along the edges of a tetrahedron, we calculate the n eigenvalues $\lambda^i_{\vec{k}_\mathrm{start}}$ and $\lambda^j_{\vec{k}_\mathrm{end}}$ of the KKR-matrix at both ends of the edge, $\vec{k}_\mathrm{start}$ and $\vec{k}_\mathrm{end}$, respectively, and want to interpolate linearly between them. Here, $i, j \in \{1, \ldots, n\}$ label the eigenvalues and $n = 2N_\mathrm{at}\,(\ell_\mathrm{max} + 1)^2$ is the size of the KKR-matrix, basically determined by the angular momentum cut-off ℓ_max, the number of atoms in the unit cell N_at and a factor 2 for spin.

Unfortunately, the order of the eigenvalues is arbitrary and determined by the computer routine computing the eigenvalues. Therefore, is is not known explicitly which of the n eigenvalues on $\vec{k}_\mathrm{end}$ eigenvalue band as a given eigenvalue at $\vec{k}_\mathrm{start}$. Here, we work with the right eigenvectors $\underline{c}^i_{\vec{k}_\mathrm{start}}$ and $\underline{c}^j_{\vec{k}_\mathrm{end}}$ and the corresponding left eigenvectors, denoted by $\tilde{\cdot}$. Because the eigenvectors represent the wavefunction, they inherit the orbital character of the (physical) band and this changes smoothly when changing $\vec{k}$ by a small amount within the same band, but usually changes abruptly when also the band is changed. Thus, we compute the projections

$$p_{ij} = \left(\underline{\tilde{c}}^i_{\vec{k}_\mathrm{start}}\right)^* \cdot \underline{c}^j_{\vec{k}_\mathrm{end}} \ , \tag{4.1}$$

where the star denotes complex conjugation. We will usually obtain $|p_{ij}|^2 \approx 1$ if i and j label the the same eigenvalue band at the two ends of the edge and $|p_{ij}|^2 \ll 1$ for different bands. In some cases, the p_{ij}'s are not that clearly different for different bands, *e.g.* near avoided crossing the orbital character of the (physical) bands might change considerably on the length scale of the edge. This is the case for the Fermi-surface of bcc-Fe with spin-orbit coupling. Then, we divide the total edge into M sub-intervals with sampling points

$$\vec{k}_l = \vec{k}_\mathrm{start} + \frac{l}{M}\left(\vec{k}_\mathrm{end} - \vec{k}_\mathrm{start}\right) \ , \qquad (l = 0 \ldots M) \ , \tag{4.2}$$

and find the connections from $\vec{k}_0$ to $\vec{k}_1$, from $\vec{k}_1$ to $\vec{k}_2$ and so on. By comparison we arrive at the connection from $\vec{k}_0 = \vec{k}_{\text{start}}$ to $\vec{k}_M = \vec{k}_{\text{end}}$.

Once the connection between the eigenvalues is known, we linearly interpolate between the two k-points,

$$\begin{aligned} \lambda^{\text{appr.}}(s) &= \lambda^i_{\vec{k}_{\text{start}}} + s\left(\lambda^j_{\vec{k}_{\text{end}}} - \lambda^i_{\vec{k}_{\text{start}}}\right) , && (4.3) \\ \vec{k}^{\text{appr.}}(s) &= \vec{k}_{\text{start}} + s\left(\vec{k}_{\text{end}} - \vec{k}_{\text{start}}\right) , \qquad \text{with } 0 \leq s \leq 1 . && (4.4) \end{aligned}$$

By doing so, we find an approximate k-point of the intersection between the edge under consideration and the Fermi surface,

$$\begin{aligned} \vec{k}^{\text{appr.}}_{\text{FS}} &= (1 - s_0)\,\vec{k}_{\text{start}} + s_0\,\vec{k}_{\text{end}} , && (4.5) \\ \text{with} \qquad s_0 &= -\lambda^i_{\vec{k}_{\text{start}}} \Big/ \left(\lambda^j_{\vec{k}_{\text{end}}} - \lambda^i_{\vec{k}_{\text{start}}}\right) . \end{aligned}$$

Because the eigenvalues are complex numbers, their real and imaginary part do not necessarily vanish at the same k-point due to numerical reasons. A big influence on the numerical accuracy has the size of the tight-binding cluster when calculating the Green function of the tight-binding reference system (*cf.* appendix A.2.1 of Ref. [52]). Therefore, one determines s_0 in Eq. (4.5) by taking either the real or the imaginary part of the eigenvalues and accepts it only if the other part is reasonably small. Throughout this thesis, cluster sizes of at least 249 atoms have been used and s_0 was determined using the imaginary part of the eigenvalues.

The so found k-point can be refined by a nested intervals method (false position method, *cf.* Ref. [86]) and the root converges to numerical accuracy within a few iterations (usually 3-5 iterations are enough).

To finish the description of the first step, we comment on the efficiency of the code: because the six tetrahedra of one cube share many edges with each other, it is reasonable to search for band-structure points on the level of the underlying cubes and compute *e.g.* along the space diagonal only once per cube instead of once per tetrahedron. Counting the number of edges to be calculated for the two cases, we arrive at a speedup for this part of the code of $(6 \times 6)/19 \approx 2$. This scheme is employed in the code. An additional speedup is possible, because tetrahedra in neighboring cubes also have common edges. For example, by grouping eight neighboring cubes to a $(2 \times 2 \times 2)$-supercube, the average number of edges per cube to be calculated drops from 19 to 12.25 (being equivalent to a speedup of $(6 \times 6)/12.25 \approx 3$). This number can be even decreased by taking larger supercubes, and in the limit of very large supercubes the average number of edges per cube tends to 7 (speedup of approximately 5). However, because this method requires a more evolved logic and demands more memory, we work on the level of the small cubes and a speedup of approximately 2 for this part of the code is considered as satisfactory.

4.1.2. Step 2: group the points

Once the Fermi-surface (FS) points along the edges of a given tetrahedron are known, they have to be connected with each other yielding a piece of the Fermi surface. However, if multiple bands intersect with this tetrahedron, only the FS points belonging to the same band must be connected with each other.

To be numerically more stable, we repeat a tracing of eigenvalues (as described in the previous section), however we now start directly at an FS point $\vec{k}_1$ (which is in general somewhere between the ends of an edge) and end at the FS point $\vec{k}_2$ on another edge. The eigenvalue that vanishes at $\vec{k}_1$ will then also vanish at $\vec{k}_1$ if the two FS points belong to the same band. This procedure is iterated for all pairs of FS points on different edges.

The disadvantage of using the connections already known from the previous step is that the eigenvalues of two FS points are not connected on a straight line, but via an intermediate point being a vertex of the tetrahedron. This vertex might be a high-symmetry point with additional degeneracies and similar orbital character of the bands while in general, the Fermi-surface points do not lie on a high-symmetry line. This gives additional robustness to the method.

4.1.3. Step 3: determine the shape of the FS piece

As a last step, we determine the shape of the Fermi surface piece. For a given band and a given tetrahedron, three cases can be thought of: the band intersects with zero, three or four edges. This corresponds to different positions of the band energies at the four vertices of the tetrahedron with respect to the Fermi level [87]. No intersection with the Fermi-surface is found if the band energy at all four vertices is larger (or smaller) than the Fermi energy. The second case (intersecting three edges) occurs if the band energy at one vertex is above and at the other vertices below the Fermi energy (or vice versa), yielding a triangle as Fermi surface piece (*cf.* the blue shapes II and IV in the right panel of Fig. 4.3). The last case (intersecting four edges) occurs if the band energy at two vertices is above and at the other two vertices below the Fermi energy (see shape III in Fig. 4.3). The Fermi surface piece for the last case is an irregular quadrangle. For convenience, the quadrangle is stored as two triangles (as indicated by a dotted line) and in the rest of the code no distinction between the two cases (triangle or quadrangle) has to be made.

If the resulting triangle(s) intersect with the faces of the irreducible part of the Brillouin zone (IBZ), it it truncated to the interior of the IBZ. Then again, the resulting shape is stored in terms of triangles.

Finally, we comment on the resulting set of k-points. Because several triangles share vertices with each other, a given k-point occurs multiple times in the set. This is unfavorable when, in later steps, calculating quantities on the Fermi surface (*e.g.* the k-resolved spin-mixing parameter). By determining an irreducible set of k-points, we can reduce the number of k-points by a factor of approximately 6 and thus speed up calculations noticeably. Together with the information, which triangle vertex corresponds to which k-point in the irreducible set, we call this k-point set the *visualization set* of the Fermi surface. The set of triangles can be visualized with standard software, *e.g.* ParaView [88, 89].

The number of k-points in the visualization set might be even too large, *e.g.* for calculations of quantities that depend on more than one k-point index (*e.g.* the scattering rates $P_{kk'}$, *cf.* section 2.7). However, because such quantities are usually integrated over and not visualized, we determine another, reduced k-point set from the set of triangle vertices, which we call *integration set*. Therefore, we form a subset of all triangles corresponding to a given band in a given cube of the underlying cubic grid. This Fermi surface piece will be represented by a single k-point and its total area. As representing k-point, we choose the triangle vertex in the subset that is closest to the middle of the cube, and the total area is just the sum of areas of all triangles in the subset. By this procedure, the number of k-points can be reduced by another factor of approximately 3 to 4 depending on the Fermi surface. As a consequence, the computational demands for calculating and storing $P_{kk'}$ reduces by a factor of approximately 9 to 16.

4.1.4. Pre-processing step

In order to find Fermi surfaces of complicated shapes, especially to obtain correct small splittings due to spin-orbit interaction, a fine sampling of the Brillouin zone is required and the scheme described in the previous chapters 4.1.2 to 4.1.3 can be computationally very demanding. In order to speed up the total calculation, we perform a pre-processing step, where we exclude those regions of the Brillouin zone without Fermi-surface crossings from the cumbersome calculation described above. To achieve this, we first mark those cubes of a coarse grid that are intersecting with the Fermi surface, and then each marked cube is replaced by $(n \times n \times n)$ smaller cubes. This procedure can be even iterated m times. To achieve a good speed-up, we start from a very coarse grid (*e.g.* $15 \times 15 \times 12$ for the IBZ of FePt shown in Fig. 4.1) and choose $n = 2$ and m such that the required resolution is achieved (*e.g.* $m = 2$, resulting in a mesh of $60 \times 60 \times 48$ for the IBZ of FePt). However, the starting grid must be fine enough to resolve small Fermi surface objects such as small pockets.

To determine whether a cube contains parts of the Fermi surface, it is again searched for roots of the eigenvalues of the KKR matrix. This is done for the four space-diagonals.

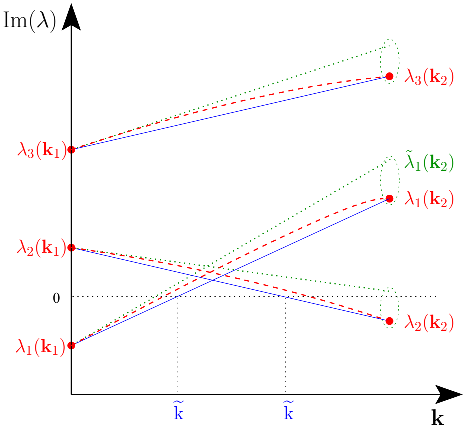

Figure 4.4.: Illustration of the perturbative approach to find the connection between the eigenvalues at two k-points ($\lambda_i(\vec{k}_1)$ and $\lambda_j(\vec{k}_2)$). Assuming the bands to evolve from $\vec{k}_1$ to $\vec{k}_2$ as the dashed line, the change in λ_i is estimated by $\tilde{\lambda}_i$. The closest (exact) eigenvalue $\lambda_j(\vec{k}_2)$ is associated with the eigenvalue at $\vec{k}_1$ and the linear interpolation yields the Fermi-surface point $\tilde{k}$.

4.2. Simpler version of the tetrahedron method

The method described above is in fact a second, more advanced implementation of a tetrahedron method. In a simpler implementation, the search for band-structure points along the edges of the tetrahedra is different. Here, the connection between the eigenvalues at different k-points is made by a scheme which we call 'estimation of eigenvalues' and is inspired by perturbation theory: when changing $\vec{k}$, we can estimate the evolution of an eigenvalue by

$$\tilde{\lambda}_i(\vec{k}) \approx \lambda_i(\vec{k}_1) + \langle \underline{\bar{c}}_i | \, \Delta \underline{\underline{M}} \, | \underline{c}_i \rangle \ , \tag{4.6}$$

where $\lambda_i(\vec{k}_1)$, $\langle \underline{\bar{c}}_i |$ and $| \underline{c}_i \rangle$ denote the eigenvalue and corresponding left and right eigenvectors, respectively, of the KKR-matrix at a reference point $\vec{k}_1$. The difference between the KKR-matrices at the two k-points under consideration, $\Delta \underline{\underline{M}} = \underline{\underline{M}}(\vec{k}, E_F) - \underline{\underline{M}}(\vec{k}_1, E_F)$, plays the role of a perturbation in this expression. By taking the closest exact eigenvalue at $\vec{k}$ with respect to the estimated eigenvalue, $\tilde{\lambda}_i(\vec{k})$, the connection between the eigenvalues at the two points $\vec{k}$ and $\vec{k}_1$ is made. This scheme is illustrated in Fig. 4.4

Similar equations as in the Rayleigh-Schrödinger perturbation-theory apply when a degeneracy is present (*cf.* [52] for details): first the correct linear combination of the eigenvectors in the degenerate subspace has to be found by diagonalization of the matrix $\left(\langle \underline{\bar{c}}_i | \, \Delta \underline{\underline{M}} \, | \underline{c}_j \rangle \right)_{ij}$, where i and j label the eigenvalues in the degenerate subspace.

In fact, in the systems under consideration later (*cf.* chapter 5.2) all bands are at least twofold degenerate due to the presence of time-reversal and space-inversion symmetry, and degenerate perturbation theory is always applied. However, when there are more degeneracies, this perturbative scheme can become numerically unstable and the projection of eigenvectors as described in chapter 4.1.1 is more favorable.

Once the connection between eigenvalues at two k-points is known, it is interpolated linearly between them (*cf.* Eq. (4.5)). Because the eigenvalues are complex numbers, we search for a k-point where the imaginary part vanishes and the real part is reasonably small enough. Here is the drawback of the method: for a relatively coarse grid (of the order $(60 \times 60 \times 60)$), the real part at the interpolated k-point can be of the same order of magnitude than other eigenvalues, which are close to zero but do not belong to a Fermi-surface point. This deficiency can be systematically overcome by increasing the number of grid points to *e.g.* $(280 \times 280 \times 280)$, and because the method is fast, it is still feasible to calculate the Fermi surface on a modern compute-cluster (approximately 140 core-hours on the JUROPA supercomputer for hcp-Re with the parameters as described in chapter 5.2, resulting in 1.9×10^6 FS points).

The same holds for the calculation of Fermi-surface properties that only depend on one k-point, *e.g.* the spin-mixing parameter $b^2_{\vec{k}}$. However, for quantities that depend on two k-points on the Fermi surface, *e.g.* the scattering matrices $P_{\vec{k},\vec{k}'}$, the number of Fermi-surface points is simply too large to be handled on compute-clusters and it becomes very expensive on supercomputers. Only the memory required to store $P_{\vec{k},\vec{k}'}$ for the example given above amounts to 100 TByte. Therefore, the simpler method yields too many k-points on the Fermi surface for the calculation of the conductivity, but for the calculation of the spin-mixing parameter, it is sufficient.

4.3. Version for 2-dimensional Brillouin zones

A similar scheme has been implemented into a version for 2-dimensional Brillouin zones. The numerical routines for the most complicated task, which is the proper connection of the KKR eigenvalues between two k-points, can be reused. Only the geometry needs to be changed: instead of (3-dimensional) cubes, the grid is based on (two-dimensional) squares and further subdivided into two triangles. Then, roots of the KKR eigenvalues are searched for along the edges of the triangles, and only two cases (compared to three in the 3D-version) can occur: (i) no intersecting edges with the Fermi surface or (ii) two intersecting edges. Thus, the geometry becomes rather simple and the resulting Fermi-surface pieces are straight lines.

This method can be used for finding the Fermi surface of *e.g.* two-dimensional films [90, 91].

5

Anisotropy of spin relaxation in metals

Parts of this chapter have been published in Refs. [92, 93].

In this chapter we describe a quantity of great importance for spintronic devices [1], namely the spin-relaxation time, and focus on its anisotropy. After injection of spin-polarized electrons into a non-magnetic metal, this non-equilibrium spin population will equilibrate on a time scale called the spin-relaxation time T_1 [94]. It is evident that an information encoded *e.g.* in the direction of the spin polarization will be lost after the time T_1 and therefore the spin-relaxation time is a crucial time scale for transfer of information. By anisotropy we mean, that the spin-relaxation time will depend on the direction of electron-spin polarization (*e.g.* polarized along $\hat{x}$ or $\hat{z}$).

For metals with structure-inversion symmetry, the dominating mechanism for spin relaxation is the Elliott-Yafet mechanism. In the theory of Elliott [34] and Yafet [55] the scattering of electrons at impurities at low temperature T or phonons at high T is described: due to spin-orbit coupling, there is a finite probability that not only the momentum is changed, but also the electron-spin is flipped due to a scattering event.

In the Elliott approximation details of the scattering potential are neglected and it is assumed that some source of scattering is present. Exploiting the properties of the wavefunctions of the pristine crystal under the presence of spin-orbit coupling, a relation between the rates of spin-flip and spin-conserving scattering events can be derived (see below) and related to the spin-mixing parameter b^2,

$$\frac{\tau_p}{T_1} \approx 4\,b^2 \;, \tag{5.1}$$

where τ_p is the momentum relaxation time. The spin-mixing (or Elliott-Yafet) parameter b^2 has since long been accepted as a measure for spin relaxation in non-magnetic, structure-inversion symmetric metals [1]. Calculations of b^2 have already been performed for various metals and successfully compared to experiments [36, 52, 56, 58, 95]. However, an anisotropy of b^2, which in consequence leads to an anisotropy in spin relaxation, has not been considered so far.

We will briefly outline the derivation of the Elliott approximation in the following section 5.1, which also gives us the possibility to introduce our notation. In the subsequent section 5.2 we turn to the calculation of b^2 for real materials and focus on the anisotropy of b^2. We found out that it can be gigantic in uniaxial crystals and stems from a large anisotropy at so-called spin-flip hot-spots. In section 5.3 we explain the microscopic origin of the effect in terms of a simple model and support our arguments by band-structure calculations of real materials (*cf.* sections 5.4 and 5.5).

5.1. Derivation of the Elliott approximation

Due to spin-orbit coupling (SOC), the eigenstates of the Hamiltonian are not of pure spin character, but a superposition of an up-state and a down-state. The combination of time-reversal and space-inversion symmetry implies that at each k-point in the Brillouin zone (BZ), we have a two-fold degeneracy. The wavefunctions can be written as

$$\begin{aligned}\Psi^{+}_{\vec{k}\hat{s}}(\vec{r}) &= \left[a_{\vec{k}\hat{s}}(\vec{r}) \quad |\uparrow\rangle_{\hat{s}} + b_{\vec{k}\hat{s}}(\vec{r}) \quad |\downarrow\rangle_{\hat{s}}\right] \mathrm{e}^{i\vec{k}\cdot\vec{r}} , &(5.2)\\ \Psi^{-}_{\vec{k}\hat{s}}(\vec{r}) &= \left[a^{*}_{-\vec{k}\hat{s}}(\vec{r}) \ |\downarrow\rangle_{\hat{s}} - b^{*}_{-\vec{k}\hat{s}}(\vec{r}) \ |\uparrow\rangle_{\hat{s}}\right] \mathrm{e}^{i\vec{k}\cdot\vec{r}} , &(5.3)\end{aligned}$$

where $\vec{k}$ is the Bloch vector, $\hat{s}$ denotes the direction of the spin-quantization axis (SQA) and $|\uparrow\rangle_{\hat{s}}$ and $|\downarrow\rangle_{\hat{s}}$ are the two basis vectors for the spin-space in this chosen representation. It can be shown easily that the spin expectation-value of the two states just differs in sign, and the two wavefunctions are labeled such that the spin expectation-value of the '+'-state along the direction $\hat{s}$ is positive,

$$\left\langle \Psi^{+}_{\vec{k}\hat{s}} \middle| \hat{s}\cdot\vec{\mathcal{S}} \middle| \Psi^{+}_{\vec{k}\hat{s}} \right\rangle = -\left\langle \Psi^{-}_{\vec{k}\hat{s}} \middle| \hat{s}\cdot\vec{\mathcal{S}} \middle| \Psi^{-}_{\vec{k}\hat{s}} \right\rangle \geq 0 , \tag{5.4}$$

where $\vec{\mathcal{S}} = \frac{\hbar}{2}\vec{\sigma}^{\mathrm{p}}$ is the spin operator, and $\vec{\sigma}^{\mathrm{p}}$ is the vector of Pauli matrices. In Eq. (5.4) the spin operator is projected onto the SQA.

The factors $a_{\vec{k}\hat{s}}(\vec{r})$ and $b_{\vec{k}\hat{s}}(\vec{r})$ exhibit the periodicity of the crystal lattice and we define

$$\begin{aligned}a^{2}_{\vec{k}\hat{s}} &:= \int_{\mathrm{u.c.}} \mathrm{d}^{3}r\, |a_{\vec{k}\hat{s}}(\vec{r})|^{2} \quad \text{and} &(5.5)\\ b^{2}_{\vec{k}\hat{s}} &:= \int_{\mathrm{u.c.}} \mathrm{d}^{3}r\, |b_{\vec{k}\hat{s}}(\vec{r})|^{2} , \quad \text{with} &(5.6)\end{aligned}$$

as the unit cell integral. The normalization of the wavefunctions requires

$$\langle \Psi^{+}_{\vec{k}\hat{s}} | \Psi^{+}_{\vec{k}\hat{s}} \rangle = a^{2}_{\vec{k}\hat{s}} + b^{2}_{\vec{k}\hat{s}} = 1 . \tag{5.7}$$

Inserting Eq. (5.2) into the expression for the spin expectation-value, Eq. (5.4), leads to

$$\begin{aligned}\left\langle \Psi^{+}_{\vec{k}\hat{s}} \middle| \hat{s}\cdot\vec{\mathcal{S}} \middle| \Psi^{+}_{\vec{k}\hat{s}} \right\rangle &= \frac{\hbar}{2}\int \mathrm{d}^2 r \ \left(|a_{\vec{k}\hat{s}}(\vec{r})|^2 - |b_{\vec{k}\hat{s}}(\vec{r})|^2 \right) && (5.8)\\ &= \frac{\hbar}{2}\left(a^2_{\vec{k}\hat{s}} - b^2_{\vec{k}\hat{s}} \right) && (5.9)\\ &= \frac{\hbar}{2}\left(1 - 2\, b^2_{\vec{k}\hat{s}} \right) > 0\ . && (5.10)\end{aligned}$$

From the second line follows that $a^2_{\vec{k}\hat{s}} \geq b^2_{\vec{k}\hat{s}}$, and we obtain the bounds $0 \leq b^2_{\vec{k}\hat{s}} \leq \frac{1}{2}$. Moreover, the last line relates the spin-mixing parameter to the spin expectation-value,

$$b^2_{\vec{k}\hat{s}} = \frac{1}{2} - \frac{1}{\hbar}\ \left\langle \Psi^{+}_{\vec{k}\hat{s}} \middle| \hat{s}\cdot\vec{\mathcal{S}} \middle| \Psi^{+}_{\vec{k}\hat{s}} \right\rangle\ . \tag{5.11}$$

Because spin-orbit coupling is weak, spin mixing is usually small ($b^2_{\vec{k}\hat{s}} \ll 0.5$) and the Bloch states are of 'nearly pure' spin character (cases where this does not hold will be described below). This can be shown by regarding spin-orbit coupling as a perturbation. The non-perturbed states ψ^{σ}_{n} are pure spin states with energy ε_n and upon including SOC get a correction of the form $\delta\psi^{\sigma}_{n} = (\delta\psi^{\sigma}_{n})^{\uparrow} + (\delta\psi^{\sigma}_{n})^{\downarrow}$, *i.e.* the correction will comprise contributions of both spin characters. First order (non-degenerate) perturbation theory yields

$$(\delta\psi^{\sigma}_{n})^{\sigma'} = \sum_{n'\neq n} \frac{\langle \psi^{\sigma'}_{n'} |\, \xi(\mathcal{L}\mathcal{S})\, | \psi^{\sigma}_{n} \rangle}{\varepsilon_n - \varepsilon_{n'}}\ \psi^{\sigma'}_{n'} \sim \frac{\xi}{\Delta}\ . \tag{5.12}$$

Here, $\xi(\mathcal{L}\mathcal{S})$ was inserted for the SOC operator, ξ is the spin-orbit coupling strength and Δ was introduced as a typical scale for the separation of bands in energy.

The magnitude of the spin-mixed character of an 'up'-state will (in leading order) be determined by $(\delta\psi^{\uparrow}_{n})^{\downarrow}$. Here, we already see that the spin-flip matrix elements of the SOC operator, $\langle \psi^{\downarrow}_{n'} | \xi(\mathcal{L}\mathcal{S}) | \psi^{\uparrow}_{n} \rangle$, are important. This observation will become important in the explanation of the anisotropy of the spin-mixing parameter in section 5.3.

At a general band-structure point, the bands are usually well separated in energy and $\xi/\Delta \ll 1$. Therefore, also the spin-mixing parameter is small. However, at some special points in the band structure, such as accidental degeneracies, BZ boundaries or high symmetry points, the denominator in Eq. (5.12) becomes small and $b^2_{\vec{k}\hat{s}}$ may increase significantly up to 0.5 (fully spin-mixed states). These point are called *spin-flip hot-spots.* The term has been coined by Fabian *et al.* [58]. They showed, taking aluminum as example, that these spin-flip hot-spots can contribute significantly to the Fermi-surface average of the spin-mixing parameter,

$$\langle b^2_{\hat{s}} \rangle := \langle b^2_{\vec{k}\hat{s}} \rangle_{\mathrm{FS}} = \frac{1}{n(\epsilon_F)} \int_{\mathrm{FS}} \frac{\mathrm{d}A}{\hbar\,|\vec{v}(\vec{k})|}\, b^2_{\vec{k}\hat{s}}\ , \tag{5.13}$$

where $n(\epsilon_F) = \int_{FS} \mathrm{d}S\; |\vec{v}(\vec{k})|^{-1}/\hbar$ is the density of states at the Fermi level and $\mathrm{d}A$ is a Fermi surface element.

Let us finally relate the spin-mixing parameter to spin relaxation. We need some source of scattering and assume a scalar scattering potential in spin space, $\delta\underline{\underline{V}} = \left(\begin{smallmatrix} \delta V & 0 \\ 0 & \delta V \end{smallmatrix}\right)$, to estimate the order of magnitude for spin-conserving and spin-flip scattering rates, $P^{++}_{\vec{k}\vec{k}'}$ and $P^{+-}_{\vec{k}\vec{k}'}$, respectively. Following [96] we derive

$$
\begin{aligned}
P^{++}_{\vec{k}\vec{k}'} &= \left| \left\langle \Psi^{+}_{\vec{k}'} \middle| \delta\underline{\underline{V}} \middle| \Psi^{+}_{\vec{k}} \right\rangle \right|^2 \approx \delta V^2\, |a|^4 \;, && (5.14) \\
P^{+-}_{\vec{k}\vec{k}'} &= \left| \left\langle \Psi^{-}_{\vec{k}'} \middle| \delta\underline{\underline{V}} \middle| \Psi^{+}_{\vec{k}} \right\rangle \right|^2 \approx 4\, \delta V^2\, |a|^2 |b|^2 \;. && (5.15)
\end{aligned}
$$

Using that $(T_1)^{-1} \sim P^{+-}$ and $(\tau_\mathrm{p}) \sim P^{++}$, as well as employing $|a|^2 \approx 1$, we arrive at the Elliott relation Eq. (5.1).

5.2. Spin-mixing parameter in $5d$ and $6sp$ metals

We now turn to the calculation of the spin-mixing parameter for various $5d$- and $6sp$-elements. We employed the local density approximation (LDA) for the exchange-correlation part. and chose the experimental crystal structure and lattice parameters, *i.e.* hcp for Lu, Hf, Re, Os and Tl; bcc for Ta and W; and fcc for Ir, Pt, Au and Pb. For simplicity, we an hcp crystal structure for La is chosen instead of the experimentally found double-hcp structure. The angular-momentum cut-off $\ell_\mathrm{max} = 4$ was used.

To calculate the Fermi surface, the Fermi velocity and the spin-mixing parameter on the Fermi surface, we solved the scalar relativistic approximation (SRA) plus the spin-orbit coupling (SOC) operator of the Pauli form $\vec{\mathcal{L}} \cdot \vec{\mathcal{S}}$. However, at the time when the calculations were performed, we could not include SOC in a self-consistent fashion. As input-potential for this step, we used a converged potential as solution of the fully relativistic Dirac equation, to take SOC effects properly into account.

We used the simpler implementation of the tetrahedron method (*cf.* section 4.2) and chose a very dense grid in the whole BZ with at least 280 k-points per direction. We calculate the spin-mixing parameter $b^2_{\vec{k}\hat{s}}$ at every k-point on the Fermi surface, with a fixed direction of the SQA $\hat{s}$ and show the results in Fig. 5.1 and Fig. 5.2 for elements with cubic and hcp crystal structure, respectively.

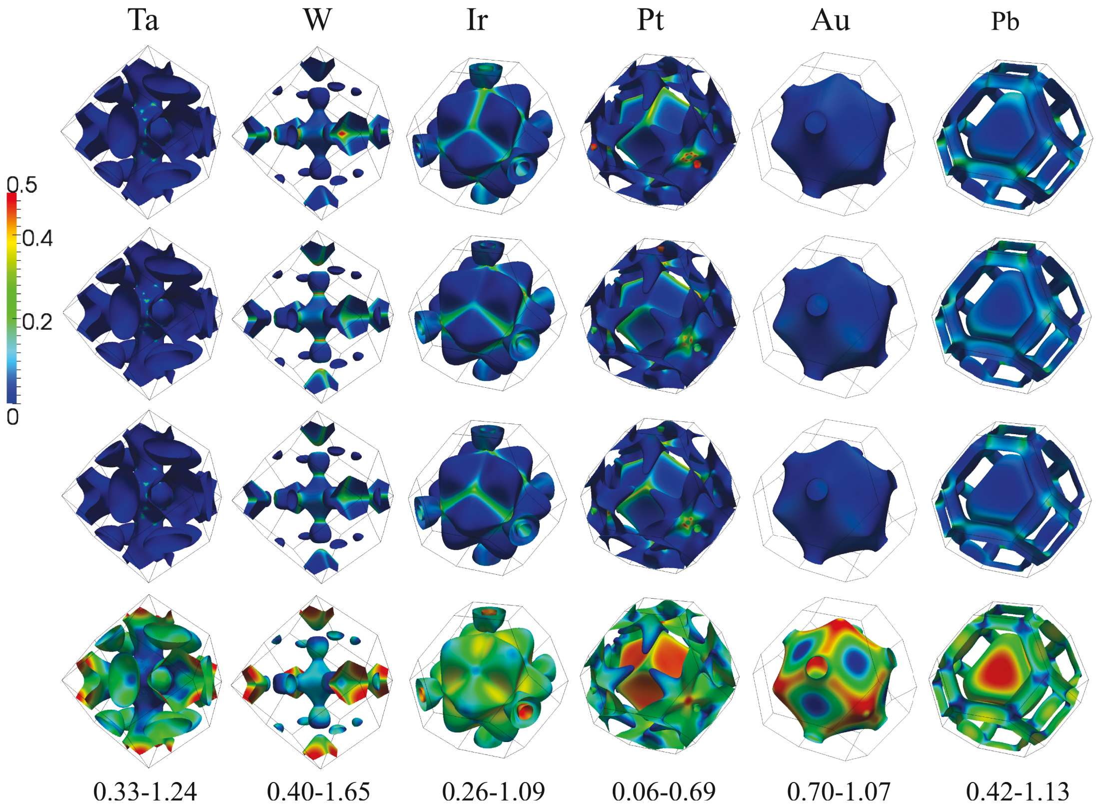

Figure 5.1.: Fermi surfaces for various cubic elements. The first, second and third row show $b^2_{\vec{k}\hat{s}}$ as color code for $\hat{s}$ along [001], [110] and [111], respectively. In the lower row, the absolute value of the Fermi velocity is shown. The same color legend is used as for the spin-mixing parameter, but with the limits as indicated below the plots (in atomic Rydberg unis, *i.e.* the speed of light $c \approx 274$).

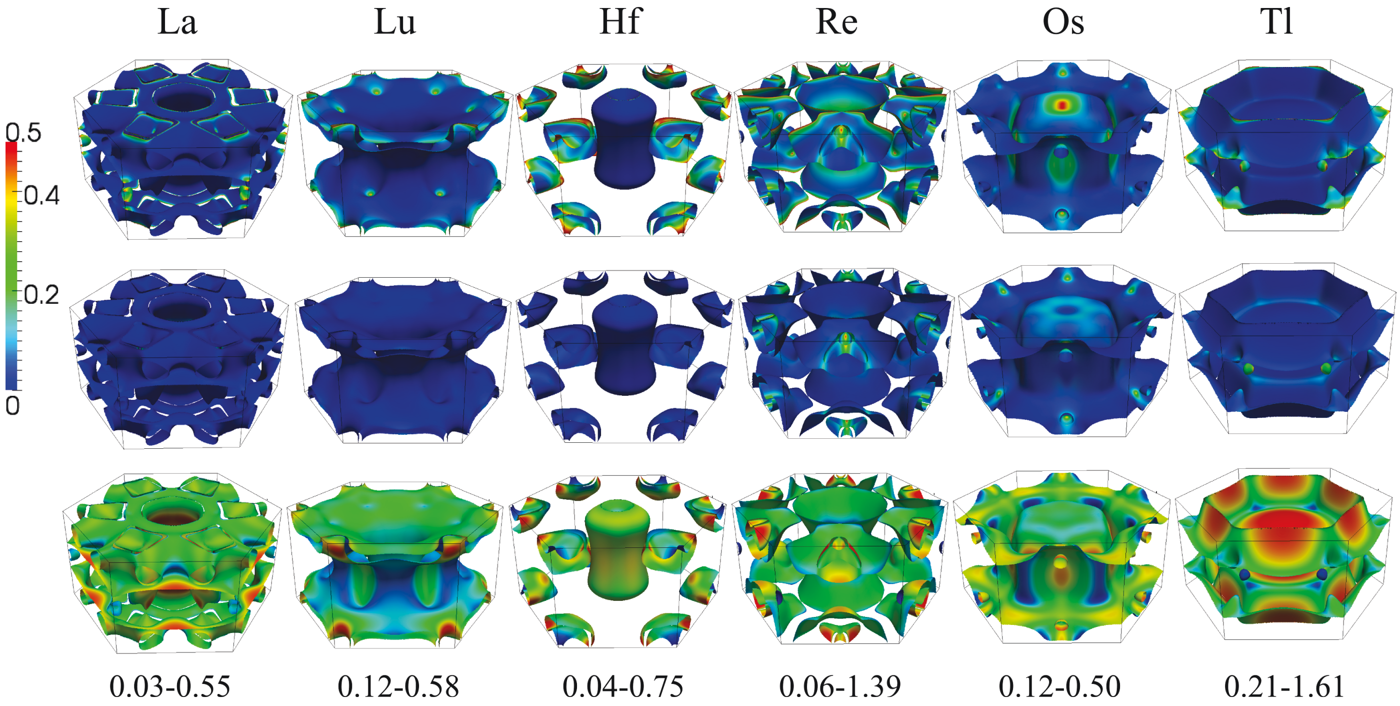

Figure 5.2.: Fermi surfaces for various hcp elements. The first and second row show $b^2_{\vec{k}\hat{s}}$ as color code for $\hat{s}$ in the *ab*-plane and along the *c*-axis, respectively. In the lower row, the absolute value of the Fermi velocity is shown. The same color legend is used as for the spin-mixing parameter, but with the limits as indicated below the plots (in atomic Rydberg unis, *i.e.* the speed of light $c \approx 274$).

k-resolved spin-mixing parameter

Let us first look at the k-resolved spin-mixing parameter $b^2_{\vec{k}\hat{s}}$ for a fixed direction $\hat{s}$: for the majority of the crystals and directions of the SQA, regions with significantly enhanced spin-mixing parameter occur (shown as green to red color in the upper panels of Figs. 5.1 and 5.2, respectively). This is in contrast to the monovalent metal Au (and similarly also for Cu [52] and the alkali metals, not shown here), where $b^2_{\vec{k}\hat{s}}$ is more or less equal in magnitude throughout the Fermi surface. This formation of 'spin-flip hot-spots' was first reported by Fabian *et al.* for fcc-Al [58]. Interestingly, for some points in the BZ and some directions of the SQA, the spin-mixing parameter even reaches the maximal value 0.5, meaning that the corresponding states are fully spin mixed.

In Fig. 5.2 we show the spin-mixing parameter for only two high-symmetry directions in hcp-metals, namely along the crystallographic directions [0001] (parallel to the c-axis) and $[11\bar{2}0]$ (defined as x, in the ab-plane). In fact there exists another high-symmetry direction in the ab-plane being not equivalent to the other two, namely $[\bar{1}100]$ (defined as y). It is perpendicular to both of the formerly mentioned directions. However, the texture of the spin-mixing parameter is very similar for $\hat{s}$ along x or y, respectively, and the former is chosen as representative for the whole ab-plane.

Following the simple picture behind the Elliott-Yafet theory, these fully spin-mixed states correspond to 'erasers' of information encoded in and transported by the electron spin. This becomes evident when considering two successive scattering events: during the first scattering event, an electron prepared to be in a +-state $|\,\vec{k}_1,+\,\rangle$ scatters into a fully spin mixed state $|\,\vec{k}_2,\;\pm\,\rangle$. The transition probabilities are of equal magnitude for the two intermediate states labeled by $+$ or $-$. Similarly, in a successive scattering event, the transition probability will also be of the same magnitude to scatter into the final state $|\,\vec{k}_3,+\,\rangle$ or $|\,\vec{k}_3,-\,\rangle$, and the initial information is lost.

Anisotropy

Next, we present the Fermi-surface averaged values of the spin-mixing parameter, $\langle b^2_{\hat{s}}\rangle$ (*cf.* Eq. (5.13)). It is this average which enters the Elliott-Yafet relation (*cf.* Eq. (5.1)) and is therefore relevant for the connection to spin-relaxation.

In Table 5.1 and Fig. 5.3, the averaged spin-mixing parameter is presented for different high-symmetry directions of $\hat{s}$. The values of $\langle b^2_{\hat{s}}\rangle$ are within the same order of magnitude (10^{-2}), because the strength of spin-orbit coupling is similar in these systems. For lighter elements, the spin-mixing parameter can be different by several orders of magnitude (*e.g.* $\langle b^2_{\hat{s}}\rangle \approx 10^{-3}$ for Cu or even 10^{-5} for Al [52, 56, 58]). Surprisingly, these values can even be enhanced for hcp-elements by turning the SQA from the c-axis into the ab-plane. The effect is most striking for hcp-Hf, where $\langle b^2_{\hat{s}}\rangle$

	cubic				
	[001]	[110]	[111]	Polycrystal	$\mathcal{A}$ [%]
Ta	1.75	1.75	1.75	1.75	0.2
W	6.49	6.26	6.14	6.27	5.7
Ir	5.50	5.54	5.55	5.53	0.9
Pt	5.27	5.26	5.25	5.25	0.4
Au	3.25	3.25	3.25	3.25	0.1
Pb	6.62	6.61	6.61	6.61	0.1

	hexagonal close packed			
	c-axis	ab-plane	Polycrystal	$\mathcal{A}$ [%]
La	1.40	3.46	2.62	150
Lu	1.10	3.33	2.53	200
Hf	1.62	15.1	9.55	830
Re	6.42	12.1	9.98	88
Os	4.85	7.69	6.66	59
Tl	5.04	5.99	5.61	19

Table 5.1.: Fermi-surface averaged spin-mixing parameter $\langle b_{\hat{s}}^2 \rangle$ multiplied by a factor 10^2 for cubic and hcp metals for high-symmetry directions of $\hat{s}$, for polycrystalline samples and its anisotropy as defined in Eq. (5.16).

can be increased by almost an order of magnitude from 1.6×10^{-2} to 15.1×10^{-2}. By defining the anisotropy as

$$\mathcal{A} = \frac{\max_{\hat{s}} \langle b_{\hat{s}}^2 \rangle - \min_{\hat{s}} \langle b_{\hat{s}}^2 \rangle}{\min_{\hat{s}} \langle b_{\hat{s}}^2 \rangle} \ , \tag{5.16}$$

where the maximum and minimum of $\langle b_{\hat{s}}^2 \rangle$ is taken over all directions of $\hat{s}$, we obtain a gigantic anisotropy of 830% for Hf. The other $5d$ metals with hcp crystal structure also exhibit large anisotropies of the averaged spin-mixing parameter $\langle b_{\hat{s}}^2 \rangle$. In contrast, the anisotropy for cubic $5d$ and $6sp$ metals is usually very small and represents less than 1%, except for W where also a relatively large anisotropy of 5.7% is reached. This is because in W, the Fermi surface is highly directional with “arms” along the main axes (x, y and z, *cf.* Fig. 5.1c). The other Fermi surfaces of cubic elements contain sheets that are more spherical (*e.g.* Ir).

Before analyzing the origin of the gigantic anisotropy, we comment on symmetries: For the determination of the extremal values of $\langle b_{\hat{s}}^2 \rangle$ (and thus also for the determina-

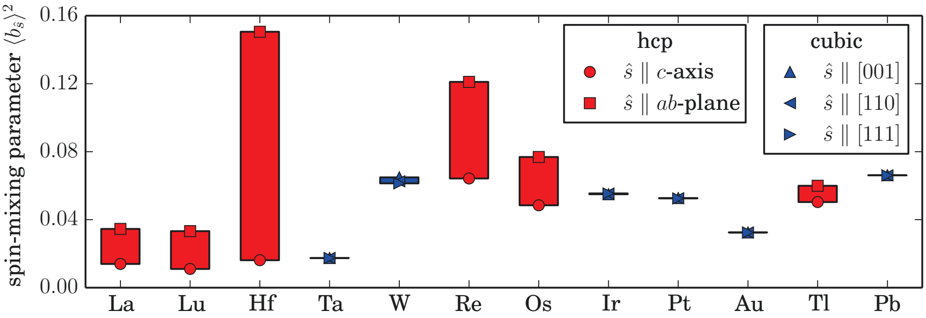

Figure 5.3.: Visualization of the values presented on Table 5.1. Red and blue symbols represent the values for high-symmetry directions in hcp and cubic elements, respectively. The red areas represent values of $\langle b^2_{\hat{s}} \rangle$ that could be reached by variation of the direction of $\hat{s}$ in hcp metals, being largest for hcp-Hf.

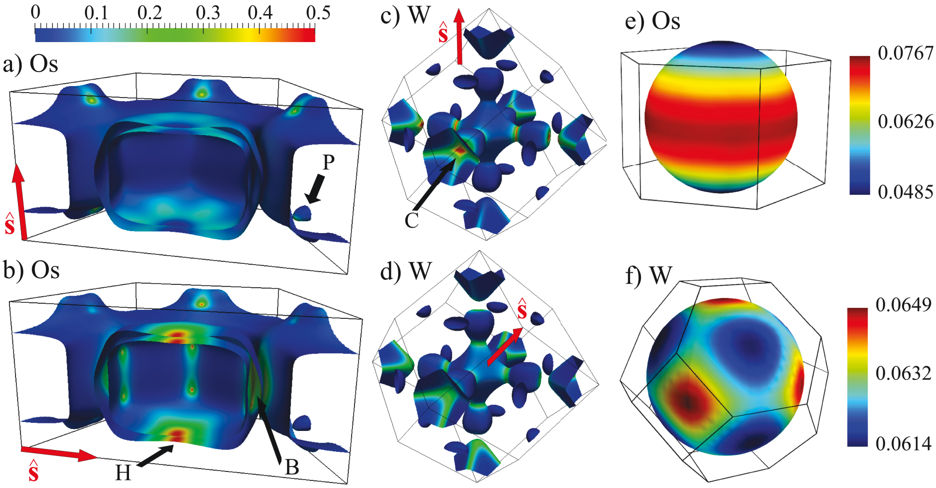

Figure 5.4.: (a-d) Spin-mixing parameter $b^2_{\vec{k}\hat{s}}$ as color-code (corresponding to the color legend given in the top left corner) on the Fermi surface of Os and W for two different directions of the SQA. For Os, only half of the Fermi surface is shown to visualize the two inner nested sheets. The SQA is chosen along the c-axis (a) and within the ab-plane (b). For W, the SQA was chosen along the crystallographic axes [001] (c) and [111] (d). In (e) and (f) the dependence of the averaged spin-mixing parameter on the direction of $\hat{s}$ is shown as color code on the unit sphere and thus represents the anisotropy.

tion of the anisotropy) it is enough to only consider the high-symmetry directions of $\hat{s}$, as was tested for a couple of systems by scanning through all directions of $\hat{s}$. This is exemplified here for Os (Fig. 5.4e) and W (Fig. 5.4f), where the color-code on the unit sphere corresponds to the value of $\langle b^2_{\hat{s}} \rangle$ as function of the direction of $\hat{s}$. Clearly the symmetry of the crystal lattice is transferred to the unit-sphere distribution. The anisotropy within the *ab*-plane of the hcp elements is negligible, as can be seen by the rotationally invariant color code, but it is gigantic between the 'poles' and the 'equator' of the sphere. For W, $\langle b^2_{\hat{s}} \rangle$ is maximal for $\hat{s} \parallel [001]$ and minimal for $\hat{s} \parallel [111]$ (red and blue in Fig. 5.4f).

Next, we search for the origin of the gigantic anisotropy and analyze the *k*-resolved spin-mixing parameter by comparing the Fermi-surface distribution of $b^2_{\vec{k}\hat{s}}$ for the same element but different directions of the SQA.

For hexagonal elements, we observe drastic changes in the Fermi-surface distribution of the spin-mixing parameter when the direction of $\hat{s}$ is changed from the *c*-axis to the *ab*-plane (*cf.* Fig. 5.2). Interestingly, we find for all calculated hcp-elements regions on the Fermi surface, where the value of $b^2_{\vec{k}\hat{s}}$ varies maximally by changing the direction of the SQA. These are points (*e.g.* Lu), broad regions (*e.g.* Os and Hf) or lines (*e.g.* Re, Hf, Tl) that are maximally spin-mixed for the case when $\hat{s}$ is parallel to the *ab*-plane, and are nearly not spin-mixed for $\hat{s} \parallel c$-axis. A good example is the region around the point labeled "H" in Fig. 5.4b). This behavior stems from a degeneracy or near-degeneracy of bands at the Fermi energy with peculiar orbital symmetry of the states, as we will explain in detail for Os and also validate for Hf, Tl and Re in the next sections.

We continue our description of the *k*-resolved spin-mixing parameter and its anisotropy for elements with cubic crystal structure (*cf.* Fig. 5.1). The differences in the spin-mixing parameter on the Fermi surface for different directions of $\hat{s}$ are also clearly visible, however it is often only the intensity of a spin-flip hot-spot or hot-region that changes. As example we refer to the point on the Fermi surface of W denoted by "C" in Fig. 5.4c, where the value of the spin-mixing parameter changes from 0.5 for $\hat{s} \parallel [001]$ to only 0.25 for $\hat{s} \parallel [111]$.

In the suppression of the anisotropy, the high symmetry of the cubic lattice that plays an important role: this can be seen best by looking at the cone-like shapes of the Fermi-surface of W containing the point "C". Here, the SQA along the [001]-direction preserves the four-fold rotation axis of the crystal structure around the axis (*z*-axis), and the spin-mixing parameter on the four cones in the *xy*-plane is equivalent to each other due to this symmetry: all four cones contain a spin-flip hot-spot. Interestingly, the two cones *along* the *z*-axis do not exhibit a spin-flip hot-spot, but the spin-mixing parameter has a rather low value. Similarly to Os, here we also have a maximal anisotropy, however for the *same* direction of $\hat{s}$ and different positions in the Brillouin zone. The contribution of all the six cones to the Fermi-surface averaged value will therefore be of intermediate value. When the SQA is turned away from the *z*-axis towards the [111]-direction, the intensity of the spin-flip hot-spots on the

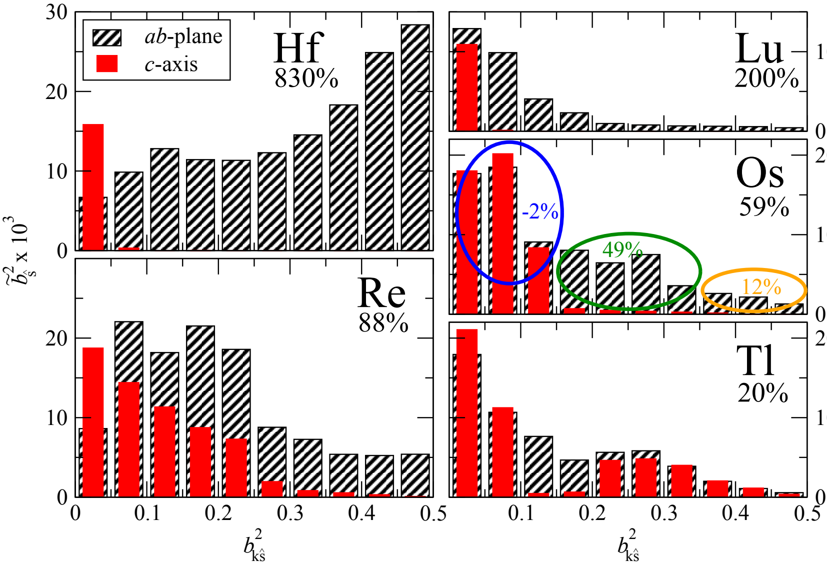

Figure 5.5.: Contribution $\tilde{b}_{\hat{s}}^2$ (as defined in the text) to the Fermi-surface average, $\langle b_{\hat{s}}^2 \rangle = \sum \tilde{b}_{\hat{s}}^2$, as function of $b_{\vec{k}\hat{s}}^2$ for selected hcp-elements and the SQA in the ab-plane and along the c-axis, respectively. The numbers below the symbol of the element give the total anisotropy $\mathcal{A}$. For Os, additional numbers are given representing the respective contribution $\tilde{\mathcal{A}}$ of each region to the anisotropy.

four cones in the xy-plane decreases to an intermediate value of approximately 0.25, and the spin-mixing parameter on the two cones along z increases to a similar value (compare Figs. 5.4c and 5.4d). In total, this leads to a nearly constant contribution to the Fermi-surface averaged value and yields a low anisotropy. When we turn the SQA even further to the x-axis (being crystallographic equivalent to the z-axis), the same picture as in Fig. 5.4c but rotated by 90° is obtained (not shown). Of course, now the cones along z and the ones along x will have exchanged their role, with $b_{\vec{k}\hat{s}}^2 \approx 0$ for the one pair and $b_{\vec{k}\hat{s}}^2 \approx 0.5$ for the other, but the Fermi-surface integrated value is the same due to the symmetry of the crystal lattice.

In Fig. 5.5, we analyze the spin-flip hot-spot contribution to the averaged $\langle b_{\hat{s}}^2 \rangle$ and anisotropy $\mathcal{A}$ for hcp elements. In order to do so, we calculate integrals similar to Eq. (5.13), but restrict the integration to the part of the Fermi surface where $b_{\vec{k}\hat{s}}^2$ lies in certain intervals, $x_i < b_{\vec{k}\hat{s}}^2 \leq x_{i+1}$, with $x_i = 0, 0.05, 0.10, \ldots$ This integration results in values $\tilde{b}_{\hat{s}}^2$ which form the histogram presented in Fig. 5.5. As we can see for Os and $\hat{s}$ along the c-axis (red symbols), $\langle b_{\hat{s}}^2 \rangle$ is mainly determined by regions with relatively low spin-mixing parameter ($b_{\vec{k}\hat{s}}^2 < 0.15$). For $\hat{s}$ in the ab-plane (black hashed symbols) there is a significant contribution from regions with $b^2_{\vec{k}\hat{s}} > 0.15$. Comparing the two histograms for different SQA, we can draw conclusions about the respective contribution of each interval to the total anisotropy, $\tilde{\mathcal{A}} = (\tilde{b}^2_{ab} - \tilde{b}^2_c)/b^2_c$. Interestingly, the anisotropy originates not only from the spin-flip hot-spots with $b^2_{\vec{k}\hat{s}} > 0.35$ contributing only by $\tilde{\mathcal{A}} = 12\%$, but mainly from the areas with smaller but still large spin mixing $0.15 < b^2_{\vec{k}\hat{s}} \leq 0.35$ around the spin-flip hot-spots, resulting in $\tilde{\mathcal{A}} = 49\%$. The large area with low spin-mixing, $b^2_{\vec{k}\hat{s}} \leq 0.15$, does not contribute to the anisotropy significantly ($\tilde{\mathcal{A}} = -2\%$).

Also in the elements Lu, Re and Tl, the most important contributions to the total anisotropy stem from the regions with intermediate or small $b^2_{\vec{k}\hat{s}}$. Only in Hf, the contribution from the spin-flip hot-regions with maximal $b^2_{\vec{k}\hat{s}}$ dominates the integral. Two reasons can be found to explain this abnormal behavior in Hf: Firstly, the Fermi surface of Hf consists to a large part of the two sheets around the H-point (corner of the BZ, *cf.* Fig. 5.8e), where $b^2_{\vec{k}\hat{s}}$ depends strongly on the direction of the SQA (*cf.* Fig. 5.2). Secondly, the spin-mixing parameter is weighted with the inverse of the Fermi velocity when determining the FS average (*cf.* Eq. 5.13) and for Hf the areas of maximal anisotropy coincide with a minimal Fermi velocity. In fact, the Fermi velocity nearly vanishes around the H-point, strongly enhancing the weight of this Fermi-surface piece. The FS region around the H-point corresponds to a band just touching the Fermi level (*cf.* Fig. 5.8). We quantify the enhancement of the anisotropy due to this peculiar effect in Hf from about 500% to the value presented above (830%), as was estimated by calculating the spin-mixing parameter at an energy 0.1 eV above the Fermi level and thus skipping this band. This further shows, that the anisotropy will be temperature dependent, because the occupation of the bands, especially the one just touching the Fermi level, will change.

5.3. Simple model explaining the high anisotropy at certain k-points

In the previous section we have seen that for some k-points in the Brillouin zone, the states are maximally spin-mixed for a certain direction of the SQA ($b^2_{\vec{k}\hat{s}} \approx 0.5$) and are nearly not spin-mixed for another direction of the SQA ($b^2_{\vec{k}\hat{s}} \approx 0$), *e.g.* around the point "H" in hcp Os (*cf.* Figs. 5.4(a) and (b)). In this section, we want to analyze this point further in terms of a simple model and identify the mechanism leading to such a strong anisotropy. At the end of this section, we develop some criteria for the emergence of the maximally anisotropic spin-flip hot-spots in real materials.

We start our analysis by splitting the spin-orbit operator in a spin-conserving and a spin-flip part,

$$\xi \vec{\mathcal{L}} \cdot \vec{\mathcal{S}} = \xi (\mathcal{L}\mathcal{S})_{\parallel} + \xi (\mathcal{L}\mathcal{S})^{\uparrow\downarrow} = \xi \mathcal{L}_{\hat{s}} \mathcal{S}_{\hat{s}} + \xi \; \frac{1}{2} \left(\mathcal{L}^+_{\hat{s}} \mathcal{S}^-_{\hat{s}} + \mathcal{L}^-_{\hat{s}} \mathcal{S}^+_{\hat{s}} \right) \;, \tag{5.17}$$

where $\mathcal{L}_{\hat{s}} = \vec{\mathcal{L}} \cdot \hat{s}$, and $\mathcal{L}_{\hat{s}}^{\pm}$ are ladder operators with respect to the SQA $\hat{s}$ (similarly for the spin operators). If the SQA is chosen along z (*i.e.* the component $\mathcal{S}_z$ is diagonal and thus proportional to the Pauli-matrix $\sigma_3^{\mathrm{P}} = \left(\begin{smallmatrix} 1 & 0 \\ 0 & -1 \end{smallmatrix}\right)$), then the spin-conserving part contains the $\mathcal{L}_z$-component of the orbital momentum operator and the ladder operators entering the spin-flip part read $\mathcal{L}_z^{\pm} = \mathcal{L}_x \pm i\,\mathcal{L}_y$. However, if the x-axis is chosen as SQA, $\mathcal{S}_x$ becomes diagonal and consequently $\mathcal{L}_x$ enters the spin-conserving part. Also the ladder operators will have a different form, namely $\mathcal{L}_x^{\pm} = -\mathcal{L}_z \pm i\,\mathcal{L}_y$. The last term can be directly understood by changing the reference frame by a rotation of 90° around the y-axis. Then we have in the new reference frame $x' = -z$, $y' = y$ and $z' = x$.

Thus, although the total SOC term is a scalar product and does not depend on the choice of the SQA, the single parts (spin-conserving and spin-flip) do.

Let us relate these two parts of the spin-orbit operator to the spin-mixing parameter. It is clear that the spin-conserving part keeps spin as a good quantum number. Therefore, an eigenstate of the Hamiltonian including the spin-conserving part only (excluding the spin-flip part) will have pure spin states, say $\psi_n = \psi_n^{\uparrow}$. When we now also include spin-flip SOC into the system, the state will acquire an admixture of the different spin character, which we denote as $(\psi_n^{\uparrow})^{\downarrow}$. Within first-order (non-degenerate) perturbation theory, we find for this admixture (*cf.* Eq. (5.12))

$$(\psi_n^{\uparrow})^{\downarrow} = \xi \sum_{m \neq n} \frac{\langle \psi_m^{\downarrow} | \, (\mathcal{L}\mathcal{S})^{\downarrow\uparrow} \, | \psi_n^{\uparrow} \rangle}{\varepsilon_n - \varepsilon_m} \, \psi_m^{\downarrow} \tag{5.18}$$

Comparing to Eq. (5.2), we directly see that $(\psi_n^{\uparrow})^{\downarrow}$ represents the part containing $b_{\vec{k}\hat{s}}$ and consequently, the spin-mixing parameter is caused by the spin-flip part of SOC.

Next, we apply the perturbative procedure explained above and discuss the effects on the states in more detail. A simple model of six p-orbitals is able to reproduce the anisotropy of the spin-mixing parameter and reveals the origin of the effect. We neglect SOC for a moment and choose the atomic orbitals p_x^{σ}, p_y^{σ} and p_z^{σ} with $\sigma \in \{\uparrow, \downarrow\}$ labeling the spin of the orbitals, and place them at energies ε, $\varepsilon + \delta$ and $\varepsilon + \Delta$ (the levels are chosen to be spin-degenerate, which is reasonable for a paramagnet). The four orbitals p_x^{σ} and p_y^{σ} shall be very close in energy compared to the position of the p_z^{σ} orbitals ($\delta/\Delta \ll 1$). By this choice we introduced a uniaxiality along the z-direction into our model. The positions of the states are indicated in the left column of Fig. 5.6 for the case that $\delta = 0$, that we consider now. Later we will come back to the dependence on δ.

In the next step we include the spin-orbit operator, first the spin-conserving and then the spin-flip part. The SOC strength is given by ξ, with $\xi/\Delta \ll 1$. Let us first consider the case that the SQA is along z. Upon inclusion of spin-conserving SOC, the orbitals hybridize and form linear combinations. For this specific case, the eigenstates are given as $(p_x^{\sigma} \pm i\, p_y^{\sigma})/\sqrt{2}$ and p_z^{σ} with $\sigma \in \{\uparrow, \downarrow\}$ with energies $\varepsilon \pm \xi$ and $\varepsilon + \Delta$ as sketched in the top-middle panel of Fig. 5.6 (*cf.* chapter A.3 for a derivation).

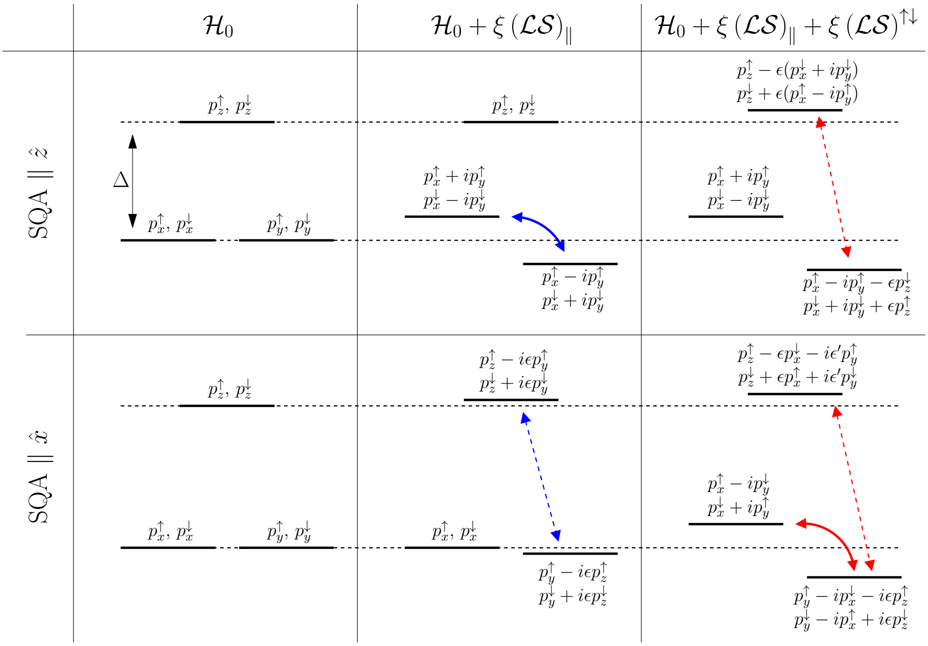

Figure 5.6.: Spectrum of the p-orbital model upon subsequent inclusion of the spin-conserving ($\xi\mathcal{LS}_\parallel$) and spin-flip part ($\xi\mathcal{LS}^{\uparrow\downarrow}$) of spin-orbit coupling. The top and bottom row correspond to the case for a spin-quantization axis (SQA) along z and x, respectively. Each level is twofold degenerate and the orbital and spin-character of the (hybridized) states is indicated (here, ϵ and ϵ' are small numbers). Blue and red arrows represent transitions between states of the same and different spin character, respectively.

These hybridized states are still pure spin-states. In the next step, we include the spin-flip part of SOC in perturbation theory (*cf.* Eq. (5.18)). The only non-vanishing matrix elements are $\langle p_x^{\uparrow} - i\, p_y^{\uparrow} |\, \xi(\mathcal{L}\mathcal{S})^{\uparrow\downarrow}\, | p_z^{\downarrow} \rangle = 2\xi$ and $\langle p_x^{\downarrow} - i\, p_y^{\downarrow} |\, \xi(\mathcal{L}\mathcal{S})^{\uparrow\downarrow}\, | p_z^{\uparrow} \rangle = -2\xi$. These transitions are well separated in energy, leading to an energy denominator in the perturbation expression of order Δ (*cf.* right top-panel of Fig. 5.6). Thus the admixture of down character in the spin-up state and vice versa is small (of the order ξ/Δ), and consequently we obtain a small spin-mixing parameter, $b^2 \sim (\xi/\Delta)^2 \ll 1$.

Let us repeat this analysis, but put the SQA along x: Now the spin-conserving SOC forms linear combinations of p_y^{σ} and p_z^{σ}-orbitals (same spin character). Because these states are well separated in energy by Δ, the admixture of p_z-character into the p_y-orbitals is small, represented by a small parameter ϵ in Fig. 5.6. Also the energy of the hybridized states is only shifted by a small amount of $(\xi/\Delta)^2$. The p_x^{σ}-orbitals are not affected by the spin-conserving SOC. Upon inclusion of the spin-flip part of SOC, there exist now four non-vanishing matrix elements (all of order ξ). Two of these transitions are very close in energy (separated by ξ^2/Δ), leading to a high spin-mixing of the states, as highlighted by a thick red arrow in the right column in Fig. 5.6. The magnitude of $(\psi_n^{\uparrow})^{\downarrow}$ in this first-order perturbation theory approach can be estimated to be of order $\Delta/\xi \gg 1$. Here, higher orders in perturbation theory become necessary, because the spin-mixing is limited to $b^2 \leq \frac{1}{2}$. The eigenstates of the full Hamiltonian are presented in the right column of the figure. Indeed, the states of the two lowest (degenerate) levels are nearly fully spin mixed and $b^2 \approx \frac{1}{2}$.

Let us explain what we have just seen in a more general context: the two low-lying states are of such orbital characters, that they can form eigenstates ϕ_m and $\phi_{m'}$ of the $\mathcal{L}_{\hat{n}}$-operator for a certain direction $\hat{n}$ with $|m - m'| \neq 1$. In our model, this is achieved for $\hat{n} = z$ and the eigenstates of $\mathcal{L}_z$ are the complex spherical harmonics $\phi_{\pm 1} = Y_{\ell=1,m=\pm 1} = p_x \pm i\, p_y$. Hence we have $|m - m'| = 2$ for these states which are very close in energy. If the spin-quantization axis is along this distinguished direction, the $\mathcal{L}_{\hat{n}}$-operator appears in the spin-conserving part of SOC and the eigenstates are formed from the degenerate orbitals with the same spin. At the same time, because the spin-flip part of SOC only couples states of orbital character with $|m - m'| = 1$, the system is protected against large spin-flip transitions. The only transitions mediated by the spin-flip operator $(\mathcal{L}\mathcal{S})^{\uparrow\downarrow}$ are with the third, high lying level $p_z = \phi_0 = Y_{\ell=1,m=0}$. The situation changes when we rotate the spin-quantization axis to the x-axis (and consequently also the quantization axis of orbital moment). The initial coordinate system $(x\, y\, z)$ transforms into $(\overline{x}\, \overline{y}\, \overline{z}) = (-z\, y\, x)$ and also the initial states have a different orbital character with respect to the new quantization axis, *e.g.* $p_x \rightarrow p_{\overline{z}}$ and vice versa. Now the degenerate states have the orbital character $p_{\overline{z}} = \phi_0$ and $p_{\overline{y}} \sim \phi_{-1} + \phi_1$, and these contain transitions with $|\overline{m} - \overline{m}'| = 1$. Therefore, spin-flip transitions between the degenerate levels are allowed and lead to a large spin-mixing of the states.

Up to now we worked in the limit of degenerate low-lying states, $\delta = 0$. In the left panel of Fig. 5.7 we analyze the dependence of the spin-mixing parameter if the two

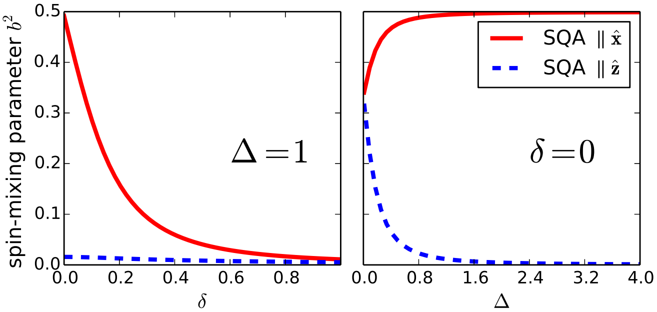

Figure 5.7.: Dependence of the spin-mixing parameter of the lowest state on the parameters δ and Δ of the p-model for fixed SOC strength $\xi = 0.1\,\mathrm{eV}$. The values for δ and Δ are given in eV. See text for details.

lower levels are not degenerate, but separated by δ. The SOC strength was fixed to $\xi = 0.1\,\mathrm{eV}$ and the higher level was put at $\Delta = 1\,\mathrm{eV}$. The spin-mixing parameter b^2 for SQA along x (red solid line) approaches the maximal value for small δ and drops with increasing δ. For the other direction of the SQA along z (blue dashed line), b^2 is small for all δ. The anisotropy, which is the difference between the two curves, is basically determined by the behavior of the red curve. Here we see, that not only an exact degeneracy is required, but also a near-degeneracy is sufficient to obtain a large anisotropy. The transition between the two regimes (high and low anisotropy), where b^2 and also the anisotropy drops to half of the maximal possible value, takes place at $\delta \approx 0.1\,\mathrm{eV}$. This energy scale is determined by the strength of spin-orbit coupling ξ. Relating this result to realistic band structures, in a material with larger spin-orbit coupling the conditions for a large anisotropy of $b^2_{\vec{k}\hat{s}}$ will be not only met at a degeneracy, but also at k-points further away. This leads to spin-flip hot-spots of larger spread on the Fermi surface for heavy elements with large SOC (see also the band-structure analysis in the next section 5.4).

The dependence of the spin-mixing on the other parameter entering our model, the position of the high lying state, is shown in the right panel of Fig. 5.7. The states must be well separated in energy to get a large anisotropy, $\Delta \gg \xi$, in order to suppress the spin-flip amplitude for the case when $\hat{s}$ is parallel to the distinguished direction $\hat{n}$.

We close this section by summarizing the general conditions to predict a large anisotropy of the spin-mixing parameter $b^2_{\vec{k}\hat{s}}$ for a real material: First, a degeneracy or near-degeneracy additional to the spin degeneracy at the Fermi energy must be present, which is lifted (or increased) by SOC. Secondly, the two Bloch states at this k-point should be of certain orbital character. They can be expanded in a tight binding picture as $\Psi^{1,2}_{\vec{k}} = \sum_{\ell,m} c^{1,2}_{\ell,m}\,\phi_{\ell,m}$ and the coefficients $c^2_{\ell,m'}$ shall vanish if $c^1_{\ell,m} \neq 0$ and $|m - m'| = 1$ for some direction $\hat{n}$ of the quantization axis. This enables a

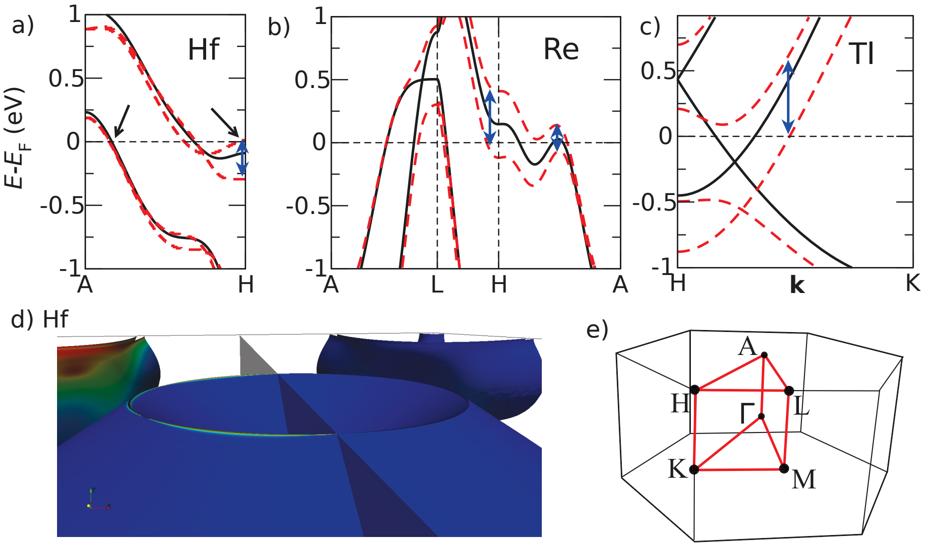

Figure 5.8.: Band-structures around the Fermi energy without (solid lines) and with (dashed lines) SOC for Hf (a), Re (b) and Tl (c) along a chosen path in the BZ. A large splitting of the bands at the Fermi energy due to SOC (denoted by the double arrows) is a prerequisite for a possibly high spin-mixing parameter and potential high anisotropy. Solid lines are four-fold and dashed lines in (except on the path $\overline{AL}$) are two-fold degenerate. A zoom onto the center of the hexagonal face for the Fermi-surface of Hf is shown in (d). The color code on the left and right hand side of the vertical plane shows the spin-mixing parameter for the SQA in the *ab*-plane and along the *c*-axis, respectively. In (e), the hexagonal BZ with high symmetry points is shown.

large spin-mixing parameter for some direction of $\hat{s}$ perpendicular to the direction $\hat{n}$. As third point, other states which contain an orbital character where the criterion $|m - m'| = 1$ is met, shall be far away from the Fermi energy. This prohibits large spin-flip amplitudes when $\hat{s}$ is parallel to $\hat{n}$.

5.4. Verification of model results by band-structure analysis

In the previous section we have deduced general conditions for the emergence of a large anisotropy of $b^2_{\vec{k}\hat{s}}$ with the help of a simple model. Now we want to go back to real materials and exemplify these conditions in terms of band-structure calculations.

One requirement for a large anisotropy is the presence of a degeneracy in addition to the spin degeneracy at the Fermi energy, which is lifted by SOC. Exemplary, in Fig. 5.8 we show the band structure with and without SOC for selected elements (*i.e.* Hf, Re and TL) along a chosen path in reciprocal space where the situation of a SOC-lifted degeneracy is met. The large spin-orbit splitting of bands (denoted by the double arrows in the panels a-c) can lead to broad spin-flip hot regions on the Fermi surface, compare *e.g.* for Hf to the part of the Fermi surface around the H-point (*cf.* Fig. 5.2). In contrast, the lower band in Hf exhibits only a very small SOC splitting at the Fermi energy (denoted by the solid arrow in Fig. 5.8a). In our model it means that the SOC strength ξ is very small for this band. This leads only to a very thin line of anisotropic spin-mixing parameter directly at the hexagonal face of the BZ (see Fig. 5.8d and compare to Fig. 5.2). This has the following origin: as soon as we go away from the hexagonal face into the interior of the BZ, the additional degeneracy will be lifted and the energy splitting of the states exceeds the SOC strength. Thus the criterion $\delta \lesssim \xi$ is immediately violated when going away from the hexagonal face and leads to a very small region of anisotropic spin-mixing, as was already pointed out in the previous section.

Another example for this phenomenon can be seen in the band structure of Re: on the path from the A-point to the L-point in the BZ, the four-fold degenerate band most to the left in Fig. 5.8b is not split by SOC on this high-symmetry line. The k-point where this band crosses the Fermi energy is represented by the touching point of the inner cylindrical Fermi-surface sheet with the outer sheets (*cf.* Fig. 5.2). As soon as we move away into the interior of the BZ, the spin-mixing (for an SQA in the ab-plane) disappears very quickly for the same reason as explained before: the crystal field splits the states with appropriate orbital character, and their energy separation δ exceeds the small spin-orbit strength ξ for this band so that the influence of SOC is drastically decreased.

The second requirement, a peculiar orbital character of the Bloch states, is analyzed for Os for the point of large anisotropy along the path from the center of the BZ (Γ-point) to the center of the hexagonal face (A-point). In Fig. 5.9 draw the band structure along this path and recognize two bands (indicated by “1” and “2” in Fig. 5.9) crossing the Fermi level. These form the two inner, nested Fermi surface sheets visible in Fig. 5.4b around the point indicated by “H” in the figure. The bands are purely split by SOC, as was validated by the fact that they fall on top of each other when the SOC strength is scaled to zero (not shown). The four degenerate states at the Fermi energy have mainly the orbital character d_{xz} and d_{yz} (both are also spin-degenerate), which are superpositions of the states $|\,2,+1\,\rangle$ and $|\,2,-1\,\rangle$.[1] Hence, the requirement that $|m-m'| \neq 1$ for the degenerate states is fulfilled for $\hat{s}=z$, and the matrix elements of the spin-flip part of SOC vanish. Rotating the quantization axis into the x-direction, the states transform from d_{xz} to $d_{\overline{x}\,\overline{z}}$, having a projection onto

---

[1] We remind that here we use the notation $|\,\ell,m\,\rangle = \mathcal{Y}_{\ell,m}$ to denote the (complex) spherical harmonics, which are eigenfunctions of the $\mathcal{L}_z$-operator. For d-states, we have $\ell=2$.

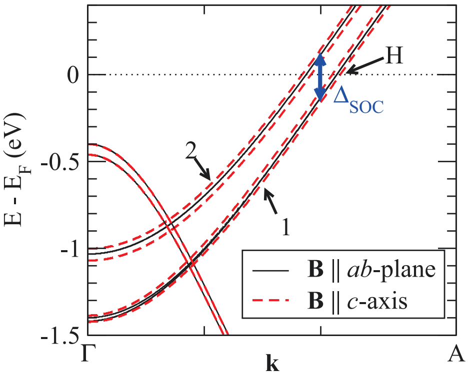

Figure 5.9.: Band structure of Os around the Fermi level, along the direction $\Gamma - A$ of the BZ with applied B-field of 40 meV. The exchange splitting of the two bands crossing the Fermi energy (1 and 2) depends on the direction of $\vec{B}$, reflecting the anisotropy of the spin-mixing at the spin-flip hot-spot "H". For band 3, the exchange splitting is isotropic with respect to the direction of $\vec{B}$.

the atomic orbitals $\left|\,\overline{2,\pm 1}\,\right\rangle$, while d_{yz} becomes $d_{\overline{x}\,\overline{y}}$, having a projection on $\left|\,\overline{2,\pm 2}\,\right\rangle$. As a result, in the new reference frame the degenerate states now *include* orbitals with $|\overline{m} - \overline{m}'| = 1$, allowing for for non-zero matrix elements of the spin-flip part of SOC and a large spin-mixing.

Both requirements are generally met in hcp-metals. As can be shown by group theory [97], an additional degeneracy is present at the hexagonal face of the hcp Brillouin-zone boundary due to the non-symmorphic space group of the hcp lattice, which can only be lifted by spin-orbit coupling. Due to the uniaxiality of the systems, the states exhibit the proper symmetry to form an eigenstate of the $\mathcal{L}_z$-operator. Therefore, hcp-elements cutting through the hexagonal face (all of the elements investigated here except for Os) exhibit spin-flip *hot-loops* at the hexagonal face of the BZ for an SQA in the ab-plane.

5.5. Application of an exchange B-field

Finally, we analyze the response of the states under the application of an exchange B-field of the form $\vec{B} \cdot \vec{\sigma}^{\mathrm{P}}$ for Os and Hf. The external B-field breaks the time reversal symmetry of the system and in general will lead to a lifting of degeneracies. Additionally, the direction of the spin-quantization axis is aligned parallel to the applied field. In Fig. 5.9 the band structure of Os is shown for two directions of the B-field with a magnitude of $|\vec{B}| = 40$ meV. The response of the bands "1" and "2"

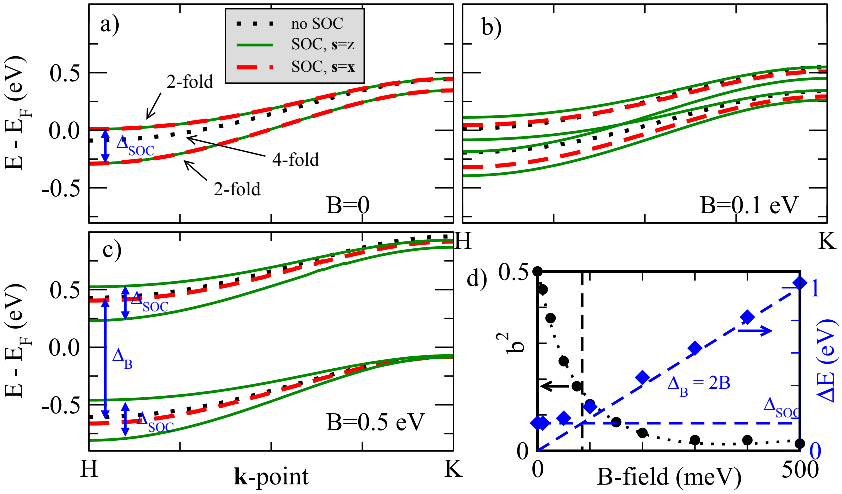

Figure 5.10.: (a)-(c): The splitting of the 4-fold degeneracy in presence of SOC and an exchange B-field is shown for Hf along the path $\overline{\mathrm{HK}}$ for $B = 0$, 100 and 500 meV. Dotted lines represent bands without SOC, full and dashed lines with SOC and $\hat{s}$ along z and x, respectively. In d), the spin-mixing parameter (points) and splitting of energy bands (diamonds) for a certain k-point on the path $\overline{\mathrm{HK}}$ and $\hat{s} = x$ as function of the field strength B is shown. A strong increase of b^2 with decreasing B is observed, also changing the type of energy splitting from exchange-dominated to SOC-dominated. The crossover is indicated by the vertical line. See text for details.

is different with respect to the direction of the field: for a field along z, each band splits into a single, non-degenerate band. However, for a B-field along x, the bands do not split and remain two-fold degenerate. This result reflects the anisotropy of the spin-mixing parameter, as can be easily seen by relating the energy shifts of the levels to the B-field via perturbation theory. In first order, the response of a state ψ_k is

$$\delta\varepsilon_k = |\vec{B}|\,\langle\psi_k|\,\sigma^{\mathrm{P}}_{\hat{s}}\,|\psi_k\rangle = |\vec{B}|\,\left(1 - 2\,b^2_{\vec{k}\hat{s}}\right)\ . \tag{5.19}$$

Thus, a vanishing splitting indicates fully spin-mixed states ($b^2_{\vec{k}\hat{s}} = 0.5$).

Additionally, we investigate the different contributions of the two parts of spin-orbit coupling, namely the spin-conserving part $\xi(\mathcal{LS})_{\|}$ and the spin-flip part $\xi(\mathcal{LS})^{\uparrow\downarrow}$ on the states in Hf along the path $\overline{HK}$ in the Brillouin zone. We show that it is the direction of the SQA that dictates which part dominates and causes the SOC-splitting Δ_{SOC}. By additionally applying an exchange B-field, we are able to reduce the effect of the spin-flip part on the states, whereas the spin-conserving part remains at its full strength, as we explain in the following. Let us first consider a vanishing B-field (*cf.* Fig. 5.10a): the degeneracy of the fourfold degenerate band is lifted by SOC into two twofold degenerate pairs. On the one hand, the splitting Δ_{SOC} is caused by the spin-conserving part if the SQA is along the z-axis, and on the other hand the same splitting is caused by the spin-flip part for a SQA along x. This also was checked by only taking the diagonal and off-diagonal elements of $\vec{\mathcal{L}} \cdot \vec{\mathcal{S}}$, respectively, when calculating the band structure of Fig. 5.10a (not shown).

Let us now apply a strong B-field of $0.5\,\mathrm{eV}$ (*cf.* Fig. 5.10c) and think of including the SOC-operator in a second step: first, the four bands are exchange split into a pair of up-states and down-states, respectively, with an energy difference between the pairs of $\Delta_B = 2B = 1\,\mathrm{eV}$. Inclusion of SOC leads to a coupling between states and may cause an additional SOC-splitting, depending on the direction of the B-field. If the B-field (and thus the SQA) is chosen along z, the dominant spin-conserving part of SOC couples states of the same spin character. These are at the same energy and this leads to a full SOC splitting of the two pairs. This splitting is independent on the strength of B, leading to the same form of the SOC-split bands in Fig.5.10a-c.

Let us now imagine that the strong B-field was applied along x (putting the SQA along x). The situation without SOC is the same as before: we have two degenerate bands. The two states within the same band are of the same spin character. Because the spin-flip part is now dominant, it couples states of different spin-character, which are separated in energy by $2B$. Now, only a very weak influence of SOC on the states is observed for a strong B-field (the dotted and dashed line in Fig. 5.10c nearly fall on top of each other). For intermediate B-fields, where the exchange-splitting is comparable to the (full) SOC splitting (*cf.* dashed line in Fig. 5.10b), the degeneracy is still present because both states in the up-band couple to the states in the down-band the same way due to their special symmetry, but the effect of SOC increases smoothly, as can be seen by the shape of the bands (compare Figs. 5.10a-c). A detailed analysis of the SOC splitting as function of the strength of the B-field (along x) is shown in Fig. 5.10d for a selected k-point on the path $\overline{\mathrm{HK}}$. Here, a crossover between SOC-dominated and exchange-dominated regimes can be seen with increasing B. Simultaneously, the spin-mixing of the states decreases, clearly identifying the strength of $(\mathcal{LS})^{\uparrow\downarrow}$ as the source for large spin-mixing.

6

Skew-scattering contribution to the Hall effects in ferromagnets

In this chapter we analyze the effect of various impurities or disorder on transport properties of some ferromagnetic materials. We selected the following three magnets, which are commonly investigated – both experimentally and theoretically: (1) the ferromagnetic material bcc-Fe, (2) the ordered alloy FePt and (3) the exotic magnetic material MnSi, which crystallizes in the low-symmetry B20 crystal structure.

In section 6.1, we investigate the ferromagnetic material bcc Fe, and concentrate on impurities from the $3d$ series of the periodic table (*i.e.* Sc, Ti, V, Cr, Mn, Co, Ni and Cu). We successfully compare our results for longitudinal conductivities and magnetic properties to previous findings, and present theoretical values for the skew-scattering induced anomalous Hall effect in bcc Fe for the first time. We delve into the anomalous Hall effect in terms of an analysis of the Fermi-surface contributions to the transverse charge conductivity and discover a strongly peaked behavior around spin-orbit split bands. However, these large contributions appear in pairs of opposite signs, and also in different parts of the Fermi surface depending on the impurity, which makes the overall behavior of the anomalous Hall conductivity (AHC) quite complicated. Beyond the systematic analysis of the $3d$ impurities, we also calculated selected impurities from the $4d$ and $5d$ series, and some sp impurities.

In section 6.2, we investigate the ordered FePt alloy in the $L1_0$ crystal structure and introduce disorder in two ways. A weak deviation from the stoichiometric 1:1-ratio is simulated by replacing Pt atoms by Fe atoms or vice versa. Another kind of disorder, namely the simultaneous switching of an Fe and Pt atom, shows that our method is also capable of treating more complicated defects.

In section 6.3 we analyze the effect of dilute alloying of the exotic material MnSi by Fe or Ge impurities, *i.e.* the $\mathrm{Fe}_x\mathrm{Mn}_{1-x}\mathrm{Si}$ and $\mathrm{MnSi}_{1-x}\mathrm{Ge}_x$. The host crystal itself shows already very interesting phenomena (*e.g.* non-collinear magnetism at zero external fields [98], the emergence of skyrmions [7] and the closely related *topological Hall effect* [21] with external magnetic field). Some of them are related to the unusual space group of the B20 crystal structure [99]. Therefore, we first emphasize the importance of symmetries and symmetry-breaking in the presence of spin-orbit coupling and their influence on the Fermi surface. We also discuss numerical difficulties in the solution of the Boltzmann equation, which are closely related to the lack of symmetries in the Brillouin zone. We further present first results on the transport properties for the two selected alloys and discuss also the dependence on the magnetization direction. Besides the physical importance of this system, it serves as a candidate to show the numerical power of our method.

6.1. Substitutional impurities in bcc Fe

In this section we investigate the skew-scattering contribution of various impurities in bcc Fe, with special focus on the 3*d* series of impurities (Sc, Ti, V, Cr, Mn, Co, Ni, Cu).

6.1.1. Magnetic moments

We first describe the magnetic spin-moments of 3*d* impurities in Fe, see left panel of Fig. 6.1. The general trend that the magnetic moments of the early 3*d*-transition metal impurities (Sc-Cr) couple anti-ferromagnetically to the Fe host, and that late ones (Co-Ni) couple ferromagnetically agree to previous findings [100]. This trend is

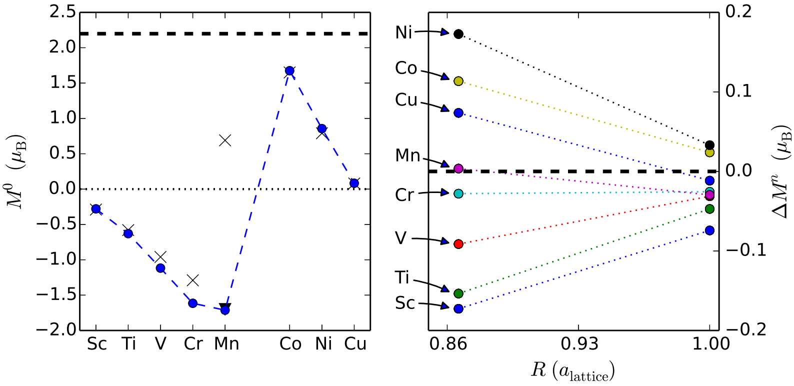

Figure 6.1.: Left panel: local spin moments M^0 at the impurity site for 3*d* impurities in an Fe host. The thick dashed line corresponds to the magnetic moment of pure bcc-Fe, $M^{\rm host} = 2.2\,\mu_{\rm B}$. Reference values from other KKR calculations are also presented (crosses correspond to Ref. [100] and the triangle to Ref. [101]). Right panel: changes of the local spin moment at the Fe sites in the first two shells ($n = 1, 2$) around the impurity atom, $\Delta M^n = M^n - M^{\rm host}$, as function of the distance R to the impurity site.

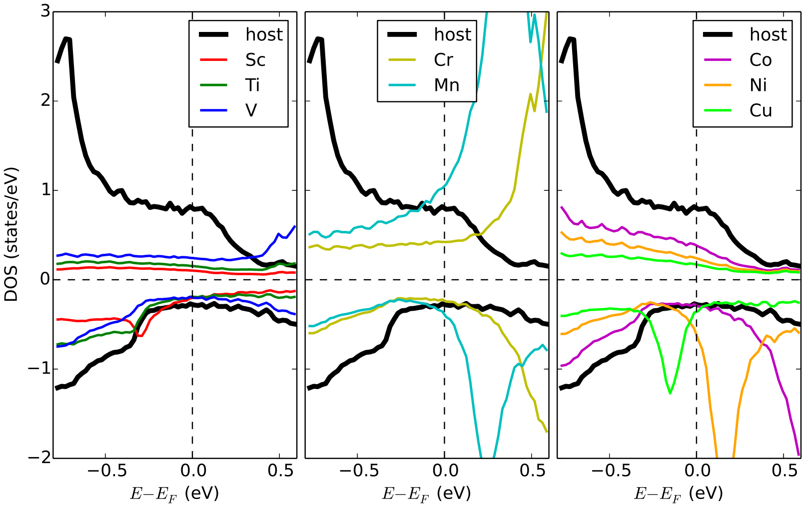

Figure 6.2.: Local density of states (LDOS) at the impurity site (thin lines) in comparison to the DOS of the host crystal (thick lines) for various impurities in bcc-Fe around the Fermi energy E_F. Positive and negative DOS-values correspond to up- and down-states, respectively.

also seen in the local density of states (LDOS): for Sc-V, the up-states are unoccupied (see left panel of Fig. 6.2) and a negative magnetic moment is formed. With increasing impurity atomic number Z_imp, the virtual bound states get shifted to lower energies. For Mn impurities, the peak of the density of states lies close to the Fermi energy and shifts below the Fermi energy for Co, Ni and Cu.

A Mn impurity in Fe is a delicate case: There are contradicting result in the literature, *e.g.* Akai *et al.* find a magnetic moment for Mn of $-1.7\,\mu_\mathrm{B}$ [101]. This contradicts with Drittler *et al.* , who determine the magnetic moment to be $+0.7\,\mu_\mathrm{B}$ [100]. However, Drittler and coworkers also argue that the magnetic spin-moment of Mn impurities in Fe depends strongly on details, *e.g.* the choice of the XC-functional and the cutoff parameter ℓ_{max}. Indeed, we find experienced some difficulties in the convergence of the impurity potentials, but after carefully doing it, we find a magnetic moment of $-1.7\,\mu_\mathrm{B}$, in agreement with Akai *et al.* .

6.1.2. Transport properties

Let us now turn to the discussion of impurity-driven transport properties in bcc Fe. The main results for $3d$ impurities are presented in Fig. 6.3 and Tab. 6.1. In the left panel of Fig. 6.3, the longitudinal conductivity σ_{xx} (orange) and momentum

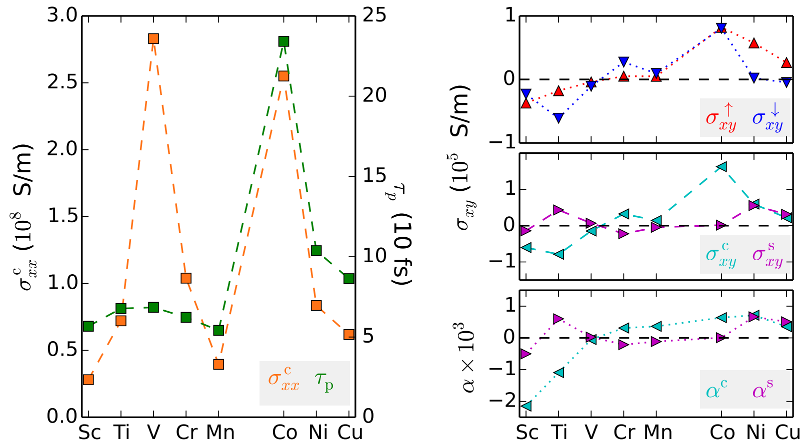

Figure 6.3.: Transport properties of iron due to scattering off $3d$ impurities. Left: Longitudinal charge conductivity σ^{c}_{xx} and momentum relaxation time τ_{p} as function of the impurity atom. Right: transverse spin-up ($\sigma^{\uparrow}_{xy}$), spin-down ($\sigma^{\downarrow}_{xy}$), charge (σ^{c}_{xy}) and spin conductivities (σ^{s}_{xy}), as well as the anomalous and spin Hall angles (α^{c} and α^{s}, respectively). All values for conductivities are given at an impurity concentration of 1 at.%.

relaxation times τ_{p} (green) follow the same trend. The missing peak in τ_{p} for V impurities originates from the definition of τ_{p} in Eq. (3.29), where the integral is taken over the inverse lifetimes, $\tau_{\mathrm{p}}^{-1} \sim \int \mathrm{d}S\, \tau_{\vec{k}}^{-1}$. This definition is inspired by the definition of the spin-relaxation time T_1 (*cf.* Eq. (3.28)). However, an appropriate averaging for a comparison to the longitudinal conductivity would require an integration over the direct lifetimes (*cf.* Eq. (3.22)), yielding a transport lifetime $\tau_{\mathrm{tr}} \sim \int \mathrm{d}S\, \tau_{\vec{k}}$. The two lifetimes differ if $\tau_{\vec{k}}$ is strongly anisotropic on the Fermi surface. This is especially the case for V impurities in Fe.

The transverse charge and spin conductivities, σ^{c}_{xy} and σ^{s}_{xy}, respectively (*cf.* right middle panel of Fig. 6.3), show a less intuitive dependence on the impurity atom. While the sign of σ^{s}_{xy} switches several times within the $3d$ series, for the charge conductivity it changes only once. The corresponding anomalous Hall angle (α^{c} in the lower right panel of Fig. 6.3) increases monotonous almost within the whole $3d$ series (except at the end of the series from Ni to Cu) due to the normalization by the longitudinal conductivity.

Let us analyze the conductivities further by imagining that we have two separate electron-systems for spin-up and spin-down electrons. In this so-called *two-current model*, where spin-flip terms are neglected and all states are imagined to be of pure spin character, separate conductivities for up- and down-electrons, $\sigma^{\uparrow}_{xy}$ and $\sigma^{\downarrow}_{xy}$ respectively, can be defined. Then, the charge conductivity is the sum of the two, and the spin-conductivity is the difference. Although our calculation takes all scattering processes (including spin-flip) into account and the host-states can be of spin-mixed character (where the spin expectation-value can be less than $\hbar/2$), we can estimate the conductivities for the two spin channels by

$$\sigma^{\uparrow}_{xy} = \frac{1}{2}\left(\sigma^{\mathrm{c}}_{xy} + \sigma^{\mathrm{s}}_{xy}\right) \tag{6.1}$$

$$\sigma^{\downarrow}_{xy} = \frac{1}{2}\left(\sigma^{\mathrm{c}}_{xy} - \sigma^{\mathrm{s}}_{xy}\right) \; . \tag{6.2}$$

The results are shown in the top right panel of Fig. 6.3. Interestingly, the transverse conductivities for up- and down-electrons are of the same sign for a given impurity (again with the exception of Cu impurities), meaning that both kinds of electrons get skew-scattered to the same side. This is in contrast to the naive picture, where electrons of different spin are said to scatter into different transverse directions. This statement is only true for the pure spin Hall effect,

However, the magnitude of the effect for transverse transport is very small for $3d$ impurities, *e.g.* the Hall angles are of the order 10^{-4}. A possible reason is the low spin-orbit coupling of both, the host and impurity atoms. In the investigation of the spin Hall effect in Cu and Au, Gradhand *et al.* found, that large spin Hall angles are achieved for heavy impurities in light hosts (*e.g.* Pt or Bi in Cu), or vice versa (*e.g.* C in Au) [37, 40].

We also calculated several other impurities in bcc Fe (see Tab. 6.1). The Hall angles due to scattering off heavy impurities with strong spin-orbit coupling (*i.e.* W and Pt and Au) are one order of magnitude larger than the ones of $3d$ impurities, in agreement with the arguments presented by Gradhand *et al.* . However, there are also exceptions: surprisingly, the anomalous Hall angle for the very light impurity Si is the largest among all impurities considered here. Also for Ge, which is of similar atomic weight as Fe, yields a large AHA. We can conclude that also fine details of the impurity states matter.

6.1.3. Fermi-surface contributions to the AHC

To get a deeper insight into the nature of the skew-scattering contribution to the anomalous Hall effect, we recall Eq. (3.22), where the conductivity tensor was defined, and write for the transverse component

$$\sigma^{\mathrm{c}}_{yx} = \frac{\mathrm{e}^2}{\hbar}\frac{1}{(2\pi)^3}\int \mathrm{d}S \; \frac{v_{\vec{k},y}\,\lambda_{\vec{k},x}}{|\vec{v}_{\vec{k}}|} \; . \tag{6.3}$$

Note that here we analyze the yx-component of the charge conductivity tensor, which is related to the previously shown xy-component just by a minus sign, $\sigma_{yz} = -\sigma_{xy}$.

	α^{c}	α^{s}	σ_{xx}^{c}	σ_{xy}^{c}	σ_{xy}^{s}	τ_{p}	M_0
	(10^{-3})		(10^7 S/m)	(10^4 S/m)		(fs)	(μ_{B})
Sc	−2.1	−0.5	2.8	−6.0	−1.4	57	−0.28
Ti	−1.2	0.6	7.2	−7.9	4.3	68	−0.63
V	−0.05	0.02	28.3	−1.5	0.7	68	−1.12
Cr	0.3	−0.2	10.4	3.2	−2.2	62	−1.62
Mn	0.4	−0.1	4.0	1.4	−0.5	54	−1.71
Co	0.6	0.01	25.5	16.3	0.1	234	1.68
Ni	0.7	0.7	8.4	6.0	5.5	104	0.86
Cu	0.4	0.5	6.2	2.2	3.1	86	0.08
Zn	1.4	1.2	3.8	5.2	4.6	54	−0.09
Si	4.5	1.7	2.0	9.0	3.4	37	−0.15
Ge	2.4	0.3	2.0	4.7	0.5	34	−0.12
Ru	1.0	−1.9	8.4	8.6	−15.9	69	0.24
Rh	−1.3	−3.2	15.6	−19.6	−49.2	364	0.64
Pd	−0.05	−0.6	15.7	−0.8	−9.8	154	0.48
Ag	−1.2	−1.5	7.0	−8.7	−10.3	81	0.08
W	−2.5	−1.8	6.3	−15.9	−11.1	60	−0.54
Pt	−1.3	−2.4	13.9	−17.9	−33.7	262	0.45
Au	−3.4	−4.4	8.0	−26.9	−34.9	89	0.22

Table 6.1.: Transport properties of several impurities in bcc Fe: the anomalous Hall angle α^{c}, spin Hall angle α^{s}, the longitudinal charge conductivity σ_{xx}^{c}, the transverse charge and spin conductivity $\sigma_{xy}^{\mathrm{c/s}}$ and momentum relaxation time τ_{p}. Additionally, the magnetic moment at the impurity site, M_0 is given.

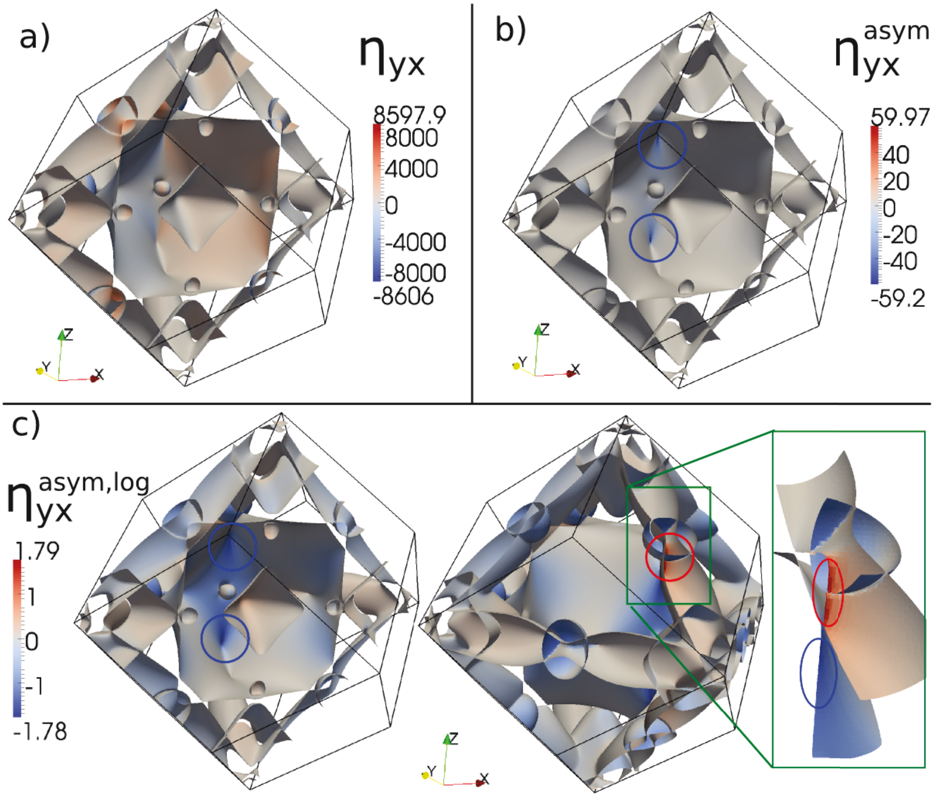

Figure 6.4.: Analysis of the contributions to the AHC on the Fermi surface for Co impurities in Fe. (a) The integrand η_{yx} of the transverse charge conductivity has a nearly anti-symmetric color code with respect to the yz-plane. Only half of the Fermi surface is shown. (b) The anti-symmetric part $\eta_{yx}^{\mathrm{asym}}$ is strongly peaked around certain points ("hot spots") on the Fermi surface (circles). (c) Displaying the anti-symmetric part on a logarithmic color scale (*cf.* Eq. (6.6)) reveals the dominating negative contributions to σ_{yx} (left panel), but also positive contributions on the outer Fermi-surface sheet (right panel) exist and partly compensate the negative ones. The values for η_{yx} and $\eta_{yx}^{\mathrm{asym}}$ are given in units of $a/(2\pi)$.

We define the integrand as $\eta_{yx}(\vec{k}) = \frac{v_{\vec{k},y}\lambda_{\vec{k},x}}{|\vec{v}_{\vec{k}}|}$ and show this quantity in Fig. 6.4a. We observe that the values of η_{yx} cover a large range between -8606 and $+8598$ (in units of $a/(2\pi)$). However, the color scale is nearly anti-symmetric with respect to the xz-plane and thus large values partly cancel each other. In fact, without spin-orbit coupling, each value at a given point $\vec{k} = (k_x, k_y, k_z)^{\mathrm{T}}$ is exactly canceled by another point $\vec{k}\,' = (k_x, -k_y, k_z)^{\mathrm{T}}$. Therefore, we define the part of η_{yz} that actually contributes to the transverse transport,

$$\begin{aligned}\eta_{yx}^{\mathrm{asym}}(\vec{k}) &= \frac{\eta_{yx}(\vec{k}) + \eta_{yx}(\vec{k}\,')}{2} && (6.4)\\ &= \frac{v_{\vec{k},y}}{2}\left(\lambda_{\vec{k},x} - \lambda_{\vec{k}\,',x}\right) \; . && (6.5)\end{aligned}$$

Here we have used that $\eta_{yx}(\vec{k})$ and $\eta_{yx}(\vec{k}\,')$ are different in sign because of the different sign of the x-component of the Fermi velocity ($v_{\vec{k},x} = -v_{\vec{k}\,',x}$). Thus, the non-vanishing $\eta^{\mathrm{asym}}(\vec{k})$ originates from an asymmetry in the mean free path, and this imbalance originates from an asymmetry in the scattering rates $P_{\vec{k},\vec{k}\,'}$ due to SOC.

The anti-symmetric part $\eta_{yx}^{\mathrm{asym}}$ (shown in Fig. 6.4b) nearly vanishes for large parts of the Fermi surface and is strongly enhanced around single points on the Fermi surface (highlighted by a blue circle). Therefore, we show a logarithmic color scale in Fig. 6.4c, where we define

$$\eta_{yx}^{\mathrm{asym,log}} = \mathrm{sign}(\eta_{yx}^{\mathrm{asym}}) \times \log(|\eta_{yx}^{\mathrm{asym}}| + 1) \; . \tag{6.6}$$

Note that through this definition, we are able to use a logarithmic scale and can also encode the sign of $\eta_{yx}^{\mathrm{asym}}$, *i.e.*

$$\eta_{yx}^{\mathrm{asym}} \lesseqgtr 0 \qquad \Longrightarrow \qquad \eta_{yx}^{\mathrm{asym,log}} \lesseqgtr 0 \; . \tag{6.7}$$

In the left and middle panels of Fig. 6.4c we see that the negative contributions dominate the Fermi surface. However, also strongly peaked positive contributions exist (enclosed by a red circle in the middle panel of Fig. 6.4c), which are of similar magnitude as the peaked negative contributions. A closer look into this region of the Fermi surface (right panel) reveals that the strong positive and negative contributions actually stem from the same (non-relativistic) band. An avoided crossing occurs due to spin-orbit coupling (as was verified by scaling the spin-orbit strength to zero), and the upper and lower Fermi surface sheets contribute with a positive and negative contribution, respectively, to the skew-scattering. Actually, all regions highlighted by a blue circle (also in the closeup) are equivalent to each other due to the fourfold rotational symmetry around the z-axis. These mutually existing positive and negative contributions are similar to the intrinsic contribution to the anomalous Hall conductivity (related to the Berry curvature of the relativistic electronic band structure), where the Berry curvature is strongly peaked around avoided crossings of SOC-split bands [102]. Here, the Fermi surface sheets containing the extremal contributions to $\eta_{yx}^{\mathrm{asym}}$ are of the same spin character (spin-up for Co impurities), implying that the spin-conserving part of SOC plays an important role.

The observation that $\eta_{yx}^{\mathrm{asym}}$ is strongly peaked at certain points, and that these points occur in pairs of opposite sign and similar magnitude, is not limited to Co impurities in Fe, but is a general phenomenon for impurities in Fe. For Ni and Cu impurities, a

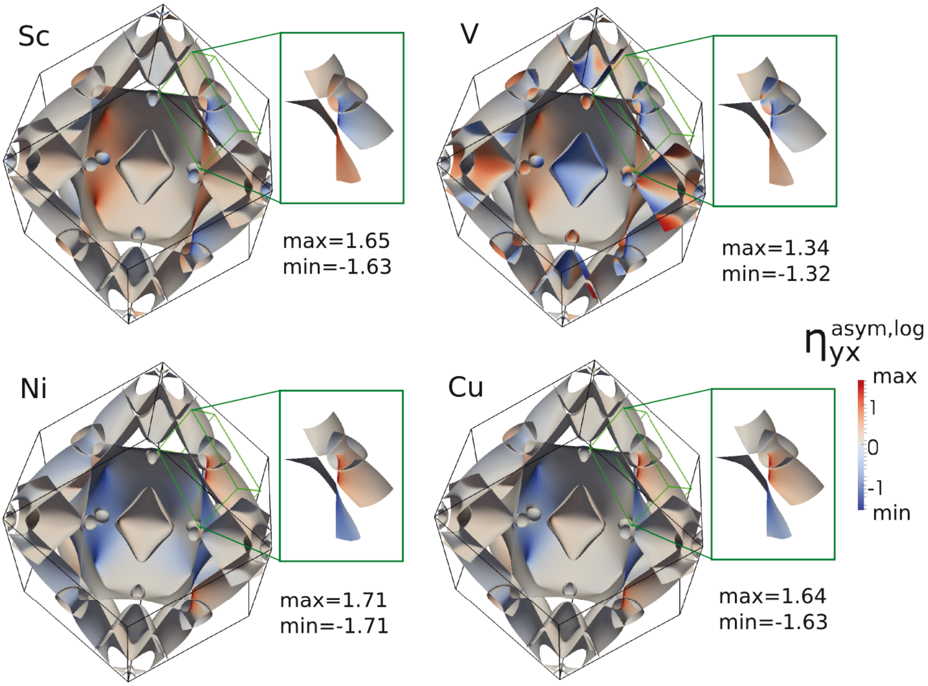

Figure 6.5.: Analysis of the contributions to the AHC on the Fermi surface for Sc, V, Ni and Cu impurities in Fe. The color code shows the logarithmic color scale $\eta_{xy}^{\mathrm{sym,log}}$ (*cf.* Eq. (6.6)) with the maximal and minimal values of the color scale given in each panel. The zoom magnifies the region where these extremal values are reached. The two upper panels have a similar color code in this region, whereas the color code of the lower panels is inverted with respect to the upper ones.

very similar distribution of $\eta_{yx}^{\mathrm{asym}}$ to the one shown in Fig. 6.4 occurs, with extremal values located at the same points as for Co impurities (see lower panels in Fig. 6.5). For Sc, Ti and V impurities, we also find the extremal values at those parts of the Fermi surface, but with a different sign (compare the magnified plot of the upper panels to the lower panels of Fig. 6.5). Overall, we observe that also the sign of the total transverse conductivity σ_{xy}^{c} is linked to this sign change: we have the same (negative) sign for Sc, Ti and V impurities and the same (positive) sign for Co, Ni and Cu impurities in Fe.

In contrast to this, the behavior for Cr and Mn impurities is somehow different: here, the extremal values are reached in other parts of the Fermi surface, where these sheets originate from spin-down bands (as opposed to spin-up bands for the other 3*d* impurities). However, also here, the minimal and maximal contributions occur in pairs near an avoided crossing, which resembles the behavior as previously discussed.

6.1.4. Numerical stability and symmetries

When calculating the Fermi surface of the bcc Fe host by means of the tetrahedron method, we observed that it is important to include as many symmetries in the Brillouin zone (BZ) as possible to achieve good numerical stability of the conductivity tensor. First tests, where the Fermi surface was calculated in the whole BZ lead to a conductivity tensor of wrong symmetry, *i.e.* $\sigma_{xy} \neq -\sigma_{yx}$. The reason is connected to the strongly peaked nature of η_{yz}: imagine a certain point $\vec{k}_1$ that represents a portion of the Fermi surface (with a weight proportional to the area that it represents). This portion has a symmetry-related equivalent Fermi-surface portion, *e.g.* mirrored at the yz-plane as in the example mentioned above (*cf.* Fig. 6.4). However, this second Fermi-surface piece might be represented by a slightly shifted point $\vec{k}_1{}' + \delta\vec{k}$ due to *e.g.* a different orientation of the tetrahedron. Because the sum of the two integrals over η_{yz} of two symmetry-related portions is very small compared to the magnitude of the bare values (*i.e.* $|\eta_{yx}^{\mathrm{asym}}|/|\eta_{yz}| \approx 10^{-2}$, *cf.* Figs. 6.4a and 6.4b), the numerical approximation can have a large value (which is random and depends on $\delta\vec{k}$). This disadvantage can be overcome by using either a denser mesh to calculate the Fermi surface (decreasing $\delta\vec{k}$), or preferably employing symmetries in the calculation of the Fermi surface, when $\delta\vec{k} = 0$ is enforced. For the latter solution, the Fermi surface is only calculated in an irreducible wedge of the BZ and then the symmetry operations are applied to "rotate" this Fermi-surface piece to the full BZ.

6.1.5. Convergence analysis

As discussed in the previous subsection 6.1.4, numerical details can have a large impact on the final result, the anomalous Hall conductivity or the anomalous Hall angle. Careful convergence tests are needed to estimate the error in the computed quantities. An apparent numerical parameter in the calculation of the conductivity is N_k, the number of k-points for the sampling of the Fermi surface. The influence of this parameter on the anomalous Hall angle (α^{c}) and spin Hall angle (α^{s}) is shown in the left upper and lower panel, respectively, of Fig. 6.6. It is enough to use only $N_k \approx 10.000$ to obtain a relative accuracy of approx. 10% for α^{c}. At first glance, this is surprising when we recall the discussion of Fig. 6.4, where we noticed that the integrand $\eta_{yx}^{\mathrm{asym}}$ is strongly peaked at certain spots. However, if the total value of the integral over the Fermi surface is dominated by the large parts where the integrand is relatively small, only relatively few points on the Fermi surface are enough to approximate the value of the integral, as it is the case *e.g.* for V impurities. However, the spiky behavior of the integrand is more pronounced *e.g.* for Sc or Co impurities (see Fig. 6.5) and thus also the variation of the Hall angles as function of N_k is larger, as can be seen in Fig. 6.6.

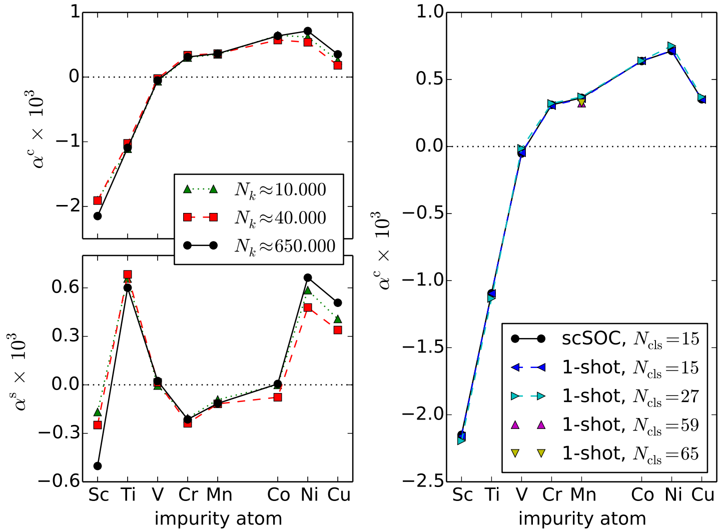

Figure 6.6.: Left: Convergence test for different k-meshes with N_k points on the Fermi surface (in the full Brillouin zone). The anomalous Hall angle α^c and spin Hall angle α^s for the various $3d$ impurities in an Fe host are shown in the top and bottom panel, respectively. Both quantities are converged with respect to the number of k-points. Right: comparison between calculations, where SOC is treated self-consistently (scSOC) or only in the last iteration (1shot-SOC). Additionally, for the latter ones the impurity-cluster size has been varied. Calculations were done with the densest k-mesh. The results are converged with respect to these parameters.

So far, all results were obtained using SOC in all steps, *i.e.* in the self-consistent determination of the host and the impurity potential, as well as in the calculation of the Fermi surface, the Bloch wavefunctions and transition matrix $T_{kk'}$ (in the following labeled as “self-consistent SOC” or “scSOC”). However, a possibility to reduce the computational effort enormously is to neglect SOC during the convergence of the host and the impurity potentials, while SOC is included in the last step when the Fermi-surface, wavefunctions and transition matrix are calculated (also called “1-shot SOC”). A comparison between these two approaches reveals that the latter captures the important effects to determine the anomalous Hall angle sufficiently well (compare the black and blue curves in the right panel of Fig. 6.6).

Finally, we analyze the accuracy of the anomalous Hall angle on the impurity cluster size. We used the “1-shot SOC”-approach because of its numerical efficiency and increased the cluster size from 15 atoms (next-nearest neighbors) to 27 atoms (including 3 shells around the impurity). A distinction of the blue and cyan curves in the

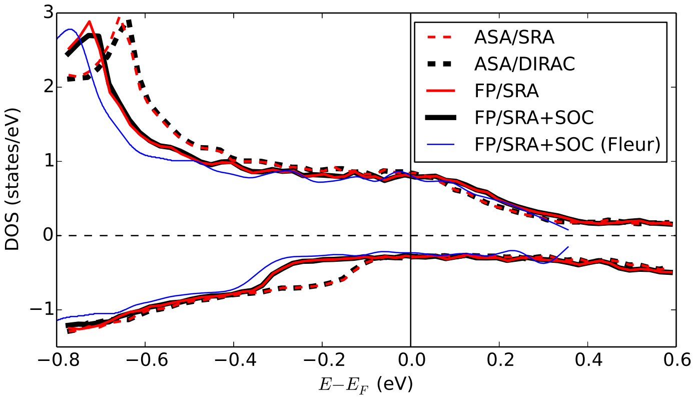

Figure 6.7.: Influence of different levels of approximations on the density of states of the bcc-Fe host crystal. Red and black curves represent results obtained by the KKR method. The DOS for the atomic sphere approximation solving either the scalar relativistic approximation (ASA/SRA) or the Dirac equation (ASA/DIRAC) are similar to each other. Taking into account also non-spherical contributions to the potential, *i.e.* the full potential (FP), changes the DOS considerably, independent of whether spin-orbit coupling is taken into account (FP/SRA vs. FP/SRA+SOC). For comparison, also the DOS computed with the FLAPW method [103] is shown (FP/SRA+SOC (Fleur)), which is in reasonable agreement to the KKR full-potential results.

right panel of Fig. 6.6 is barely possible, showing that the values are converged with respect to the cluster size. For the Mn impurity we even increased the cluster size to contain 59 and 65 atoms (corresponding to 5 and 6 shells, respectively) without a significant change.

6.1.6. Comparison to other data: importance of full potential

Finally, we examine the influence of the full potential as compared to the atomic sphere approximation (ASA). In the latter approximation, only the spherical component of the potential is kept, and as a result many equations simplify. This approach has been shown to reproduce correct results for many observables in bulk systems, *e.g.* impurity magnetic moments or even transport properties as the longitudinal conductivity or spin-relaxation times. However, the full potential already becomes important for low-dimensional or open structures, *e.g.* for relaxation processes in ultra-thin films [52]. Thus, the question seems justified, how important is the full potential for the anomalous and spin Hall conductivities.

To analyze this point, we first calculated the density of states (DOS) of the bcc-Fe host with different approximations:

- ASA for the potential solving the scalar relativistic approximation (SRA), *i.e.* neglecting spin-orbit coupling (SOC)
- ASA for the potential solving the Dirac equation, thus incorporation of all relativistic effects including SOC
- Full potential solving the scalar relativistic approximation (*i.e.* without SOC)
- Full potential solving the scalar relativistic approximation plus SOC Hamiltonian

The results are shown in Fig. 6.7 and allow for two clear statements: the density of states from the two ASA calculations lie basically on top of each other. This is also the case for the two full-potential calculations. Thus, the influence of SOC on the DOS is negligible. However, the difference between the ASA and full potential results is large. The ASA states seem to be shifted by approximately 0.1 eV towards higher energies with respect to the full-potential result. This clearly influences the states at the Fermi energy and might have an influence on the transverse transport coefficients.

Of course, a complete analysis of this point requires a re-calculation also of the impurity potentials and the conductivity tensor in ASA. However, due to computational restrictions we omit this step and compare instead to ASA results obtained by M. Gradhand [104]. He also uses the semi-classical Boltzmann equation (*cf.* section 3.5), but based on a fully relativistic version of the KKR method. For Mn impurities, he finds a different anomalous Hall angle of -0.1×10^{-3}, which is of different sign compared to our value of 0.4×10^{-3}. The difference might either come from the description of the potential (ASA vs. FP) or from the incorporation of SOC (fully relativistic vs. SRA+SOC). Due to the effect of the different approximations on the host density of states (see Fig. 6.7), we speculate that the full potential is important to describe the anomalous Hall effect correctly, and that in our description, SOC effects are well taken care of. This shows at the same time, that the AHC is a delicate quantity and details matter for its calculation. Therefore each analysis has to be conducted with care.

Unfortunately there is currently no systematic experimental analysis of the skew-scattering contribution to the anomalous Hall effect off $3d$ impurities in bcc-Fe. An attempt was made by Shiomi [105], but the assumptions made in the extraction of skew-scattering contribution are questionable. In his analysis of (Ti-Cu) impurities in bcc-Fe, the values reported as the anomalous Hall angles are 1-2 orders of magnitude larger than the ones calculated here. However, some features agree, *e.g.* the sign change between V and Cr. Additionally, experiments by Tian *et al.* [77] on Fe films indicate an anomalous Hall angle of the order of 10^{-3}, which agrees with our findings.

6.2. Defects in the $L1_0$-ordered FePt-alloy

We now turn to another ferromagnetic material, which is computationally more demanding and also exhibits a lower symmetry. This allows us to study several types of defects, which are similar to each other and lead to a subtle interplay of different skew-scattering contributions.

6.2.1. Crystal structure and symmetries

The $L1_0$ ordered FePt alloy can be described by a tetragonal crystal structure. The lattice constants were chosen as $a = 5.16\, a_{\mathrm{B}}$ and $c/a = 1.39$. The two atoms in the unit cell are located at positions $(0, 0, 0)$ and $(\frac{1}{2}, \frac{1}{2}, \frac{1}{2})$ (in units of the Bravais vectors) for Fe and Pt atoms, respectively. The magnetization direction was chosen along the c-axis of the crystal, as this is the easy-axis determined by the magneto-crystalline anisotropy (MCA) [106]. The calculation of the total magnetic spin-moment reveals $3.21\, \mu_{\mathrm{B}}$ per unit cell, of which the Fe- and Pt-atoms contribute $2.88\, \mu_{\mathrm{B}}$ and $0.33\, \mu_{\mathrm{B}}$, respectively.

In the presence of spin-orbit coupling, we employ 8 symmetry operations corresponding to a 4-fold rotation axis around the c-axis (with and without inversion) to determine the irreducible part of the Brillouin zone.

6.2.2. Self-substitutional defects

First we examine some defects that are probably very common in an experimental situation, when the concentration of one atomic species is slightly larger, *i.e.* $\mathrm{Fe}_{1+x}\mathrm{Pt}_{1-x}$ with $|x| \ll 1$. Therefore we calculate substitutional (i) Fe-impurities on the Pt-site

	σ^{c}_{xx}	σ^{c}_{zz}	σ^{c}_{xy}	σ^{s}_{xy}	α^{c}_{xy}	α^{s}_{xy}
Fe on Pt-site ($x > 0$)	131.7	111.8	1.15	0.883	8.8	6.7
Pt on Fe-site ($x < 0$)	64.5	33.8	−0.175	−0.141	−2.7	−2.1
1:1 mixture (uncorr., $x = 0$)	70.7	46.3	0.064	0.093	0.9	1.3
Fe-Pt dimer (averaged)	76.9	51.4	0.118	0.057	1.5	0.7
Matthiessen rule	86.6	52.0	0.092	−0.040	1.1	−0.5

Table 6.2.: Disorder-induced transport properties of the $L1_0$-ordered FePt alloy. Conductivities are given in units of 10^6 S/m = $(\mu\Omega\,\mathrm{m})^{-1}$ at an impurity concentration of 1 at.%. Hall angles are given in units of mrad = 10^{-3}.

(increasing the concentration of Fe, $x > 0$), and (ii) Pt-impurities on the Fe-site (increasing the concentration of Pt, $x < 0$) in the crystal. From now on we refer to these impurities as *single* impurities. The resulting conductivity tensor is of the form[1]

$$\overset{\leftrightarrow}{\sigma} = \begin{pmatrix} \sigma_{xx} & \sigma_{xy} & 0 \\ -\sigma_{xy} & \sigma_{xx} & 0 \\ 0 & 0 & \sigma_{zz} \end{pmatrix} . \tag{6.8}$$

The results of our calculations are given in Tab. 6.2. Interestingly, the two impurities have a different sign in the transverse component of the conductivity tensor, and the anomalous and spin Hall angles for larger Fe-concentrations ($x > 0$) are among the largest ones found in this work (compare to impurities in bcc-Fe, *cf.* Tab. 6.1).

In an experimental situation, however, one can imagine that a mixture of the two types of impurities described above is present. Then, the concentration of one specimen is not higher for a 1:1 mixture ($x = 0$), however we have a disordered system. Assuming that electrons scatter independently off the two types of impurities (*i.e.* assuming non-interacting impurities), we can average on the level of the transition rates [107],

$$P^{\mathrm{avg}}_{kk'} = \frac{1}{2} \left(P^{\mathrm{Fe}}_{kk'} + P^{\mathrm{Pt}}_{kk'} \right) , \tag{6.9}$$

converge the mean free path and finally calculate the conductivity tensor. Comparing the results of this mixture presented in Tab. 6.2 to the single impurities, we observe that the anomalous Hall conductivity is smaller compared to skew-scattering off the single impurities (0.064 for the mixture compared to 1.15 (Fe) and 0.175 (Pt)). An heuristic argument could be, that the skew-scattering off the Pt-part partly compensates the skew-scattering produced by the Fe-part due to their different sign. However, the approximation of averaging over the transition rates neglects some interference effects between the two impurities, because we loose a phase: $|T_{\mathrm{Fe}} + T_{\mathrm{Pt}}|^2 \approx |T_{\mathrm{Fe}}|^2 + |T_{\mathrm{Pt}}|^2$. One might call them impurity-correlation effects.

To estimate the impact of those interference effects between two impurities on transport properties, we calculated another interesting type of disorder. Here, two neighboring Fe and Pt atoms swap their positions and form a dimer (*cf.* Fig. 6.8). This can be seen as the limiting case of maximal correlation effects between the two single-impurity types. In this case, the bond of a single dimer breaks the tetragonal symmetry of the crystal and leads to a full conductivity tensor. E.g. the dimers 1 and 2

---

[1] The magnetic moment is chosen along the c-axis, which is parallel to the z-axis of the coordinate system

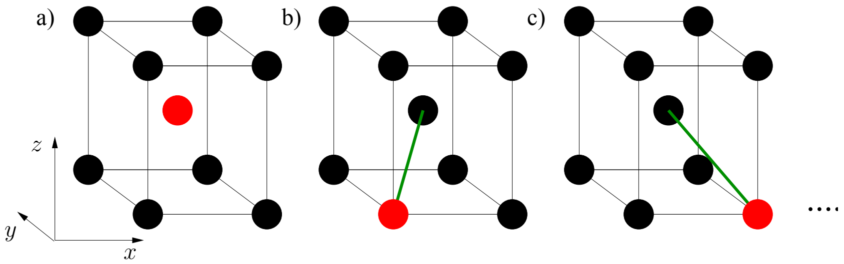

Figure 6.8.: Illustration of disorder in FePt. (a) $L1_0$-ordered FePt in the 2-atomic unit cell. Black and red spheres represent Fe and Pt atoms, respectively. (b) and (c): Swapping the positions of nearest-neighbor Fe and Pt atoms creates a dimer. The bond direction (green line) breaks the tetragonal symmetry of the lattice. In total there are eight differently oriented dimers.

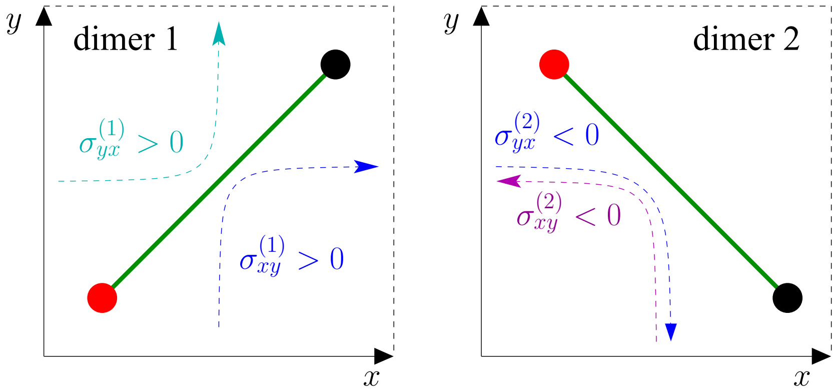

Figure 6.9.: Geometrical analysis of the transverse conductivity for the two dimers illustrated in Fig. 6.8. The dashed lines with arrows represent electron trajectories. The dimer bond acts as an electron mirror. However, the deflection is fundamentally different from the spin-orbit induced skew-scattering, because here the sign of σ_{xy} and σ_{yx} is the same. The blue trajectories in the left and right panel correspond to the same situation, but rotated by 90°. This explains the symmetry $\sigma_{xy}^{(1)} = -\sigma_{yx}^{(2)}$.

illustrated in Figs. 6.8b) and 6.8c) lead to the conductivity tensor

$$\overleftrightarrow{\sigma}_1 = \begin{pmatrix} 38.95 & 0.77 & 0.32 \\ 0.63 & 39.02 & 0.32 \\ 0.22 & 0.42 & 26.21 \end{pmatrix} \times 10^6 \, \frac{\mathrm{S}}{\mathrm{m}} \,, \quad \vec{\tau}_{\mathrm{Fe}} - \vec{\tau}_{\mathrm{Pt}} = \left(\frac{a}{2}, \frac{a}{2}, \frac{c}{2}\right)^{\mathrm{T}}$$

$$\overleftrightarrow{\sigma}_2 = \begin{pmatrix} 39.02 & -\,0.63 & -\,0.32 \\ -\,0.77 & 38.95 & 0.32 \\ -\,0.42 & 0.22 & 26.21 \end{pmatrix} \times 10^6 \, \frac{\mathrm{S}}{\mathrm{m}} \,, \quad \vec{\tau}_{\mathrm{Fe}} - \vec{\tau}_{\mathrm{Pt}} = \left(-\frac{a}{2}, \frac{a}{2}, \frac{c}{2}\right)^{\mathrm{T}}$$

We arrive at $\overset{\leftrightarrow}{\sigma}_2$ by interchanging the x and y-components of $\overset{\leftrightarrow}{\sigma}_1$, and adding a minus-sign for the off-diagonal components containing x. This is largely a geometrical effect caused by a preferential direction, determined by the dimer bond, as can be seen from inspecting Fig. 6.9. However, spin-orbit coupling causes the σ_{xy} and σ_{yx}-components of the tensor to have an anti-symmetric component.

There are eight possible orientations for the nearest-neighbor dimer, and in a realistic situation the dimers would have uniformly distributed orientations. We achieve this by averaging the transition rates of all eight dimers,

$$P_{kk'}^{\mathrm{avg}} = \frac{1}{8} \sum_{i=1}^{8} P_{kk'}^{i} \, , \tag{6.10}$$

and solve the Boltzmann equation (3.15) using $P_{kk'}^{\mathrm{avg}}$. By doing so, we have restored the tetragonal symmetry and obtain a conductivity tensor of the form in Eq. (6.8) with the values reported in Tab. 6.2. Note that we now have 2 atomic impurities per dimer. Thus the conductivities calculated by the code have to be multiplied by a factor 2 to compare to the previous results. We can conclude, that correlation effects affect the diagonal conductivities by only 10%, but the transverse charge conductivity is increased by a factor of 2 for the Fe-Pt dimer as compared to the 1:1 mixture of uncorrelated scattering centers. Interestingly, the transverse spin-conductivity is decreased by a factor of 2 with respect to the uncorrelated mixture of scatterers.

Finally, we mention that the empirical Matthiessen rule [107] is only valid to a very limited extend for this system, in contrast to ternary alloys based in a Cu host [108]. The rule states that the resistivities (being equal to the inverse conductivities) of independent scattering mechanisms can just be added,

$$\left(\overset{\leftrightarrow}{\sigma}_{\mathrm{tot}}\right)^{-1} = \left[\left(\overset{\leftrightarrow}{\sigma}_{\mathrm{Fe}}\right)^{-1} + \left(\overset{\leftrightarrow}{\sigma}_{\mathrm{Pt}}\right)^{-1}\right] /2. \tag{6.11}$$

These values (see last row in Tab. 6.2) differ from the explicit calculation of the uncorrelated scatterers by about 10-20% for the diagonal and 40-50% for the transverse conductivities. It however evidently fails for the spin conductivity, being even of different sign.

6.2.3. Comparison to some experimental results

The anomalous Hall effect in the FePt $L1_0$-ordered alloy has been studied experimentally and a value for the anomalous Hall angle has been extracted, $|\alpha_{\mathrm{exp}}^{\mathrm{c}}| = (11 \pm 2) \times 10^{-3}$ [76]. The sign of the experimental value is undetermined, since it is not stated whether the σ_{xy}^{c} or σ_{yx}^{c} component is considered. Thus, we restrict ourselves to point out that our results are in the same order of magnitude ($1 - 9 \times 10^{-3}$ depending on the impurity type). Another study (Ref. [78]) turns to disordered fcc FePt thin films and extracts a skew-scattering angle of about 10^{-2}.

6.3. Defects in MnSi

After having discussed two important ferromagnetic systems, we turn to a more complicated system, namely MnSi. For this system, the chemical unit cell contains 8 atoms, and thus represents a challenge in terms of computational resources. On the other hand, the system is very rich in terms of interactions, symmetry and physical properties.

6.3.1. Crystal structure and symmetries

The B20 type crystal structure can be described by a simple-cubic lattice with lattice parameter $a = 8.613\,a_\mathrm{B} = 4.558\,\text{Å}$ and a unit cell containing 4 Mn and 4 Si atoms. The eight positions are given as:

$$\begin{aligned}
\vec{R}_{\mathrm{Mn},1} &= (\quad u_\mathrm{Mn}, \quad u_\mathrm{Mn}, \quad u_\mathrm{Mn} \quad) ,\\
\vec{R}_{\mathrm{Mn},2} &= (\quad -0.5 + u_\mathrm{Mn}, \quad 0.5 - u_\mathrm{Mn}, \quad -u_\mathrm{Mn} \quad) ,\\
\vec{R}_{\mathrm{Mn},3} &= (\quad -u_\mathrm{Mn}, \quad -0.5 + u_\mathrm{Mn}, \quad 0.5 - u_\mathrm{Mn} \quad) ,\\
\vec{R}_{\mathrm{Mn},4} &= (\quad 0.5 - u_\mathrm{Mn}, \quad -u_\mathrm{Mn}, \quad -0.5 + u_\mathrm{Mn} \quad) ,
\end{aligned} \tag{6.12}$$

and

$$\begin{aligned}
\vec{R}_{\mathrm{Si},1} &= (\quad -u_\mathrm{Si}, \quad -u_\mathrm{Si}, \quad -u_\mathrm{Si} \quad) ,\\
\vec{R}_{\mathrm{Si},2} &= (\quad 0.5 - u_\mathrm{Si}, \quad -0.5 + u_\mathrm{Si}, \quad u_\mathrm{Si} \quad) ,\\
\vec{R}_{\mathrm{Si},3} &= (\quad u_\mathrm{Si}, \quad 0.5 - u_\mathrm{Si}, \quad -0.5 + u_\mathrm{Si} \quad) ,\\
\vec{R}_{\mathrm{Si},4} &= (\quad -0.5 + u_\mathrm{Si}, \quad u_\mathrm{Si}, \quad 0.5 - u_\mathrm{Si} \quad) ,
\end{aligned} \tag{6.13}$$

with $u_\mathrm{Mn} = 0.138$ and $u_\mathrm{Si} = 0.155$. We note that the crystal structure is often described differently in the literature [99, 109], where the atom positions for the Mn and Si atoms are of the same form, namely

$$\begin{aligned}
\vec{R}_1 &= (\quad u, \quad u, \quad u \quad) ,\\
\vec{R}_2 &= (\quad 0.5 + u, \quad 0.5 - u, \quad -u \quad) ,\\
\vec{R}_3 &= (\quad -u, \quad 0.5 + u, \quad 0.5 - u \quad) ,\\
\vec{R}_4 &= (\quad 0.5 - u, \quad -u, \quad 0.5 + u \quad) ,
\end{aligned} \tag{6.14}$$

and the internal parameters are $u_\mathrm{Mn} = 0.138$ (as before) and $u_\mathrm{Si} = 0.845$. However, we can transform the coordinates from Eqs. (6.12) and (6.13) into the representation as given in Eq. (6.14) just via a translation by lattice vectors. Thus, the crystal structure used here is identical to the one considered in Ref. [109]. In other works, a slightly different parameter $u_\mathrm{Mn} = 0.137$ was reported [99, 110]. In yet another paper [111], the same form for the atom positions as presented in Eq. (6.14) was used, albeit using different u-parameters of 0.113 (Mn) and 0.404 (Si). The resulting crystal structure is equivalent to the one described above, and can be transformed into one another by a simple rotation and translation: $\vec{R}_i \to (0.25, 0.25, 0.25) + \mathcal{R}\vec{R}_i$, where $\mathcal{R}$ is a rotation matrix, *e.g.* around the $(1, -1, 0)$-axis.

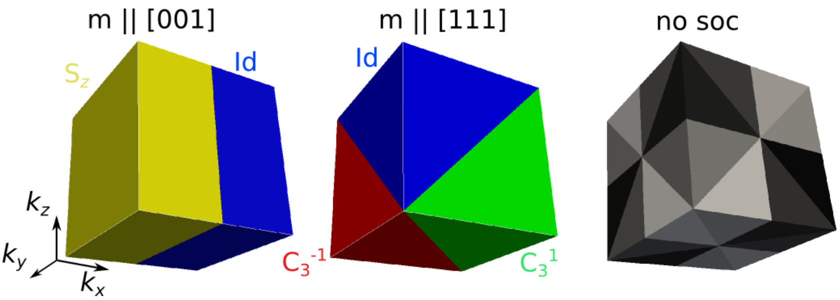

Figure 6.10.: Symmetries in the Brillouin zone of MnSi with spin-orbit coupling and magnetization direction along [001] (left panel) and [111] (middle panel). Without SOC, in total 24 symmetries are present in the Brillouin zone (the 12 real-space symmetries plus the ($\vec{k} \rightarrow -\vec{k}$)-symmetry from time reversal symmetry) and reduce the IBZ enormously (right panel). The colors represent the symmetry operations that transform the irreducible part (blue) to recover the full BZ.

The crystal structure possesses the space group P$2_1$3, which has no center of inversion. The implication of this fact is that the crystal structure is not equivalent to its mirror image, and therefore it is called chiral. However, there exist (neglecting spin-orbit coupling) 12 symmetry operations. Only three out of these 12 operations are symmorphic, corresponding to a 3-fold rotation around the [111]-axis. The rotation matrices $\mathcal{R}$ read

$$\mathrm{C}_3^0 = \mathrm{Id}: \begin{pmatrix} 1 & 0 & 0 \\ 0 & 1 & 0 \\ 0 & 0 & 1 \end{pmatrix}, \quad \mathrm{C}_3^1: \begin{pmatrix} 0 & 0 & 1 \\ 1 & 0 & 0 \\ 0 & 1 & 0 \end{pmatrix}, \quad \mathrm{C}_3^{-1}: \begin{pmatrix} 0 & 1 & 0 \\ 0 & 0 & 1 \\ 1 & 0 & 0 \end{pmatrix} \tag{6.15}$$

The remaining 9 operations correspond to screw-axes, *i.e.* rotations combined with a translation $\vec{\tau}$, which is not a multiple of a lattice vector. One of them is particularly important for our investigations. This is the 2-fold screw axis along the z-direction with a translation $\vec{\tau} = (\frac{1}{2}, 0, \frac{1}{2})$, with the transformation equation

$$\mathrm{S}_z: \quad (x, y, z) \rightarrow (\frac{1}{2} - x, -y, \frac{1}{2} + z) \; . \tag{6.16}$$

Apart from the identity operation, this is the only symmetry operation that survives if spin-orbit coupling is included in the calculation and the magnetization direction is chosen along [001], because it also leaves the spin-quantization axis unchanged. It helps us to calculate the Fermi surface in the irreducible part of the Brillouin zone (IBZ) which is only half of the full one (*cf.* left panel of Fig. 6.10). As it turns out, the restriction to the IBZ is particularly important for the convergence of the Boltzmann equation (see the discussion at the beginning of section 6.3.6).

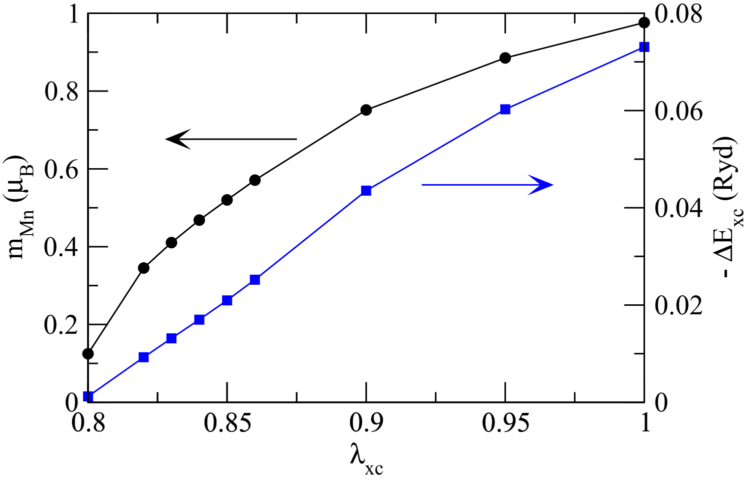

Figure 6.11.: Scaling of the magnetic moment in MnSi through variation of the magnetic part of the exchange-correlation potential, determined by λ_{xc}. The energy difference $\Delta E_{\mathrm{xc}} = E_{\mathrm{xc}}[\rho, m] - E_{\mathrm{xc}}[\rho, 0]$ is also shown.

On the other hand, if the magnetization direction is chosen along [111], the symmetry operations presented in Eq. (6.15) survive, because they leave the SQA unchanged. Then, the volume of the IBZ can be reduced to 1/3 of the one from the full Brillouin zone (*cf.* middle panel of Fig. 6.10).

6.3.2. Scaled magnetic moments in the ferromagnetic state

The experimentally detected ground state without external fields and at small temperatures is a helical spin spiral along [111] with a period length of 180 Å[98]. We can approximate the ground state by the ferromagnetic configuration due to the very long period length of the spin spiral. Moreover, ferromagnetic order can be reached upon an application of an external magnetic field.

However, the standard LDA functionals (we use the parametrization by Vosko, Wilk and Nusair [46]) yield a magnetic moment of nearly $1\,\mu_{\mathrm{B}}$ per Mn atom, although the experimentally determined moment is about $0.4\,\mu_{\mathrm{B}}$. In this case, the theoretically obtained electronic structure would be very different from the experimentally obtained one. Therefore, we introduce a scaling parameter λ_{xc} to scale the magnetic part of the exchange-correlation energy, as was first introduced by Hoshino *et al.* [112] and was successfully applied to study the weak itinerant magnetism in $\mathrm{Ni_3Al}$ [113] and spin-polarization energy of impurities in monovalent hosts [114]. As described in

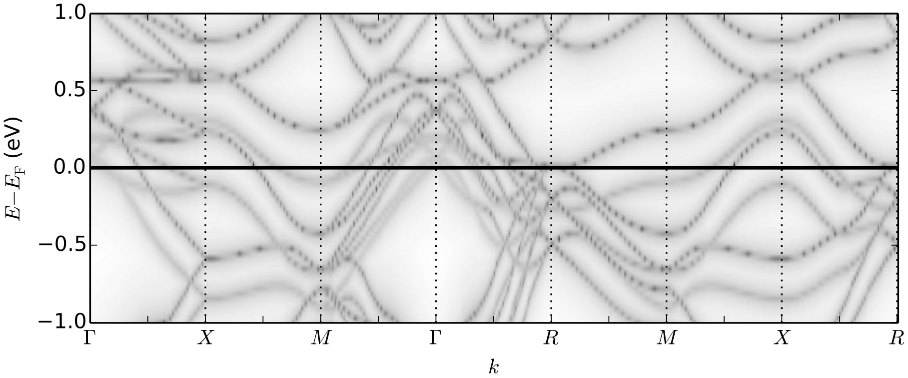

Figure 6.12.: Band structure of MnSi without SOC. Several unusual features as described already in Ref. [99] can be observed. See text for details. Due to the low resolution, some bands are hardly visible, *e.g.* the threefold degenerate level at Γ just above the Fermi energy E_F.

Ref. [114], the total energy then reads

$$E[\rho, m; \lambda_\mathrm{xc}] = E[\rho, m] + (\lambda_\mathrm{xc} - 1)(E_\mathrm{xc}[\rho, m] - E_\mathrm{xc}[\rho, 0])\,, \tag{6.17}$$

where $\rho(\vec{r})$ and $m(\vec{r})$ are the electron density and magnetization density, respectively. As shown in Ref. [114], this is equivalent to constraining the magnetic moment (as done in Ref. [99]) through a fictitious external magnetic field. We found that $\lambda_\mathrm{xc} = 0.83$ yields a magnetic moment of $0.41\,\mu_\mathrm{B}$ per Mn atom (*cf.* Fig. 6.11), which is closest to the experimentally obtained value. This value for λ_xc was used throughout the calculations. More precisely, we used the same scaling in the impurity calculations for the impurity atoms. We also note that an uncertainty of $0.01\,\mu_\mathrm{B}$ leads to an uncertainty of the position of bands (and also of the Fermi energy) of roughly 10 meV.

6.3.3. Electronic structure and spin-mixing parameter

First, we computed the band structure (*cf.* Fig. 6.12), which shows qualitatively the same features as described in Ref. [99]. From the unusual space group of MnSi follow as well some unusual features in the band structure. Among them are "sticking" of bands at the BZ face (see the paths $\overline{XM}$ and $\overline{RMXR}$, where all levels are at least twofold degenerate) and bands with non-zero velocities at the BZ boundary (*e.g.* the lowest levels at R) [99].

The Fermi-surface without SOC (*cf.* left panel of Fig. 6.13) also compares well to Ref. [99], except the shape of the little hole-shapes centered around the BZ corner

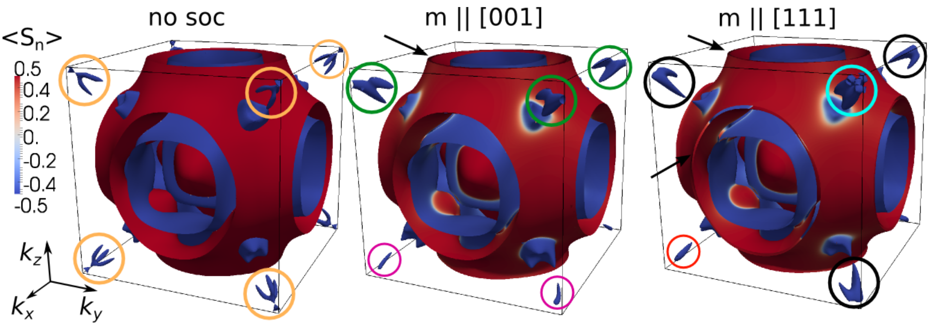

Figure 6.13.: Fermi surfaces without spin-orbit coupling (left) and with spin-orbit coupling with magnetization in [001] (center) and [111] directions (right). The Fermi surface shapes are different for the three cases, best seen at the hole-shapes around the BZ corner (R-point). Circles of the same color highlight equivalent hole-shapes. The spin expectation-value is presented as color code on the Fermi surface. For the case without SOC, red and blue colors correspond to majority and minority states, respectively. White color corresponds to fully spin-mixed states. The lifted band-sticking is highlighted by arrows.

(R-point). However, this shape stems from a band very close to E_F and is certainly affected by the uncertainty in the magnetic moment (*e.g.* we have constrained the magnetic moment to $0.41\,\mu_\mathrm{B}$ compared to $0.4\,\mu_\mathrm{B}$ in Ref. [99]). The sticking of bands at the BZ faces is clearly observed. Including SOC with the magnetization direction along [001] (see the middle panel of Fig. 6.13) yields a reduction of the symmetry, as can be observed best by the different hole-shapes around the R-point in $+k_z$ and $-k_z$ direction (highlighted by green and purple circles, respectively). Additionally, the sticking of bands at faces parallel to the k_z-direction is still present and can be attributed to the non-symmorphic symmetry, which we called S_z (*cf.* Eq.(6.16)), whereas the bands on the top and bottom BZ face are now slightly SOC-split (highlighted by the arrow). However, this splitting is due to the spin-conserving part of the SOC operator and yields nearly pure spin-states, indicated by the red and blue color at the $\vec{k} = (k_x, k_y, +\pi/a)$ face. In regions of the BZ where majority and minority-states intersect, a large spin-mixing parameter (and consequently states with a small spin expectation-value, $S_z \approx 0$) are present (white color). Turning the magnetization direction along [111] (right panel of Fig. 6.13) yields another breaking of non-symmorphic symmetries and the sticking of bands is lifted on all BZ faces. However, the color code on the whole Fermi surface, representing the spin-mixing parameter, does not change much when the magnetization is tilted. This is reflected in a small anisotropy $\mathcal{A} = 0.5\%$ of the Fermi-surface averaged spin-mixing parameter: $\langle b_{\hat{s}}^2 \rangle = 4.65 \times 10^{-2}$ and 4.63×10^{-2} for magnetization in [001] and [111] directions.

6.3.4. Defect magnetic moments and charge relaxation

Several studies investigate the effect of Fe-doping in MnSi, $\mathrm{Fe}_x\mathrm{Mn}_{1-x}\mathrm{Si}$ [21, 110, 115]. Therefore we study the scattering and transport properties of this defect in the low-concentration limit. Evidently, the Fe atoms will statistically replace the four non-equivalent Mn atoms, similarly to the eight possible orientations of an Fe-Pt dimer described in section 6.2. Thus, we also perform the averaging on the level of the transition-rate matrix $P_{kk'}$ as described in Eq. (6.10) to account for this statistical average. As a counterpart to the replacement of the magnetic atom, we also investigate the Ge-doping on the Si-site in the low-concentration limit.

Neighboring atoms of the impurity with distance of up to one lattice parameter were included in the real-space impurity cluster. Due to the different u-parameter for the two atomic species, this results in different cluster sizes containing 41 and 35 atoms for Fe and Ge impurities, respectively. Since this is computationally very demanding, we chose the “1-shot SOC” approach described in section 6.1.5 which includes spin-orbit coupling (SOC) only in the last iteration and determines the self-consistent potentials (for the host system and impurity cluster) without SOC.

Let us first look at the impurity magnetic moments (calculated without SOC): For

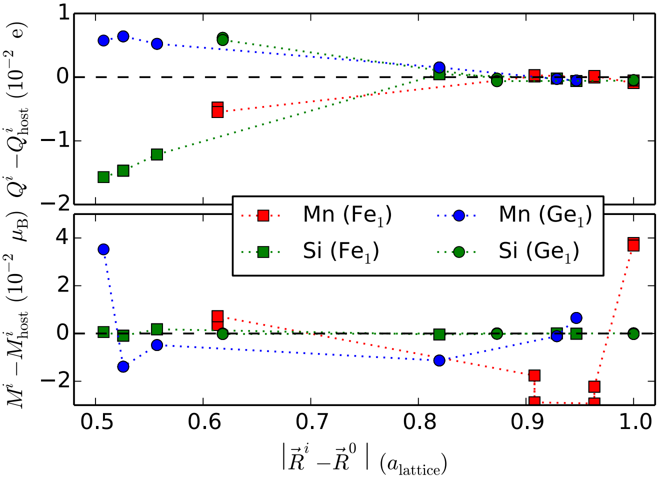

Figure 6.14.: Top: deviations in the atomic charges from the ideal host values $Q^{\mathrm{Mn}}_{\mathrm{host}} = 25.141$ and $Q^{\mathrm{Si}}_{\mathrm{host}} = 13.859$ electrons. The charges are given separately for Mn (red and blue) and Si atoms (green) around an Fe-impurity occupying the first Mn site (red and green squares) or around a Ge-impurity occupying the first Si site (blue and green circles). Bottom: the same for the magnetic moments.

the Fe impurities at the Mn site, we obtain a magnetic moment of $0.191\,\mu_\mathrm{B}$. Our numerical accuracy is limited by *e.g.* the chosen cut off in the spherical harmonics expansion, and thus the magnetic moment of the Fe impurity is slightly different if we place it at the four different Mn positions ($\delta m \approx 10^{-4}\,\mu_\mathrm{B}$), although they should be identical due to symmetry. However, these deviations are very small and can be considered as negligible. The same holds for the Ge-impurities at the Si site, where a very small magnetic moment of $-0.009\,\mu_\mathrm{B}$ is obtained (with negligible $\delta m = 10^{-6}\,\mu_\mathrm{B}$).

For the surrounding cluster atoms around the impurity site, we find a long-ranged oscillation of the disturbed Mn-magnetic moments. The deviations from the bulk magnetic moment are of the order of $\pm 0.04\,\mu_\mathrm{B}$ and decay quickly for a (non-magnetic) Ge impurity (*cf.* blue circles in the lower panel of Fig. 6.14). However, the spin-polarized Fe impurity induces strong oscillations in the magnetic moments of the surrounding Mn atoms, that do not decay within the chosen impurity cluster (*cf.* red squares in the lower panel of Fig. 6.14). However, because of the insensitivity of our results to the impurity-cluster size for magnetic impurities in Pd (*cf.* section 7.1), where so-called giant moments are formed, we believe that truncating the cluster size after one lattice constant is sufficient. The Si atoms stay non-spin-polarized ($m_\mathrm{Si} \approx -0.01\,\mu_\mathrm{B}$).

Looking at the charge relaxation around the impurity site (upper panel of Fig. 6.14), we see that the extra charge of 1 electron at the Fe site is well screened by the surrounding cluster atoms. The difference between the perturbed and unperturbed charge values decay reasonably fast for both atomic types (red and green squares). Also the charges around the Ge atom relax quickly within the distance of one lattice constant from the impurity center (blue and green circles).

6.3.5. Lifetimes

In Fig. 6.15 we show the electron lifetimes $\tau_{\vec{k}}$ (as defined in Eq. (3.16)) on the Fermi surface for the dilute alloy $\mathrm{Fe}_x\mathrm{Mn}_{1-x}\mathrm{Si}$ at an impurity concentration of $x = 1\%$. Without spin-orbit coupling (*cf.* left panel), the lifetimes for up-electrons range between 1200 fs and 1570 fs, and the corresponding Fermi surface sheets appear in orange to red. In contrast, the Fermi-surface sheets belonging to the spin-down states appear in light blue color, indicating a small lifetime of 500-600 fs. Clearly, there is a quantitative difference between the lifetimes for up- and down-states. However, the spread of lifetimes in a chosen spin channel is much smaller.

In some approaches to electron transport, the same (averaged) lifetime is used for all states at the Fermi level, which is called *constant relaxation time approximation.* This approach may be refined by defining an averaged lifetime for the two spin channels

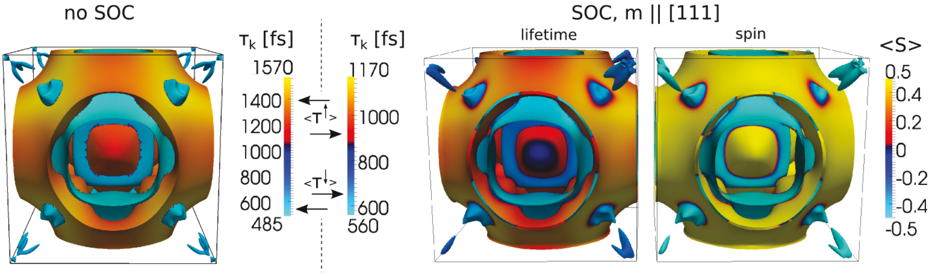

Figure 6.15.: Left and central image: Electron lifetimes $\tau_{\vec{k}}$ for Fe-impurities in MnSi (at an impurity concentration of 1 at.%). The arrows next to the color legend indicate the value for the averaged spin-up and spin-down lifetimes. Right: spin expectation-value on the Fermi surface for magnetization along the [111] direction. The same data as in the right panel of Fig. 6.13 is shown, but with a different color scale for comparison to the lifetimes.

separately. Therefore, we define the averaged lifetime for the up-states, $\langle \tau^{\uparrow} \rangle$, by

$$1/\langle \tau^{\uparrow} \rangle = \frac{1}{n^{\uparrow}(E_{\mathrm{F}})} \int\limits_{\langle S \rangle > 0} \mathrm{d}S \, \frac{\tau_{\vec{k}}^{-1}}{\hbar \, |\vec{v}_{\vec{k}}|} \,, \tag{6.18}$$

where $n^{\uparrow}(E_{\mathrm{F}})$ is the density of up-electrons at the Fermi level and the integration is only performed over the part of the Fermi surface where the spin expectation-value is positive (similarly we define $\langle \tau^{\downarrow} \rangle$ for the spin-down states). This yields averaged lifetimes of 1350 fs (spin-up) and 530 fs (spin-down, as indicated by the arrows next to the color legend of Fig. 6.15), being different by a factor of 2.5.

Usually, two arguments are used to explain a clear difference in the scattering properties that in the end lead to the different lifetimes for the up- and down-electrons. The first one is based on the host material and it is related to a difference in the density of states at the Fermi level: if the DOS at the Fermi level was larger for, say, spin-down electrons, then the phase space of states to scatter into would be larger and result in a shorter lifetime. However, in MnSi, the DOS is very similar for up- and down-electrons (*cf.* Fig. 6.16) and this argument does not work. The second one is based on the scattering properties of the scatterer: if the states of the Fe-impurity are similar to the ones from the substituted Mn host-atom for one spin channel, then the electrons only feel the impurity weakly and have a longer lifetime. However, this case also does not apply in our situation, as the deviation between the DOS at the Mn and Fe site is similar for the two spin channels (see Fig. 6.16). Here again, the true scattering rates need to be computed to obtain the correct result and it is difficult to make a prediction from a density-of-states analysis.

We now include SOC with magnetization direction along [111] (central panel of

	$\mathrm{Fe}_x\mathrm{Mn}_{1-x}\mathrm{Si}$			$\mathrm{MnSi}_{1-x}\mathrm{Ge}_x$		
	τ_{p}	$\langle\tau^{\uparrow}\rangle$	$\langle\tau^{\downarrow}\rangle$	τ_{p}	$\langle\tau^{\uparrow}\rangle$	$\langle\tau^{\downarrow}\rangle$
no SOC	1560	1350	530	33400	16930	16460
$\vec{m} \parallel [001]$	1630	1270	560	34680	16810	17990
$\vec{m} \parallel [111]$	1570	990	640	35360	18700	16650

Table 6.3.: Momentum relaxation times in fs per at.% impurity concentration.

Fig. 6.15). There is still a clear distinction between the lifetimes of states with positive and negative spin expectation-value (*cf.* right panel of Fig. 6.15). However, in regions with large spin-mixing (but not only there) we get a large reduction (amplification) of lifetimes for the spin-up (spin-down) electrons due to spin-orbit coupling, as seen by the emergence of darker color code in the figure. This trend is also reflected in the averaged lifetimes, yielding values of 990 and 640 fs for spin-up and spin-down electrons, respectively (indicated by the arrows close to the color legend moving closer to each other). The reduction of lifetimes upon inclusion of SOC can be easily understood, because additional scattering channels to states of different spin character open up.

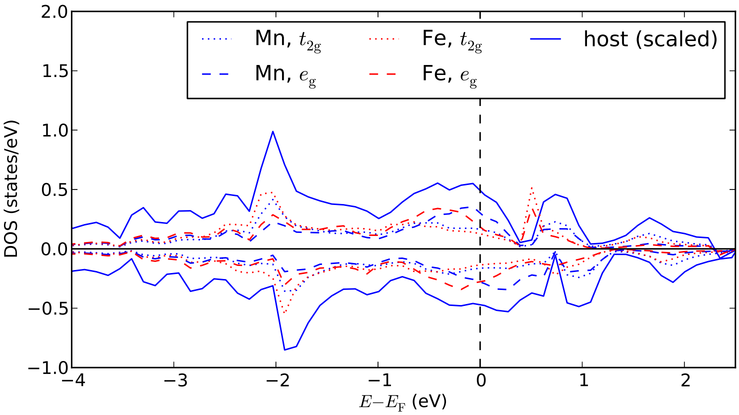

Figure 6.16.: Total DOS (solid lines, scaled down by a factor of 10) and local DOS at the Mn site of e_g and t_{2g}-states (blue dotted and dashed lines) for pure MnSi, as well as the local DOS for an Fe-impurity in MnSi (red dotted and dashed lines).

In Tab. 6.3, the lifetimes and spin-resolved lifetimes are summarized, also for the [001] magnetization-direction. The spin-resolved lifetimes depend stronger and may vary by up to 30% for the up-electrons. However, the total lifetimes only depend on the magnetization direction up to an anisotropy of about 5%, because the effects for up- and down-electrons have opposite sign (as mentioned above).

In Tab. 6.3 also lifetimes for the dilute alloy $\mathrm{MnSi}_{1-x}\mathrm{Ge}_x$ are presented. In general, they are much larger compared to Fe-impurities, because here the much weaker scattering off the Ge s-states leads to longer lifetimes (and consistently also to high conductivities, see below). The lifetimes for spin-up and -down electrons are now very similar to each other (only different by 3% instead of a factor 2.5 for Fe impurities), but the difference increases upon inclusion of spin-orbit coupling.

By comparison of the results for Fe and Ge impurities, we can conclude that the magnetic moment of the Fe impurities is responsible for the large deviation of spin-up and -down lifetimes.

6.3.6. Conductivities

Let us now turn to the calculation of the conductivity for the dilute alloy $\mathrm{Fe}_x\mathrm{Mn}_{1-x}\mathrm{Si}$ including spin-orbit coupling and with magnetization in the [001]-direction.

One problem that arises is the convergence of the Boltzmann equation: let us recall

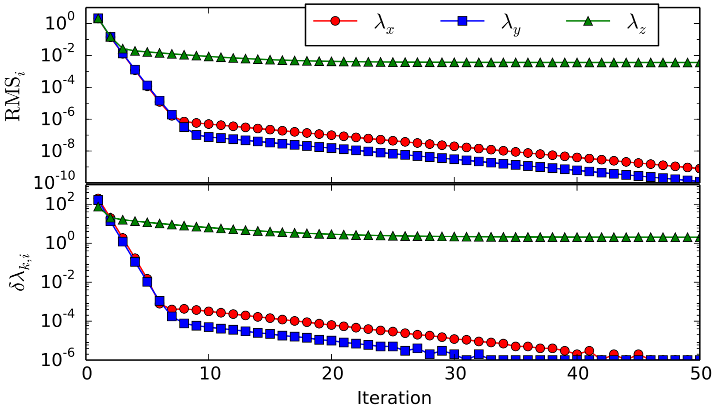

Figure 6.17.: Convergence problems for the mean free path. Top: Root mean square for the three Cartesian components of the mean-free path as function of the iteration number. Bottom: The change in the mean-free path from one iteration to the next for an arbitrarily chosen k-point. See text for details.

that the Boltzmann equation for the vector mean-free path is actually decoupled for the three spatial components (*cf.* Eq. (3.15)). This means we can solve the Boltzmann equation for each component separately, $\underline{\lambda}_x$, $\underline{\lambda}_y$ and $\underline{\lambda}_z$, where the underline denotes a vector in the index k. As it turns out, the x and y-components converge, and the z-component does not. This is illustrated in the top panel of Fig. 6.17, where the root mean square (RMS) as defined in Eq. (3.19) is plotted against the iteration number to solve the Boltzmann equation for each component. A very good numerical accuracy of 10^{-6} for the x- and y-component is already obtained after 10 iterations, whereas the RMS of $\underline{\lambda}_z$ is approaching a constant of about 10^{-2}. Two possibilities could lead to a non-vanishing RMS, either an oscillating (or precessing) vector $\underline{\lambda}_z$ (remember that the vector lives in the high-dimensional space spanned by the index $\vec{k}$), or a smooth drift of this vector. By looking at the difference in the mean-free path from one iteration the next path for a fixed (arbitrarily chosen) k-point, $\delta\lambda_{k,i} = \lambda^{(n+1)}_{\vec{k},i} - \lambda^{(n)}_{\vec{k},i}$, (see lower panel of Fig. 6.17), we observe that there is a nearly constant increase in the z-component of the mean free path for this k-point from one iteration to the next. We trace this problem back to a lacking symmetry along z-direction, which causes that the z-component of the sum of the Fermi velocity, $\sum_k v^z_{\vec{k}}$, does not vanish. In contrast, due to the 180°-rotation symmetry around the z-axis, the sum over the x- and y-components of the Fermi velocity vanishes.

Because of this problem, we only show the charge- and spin-conductivity tensor in the xy-subspace for magnetization direction along the [001]-direction (for an impurity-concentration of 1 at.%):

$$\begin{aligned}
\overset{\leftrightarrow}{\sigma}{}^{\mathrm{c}}_{[001]} &= \begin{pmatrix} 111.375 & 0.151 \\ 0.203 & 110.920 \end{pmatrix} \times 10^6 \ \mathrm{S/m} \\
\overset{\leftrightarrow}{\sigma}{}^{\mathrm{s}}_{[001]} &= \begin{pmatrix} 32.225 & 0.126 \\ 0.056 & 32.179 \end{pmatrix} \times 10^6 \ \mathrm{S/m}
\end{aligned}$$

we see that the off-diagonal components of charge and spin-conductivity are not anti-symmetric any more as compared to the simple crystal structures. More precisely, we have a symmetric and anti-symmetric component, *e.g.* for the charge conductivity

$$\sigma^{\mathrm{c,sym}}_{xy} = \left(\sigma^{\mathrm{c}}_{xy} + \sigma^{\mathrm{c}}_{yx}\right)/2 = 17.7 \times 10^4 \ \mathrm{S/m} \qquad \text{and} \tag{6.19}$$

$$\sigma^{\mathrm{c,asy}}_{xy} = \left(\sigma^{\mathrm{c}}_{xy} - \sigma^{\mathrm{c}}_{yx}\right)/2 = -2.6 \times 10^4 \ \mathrm{S/m} \ . \tag{6.20}$$

The anomalous and spin Hall conductivities correspond to the anti-symmetric component only. The symmetric component is a consequence of the low symmetry of the lattice. It is already present when we exclude spin-orbit coupling in the calculations, where we can converge all components of the vector mean free path and give the full conductivity tensor, due to the 24 symmetries in the BZ without SOC:

$$\overset{\leftrightarrow c}{\sigma}_{\text{noSOC}} = \begin{pmatrix} 117.025 & -0.010 & 0.011 \\ -0.010 & 117.025 & 0.002 \\ 0.011 & 0.002 & 117.025 \end{pmatrix} \times 10^6 \text{ S/m}$$

$$\overset{\leftrightarrow s}{\sigma}_{\text{noSOC}} = \begin{pmatrix} 42.979 & -0.010 & 0.011 \\ -0.010 & 42.979 & 0.002 \\ 0.011 & 0.002 & 42.979 \end{pmatrix} \times 10^6 \text{ S/m}$$

These tensors are symmetric (up to our numerical precision, which we estimate to be about 10^3 S/m). Comparing this result with the tensor in the xy-subspace of the calculation including SOC, we observe that SOC induces an anti-symmetric part of the both conductivity tensors, but also changes the symmetric part significantly: the sign is changed and the value increases by one order of magnitude.

Finally, we rotate the magnetization-direction into the crystallographic [111]-direction. In this case, we do not have the (non-symmorphic) symmetry S_z (*cf.* Eq. (6.16)), which enforces $\sum_k v_k^x = \sum_k v_k^y = 0$. Therefore, no component of the conductivity tensor converges in the coordinate system (xyz). However, for this chosen magnetization direction, a three-fold symmetry along the [111] axis is present and by choosing a rotated coordinate system spanned by the basis vectors

$$\vec{e}_1 = \frac{1}{\sqrt{2}} \begin{pmatrix} 1 \\ -1 \\ 0 \end{pmatrix}, \quad \vec{e}_2 = \frac{1}{\sqrt{6}} \begin{pmatrix} 1 \\ 1 \\ -2 \end{pmatrix}, \quad \vec{e}_3 = \frac{1}{\sqrt{3}} \begin{pmatrix} 1 \\ 1 \\ 1 \end{pmatrix}, \tag{6.21}$$

we can restore the symmetry $\sum_k \vec{v}_k \cdot \vec{e}_1 = \sum_k \vec{v}_k \cdot \vec{e}_2 = 0$ and only the component parallel to $\vec{e}_3$ does not converge. Then we can analyze the conductivity tensor in the subspace spanned by the vectors $\vec{e}_1$ and $\vec{e}_2$. Concretely, the tensor element σ_{12} corresponds to an applied electric field along the crystallographic direction $[11\bar{2}]$, and the resulting current is measured in the $[1\bar{1}0]$-direction.

The results are presented in Tab. 6.4, together with the previous reported values for the compound $\text{Fe}_x\text{Mn}_{1-x}\text{Si}$. We see a strong decrease of the longitudinal charge conductivity by 13% when rotating the magnetization direction from the [001] into the [111] direction (from 11.1×10^7 to 9.6×10^7 S/m). This effect is related to the anisotropic magneto-resistance (AMR), although we vary the direction of electric field and of the magnetization simultaneously, whereas in AMR experiments usually only the latter is varied through an external magnetic field.

Analyzing the anisotropy of the transverse charge conductivity, we observe that the symmetric and anti-symmetric (anomalous Hall) part depend strongly on the magnetization direction and vary by a factor of roughly 60 and 2, respectively.

	charge				spin			
	longitudinal		transverse		longitudinal		transverse	
	σ_{11}	σ_{22}	$\sigma_{12}^{\mathrm{sym}}$	$\sigma_{12}^{\mathrm{asy}}$	σ_{11}	σ_{22}	$\sigma_{12}^{\mathrm{sym}}$	$\sigma_{12}^{\mathrm{asy}}$
$\mathrm{Fe}_x\mathrm{Mn}_{1-x}\mathrm{Si}$								
no SOC	11.703	11.703	−1.0	0	4.298	4.298	−1.0	0
$\vec{m} \parallel [001]$	11.137	11.092	17.7	−2.6	3.223	3.218	9.1	3.5
$\vec{m} \parallel [111]$	9.640	9.648	−0.3	−4.1	1.057	1.066	−0.2	2.8
$\mathrm{MnSi}_{1-x}\mathrm{Ge}_x$								
no SOC	214.878	214.878	−0.3	0	−28.420	−28.420	0.2	0
$\vec{m} \parallel [001]$	214.523	213.452	318.7	13.5	−33.029	−34.246	59.3	−37.4
$\vec{m} \parallel [111]$	213.610	213.720	102.0	10.1	−16.585	−16.653	−137.3	62.7

Table 6.4.: Charge- and spin-conductivities for dilute alloys ($x = 1\,\mathrm{at.\%}$) based on MnSi in 10^7 S/m (for longitudinal components) and 10^4 S/m (for transverse components). Spin-orbit coupling was neglected (no SOC) or included in the calculation, for the latter case with magnetization $\vec{m}$ along two high-symmetry directions. The transverse component was decomposed into a symmetric and anti-symmetric part according to Eqs. (6.19) and (6.20). For the cases 'no SOC' and '$\vec{m} \parallel [001]$', the subscripts 1 and 2 stand for the x- and y-directions, respectively. For the case '$\vec{m} \parallel [111]$', 1 and 2 stand for the crystallographic directions $[1\bar{1}0]$ and $[11\bar{2}]$, respectively.

	charge		spin	
	α^{c}	$\mathcal{A}$	α^{s}	$\mathcal{A}$
$\mathrm{Fe}_x\mathrm{Mn}_{1-x}\mathrm{Si}$				
$\vec{m} \parallel [001]$	-2.3	80%	3.2	10%
$\vec{m} \parallel [111]$	-4.2		2.9	
$\mathrm{MnSi}_{1-x}\mathrm{Ge}_x$				
$\vec{m} \parallel [001]$	0.6	20%	-1.7	300%
$\vec{m} \parallel [111]$	0.5		2.9	

Table 6.5.: Anomalous and spin Hall angles (multiplied by a factor of 10^4) and its anisotropy with respect to the direction of magnetization.

The same statements as made for the charge conductivity are also valid for the spin-conductivity tensor. Finally, they also remain true for the other dilute alloy, $\mathrm{MnSi}_{1-x}\mathrm{Ge}_x$. However, scattering off the Ge impurities is much weaker and causes an overall increase of the conductivities by one order of magnitude.

Finally, in Tab. 6.5 we present the anomalous Hall angle $\alpha^{\mathrm{c}} = \sigma_{12}^{\mathrm{c,asy}}/\sigma_{11}^{\mathrm{c}}$ and spin Hall angle $\alpha^{\mathrm{s}} = \sigma_{12}^{\mathrm{s,asy}}/\sigma_{11}^{\mathrm{c}}$ for the different impurities and different magnetization directions. They are of the order of 10^{-4} and thus about one order of magnitude smaller than those of $3d$ impurities in bcc Fe. This confirms the assumption made in Ref. [21] that the intrinsic Berry-phase contribution to the anomalous Hall effect is the dominant mechanism in MnSi. Interestingly, the sign of the spin Hall angle in $\mathrm{MnSi}_{1-x}\mathrm{Ge}_x$ changes upon rotation of the magnetization direction, leading to a large anisotropy $\mathcal{A}$, defined similarly to the anisotropy of the spin-mixing parameter in Eq. (5.16). Contrary, the other Hall angles presented in Tab. 6.5 do not change sign upon rotation of the magnetization.

7 Skew-scattering off magnetic impurities in non-magnetic hosts

After having investigated the skew-scattering contribution and anomalous Hall effect in ferromagnetic hosts, we turn our attention to *magnetic* impurities in *non-magnetic* hosts. As hosts we chose the experimentally relevant materials Pd and Pt, which have the same valence configuration but differ in their spin-orbit coupling strength. Additionally, we choose Au as host metal, where mainly s electrons contribute to transport. Potential candidates for magnetic impurities in these hosts are the $3d$ transition metal atoms. The skew-scattering contribution is of particular importance for these systems, since the intrinsic contribution vanishes due to the presence of time-reversal symmetry for non-magnetic hosts.

7.1. $3d$ impurities in Pd

In this section, we analyze the anomalous Hall effect induced by magnetic $3d$ impurities in palladium (Pd). The paramagnetic material Pd is a special case, because it can create so called *giant moments*. This means, that a magnetic impurity embedded in the Pd host spin-polarizes the neighboring Pd atoms by a considerable amount not only for nearest neighbors, but for a larger number of shells around the impurity atom. The total spin magnetic moment associated with an impurity, which comprises the local spin moment at the impurity site and the spin moment associated with the whole spin-polarization cloud of the Pd host atoms around the impurity, can then reach very large values ($M^{\text{tot}} \approx 10\,\mu_{\text{B}}$, *cf.* [116]). This value exceeds the maximal possible spin moment of a single transition-metal impurity, which is by Hund's rule for single atoms limited to $5\,\mu_{\text{B}}$, by a factor 2.

7.1.1. Giant magnetic moments

Let us first describe the trend for the local spin moments of substitutional $3d$ impurities in Pd (Fig. 7.1a). The early transition metal impurities Sc, Ti and V turn out to be non-magnetic in Pd, whereas for Cr, Mn, Fe, Co and Ni impurities a finite

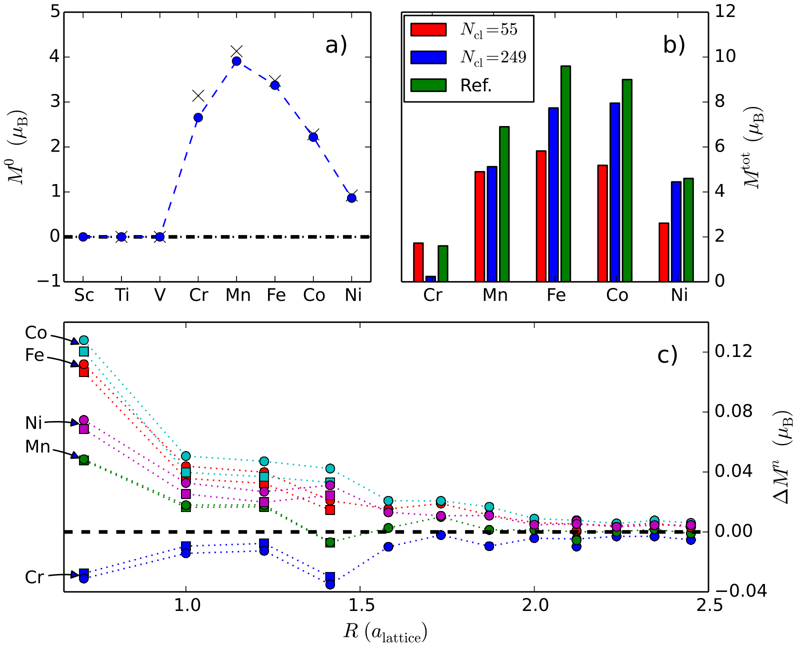

Figure 7.1.: Giant moments of impurities in Pd. (a) Local moments M^0 at the impurity site (circles) for substitutional impurities in Pd. As reference, the values given in [116] are also shown (crosses). (b) Giant moments M^{tot}, *i.e.* the magnetic moment of the whole impurity cluster including neighboring Pd atoms for two different cluster sizes. The estimates for an infinitely large impurity cluster from [116] are also shown. (c) Spin-polarization of the Pd host: Local moments M^n at the nth shell around the impurity atom versus the distance to the impurity center. Squares and circles correspond to calculations with cluster sizes of 55 ($n \leq 4$) and 249 atoms ($n \leq 13$), respectively. The induced spin-polarization of the Pd atoms decays only slowly with distance R to the impurity site.

moment is found. The largest local moment is reached for Mn (3.9 μ_B). Our data is consistent with previous first-principles calculations and experimental measurements [116]. In Fig. 7.1c the local spin moments of the neighboring Pd-host atoms (M^n for $n \geq 1$) as a function of the distance R to the impurity center are displayed. The Pd atoms around a Cr impurity couple antiferromagnetically to the Cr moment (blue curve in Fig. 7.1c), whereas the coupling between the Pd host and Fe, Co and Ni impurities, respectively, is ferromagnetic. The coupling between the Pd host and a Mn impurity is ferromagnetic for the first 3 shells, and the induced magnetic moment oscillates around zero for larger distances from the impurity center. The squares and dots in the figure correspond to calculations, where charge relaxations for an impurity cluster containing 55 atoms (corresponding to $n \leq 4$ nearest neighbor shells) and 249 atoms ($n \leq 13$), respectively, were taken into account. The local moments in the inner shells ($R < 1.5$) depend only weakly on the size of the cluster. This is also true for the local moments at the impurity site, M^0, which agree up to a relative accuracy of less than 0.1% (not shown).

However, the induced moments decay very slowly with distance to the impurity center. This leads to a large contribution of the polarization cloud to the total moment $M^{\text{tot}} = \sum_{n=0}^{N} M^n$, and also to a strong dependence of M^{tot} on the cluster size. This dependence is illustrated in Fig. 7.1b by red and blue bars for the two cluster sizes. Additionally, the values for an infinitely large impurity cluster from Ref. [116] are shown in green. In fact, these values were estimated from a 43 cluster-atoms calculation and applying a scaling technique to infinitely large clusters. It is evident that truncating the impurity cluster leads to a considerable error in the total moments, and it is questionable how this truncation influences the transport properties such as the anomalous Hall angles. This point will be also addressed in the next sub-section (see Tab. 7.1).

7.1.2. Conductivities

The values for the transport properties of Pd due to scattering off magnetic and non-magnetic $3d$ impurities are presented in Tab. 7.1 and illustrated in Fig. 7.2. Let us first compare the spin-relaxation and momentum relaxation times: they follow the same trend as expected from the Elliott approximation, which relates the two quantities, $\tau/T_1 \approx 4\langle b^2 \rangle = \text{const}$ (*cf.* chapter 5). Here, the spin-relaxation times are about 20 times larger than the momentum relaxation times. The k-resolved values for τ_{p} and T_1 are displayed in Fig. 7.3.

The longitudinal charge conductivity σ^{c}_{xx} and the momentum relaxation time τ_{p} also follow the same chemical trend, yielding a strong argument for the so-called relaxation time approximation to be valid for longitudinal transport in Pd. As outlined by Mertig [62], this approximation holds when the anti-symmetric part of the scattering matrix $P_{k,k'}$ is small, and then the mean free path can be approximated by $\vec{\lambda}_{\vec{k}} \approx \vec{v}_{\vec{k}}\, \tau_{\text{p}}$ in the solution of the Boltzmann equation. Two maxima in the conductivity at Mn and Ni can be identified when going through the $3d$ series. Thus, Mn and Ni impurities act as weak scatterers in Pd. For Ni impurities, this is also expected, because it is iso-electronic to Pd (meaning that they have the same number of valence electrons). The alternating behavior between weak and strong scattering has already been discussed in the context of $3d$ impurities in a Cu host [117]: the impurity d-states shift through the Fermi energy when going across the $3d$ series, leading to strong scattering. The up- and down-states are exchange-split due to the magnetic moment, leading to enhanced scattering (meaning low conductivity) at two different

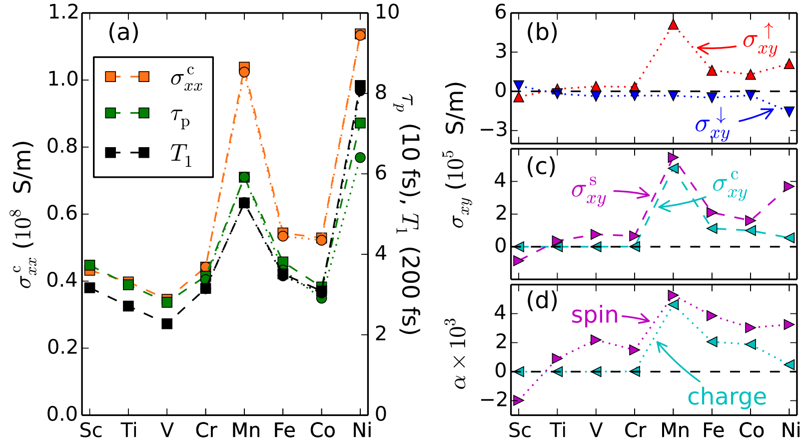

Figure 7.2.: Transport properties of Pd due to scattering off $3d$ impurities. (a) Longitudinal charge conductivity σ^{c}_{xx} (orange symbols), momentum relaxation time τ_{p} (green) and spin relaxation time T_1 (black) for an impurity concentration of 1 at.%. Note the different scaling for τ_{p} and T_1. Changing the size of the impurity cluster from 55 atoms (squares) to 249 (circles) does not have a big influence on the data (only calculated for the magnetic impurities Cr-Ni). (b-c): Transverse charge (spin) conductivity $\sigma^{\mathrm{c(s)}}_{xy}$ as defined by Eq. (3.23), as well as their decomposition into spin-up and spin-down contributions $\sigma^{\uparrow(\downarrow)}_{xy}$. (d) Anomalous Hall angle $\alpha^{\mathrm{c}} = \sigma^{\mathrm{c}}_{xy}/\sigma^{\mathrm{c}}_{xx}$ (denoted by charge) and spin Hall angle $\alpha^{\mathrm{s}} = \sigma^{\mathrm{s}}_{xy}/\sigma^{\mathrm{c}}_{xx}$ (spin). All lines are guides to the eye.

positions in the series. However, for our case of a Pd host the situation is more complicated, because of the more complicated electronic structure compared to the free electron-like host in Cu.

Having discussed the trend for the longitudinal conductivity, which can be well described by the symmetric part of the scattering matrix, we turn to the transverse components of charge and spin conductivity, where the anti-symmetric part is crucial [37] and the full Boltzmann equation has to be solved. The transverse charge and spin conductivities, σ^{c}_{xy} and σ^{s}_{xy}, respectively, and the resulting Hall angles are shown in panels (c) and (d) of Fig. 7.2. The anomalous Hall angle α^{c} represents the efficiency of generating a transverse charge flow. The direction of this charge flow is perpendicular to both, the direction of the driving electric field and the magnetization direction. The same symmetry considerations hold for the spin conductivity, standing for the flow of spin angular momentum instead of charge, and the spin Hall angle α^{s} is a figure of merit for converting a charge current (in the longitudinal direction) into a

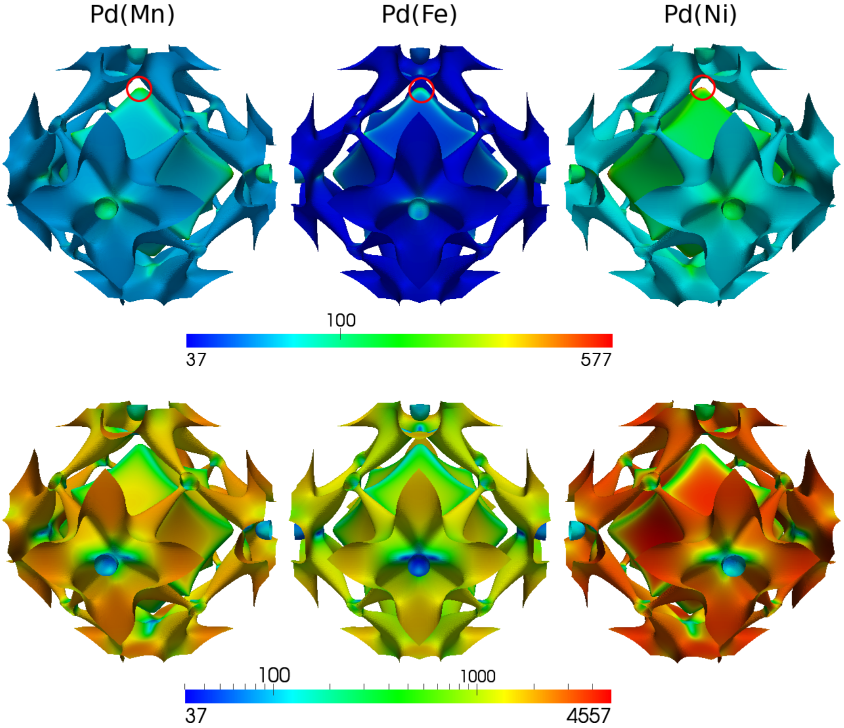

Figure 7.3.: k-resolved spin-conserving relaxation time ($\tau^{sc}_{\vec{k}}$, top row) and spin-relaxation time ($T_{1\vec{k}}$, bottom row) for Mn, Fe and Ni impurities in Pd, respectively. Note that a logarithmic color scale is used. The circles denote the points of strongly enhanced $\tau^{sc}_{\vec{k}}$.

spin current (in the transverse direction).

Let us first comment on the non-magnetic, early impurities of the $3d$ series (Sc, Ti and V): the transverse charge conductivity σ^{c}_{xy} vanishes due to the preservation of time-reversal symmetry. In contrast, the transverse spin conductivity is finite and changes the sign from Sc to Ti.

For the magnetic impurities (Cr to Ni), the chemical trend between the charge and spin conductivities (and consequently also for the anomalous and spin Hall angles) clearly resemble each other, except for Ni impurities. For all magnetic $3d$-impurities in Pd, the transverse charge conductivity is smaller than the accompanied spin-conductivity.

By employing the two-current model, and we can extract a separate conductivity for up- and down-electrons according to Eqs. (6.1) and (6.2). This decomposition of the

Imp.	N_{cls}	τ_{p}	T_1	σ^{c}_{xx}	σ^{c}_{xy}	σ^{s}_{xy}	α^{c}	α^{s}
		(fs)		(10^8 S/m)	(10^5 S/m)		(10^{-3})	
Sc	55	37.3	634	0.432	0	-0.856	0	-1.979
Ti	55	32.4	543	0.397	0	0.360	0	0.907
V	55	28.1	455	0.346	0	0.756	0	2.188
Cr	55	34.6	630	0.442	0.009	0.661	0.020	1.496
	249	33.7	629	0.442	0.008	0.667	0.018	1.508
Mn	55	59.2	1056	1.038	4.804	5.471	4.627	5.270
	249	59.2	1058	1.024	4.649	5.322	4.542	5.200
Fe	55	38.1	702	0.544	1.120	2.097	2.060	3.858
	249	36.1	693	0.534	1.099	2.047	2.057	3.833
Co	55	31.9	617	0.529	0.994	1.602	1.879	3.030
	249	29.1	608	0.522	0.986	1.575	1.889	3.017
Ni	55	72.6	1639	1.138	0.544	3.696	0.478	3.248
	249	64.1	1613	1.133	0.564	3.616	0.498	3.191

Table 7.1.: Transport parameters for impurities in Pd. Presented are the momentum (τ_{p}) and spin-relaxation times (T_1), the longitudinal charge conductivity (σ^{c}_{xx}), the transverse charge and spin conductivity ($\sigma^{\mathrm{c/s}}_{xy}$) and the anomalous and spin Hall angles ($\alpha^{\mathrm{c/s}}$). The results for the magnetic impurities have been calculated with two different cluster sizes (N_{cls} is the number of atoms in the impurity cluster). All values are given at an impurity concentration of 1 at.%.

data presented in Fig. 7.2c leads to different signs of $\sigma^{\uparrow}_{xy}$ and $\sigma^{\downarrow}_{xy}$ (*cf.* Fig. 7.2b) for all considered impurities in Pd, meaning that on average the up- and down-electrons scatter to opposite directions. This presents a different view on the previously made observation, that the transverse spin conductivity is always larger than the charge conductivity.

Moreover, the chemical trend of the total transverse conductivity $\sigma^{\mathrm{c/s}}_{xy}$ is determined by $\sigma^{\uparrow}_{xy}$, whereas $\sigma^{\downarrow}_{xy}$ is constantly small across the different impurities, only being enhanced for Ni.

Let us try to relate this trend to the density of states at the impurity site (see Fig. 7.4).

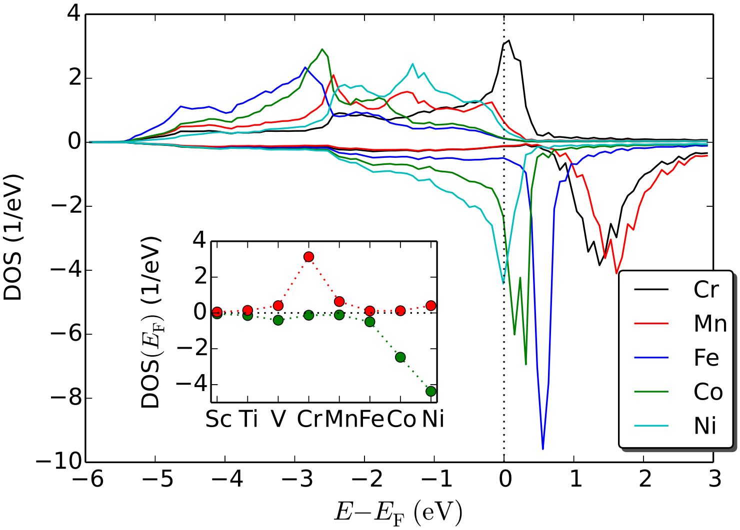

Figure 7.4.: Spin-resolved density of states (DOS) for the d-states at the impurity site for magnetic $3d$ impurities in Pd. The inset shows the DOS at the Fermi level, red for spin-up and green for spin-down.

We observe that spin-down DOS is peaked at the Fermi level for Ni impurities. However, this cannot be the only reason for a large transverse spin-down conductivity, because also the spin-down states of Co or the spin-up states of Cr have an enhanced DOS at the Fermi level (see inset of Fig. 7.4) without a corresponding characteristic in the spin-resolved transverse conductivities $\sigma_{xy}^{\uparrow(\downarrow)}$. The effect is more subtle and details of the electronic structure matter, as already shown by phase shift models for the pure spin Hall effect in Cu [41, 118].

Among the magnetic impurities in Pd, the lowest values for both, the anomalous and spin Hall angles are obtained for Cr impurities. Interestingly, α^{c} and σ_{xy}^{c} nearly vanish for this specific system although time-reversal symmetry is broken due to the finite magnetic moment of the Cr impurity. This is due to an (accidental) compensation of $\sigma_{xy}^{\uparrow}$ and $\sigma_{xy}^{\downarrow}$. It means that a pure spin-current can be generated in this system and the direction of spin-flow could be switched by the direction of the magnetic moment (adjustable by an external magnetic field). The fact that the intrinsic contribution to the charge conductivity vanishes due to the time-reversal symmetry of the non-magnetic host enhances the importance of the skew-scattering in this system. Additionally, in the dilute limit, the skew-scattering contribution dominates over the side-jump contribution.

The overall chemical trend of $\sigma_{xy}^{\mathrm{c/s}}$ on the one hand and σ_{xx}^{c} on the other resemble each other. This is at first sight counter-intuitive, because one would assume that a strong scattering is needed for a large transverse conductivity, and thus the longitudinal conductivity would be small. However, it is only the *asymmetry* of scattering (induced by spin-orbit coupling), that leads to a large transverse component. Thus, the situation is again more complicated than the naive picture.

We now comment on the sensitivity of our data to the aforementioned cluster size (*cf.* left panel of Fig. 7.2 and Tab. 7.1). The dependence of the transport properties is only very small. Bearing in mind that the magnetic impurities in Pd generally form giant moments, we can deduce that the actual size of the (induced) host magnetic moments does not influence the transport values significantly.

	Fe	Co	Ni
this work	2.1	1.9	0.5
Refs. [119, 120]	2.7	2.1	−2.0

Table 7.2.: Comparison of the anomalous Hall angle α^{c} (multiplied by a factor 10^3) of Fe, Co and Ni impurities in Pd to reference values.

Let us finally compare some of the results to calculations by other authors: values for the transverse charge conductivity σ_{xy}^{c} have been obtained for Fe, Co and Ni impurities in Pd [104, 119, 120]. Our values of Fe and Co impurities in Pd agree nicely to the reference values, but for Ni in Pd different signs for σ_{xy}^{c} are obtained. This is also reflected in the anomalous Hall angles presented in Tab. 7.2. This might be again related to the peaked spin-down density of states of the Ni impurity around the Fermi level: small changes in the position of the peak due to a different treatment of relativistic effects or different shape approximations to the potential may induce such a change of sign for α^{c}.

7.2. $3d$ impurities in Au

Let us now turn to $3d$ impurities in a Au host. The impurities from V to Co are magnetic, whereas the commonly magnetic impurity Ni turns out to be non-magnetic in Au. Also the early transition metal impurities Sc and Ti are non-magnetic (*cf.* Fig. 7.5). The values of the local spin moments are in a good agreement to the literature [121]. For magnetic impurities, the induced moments at the nearest-neighbor Au atoms are already very small (smaller than $0.02\,\mu_{\mathrm{B}}$) and decay quickly with increasing distance to the impurity atom. The impurity cluster was chosen to comprise nearest and next-nearest neighbors throughout the calculation (corresponding to a 19 atoms in the impurity cluster).

Next, we describe the transport properties caused by scattering off impurities, which are presented in Fig. 7.6 and Tab. 7.3. Also for the Au host, we again get a nice agreement between the chemical trends for the longitudinal conductivity σ^{c}_{xx}, the momentum relaxation time τ_{p} and the spin relaxation time T_1. The ratio between spin and momentum relaxation times is smaller than in Pd due to the slightly higher spin-mixing parameter of the Au host ($\langle b^2_{\tilde{s}} \rangle = 2.68 \times 10^{-2}$ for Au compared to 1.87×10^{-2} for Pd). Similarly to the impurities in Pd, an enhanced longitudinal conductivity for Ni and Mn impurities in Au can be observed. Interestingly, the values of σ^{c}_{xx} range from 0.08×10^{8} S/m for Ti-doped Au to 2.8×10^{8} S/m for Ni-doped Au (at impurity concentrations of 1 at%). This is a deviation by a factor of approximately 30, whereas the same analysis for the Pd host yields only a factor of 3.

Let us now turn to the transverse transport properties and describe the spin-resolved

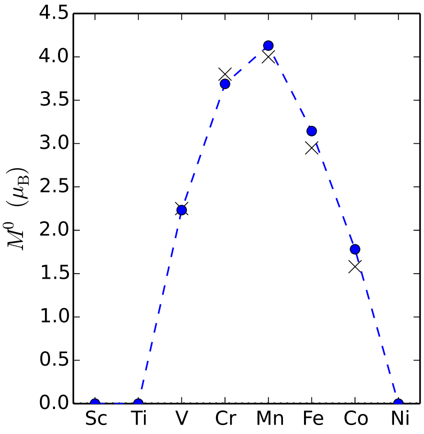

Figure 7.5.: Calculated magnetic moments of impurities in Au (circles). The agreement to previous calculations [121] (crosses) is very good.

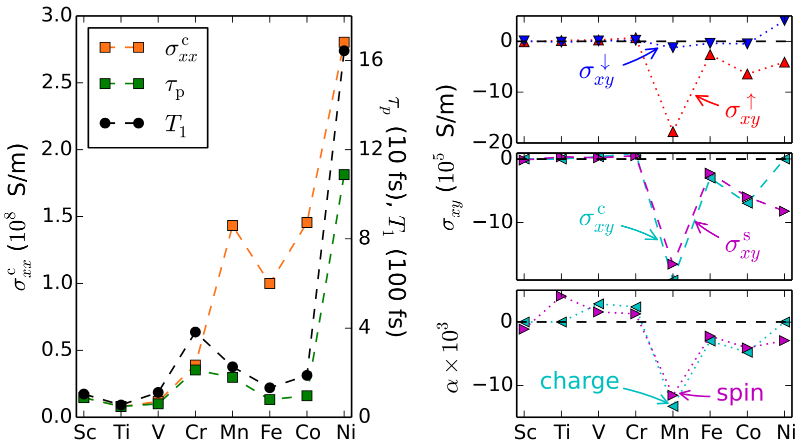

Figure 7.6.: Transport properties of Au due to scattering off 3*d* impurities. Left panel: longitudinal charge conductivity σ^{c}_{xx} (orange), momentum relaxation time τ_{p} (green) and spin relaxation time T_1 (black) for an impurity concentration. Right panels: transverse charge (spin) conductivity $\sigma^{\mathrm{c(s)}}_{xy}$, their decomposition into spin-up and spin-down contributions $\sigma^{\uparrow(\downarrow)}_{xy}$, as well as the anomalous and spin Hall angles $\alpha^{\mathrm{c/s}}$ (denoted by charge and spin, respectively). All values are given at an impurity concentration of 1 at.%.

conductivities, $\sigma^{\uparrow(\downarrow)}_{xy}$. Again, we can draw some analogies to the Pd host:

1. the conductivity of the spin-down channel is small in magnitude and only enhanced for Ni,
2. the conductivity of the spin-up channel is larger in magnitude and determines the trend of the transverse charge and spin-conductivity $\sigma^{\mathrm{c/s}}_{xy}$,
3. the conductivity of the spin-up channel is peaked for Mn impurities.

However, there are also important differences compared to the Pd host: first of all, the sign of the dominant contribution, $\sigma^{\uparrow}_{xy}$ is now negative for the late 3*d* impurities (Mn-Ni) in Au. Secondly, the two contributions $\sigma^{\uparrow(\downarrow)}_{xy}$ are of the same sign for all magnetic 3*d* impurities. This causes the charge conductivity σ^{c}_{xy} to be a bit larger in magnitude than the spin-conductivity σ^{s}_{xy} for the magnetic impurities (V-Co). In contrast, the preserved time-reversal symmetry in the systems with non-magnetic impurities forces the two contributions to be of different sign and same magnitude (Sc, Ti and Ni), so that the charge conductivity vanishes and we obtain a pure spin current.

		τ_p	T_1	σ^c_{xx}	σ^c_{xy}	σ^s_{xy}	α^c	α^s
		(fs)		(10^8 S/m)	(10^5 S/m)		(10^{-3})	
Sc	scSOC	8.8	104	0.147	0	−0.165	0	−1.121
Ti	scSOC	4.8	55	0.080	0	0.326	0	4.077
V	scSOC	6.0	111	0.118	0.336	0.186	2.858	1.584
	1-shot	6.1	107	0.120	0.327	0.177	2.725	1.473
Cr	scSOC	21.2	382	0.391	0.929	0.503	2.377	1.287
	1-shot	21.8	377	0.391	0.896	0.514	2.291	1.313
Mn	scSOC	17.9	226	1.432	−19.018	−16.514	−13.279	−11.531
	1-shot	17.6	216	1.357	−16.617	−14.126	−12.248	−10.412
Fe	scSOC	7.9	132	0.999	−2.994	−2.215	−2.995	−2.217
	1-shot	8.0	128	0.971	−2.419	−1.646	−2.492	−1.695
Co	scSOC	9.6	188	1.455	−6.938	−5.934	−4.769	−4.079
	1-shot	9.2	170	1.387	−5.606	−4.648	−4.041	−3.350
Ni	scSOC	108.8	1644	2.803	0	−8.193	0	−2.922

Table 7.3.: Transport values for impurities in Au. Presented are the momentum (τ_p) and spin-relaxation times (T_1), the longitudinal charge conductivity (σ^c_{xx}), the transverse charge and spin conductivity ($\sigma^\mathrm{c/s}_{xy}$) and the anomalous and spin Hall angles ($\alpha^\mathrm{c/s}$). The results for the magnetic impurities have been calculated by taking spin-orbit coupling self-consistently into account (scSOC) or only in the last iteration (1-shot). All values are given at an impurity concentration of 1 at.%.

We also calculated the transverse transport conductivities neglecting the spin-orbit coupling term in the convergence of the host and impurity potentials, and only included SOC in the last iteration when calculating the Fermi surface and transport properties (1-shot). This, however, only gives minor deviations in the transport quantities (*cf.* Tab. 7.3).

7.3. $3d$ and other impurities in Pt

An analysis of the local magnetic moments of $3d$ impurities in Pt (*cf.* Fig. 7.7) reveals the same trend as in Pd: the early $3d$ impurities (Sc-V) are non-magnetic, whereas the late $3d$ impurities (Cr-Ni) exhibit a magnetic moment. The spin-polarization on the nearest neighbor Pt atoms is only small (smaller than $0.1\,\mu_\mathrm{B}$) and decays quickly (approx. $0.01\,\mu_\mathrm{B}$ for the next-nearest neighbors). Again, the impurity cluster was truncated after the next-nearest neighbors, resulting in a cluster size of 19 atoms.

Let us analyze the transport properties presented in Fig. 7.8. The quantities shown in the left panel follow the same trend, as is expected. The trend for the longitudinal conductivity exhibits the same features as in the Pd or Au hosts, respectively: σ^{c}_{xx} is strongly enhanced for Ni impurities, and a peak can be seen in the middle of the series (around Cr and Mn in this case). Interestingly, the longitudinal conductivity is not enhanced for Cr impurities in Pd and Au, respectively.

For the transverse conductivity, here the same statements as in the comparison between the Pd and Au hosts can be made: (i) the conductivity in the spin-down channel is suppressed (except for Ni), (ii) the spin-up channel determines the trend for the charge and spin-conductivity, and (iii) a peak in the up-channel is obtained for Mn-impurities.

Focusing on the spin Hall angle, the same overall trend as for $3d$ impurities in Pd is obtained. An exception is the negative value for Cr impurities. But apart from this deviation, the trend is the same, including the sign change from Sc to Ti, and local maxima at V and Mn. In contrast, the anomalous Hall angle seems to deviate more

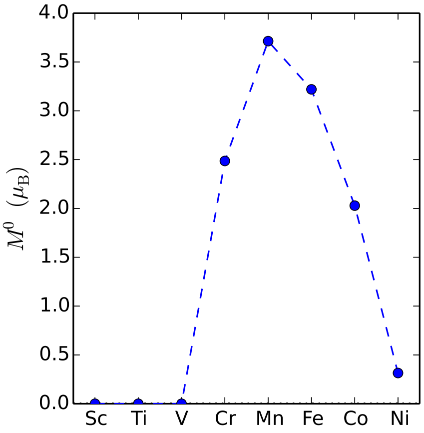

Figure 7.7.: Magnetic moments of impurities in Pt.

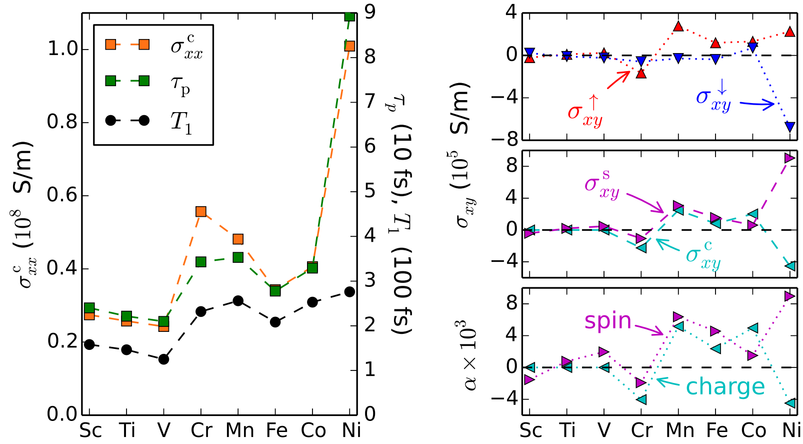

Figure 7.8.: Transport properties of Pt due to scattering off $3d$ impurities. Left panel: longitudinal charge conductivity σ^{c}_{xx} (orange), momentum relaxation time τ_{p} (green) and spin relaxation time T_1 (black) for an impurity concentration. Right panels: transverse charge (spin) conductivity $\sigma^{\mathrm{c(s)}}_{xy}$, their decomposition into spin-up and spin-down contributions $\sigma^{\uparrow(\downarrow)}_{xy}$, as well as the anomalous and spin Hall angles $\alpha^{\mathrm{c/s}}$ (denoted by charge and spin, respectively). All values are given at an impurity concentration of 1 at.%.

between the two hosts.

The similarities between Pd and Pt, respectively, may be attributed to the iso-electronic configuration of the two hosts. Although the Pt host exhibits a stronger spin-orbit coupling than Pd, the Hall angles are of similar magnitude, which shows that the character of the states is at least as important as a large difference in spin-orbit coupling.

Finally, we also calculated the heavy impurity atoms Os and Ir in Pt, and find only intermediate values for the spin Hall angle (*cf.* Tab. 7.4).

	τ_p	T_1	σ^c_{xx}	σ^c_{xy}	σ^s_{xy}	α^c	α^s
	(fs)		(10^8 S/m)	(10^5 S/m)		(10^{-3})	
Sc	24.0	158	0.274	0	-0.420	0	-1.531
Ti	22.2	146	0.257	0	0.199	0	0.773
V	21.0	125	0.243	0	0.474	0	1.955
Cr	34.3	232	0.557	-2.251	-1.067	-4.042	-1.916
Mn	35.3	256	0.482	2.485	3.068	5.160	6.371
Fe	27.8	208	0.343	0.810	1.567	2.359	4.568
Co	32.9	253	0.406	2.015	0.613	4.962	1.508
Ni	89.3	276	1.009	-4.526	9.049	-4.484	8.964
Os	22.5	149	0.251	0	0.337	0	1.342
Ir	57.7	427	0.630	0	0.061	0	0.097

Table 7.4.: Transport properties for impurities in Pt. Presented are the momentum- (τ_p) and spin-relaxation times (T_1), the longitudinal charge conductivity (σ^c_{xx}), the transverse charge and spin conductivity ($\sigma^\mathrm{c/s}_{xy}$) and the anomalous and spin Hall angles ($\alpha^\mathrm{c/s}$).

8 Spin Hall effect

In this chapter, we calculate the skew-scattering contribution to the spin Hall effect for $4d/5sp$ impurities (Y-Cd, from this point on simply called $4d$ impurities) and $5d/6sp$ impurities (Lu-Pb, simply referred to as $5d$ impurities). As hosts we chose the cubic material fcc-Ir and the uniaxial crystal hcp-Re, which have similar spin-orbit coupling strength but differ in their crystal structure.

The mechanisms behind the spin Hall effect are very similar to the one creating the anomalous Hall effect. The extrinsic skew-scattering contribution to the spin Hall effect has been already calculated by Gradhand *et al.* for impurities in a Cu and Au host [37]. Since then, many theoretical [38–41, 118, 122] studies have investigated the skew-scattering contribution to the spin Hall, mostly in Cu or Au hosts.

8.1. Spin Hall effect in fcc Ir

The spin Hall angles for the Ir host are presented in Fig. 8.1. At the beginning of the $4d$ series, the SHA shows a monotonous increase from Y to Tc. At the end of the series, the SHA decreases monotonously from Pd to Cd. Stronger variations occur for the impurities in the middle of the series, *i.e.* Ru, Rh and Pd. This might come from the fact, that Rh is iso-electronic to Ir, which results in weaker scattering and thus larger conductivities (both, longitudinal and transverse). For the series of $4d$ impurities in Ir, this scaling is a bit larger for skew-scattering than for longitudinal scattering and results in a maximum of the Hall angles in the middle of the series. However, relatively high spin Hall angles are observed for all $4d$ impurities, reaching up to 0.8% for Pd impurities. On the other hand, the magnitude of the SHE for $5d$ impurities is much lower. This can be attributed to the fact, that $5d$ impurities and the host atoms have comparable spin-orbit coupling (SOC) strength. Additionally, now the maxima of the Hall angles are obtained at the beginning and the end of the series. In between, the SHA changes sign twice and is minimal for Os impurities, being in the periodic table next to Ir.

Having observed the trend of increasing magnitude of the spin Hall angles from $5d$ to $4d$ elements, an interesting question is, whether the spin Hall angles increases even

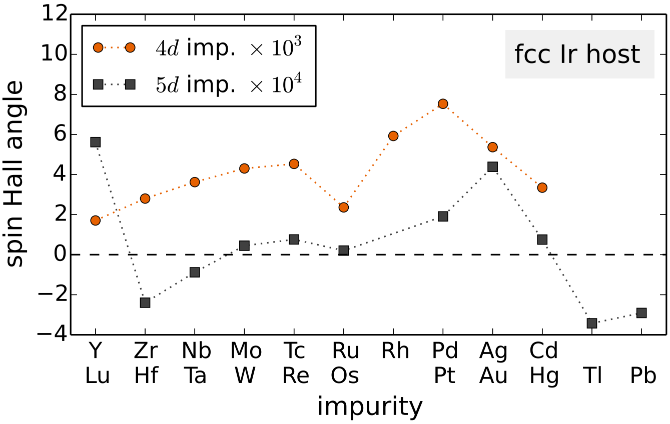

Figure 8.1.: Spin Hall angle due to skew-scattering off $4d$ impurities (orange circles) and $5d$ impurities (gray squares) in Ir. The spin Hall angle is computed as $\alpha^{\mathrm{s}} = \sigma^{\mathrm{s}}_{xy}/\sigma^{\mathrm{c}}_{xx}$ and with spin-quantization axis along z.

more for the even lighter $3d$ impurities. However, most of the $3d$ impurities will develop a magnetic moment, and thus also lead to an anomalous Hall effect. Due to the limited computational resources available, we leave this task for a later study and turn instead to another host material, the uniaxial crystal hcp-Re.

8.2. Anisotropic Spin Hall effect in hcp Re

For uniaxial crystals, an anisotropy of the spin Hall effect can be expected as was first pointed out by Freimuth *et al.* and explicitly calculated for the intrinsic contribution [93, 123]. According to his definition, we introduce the elements of the spin-conductivity tensor

$$\sigma^{i}_{jk} \equiv \sigma^{\mathrm{spin}}_{jk}(\hat{s} = \hat{e}_i) \tag{8.1}$$

with our usual definition of the spin-conductivity tensor $\overset{\leftrightarrow}{\sigma}^{\mathrm{spin}}$ (see Eq. (3.23)) and choose the spin-quantization axis $\hat{s}$ along the Cartesian direction $\hat{e}_i$.

We find three non-vanishing and distinct elements for the spin-conductivity. Three more non-vanishing matrix elements are related to the previous ones by

$$\begin{aligned} \sigma^{x}_{yz} &= -\sigma^{y}_{xz}\,, && (8.2)\\ \sigma^{y}_{zx} &= -\sigma^{x}_{zy}\,, && (8.3)\\ \sigma^{z}_{xy} &= -\sigma^{z}_{yx}\,. && (8.4) \end{aligned}$$

This also implies that $\sigma^x_{yz} \neq -\sigma^x_{zy}$, which is different from the symmetries present for the intrinsic contribution [123], where only two independent tensor elements exist.

The results for $4d$ impurities are presented in Fig. 8.2. The components of σ^x_{yz} and σ^y_{zx} (compare the red and green bars in the upper panel) are clearly distinct from each other. This is surprising, because other spin-orbit related phenomena (such as the spin-mixing parameter, *cf.* chapter 5 and Fig. 5.4f) show a very small anisotropy

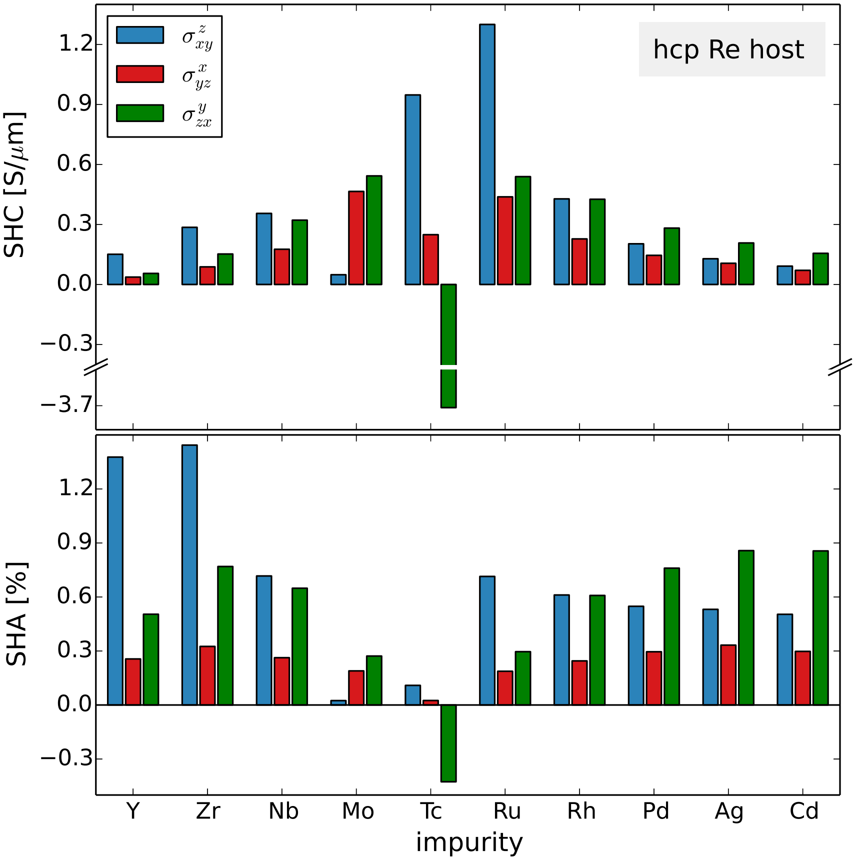

Figure 8.2.: Spin Hall conductivity (top panel) and spin Hall angle (lower panel) due to skew-scattering off $4d$ impurities in hcp-Re. The spin Hall effect is anisotropic with respect to the direction of the spin-quantization axis. The values for the conductivity are given at an impurity concentration of 1 at.%.

within the *ab*-plane. Moreover, the difference between these two tensor elements with spin-polarization within the *ab*-plane can be even larger than the tensor element with out-of-plane spin-polarization, σ^z_{xy}, (blue bar in the figure). Examples for this case are Nb or Rh impurities in hcp Re.

Our calculations reveal a gigantic anisotropy of the spin Hall conductivity for impurities in the middle of the $4d$ series (*i.e.* Mo, Tc and Ru). Note again, that Tc is iso-electronic to Re. Thus it is not surprising, that the overall magnitude of the transverse conductivities is largest for these elements, but it is surprising that also the anisotropies are the largest for these elements.

The spin Hall angles for $4d$ impurities (see lower panel of Fig. 8.2), which are defined as $\sigma^i_{jk}/\sigma^{\text{charge}}_{kk}$, are largest at the beginning and the end of the $4d$ series, and can be as large as 1.2% for Y and Zr impurities. This inversion of the trend compared to the transverse conductivities is again related to the fact, that the longitudinal conductivities are strongly peaked for Tc impurities and monotonously decrease when going outwards in the $4d$ series because the scattering increases. The skew-scattering grows weaker than the longitudinal scattering and thus the Hall angles are smallest in the middle of the series, where the values are dominated by the denominator. This stands in contrast to $4d$ impurities in Ir and it is more similar to $5d$ impurities in Ir.

However, the anisotropies remain large also for the spin Hall angles, because the longitudinal charge conductivities ($\sigma^{\text{charge}}_{xx} = \sigma^{\text{charge}}_{yy} \neq \sigma^{\text{charge}}_{zz}$) entering the denominator follow the same trend. In fact, the ratio $\sigma^{\text{charge}}_{zz}/\sigma^{\text{charge}}_{xx}$ is relatively constant across the series of impurities and ranges between 1.1 and 1.5, thus the component of longitudinal conductivity along the *c*-axis is always larger than the one within *ab*-plane. This even increases the anisotropy of the spin Hall angle as compared to the transverse conductivities when σ^x_{yz} is smallest in magnitude, *e.g.* for Pd or Ag impurities.

We now turn to $5d$ impurities in hcp Re (*cf.* 8.3). Also here, the transverse spin conductivities (see the top panel of Fig. 8.3) exhibit relatively large anisotropies across the whole series. Now the values are not peaked in the middle of the series. This leads to small spin Hall angles (*cf.* lower panel) for the impurities next to Re in the periodic table (W and Os), because also here the longitudinal conductivities are strongly enhanced. The SHA is largest at the beginning and the end of the series, with an angle for Lu impurities as large as 1.5% for spin-polarization along the *c*-axis of the hcp crystal.

Contrary to the Ir host, here the SHA for $5d$ impurities can reach values as large as for $4d$ impurities, although the host atoms and impurity atoms have similar spin-orbit coupling strength.

This leaves us with the conclusion, that the spin Hall effect in heavy non-magnetic hosts exhibits interesting trends and anomalies when changing either the impurity or the host. It seems to be a subtle interplay between host states, impurity states, their spin-orbit coupling strength and hybridization. A deeper analysis in these terms is, however, complicated and not straightforward, but would bring more insight into the

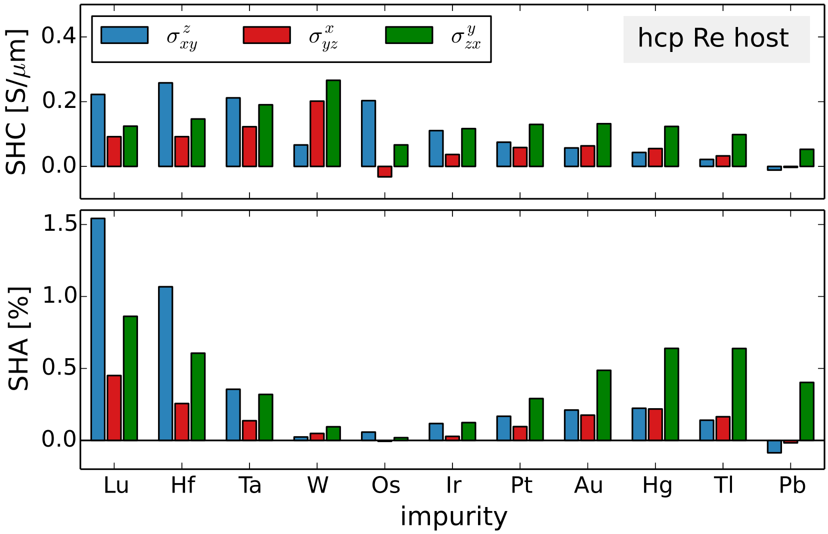

Figure 8.3.: Same as Fig. 8.2 for $5d$ impurities in hcp-Re.

mechanism behind the skew-scattering.

8.3. Validity of the optical theorem

Finally, we want to address an important issue encountered in the calculation of the result presented in the previous sections of this chapter. As explained in chapter 2 (section 2.7), the optical theorem serves as good indicator to test (a) mistakes in the code and (b) whether the chosen cutoff parameters are high enough. It is extremely sensitive and a relative deviation from the left hand side to the right hand side of Eq. (2.151) of the order of a few percent can be considered as reasonably good. If a mistake is present, the two sides of the optical theorem will usually differ by orders of magnitude.

In Fig. 8.4 we show the deviations of the optical theorem for various impurities in the two hosts under consideration. The optical theorem is very well fulfilled for $5d$ impurities in the two hosts (less than 1% deviation, see lower panel of Fig. 8.4). However, for $4d$ impurities the deviations in the optical theorem are generally larger for the two hosts, reaching up to about 25% for Ru and Rh impurities in fcc Ir. The agreement is not perfect, but a mistake in the code can be also excluded. Remarkable is the clear distinction of the quality of the optical theorem between the $4d$ impurities

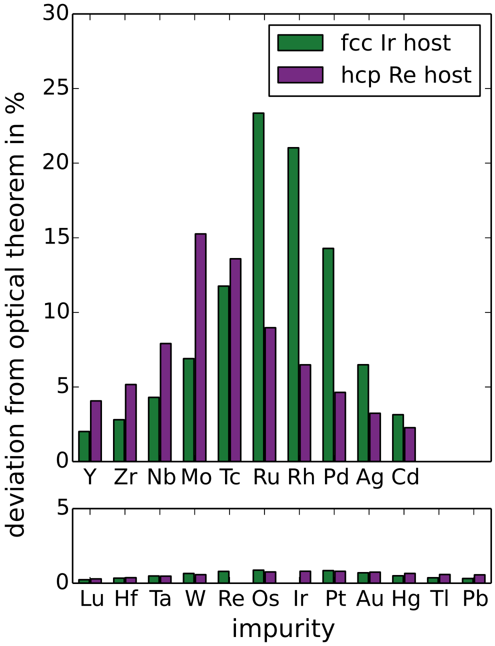

Figure 8.4.: Validity of the optical theorem for $4d$ impurities (upper panel) as well as $5d$ impurities (lower panel) in two nonmagnetic hosts, *i.e.* fcc Ir and hcp Re. Shown is the deviation from the left hand side to the right hand side of Eq. (2.151) in percent. The optical theorem is well fulfilled for $5d$ impurities (less than 1% deviation. However, there are some deviations (up to 25%) for $4d$ impurities.

on the one hand and the $5d$ impurities on the other, because in both cases the same numerical cutoff parameters have been used. Additionally, some tests with increasing the number of the Fermi-surface points left the quality of the optical theorem as well as our values for the (spin) conductivities unchanged. This leaves us with the conclusion, that some numerical difficulties arise with respect to the impurity states of the $4d$ impurities, but we do not expect major changes in the values for the conductivities and consequently the statements made in this chapter are valid.

9

Conclusions

This work sheds light on spin-orbit driven effects in solids, which manifest themselves in the phenomena of spin-relaxation, the anomalous Hall effect, as well as the spin Hall effect, investigated by *ab initio* calculations.

In order to study complex transition metal compounds, a tetrahedron method for the precise calculation of the Fermi surface of complicated shapes in the framework of the Korringa-Kohn-Rostoker Green function method was developed. Furthermore, an efficiently parallelized and thus highly scalable implementation of the accurate calculation of scattering properties was achieved.

A first application was the study of the Elliott-Yafet spin-mixing parameter of $5d$ and $6sp$ transition metals, which displays the host-crystal contribution to spin-relaxation processes in metals. Special focus was given to a yet unexplored dependence of the Elliott-Yafet parameter on the electron's spin-polarization direction (also called spin-quantization axis - SQA). This anisotropy was found to reach gigantic values in uniaxial hcp transition metals due to the emergence of large spin-flip hot-areas and hot-loops on the Fermi surface as the direction of the SQA is tilted away from the c-axis of the hcp crystal. The origin of the effect lies in the high anisotropy of the spin-flip part of SOC itself, which is amplified by a peculiar orbital character of the degenerate electronic states in an hcp crystal, superimposed by non-symmorphic symmetries. In turn, our explicit calculations show that the combination of those aspects leads to gigantic values — as high as 800% for hcp Hf — offering the possibility to tune the spin-relaxation time in a single-crystalline metal by simple means (*e.g.* an external magnetic field). However, no theoretical upper limit exists, and the race to find materials with an even higher anisotropy of the Elliott-Yafet parameter is open.

The second part dealt with the analysis of the anomalous and spin Hall effects in various dilute alloys. We performed *ab initio* calculations of the skew-scattering contribution in ferromagnetic hosts for the first time, and addressed a vast number of materials ranging from simple dilute alloys to complicated compounds. This included the calculation of substitutional impurities in a ferromagnetic bcc Fe host, where we identified a sign change in the anomalous Hall angle when the impurity atom is changed systematically across the $3d$ series of the periodic table. We delved further into the effect by determining the Fermi-surface resolved contributions to the anomalous Hall conductivity, and discovered strongly peaked contributions at small "hot spots" around spin-orbit lifted degeneracies. These contributions, however, appear in pairs of different signs and constitute an overall tiny anomalous Hall angle in bcc Fe. Larger Hall angles are achieved by considering alloys with stronger intrinsic spin-orbit coupling, and we address different kinds of disorder in the $L1_0$-ordered FePt alloy. Doping heavy, non-magnetic hosts with magnetic impurities presents an alternative to enhance the Hall effect, which was shown through the calculation of $3d$ impurities in Pd, Pt and Au hosts. An analysis of the spin-resolved conductivities in terms of a two-current model reveals a strong suppression of the skew-scattering properties in one spin channel for nearly every host-impurity combination. A close relation between transverse charge and spin currents follows, which is interesting from an application and experimental point of view, since it serves as a source of strongly spin-polarized currents.

For the generation of pure spin currents, the skew scattering mechanism for various $4d$ and $5sp$ as well as $5d$ and $6sp$ impurities in an fcc Ir and hcp Re host has been investigated. A vast range of spin Hall angles can be obtained by either changing the dopant, or — as we have shown for the first time — via a strong anisotropy of the SHE in hcp Re as function of the direction of the SQA, which can be tuned by, *e.g.* , an external magnetic field. It is surprising that a strong anisotropy exists within the *ab* plane of the hcp crystal, which is absent for the intrinsic contribution to the SHE.

Finally, the power of our newly developed method was showcased at the example of the very complicated compound MnSi. Here, the unusual space group of the B20 crystal structure leads to fascinating manifestations of spin-orbit broken symmetries, best seen by the Fermi-surface topology, anisotropy of electron lifetimes and the unusual symmetry of the conductivity tensors.

A Appendix

A.1. Tetrahedron method: details of the implementation

The cube labeled by $i = l + (m-1)\,N_x + (n-1)\,N_x\,N_y$ has the eight vertices

$$\vec{k}_i^{(1)} = \vec{k}_{l,m,n} \tag{A.1}$$

$$\vec{k}_i^{(2)} = \vec{k}_{l+1,m,n} \tag{A.2}$$

$$\vec{k}_i^{(3)} = \vec{k}_{l,m+1,n} \tag{A.3}$$

$$\vec{k}_i^{(4)} = \vec{k}_{l+1,m+1,n} \tag{A.4}$$

$$\vec{k}_i^{(5)} = \vec{k}_{l,m,n+1} \tag{A.5}$$

$$\vec{k}_i^{(6)} = \vec{k}_{l+1,m,n+1} \tag{A.6}$$

$$\vec{k}_i^{(7)} = \vec{k}_{l,m+1,n+1} \tag{A.7}$$

$$\vec{k}_i^{(8)} = \vec{k}_{l+1,m+1,n+1} \ , \tag{A.8}$$

where $l \in (0,\ldots,N_x-1)$, $m \in (0,\ldots,N_y-1)$, $n \in (0,\ldots,N_z-1)$ and N_d is the number of cubes in direction $d \in \{x,y,z\}$. The k-point grid is defined by

$$\vec{k}_{l,m,n} = \frac{l}{N_x}\,\hat{e}_x + \frac{m}{N_y}\,\hat{e}_y + \frac{n}{N_z}\,\hat{e}_z \ . \tag{A.9}$$

This samples the reciprocal space from 0 to 1 in each direction (in units of $\frac{2\pi}{a}$). If the Brillouin zone has different bounds (*e.g.* from -0.5 to 0.5 for a simple cubic lattice), the k-point grid has to be scaled and shifted accordingly.

By this we have labeled the vertices of a cube from one to eight. In a next step, each cube is cut into six tetrahedra. The jth tetrahedron of the ith cube is defined by four grid points according to Table A.1. All tetrahedra have one common edge, which is the space diagonal from vertex 1 to vertex 8. It is obvious that also another representation with a different common edge could have been chosen. It is this ambiguousness that might break symmetries in reciprocal space (*cf.* section 6.1.4).

j	cube vertex			
1	1	2	4	8
2	1	3	4	8
3	1	2	6	8
4	1	5	6	8
5	1	3	7	8
6	1	5	7	8

Table A.1.: For a given cube, the jth tetrahedron has the vertices given here

A.2. Derivation of the radial Lippmann-Schwinger equation

We recall the Lippmann-Schwinger equations for the two linear independent solutions in spin-space (Eqs. 2.53 and 2.54) and cast them into one form (with $s \in \{\uparrow, \downarrow\}$),

$$\psi^{\sigma}_{\vec{k},s}(\vec{r}) = \mathrm{e}^{i\vec{k}\cdot\vec{r}}\,\delta_{\sigma,s} + \sum_{\sigma''}\int \mathrm{d}\vec{r}'\,\mathrm{d}\vec{r}''\,g(\vec{r},\vec{r}')\;V^{\sigma,\sigma''}(\vec{r}',\vec{r}'')\;\psi^{\sigma''}_{\vec{k},s}(\vec{r}'')\;. \tag{A.10}$$

Next, we recall the expansions in real spherical harmonics for the quantities appearing in the second term on the right hand side (rhs.) of Eq. (A.10) (changing the notation for the angular part, $\hat{r} \to \Omega_r$, for clarity),

$$\begin{aligned}
g(\vec{r},\vec{r}') &= \sum_{L_2}\frac{1}{r\,r'}\;g_{\ell_2}(r,r')\;Y_{L_2}(\Omega_r)\;Y_{L_2}(\Omega_{r'})\;, && \text{(A.11)}\\
V^{\sigma\sigma''}(\vec{r}',\vec{r}'') &= \sum_{L_3,L_4}\frac{1}{r'^2}\;V^{\sigma\sigma''}_{L_3L_4}(r')\;Y_{L_3}(\Omega_{r'})\;Y_{L_4}(\Omega_{r''})\;\delta(r'-r'')\;, && \text{(A.12)}\\
\psi^{\sigma''}_{\vec{k},s}(\vec{r}'') &= \sum_{L_1,L_5} 4\pi i^{\ell_1}\;\frac{1}{r''}\;R^{\sigma''s}_{L_5L_1}(r'';E)\;Y_{L_1}(\Omega_k)\;Y_{L_5}(\Omega_{r''})\;. && \text{(A.13)}
\end{aligned}$$

We split the integration $\int \mathrm{d}\vec{r}' = \int \mathrm{d}r'\,r'^2\,\mathrm{d}\Omega_{r'}$ in (A.10) into a radial and angular part (similarly for the integration over $\vec{r}''$). Together with the delta-function in (A.12) we can execute the integral over $\mathrm{d}r''$. Further, the two integrals over the angular part can be executed with the two real spherical harmonics of the corresponding argument, *i.e.*

$$\int \mathrm{d}\Omega'\;\underbrace{Y_{L_2}(\Omega_{r'})}_{\text{from } g}\underbrace{Y_{L_3}(\Omega_{r'})}_{\text{from } V} = \delta_{L_2,L_3}\;, \tag{A.14}$$

$$\int \mathrm{d}\Omega''\;\underbrace{Y_{L_4}(\Omega_{r''})}_{\text{from } V}\underbrace{Y_{L_5}(\Omega_{r''})}_{\text{from } \psi} = \delta_{L_4,L_5}\;. \tag{A.15}$$

Executing the sum over L_3 and L_5 simplifies the second term on the rhs of Eq. (A.10) to

$$\sum_{L_1} 4\pi i^{\ell_1}\; Y_{L_1}(\Omega_k)\; \sum_{\sigma''}\sum_{L_2,L_4} Y_{L_2}(\Omega_r)\; \int \mathrm{d}r'\; \frac{g_{\ell_2}(r,r')}{r}\; V^{\sigma\sigma''}_{L_2L_4}(r')\; R^{\sigma''s}_{L_4L_1}(r';E)\ . \tag{A.16}$$

The other terms of Eq. (A.10) are expanded as

$$\begin{aligned} \psi^{\sigma}_{\vec{k},s}(\vec{r}) &= \sum_{L_1,L_2} 4\pi i^{\ell_1}\, \frac{1}{r}\, R^{\sigma s}_{L_2L_1}(r;E)\; Y_{L_1}(\Omega_k)\; Y_{L_2}(\Omega_r)\ , && \text{(A.17)}\\ \mathrm{e}^{i\,\vec{k}\cdot\vec{r}} &= \sum_{L_1} 4\pi i^{\ell_1}\; j_{\ell_1}(\kappa r)\; Y_{L_1}(\Omega_k)\; Y_{L_1}(\Omega_r) \quad \text{with } \kappa = \sqrt{E} && \text{(A.18)} \end{aligned}$$

Noticing that all terms of Eq. (A.10) contain the same factor $\sum_{L_1} 4\pi i^{\ell_1}\; Y_{L_1}(\Omega_k)$, we multiply the whole equation with $Y_L(\Omega_k)$ and integrate over $\mathrm{d}\Omega_k$,

$$\int \mathrm{d}\Omega_k\; Y_L(\Omega_k) \times \sum_{L_1} 4\pi i^{\ell_1}\; Y_{L_1}(\Omega_k) \times [\ldots] = \sum_{L_1} 4\pi i^{\ell} \delta_{L,L_1} \times [\ldots]\ , \tag{A.19}$$

and the Lippmann-Schwinger equation (A.10) reduces to

$$\begin{aligned} \frac{1}{r}\sum_{L_2} R^{\sigma s}_{L_2L}(r;E)\; Y_{L_2}(\Omega_r) &= j_\ell(\kappa r)\; Y_L(\Omega_r)\; \delta_{\sigma,s} && \text{(A.20)}\\ &+ \sum_{\sigma''}\sum_{L_2,L_4} Y_{L_2}(\Omega_r)\; \int \mathrm{d}r'\; \frac{g_{\ell_2}(r,r')}{r}\; V^{\sigma\sigma''}_{L_2L_4}(r')\; R^{\sigma''s}_{L_4L}(r';E)\ . \end{aligned}$$

The application of the same "trick" with multiplication of $Y_{L'}(\Omega_r)$ yields the final result

$$\begin{aligned} R^{\sigma s}_{L'L}(r;E) &= J_L(r;E)\; \delta_{L,L'}\; \delta_{\sigma,s} && \text{(A.21)}\\ &+ \sum_{\sigma''}\sum_{L_4} \int \mathrm{d}r'\; g_{\ell'}(r,r')\; V^{\sigma\sigma''}_{L'L_4}(r')\; R^{\sigma''s}_{L_4L}(r';E)\ , \end{aligned}$$

where we additionally multiplied by r and used $J_L(r;E) = r\, j_\ell(\kappa r)$.

A.3. Perturbative treatment of the p-model for the spin-mixing parameter

To understand the origin of the large anisotropy in uniaxial systems at special high symmetric points in the Brillouin zone, we apply a simple tight binding model.

We consider only p-states. Including the spin-degree of freedom, we end up with 6 states:

$$p_x^{\uparrow},\;\; p_y^{\uparrow},\;\; p_z^{\uparrow},\;\; p_x^{\downarrow},\;\; p_y^{\downarrow},\;\; p_z^{\downarrow} \tag{A.22}$$

We shall use this order also on the following to express operators as a matrix in this representation.

We position the p_x and p_y-orbitals at energy ε and introduce a uniaxiality by shifting the p_z-orbitals by an amount Δ. The full Hamiltonian including spin-orbit coupling reads

$$\mathcal{H} = \left(\begin{array}{ccc|ccc} \varepsilon & 0 & 0 & 0 & 0 & 0 \\ 0 & \varepsilon & 0 & 0 & 0 & 0 \\ 0 & 0 & \varepsilon+\Delta & 0 & 0 & 0 \\ \hline 0 & 0 & 0 & \varepsilon & 0 & 0 \\ 0 & 0 & 0 & 0 & \varepsilon & 0 \\ 0 & 0 & 0 & 0 & 0 & \varepsilon+\Delta \end{array}\right) + \xi \vec{\mathcal{L}} \cdot \vec{\mathcal{S}} \tag{A.23}$$

In the following we assume $\xi \ll \Delta$, where ξ is the spin-orbit coupling strength.

We divide the spin-orbit part into a spin-conserving $(\mathcal{LS})_{\parallel} = \mathcal{L}_{\hat{s}}\mathcal{S}_{\hat{s}}$ and a spin-flip contribution $(\mathcal{LS})^{\uparrow\downarrow} = \frac{1}{2}\left(\mathcal{L}^{+}_{\hat{s}}\mathcal{S}^{-}_{\hat{s}} + \mathcal{L}^{-}_{\hat{s}}\mathcal{S}^{+}_{\hat{s}}\right)$, where $\hat{s}$ denotes the spin-quantization axis.

For $\hat{s} = z$ (i.e. σ^{P}_z is diagonal) we have

$$\vec{\mathcal{L}} \cdot \vec{\mathcal{S}} = \left(\begin{array}{c|c} \mathcal{L}_z & \mathcal{L}_x - i\mathcal{L}_y \\ \hline \mathcal{L}_x + i\mathcal{L}_y & -\mathcal{L}_z \end{array}\right) . \tag{A.24}$$

For $\hat{s} = x$ (i.e. σ^{P}_x is diagonal[1] we obtain

$$\vec{\mathcal{L}} \cdot \vec{\mathcal{S}} = \left(\begin{array}{c|c} \mathcal{L}_x & -\mathcal{L}_z - i\mathcal{L}_y \\ \hline -\mathcal{L}_z + i\mathcal{L}_y & -\mathcal{L}_x \end{array}\right) . \tag{A.25}$$

In general, the spin conserving part will mix states of different orbital character, but not mix states of different spin character. The spin-flip contribution behaves differently: it will only mix states of different spin character. It is obvious, that the spin-flip contribution is causing a non-vanishing spin-mixing parameter. The effect of the spin-flip part on the states is crucial. In the following, we want to apply perturbation theory to learn something about the spin-mixed character of the states. Therefore, we treat the spin-flip contribution as a perturbation to the system, and including the spin-conserving SOC into the unperturbed Hamiltonian,

$$\mathcal{H}_0 = \mathrm{diag}(\varepsilon, \varepsilon, \varepsilon + \Delta) \otimes \mathbb{1}_{2\times 2} + \xi(LS_{\parallel}) . \tag{A.26}$$

Including the perturbation $(\mathcal{LS})^{\uparrow\downarrow}$ in first order we obtain for the states

$$|\, n \,\rangle \approx \left|\, n^{(0)} \right\rangle + \xi \sum_{m \neq n} \frac{\left\langle\, m^{(0)} \,\middle|\, (\mathcal{LS})^{\uparrow\downarrow} \,\middle|\, n^{(0)} \,\right\rangle}{E^{(0)}_n - E^{(0)}_m} \left|\, m^{(0)} \right\rangle . \tag{A.27}$$

---

[1] If we choose additionally $\sigma^{\mathrm{P}}_y = \left(\begin{smallmatrix} 0 & -i \\ i & 0 \end{smallmatrix}\right)$, the form of σ^{P}_z can be derived by the commutation relation $[\sigma^{\mathrm{P}}_a, \sigma^{\mathrm{P}}_b] = 2i \sum_c \epsilon_{abc}\, \sigma^{\mathrm{P}}_c$.

The matrix elements of the spin-flip term only mix states of different spin character into the unperturbed state $\left| n^{(0)} \right\rangle$.

Let us first consider $\hat{s} = z$: We find for the unperturbed eigenstates and energies,

$$\mathcal{H}_0 \left| n^{(0)} \right\rangle = E_n^{(0)} \left| n^{(0)} \right\rangle , \tag{A.28}$$

the six solutions:

$$\begin{array}{lcl} E_1^{(0)} = \varepsilon + \Delta & , & \left| 1^{(0)} \right\rangle = (\ 0,\ \ 0,\ 1 \ |\ 0,\ \ 0,\ 0\ )^{\mathrm{T}} \\ E_2^{(0)} = \varepsilon + \xi & , & \left| 2^{(0)} \right\rangle \sim (\ 1,\ \ i,\ 0 \ |\ 0,\ \ 0,\ 0\ )^{\mathrm{T}} \\ E_3^{(0)} = \varepsilon - \xi & , & \left| 3^{(0)} \right\rangle \sim (\ 1,\ -i,\ 0 \ |\ 0,\ \ 0,\ 0\ )^{\mathrm{T}} \\ E_4^{(0)} = \varepsilon + \Delta & , & \left| 4^{(0)} \right\rangle = (\ 0,\ \ 0,\ 1 \ |\ 0,\ \ 0,\ 1\ )^{\mathrm{T}} \\ E_5^{(0)} = \varepsilon + \xi & , & \left| 5^{(0)} \right\rangle \sim (\ 0,\ \ 0,\ 0 \ |\ 1,\ \ i,\ 0\ )^{\mathrm{T}} \\ E_6^{(0)} = \varepsilon - \xi & , & \left| 6^{(0)} \right\rangle \sim (\ 0,\ \ 0,\ 0 \ |\ 1,\ -i,\ 0\ )^{\mathrm{T}} \end{array} \tag{A.29}$$

The symbol $\sim$ denotes that a proper normalization has to be ensured. We have introduced a vertical bar in the states to separate spin-up and spin-down components. The spin-conserving part mixes p_x and p_y states (of same spin-character) completely. The energies are doubly degenerate. To each energy belongs one spin-up and one spin-down state. Evaluating now the matrix-elements appearing in Eq. A.27, we find only non-vanishing matrix elements between two pairs of states:

$$\begin{array}{lcl} \left\langle 1^{(0)} \right| (\mathcal{LS})^{\uparrow\downarrow} \left| 6^{(0)} \right\rangle = -\sqrt{2} & , & |E_6 - E_1| = \Delta + \xi \\ \left\langle 3^{(0)} \right| (\mathcal{LS})^{\uparrow\downarrow} \left| 4^{(0)} \right\rangle = \sqrt{2} & , & |E_4 - E_3| = \Delta + \xi \end{array} \tag{A.30}$$

Thus we obtain a spin-mixing of the order $\mathcal{O}\left(\frac{\xi}{\Delta}\right)$, using that $\sqrt{2}$ is of order 1 and including the ξ in front of the sum in Eq. A.27.

For the other direction of the SQA, $\hat{s} = x$, we find for the unperturbed states:

$$\begin{array}{lcl} E_1^{(0)} = \varepsilon + \alpha & , & \left| 1^{(0)} \right\rangle \sim (\ 0,\ -i\xi,\ \alpha \ |\ 0,\ 0,\ 0\ )^{\mathrm{T}} \\ E_2^{(0)} = \varepsilon & , & \left| 2^{(0)} \right\rangle \sim (\ 1,\ 0,\ 0 \ |\ 0,\ 0,\ 0\ )^{\mathrm{T}} \\ E_3^{(0)} = \varepsilon + \Delta - \alpha & , & \left| 3^{(0)} \right\rangle \sim (\ 0,\ \alpha,\ -i\xi \ |\ 0,\ 0,\ 0\ )^{\mathrm{T}} \\ E_4^{(0)} = \varepsilon + \alpha & , & \left| 4^{(0)} \right\rangle \sim (\ 0,\ 0,\ 0 \ |\ 0,\ i\xi,\ \alpha\ )^{\mathrm{T}} \\ E_5^{(0)} = \varepsilon & , & \left| 5^{(0)} \right\rangle \sim (\ 0,\ 0,\ 0 \ |\ 1,\ 0,\ 0\ )^{\mathrm{T}} \\ E_6^{(0)} = \varepsilon + \Delta - \alpha & , & \left| 6^{(0)} \right\rangle \sim (\ 0,\ 0,\ 0 \ |\ 0,\ \alpha,\ i\xi\ )^{\mathrm{T}} \end{array} \tag{A.31}$$

Again, proper normalization has to be ensured and we used the abbreviation

$$\alpha = \frac{\Delta}{2}\left(1 + \sqrt{1 + \frac{\xi^2}{(\Delta/2)^2}}\right) = \Delta\left(1 + (\xi/\Delta)^2 + \mathcal{O}\left((\xi/\Delta)^4\right)\right) . \tag{A.32}$$

Now, the spin-conserving part mixes p_y and p_z of the same spin character. The order of mixing is small, this we see by evaluating

$$\frac{\xi}{\alpha} = \frac{\xi}{\Delta} - \left(\frac{\xi}{\Delta}\right)^3 + \mathcal{O}\left((\xi/\Delta)^5\right) . \tag{A.33}$$

Evaluating the matrix elements, we find 4 different states

$$\begin{aligned}
\left\langle\, 2^{(0)} \,\middle|\, \mathcal{L}\mathcal{S}^{\uparrow\downarrow} \,\middle|\, 6^{(0)} \,\right\rangle &= i\tfrac{\alpha+\xi}{\sqrt{\alpha^2+\xi^2}} \quad , \quad |E_6 - E_2| = \alpha - \Delta \\
\left\langle\, 5^{(0)} \,\middle|\, \mathcal{L}\mathcal{S}^{\uparrow\downarrow} \,\middle|\, 3^{(0)} \,\right\rangle &= i\tfrac{\alpha+\xi}{\sqrt{\alpha^2+\xi^2}} \quad , \quad |E_3 - E_5| = \alpha - \Delta \\
\left\langle\, 2^{(0)} \,\middle|\, \mathcal{L}\mathcal{S}^{\uparrow\downarrow} \,\middle|\, 4^{(0)} \,\right\rangle &= \tfrac{\alpha-\xi}{\sqrt{\alpha^2+\xi^2}} \quad , \quad |E_4 - E_2| = \alpha \\
\left\langle\, 5^{(0)} \,\middle|\, \mathcal{L}\mathcal{S}^{\uparrow\downarrow} \,\middle|\, 1^{(0)} \,\right\rangle &= -\tfrac{\alpha-\xi}{\sqrt{\alpha^2+\xi^2}} \quad , \quad |E_1 - E_5| = \alpha \,.
\end{aligned} \tag{A.34}$$

All the matrix elements are of order $\mathcal{O}(1)$, but the energy difference for the first two transitions is small (see Eq. A.32):

$$\alpha - \Delta = \frac{\xi^2}{\Delta} + \xi \; \mathcal{O}\left((\xi/\Delta)^3\right) \, . \tag{A.35}$$

Thus, the energy denominator becomes very small for the first two transitions. Then one has to go to higher orders, or use non-degenerate perturbation theory to obtain quantitative results. But here the qualitative difference between the two cases becomes already clear.

Bibliography

[1] I. Žutić, J. Fabian, and S. Das Sarma, "Spintronics: Fundamentals and applications", Rev. Mod. Phys. **76**, 323–410 (2004).

[2] P. Gambardella, A. Dallmeyer, K. Maiti, M. C. Malagoli, W. Eberhardt, K. Kern, and C. Carbone, "Ferromagnetism in one-dimensional monatomic metal chains", Nature **416**, 301–304 (2002).

[3] P. Gambardella, S. Rusponi, M. Veronese, S. S. Dhesi, C. Grazioli, A. Dallmeyer, I. Cabria, R. Zeller, P. H. Dederichs, K. Kern, C. Carbone, and H. Brune, "Giant Magnetic Anisotropy of Single Cobalt Atoms and Nanoparticles", Science **300**, 1130–1133 (2003).

[4] M. Bode, M. Heide, K. von Bergmann, P. Ferriani, S. Heinze, G. Bihlmayer, A. Kubetzka, O. Pietzsch, S. Blügel, and R. Wiesendanger, "Chiral magnetic order at surfaces driven by inversion asymmetry", Nature **447**, 190–193 (2007).

[5] X. Z. Yu, Y. Onose, N. Kanazawa, J. H. Park, J. H. Han, Y. Matsui, N. Nagaosa, and Y. Tokura, "Real-space observation of a two-dimensional skyrmion crystal", Nature **465**, 901–904 (2010).

[6] S. Heinze, K. von Bergmann, M. Menzel, J. Brede, A. Kubetzka, R. Wiesendanger, G. Bihlmayer, and S. Blugel, "Spontaneous atomic-scale magnetic skyrmion lattice in two dimensions", Nature Phys. **7**, 713–718 (2011).

[7] S. Mühlbauer, B. Binz, F. Jonietz, C. Pfleiderer, A. Rosch, A. Neubauer, R. Georgii, and P. Böni, "Skyrmion Lattice in a Chiral Magnet", Science **323**, 915–919 (2009).

[8] L. Fu, C. L. Kane, and E. J. Mele, "Topological Insulators in Three Dimensions", Phys. Rev. Lett. **98**, 106803 (2007).

[9] C. L. Kane and E. J. Mele, "Z_2 Topological Order and the Quantum Spin Hall Effect", Phys. Rev. Lett. **95**, 146802 (2005).

[10] B. A. Bernevig, T. L. Hughes, and S.-C. Zhang, "Quantum Spin Hall Effect and Topological Phase Transition in HgTe Quantum Wells", Science **314**, 1757–1761 (2006).

[11] M. König, S. Wiedmann, C. Brüne, A. Roth, H. Buhmann, L. W. Molenkamp, X.-L. Qi, and S.-C. Zhang, "Quantum Spin Hall Insulator State in HgTe Quantum Wells", Science **318**, 766–770 (2007).

[12] C. L. Kane and E. J. Mele, “Quantum Spin Hall Effect in Graphene”, Phys. Rev. Lett. **95**, 226801 (2005).

[13] R. Yu, W. Zhang, H.-J. Zhang, S.-C. Zhang, X. Dai, and Z. Fang, “Quantized Anomalous Hall Effect in Magnetic Topological Insulators”, Science **329**, 61–64 (2010).

[14] C.-Z. Chang, J. Zhang, X. Feng, J. Shen, Z. Zhang, M. Guo, K. Li, Y. Ou, P. Wei, L.-L. Wang, Z.-Q. Ji, Y. Feng, S. Ji, X. Chen, J. Jia, X. Dai, Z. Fang, S.-C. Zhang, K. He, Y. Wang, L. Lu, X.-C. Ma, and Q.-K. Xue, “Experimental Observation of the Quantum Anomalous Hall Effect in a Magnetic Topological Insulator”, Science **340**, 167–170 (2013).

[15] I. M. Miron, T. Moore, H. Szambolics, L. D. Buda-Prejbeanu, S. Auffret, B. Rodmacq, S. Pizzini, J. Vogel, M. Bonfim, A. Schuhl, and G. Gaudin, “Fast current-induced domain-wall motion controlled by the Rashba effect”, Nature Mat. **10**, 419–423 (2011).

[16] G. Bihlmayer, Y. Koroteev, P. Echenique, E. Chulkov, and S. Blügel, “The Rashba-effect at metallic surfaces”, Surface Science **600**, 3888 –3891 (2006).

[17] I. M. Miron, K. Garello, G. Gaudin, P.-J. Zermatten, M. V. Costache, S. Auffret, S. Bandiera, B. Rodmacq, A. Schuhl, and P. Gambardella, “Perpendicular switching of a single ferromagnetic layer induced by in-plane current injection”, Nature **467**, 189–193 (2011).

[18] L. Berger, “Emission of spin waves by a magnetic multilayer traversed by a current”, Phys. Rev. B **54**, 9353–9358 (1996).

[19] J. Slonczewski, “Current-driven excitation of magnetic multilayers”, J. Magn. Magn. Mater. **159**, L1 –L7 (1996).

[20] F. Jonietz, S. Mühlbauer, C. Pfleiderer, A. Neubauer, W. Mnzer, A. Bauer, T. Adams, R. Georgii, P. Böni, R. A. Duine, K. Everschor, M. Garst, and A. Rosch, “Spin Transfer Torques in MnSi at Ultralow Current Densities”, Science **330**, 1648–1651 (2010).

[21] A. Neubauer, C. Pfleiderer, B. Binz, A. Rosch, R. Ritz, P. G. Niklowitz, and P. Böni, “Topological Hall Effect in the *A* Phase of MnSi”, Phys. Rev. Lett. **102**, 186602 (2009).

[22] R. Ritz, M. Halder, M. Wagner, C. Franz, A. Bauer, and C. Pfleiderer, “Formation of a topological non-Fermi liquid in MnSi”, Nature **497**, 231–234 (2013).

[23] C. Franz, F. Freimuth, A. Bauer, R. Ritz, C. Schnarr, C. Duvinage, T. Adams, S. Blügel, A. Rosch, Y. Mokrousov, and C. Pfleiderer, “Real-Space and Reciprocal-Space Berry Phases in the Hall Effect of $\mathrm{Mn}_{1-x}\mathrm{Fe}_x\mathrm{Si}$”, Phys. Rev. Lett. (in press) (2014).

[24] G. E. W. Bauer, E. Saitoh, and B. J. van Wees, “Spin caloritronics”, Nature Mat. **11**, 391–399 (2012).

[25] M. Dyakonov and V. Perel, “Current-induced spin orientation of electrons in semiconductors”, Phys. Lett. A **35**, 459 –460 (1971).

[26] J. E. Hirsch, “Spin Hall Effect”, Phys. Rev. Lett. **83**, 1834–1837 (1999).

[27] J. Sinova, D. Culcer, Q. Niu, N. A. Sinitsyn, T. Jungwirth, and A. H. MacDonald, “Universal Intrinsic Spin Hall Effect”, Phys. Rev. Lett. **92**, 126603 (2004).

[28] G. Y. Guo, S. Murakami, T.-W. Chen, and N. Nagaosa, “Intrinsic Spin Hall Effect in Platinum: First-Principles Calculations”, Phys. Rev. Lett. **100**, 096401 (2008).

[29] Y. K. Kato, R. C. Myers, A. C. Gossard, and D. D. Awschalom, “Observation of the Spin Hall Effect in Semiconductors”, Science **306**, 1910–1913 (2004).

[30] E. H. Hall, “XVIII. On the Rotational Coefficient in nickel and cobalt”, Phil. Mag. **12**, 157–172 (1881).

[31] N. Nagaosa, J. Sinova, S. Onoda, A. H. MacDonald, and N. P. Ong, “Anomalous Hall effect”, Rev. Mod. Phys. **82**, 1539–1592 (2010).

[32] E. Saitoh, M. Ueda, H. Miyajima, and G. Tatara, “Conversion of spin current into charge current at room temperature: Inverse spin-Hall effect”, Appl. Phys. Lett. **88**, 182509 (2006).

[33] B. F. Miao, S. Y. Huang, D. Qu, and C. L. Chien, “Inverse Spin Hall Effect in a Ferromagnetic Metal”, Phys. Rev. Lett. **111**, 066602 (2013).

[34] R. J. Elliott, “Theory of the Effect of Spin-Orbit Coupling on Magnetic Resonance in Some Semiconductors”, Phys. Rev. **96**, 266–279 (1954).

[35] M. I. Dyakonov and V. I. Perel, “Spin Relaxation of Conduction Electrons in Noncentrosymmetric Semiconductors”, Sov. Phys. Solid State **13**, 3023–3026 (1972).

[36] J. Fabian and S. Das Sarma, “Phonon-Induced Spin Relaxation of Conduction Electrons in Aluminum”, Phys. Rev. Lett. **83**, 1211–1214 (1999).

[37] M. Gradhand, D. V. Fedorov, P. Zahn, and I. Mertig, “Extrinsic Spin Hall Effect from First Principles”, Phys. Rev. Lett. **104**, 186403 (2010).

[38] D. V. Fedorov, C. Herschbach, A. Johansson, S. Ostanin, I. Mertig, M. Gradhand, K. Chadova, D. Ködderitzsch, and H. Ebert, “Analysis of the giant spin Hall effect in Cu(Bi) alloys”, Phys. Rev. B **88**, 085116 (2013).

[39] S. Lowitzer, M. Gradhand, D. Ködderitzsch, D. V. Fedorov, I. Mertig, and H. Ebert, “Extrinsic and Intrinsic Contributions to the Spin Hall Effect of Alloys”, Phys. Rev. Lett. **106**, 056601 (2011).

[40] M. Gradhand, D. V. Fedorov, P. Zahn, and I. Mertig, “Spin Hall angle versus spin diffusion length: Tailored by impurities”, Phys. Rev. B **81**, 245109 (2010).

[41] A. Fert and P. M. Levy, “Spin Hall Effect Induced by Resonant Scattering on Impurities in Metals”, Phys. Rev. Lett. **106**, 157208 (2011).

[42] P. Hohenberg and W. Kohn, “Inhomogeneous Electron Gas”, Phys. Rev. **136**, B864–B871 (1964).

[43] W. Kohn and L. J. Sham, “Self-Consistent Equations Including Exchange and Correlation Effects”, Phys. Rev. **140**, A1133–A1138 (1965).

[44] R. O. Jones and O. Gunnarsson, “The density functional formalism, its applications and prospects”, Rev. Mod. Phys. **61**, 689–746 (1989).

[45] K. Burke, *The ABC of DFT*, (2010) `http://www.chem.uci.edu/~kieron/dftold2/materials/bookABCDFT/gamma/g1.pdf`.

[46] S. H. Vosko, L. Wilk, and M. Nusair, “Accurate spin-dependent electron liquid correlation energies for local spin density calculations: a critical analysis”, Can. J. Phys. **58**, 1200–1211 (1980).

[47] U. von Barth and L. Hedin, “A local exchange-correlation potential for the spin polarized case. i”, J. Phys. C: Solid State Phys. **5**, 1629 (1972).

[48] J. P. Perdew and A. Zunger, “Self-interaction correction to density-functional approximations for many-electron systems”, Phys. Rev. B **23**, 5048–5079 (1981).

[49] K. Wildberger, P. Lang, R. Zeller, and P. H. Dederichs, “Fermi-Dirac distribution in *ab initio* Greens-function calculations”, Phys. Rev. B **52**, 11502–11508 (1995).

[50] B. H. Drittler, “KKR-Greensche Funktion methode für das volle Zellpotential”, PhD thesis (Forschungszentrum Jülich, 1991).

[51] R. Zeller, “Multiple-scattering solution of Schrödinger’s equation for potentials of general shape”, J. Phys. C: Solid State Phys. **20**, 2347 (1987).

[52] S. Heers, “Effect of spin-orbit scattering on transport properties of low-dimensional dilute alloys”, PhD thesis (RWTH Aachen, 2011).

[53] P. Mavropoulos and N. Papanikolaou, “The Korringa-Kohn-Rostoker (KKR) Green function method I. Electronic structure of periodic systems”, in *Computational Nanoscience: Do It Yourself!*, Vol. 31, edited by J. Grotendorst, S. Blügel, and D. Marx, NIC Series (John von Neumann Institute for Computing, Jülich, 2006), pp. 131–158.

[54] D. S. G. Bauer, “Development of a relativistic full-potential first-principles multiple scattering Green function method applied to complex magnetic textures of nano structures at surfaces”, PhD thesis (RWTH Aachen, 2013).

[55] Y. Yafet, “g Factors and Spin-Lattice Relaxation of Conduction Electrons”, in *Solid State Physics*, Vol. 14, edited by F. Seitz and D. Turnbull (Academic Press, 1963), pp. 1 –98.

[56] M. Gradhand, M. Czerner, D. V. Fedorov, P. Zahn, B. Y. Yavorsky, L. Szunyogh, and I. Mertig, “Spin polarization on Fermi surfaces of metals by the KKR method”, Phys. Rev. B **80**, 224413 (2009).

[57] M. Johnson and R. H. Silsbee, "Spin-injection experiment", Phys. Rev. B **37**, 5326–5335 (1988).

[58] J. Fabian and S. Das Sarma, "Spin Relaxation of Conduction Electrons in Polyvalent Metals: Theory and a Realistic Calculation", Phys. Rev. Lett. **81**, 5624–5627 (1998).

[59] F. Pientka, M. Gradhand, D. V. Fedorov, I. Mertig, and B. L. Györffy, "Gauge freedom for degenerate Bloch states", Phys. Rev. B **86**, 054413 (2012).

[60] R. Podloucky, R. Zeller, and P. H. Dederichs, "Electronic structure of magnetic impurities calculated from first principles", Phys. Rev. B **22**, 5777–5790 (1980).

[61] H. Akai, S. Blügel, R. Zeller, and P. H. Dederichs, "Isomer Shifts and Their Relation to Charge Transfer in Dilute Fe Alloys", Phys. Rev. Lett. **56**, 2407–2410 (1986).

[62] I. Mertig, "Transport properties of dilute alloys", Rep. Prog. Phys. **62**, 237 (1999).

[63] M. Schreck, *Mitschrieb zur Theoretischen Physik E: Quantenmechanik II von Prof. Dr. Klinkhamer*, (2004) `http://uni-ka.the-jens.de/html/theophys5/thse61.htm`.

[64] E. H. Hall, "On a New Action of the Magnet on Electric Currents", Am. J. Math. **2**, pp. 287–292 (1879).

[65] R. Karplus and J. M. Luttinger, "Hall Effect in Ferromagnetics", Phys. Rev. **95**, 1154–1160 (1954).

[66] J. Smit, "The spontaneous hall effect in ferromagnetics I", Physica **21**, 877 –887 (1955).

[67] E. I. Rashba, "Spin currents in thermodynamic equilibrium: The challenge of discerning transport currents", Phys. Rev. B **68**, 241315 (2003).

[68] Y. Niimi, Y. Kawanishi, D. H. Wei, C. Deranlot, H. X. Yang, M. Chshiev, T. Valet, A. Fert, and Y. Otani, "Giant Spin Hall Effect Induced by Skew Scattering from Bismuth Impurities inside Thin Film CuBi Alloys", Phys. Rev. Lett. **109**, 156602 (2012).

[69] J. Smit, "The spontaneous hall effect in ferromagnetics II", Physica **24**, 39 –51 (1958).

[70] L. Berger, "Side-Jump Mechanism for the Hall Effect of Ferromagnets", Phys. Rev. B **2**, 4559–4566 (1970).

[71] L. Berger, "Comment on Side-Jump and Side-Slide Mechanisms for Ferromagnetic Hall Effect: A Reply", Phys. Rev. B **8**, 2351–2352 (1973).

[72] L. Berger, "Account of scattering-independent contributions to the Hall conductivity in ferromagnets: A reply", Phys. Rev. B **17**, 1453–1453 (1978).

[73] Y. Mokrousov, “Anomalous Hall Effect”, in *Spintronics - From GMR to Quantum information*, Vol. 10, edited by S. Blügel, D. Bürgler, M. Morgenstern, C. M. Schneider, and R. Waser, Schriften des Forschungszentrums Jülich, Reihe Schlüsseltechnologien / Key Technologies (Forschungszentrum Jülich GmbH, 2009).

[74] J. Weischenberg, F. Freimuth, J. Sinova, S. Blügel, and Y. Mokrousov, “*Ab Initio* Theory of the Scattering-Independent Anomalous Hall Effect”, Phys. Rev. Lett. **107**, 106601 (2011).

[75] Y. Shiomi, Y. Onose, and Y. Tokura, “Extrinsic anomalous Hall effect in charge and heat transport in pure iron, $Fe_{0.997}Si_{0.003}$ and $Fe_{0.97}Co_{0.03}$”, Phys. Rev. B **79**, 100404 (2009).

[76] K. M. Seemann, Y. Mokrousov, A. Aziz, J. Miguel, F. Kronast, W. Kuch, M. G. Blamire, A. T. Hindmarch, B. J. Hickey, I. Souza, and C. H. Marrows, “Spin-Orbit Strength Driven Crossover between Intrinsic and Extrinsic Mechanisms of the Anomalous Hall Effect in the Epitaxial $L1_0$-Ordered Ferromagnets FePd and FePt”, Phys. Rev. Lett. **104**, 076402 (2010).

[77] Y. Tian, L. Ye, and X. Jin, “Proper Scaling of the Anomalous Hall Effect”, Phys. Rev. Lett. **103**, 087206 (2009).

[78] C. Ming, H. Pan, Z. Shi-Ming, and S. Zhong, “Thickness dependence of the anomalous Hall effect in disordered face-centered cubic FePt alloy films”, Chinese Phys. B **23**, 017104 (2014).

[79] A. Shitade and N. Nagaosa, “Anomalous Hall Effect in Ferromagnetic Metals: Role of Phonons at Finite Temperature”, J. Phys. Soc. Jpn. **81**, 083704 (2012).

[80] H Ebert, D Ködderitzsch, and J Minár, “Calculating condensed matter properties using the KKR-Green’s function methodrecent developments and applications”, Rep. Prog. Phys. **74**, 096501 (2011).

[81] S. G. Jacobs, “Keldysh formalism for nonequilibrium transport through quantum systems”, in *Computing Solids - Models, ab initio methods and supercomputing*, Vol. 74, edited by S. Blügel, N. Helbig, V. Meden, and D. Wortmann, Schriften des Forschungszentrums Jülich, Reihe Schlüsseltechnologien / Key Technologies (Forschungszentrum Jülich GmbH, 2014).

[82] W. Kohn and J. Luttinger, “Quantum Theory of Electrical Transport Phenomena”, Phys. Rev. **108**, 590–611 (1957).

[83] N. A. Sinitsyn, “Semiclassical theories of the anomalous Hall effect”, J. Phys.: Condens. Matter **20**, 023201 (2008).

[84] A. Weismann, M. Wenderoth, S. Lounis, P. Zahn, N. Quaas, R. G. Ulbrich, P. H. Dederichs, and S. Blügel, “Seeing the Fermi Surface in Real Space by Nanoscale Electron Focusing”, Science **323**, 1190–1193 (2009).

[85] D. Wortmann, N. Helbig, and S. Blügel, “Describing many-electron systems”, in *Computing Solids - Models, ab initio methods and supercomputing*, Vol. 74, edited by S. Blügel, N. Helbig, V. Meden, and D. Wortmann, Schriften des Forschungszentrums Jülich, Reihe Schlüsseltechnologien / Key Technologies (Forschungszentrum Jülich GmbH, 2014).

[86] W. H. Press, B. P. Flannery, S. A. Teukolsky, and W. T. Vetterling, *Numerical Recipies* (Cambridge University Press, 1989).

[87] P. E. Blöchl, O. Jepsen, and O. K. Andersen, “Improved tetrahedron method for Brillouin-zone integrations”, Phys. Rev. B **49**, 16223–16233 (1994).

[88] A. Henderson, J. Ahrens, and C. Law, *The ParaView Guide* (Kitware Inc., 2004).

[89] http://www.paraview.org.

[90] N. H. Long, P. Mavropoulos, S. Heers, B. Zimmermann, Y. Mokrousov, and S. Blügel, “Spin-flip hot spots in ultrathin films of monovalent metals: Enhancement and anisotropy of the Elliott-Yafet parameter”, Phys. Rev. B **88**, 144408 (2013).

[91] N. H. Long, P. Mavropoulos, B. Zimmermann, S. Heers, D. S. G. Bauer, S. Blügel, and Y. Mokrousov, “Spin relaxation and the Elliott-Yafet parameter in W(001) ultrathin films: Surface states, anisotropy, and oscillation effects”, Phys. Rev. B **87**, 224420 (2013).

[92] B. Zimmermann, P. Mavropoulos, S. Heers, N. H. Long, S. Blügel, and Y. Mokrousov, “Anisotropy of Spin Relaxation in Metals”, Phys. Rev. Lett. **109**, 236603 (2012).

[93] Y. Mokrousov, H. Zhang, F. Freimuth, B. Zimmermann, N. H. Long, J. Weischenberg, I. Souza, P. Mavropoulos, and S. Blügel, “Anisotropy of spin relaxation and transverse transport in metals”, J. Phys.: Condens. Matter **25**, 163201 (2013).

[94] M. Johnson and R. H. Silsbee, “Interfacial charge-spin coupling: Injection and detection of spin magnetization in metals”, Phys. Rev. Lett. **55**, 1790–1793 (1985).

[95] D. Steiauf and M. Fähnle, “Elliott-Yafet mechanism and the discussion of femtosecond magnetization dynamics”, Phys. Rev. B **79**, 140401 (2009).

[96] P. Mavropoulos, “Spin Relaxation in Nonmagnetic Metals and Semiconductors”, in *Spintronics - From GMR to Quantum information*, Vol. 10, edited by S. Blügel, D. Bürgler, M. Morgenstern, C. M. Schneider, and R. Waser, Schriften des Forschungszentrums Jülich, Reihe Schlüsseltechnologien / Key Technologies (Forschungszentrum Jülich GmbH, 2009).

[97] R. J. Elliott, “Spin-Orbit Coupling in Band Theory – Character Tables for Some “Double” Space Groups”, Phys. Rev. **96**, 280–287 (1954).

[98] Y. Ishikawa, K. Tajima, D. Bloch, and M. Roth, “Helical spin structure in manganese silicide MnSi”, Solid State Commun. **19**, 525 –528 (1976).

[99] T. Jeong and W. E. Pickett, “Implications of the B20 crystal structure for the magnetoelectronic structure of MnSi”, Phys. Rev. B **70**, 075114 (2004).

[100] B. Drittler, N. Stefanou, S. Blügel, R. Zeller, and P. H. Dederichs, “Electronic structure and magnetic properties of dilute Fe alloys with transition-metal impurities”, Phys. Rev. B **40**, 8203–8212 (1989).

[101] H. Akai, M. Akai, and J. Kanamori, “Electronic Structure of Impurities in Ferromagnetic Iron. II. $3d$ and $4d$ Impurities”, J. Phys. Soc. Jpn. **54**, 4257–4264 (1985).

[102] Y. Yao, L. Kleinman, A. H. MacDonald, J. Sinova, T. Jungwirth, D.-s. Wang, E. Wang, and Q. Niu, “First Principles Calculation of Anomalous Hall Conductivity in Ferromagnetic bcc Fe”, Phys. Rev. Lett. **92**, 037204 (2004).

[103] http://www.flapw.de.

[104] M. Gradhand, private communication, 2014.

[105] Y. Shiomi, “Skew-Scattering-Induced Anomalous Hall Effect in Impurity-Doped Fe”, in *Anomalous and Topological Hall Effects in Itinerant Magnets*, Springer Theses (Springer Japan, 2013), pp. 47–63.

[106] J. B. Staunton, S. Ostanin, S. S. A. Razee, B. L. Gyorffy, L. Szunyogh, B. Ginatempo, and E. Bruno, “Temperature Dependent Magnetic Anisotropy in Metallic Magnets from an *Ab Initio* Electronic Structure Theory: $L1_0$-Ordered FePt”, Phys. Rev. Lett. **93**, 257204 (2004).

[107] I. Mertig, R. Zeller, and P. H. Dederichs, “*Ab inito* calculations of the deviations from Matthiessens rule for dilute ternary alloys”, Phys. Rev. B **49**, 11767–11772 (1994).

[108] K. Tauber, D. V. Fedorov, M. Gradhand, and I. Mertig, “Spin Hall and spin Nernst effect in dilute ternary alloys”, Phys. Rev. B **87**, 161114 (2013).

[109] K. Everschor, “Current-Induced Dynamics of Chiral Magnetic Structures : Skyrmions, Emergent Electrodynamics and Spin-Transfer Torques”, PhD thesis (Universität zu Köln, Köln, Germany, 2012).

[110] S. V. Grigoriev, D. Chernyshov, V. A. Dyadkin, V. Dmitriev, E. V. Moskvin, D. Lamago, T. Wolf, D. Menzel, J. Schoenes, S. V. Maleyev, and H. Eckerlebe, “Interplay between crystalline chirality and magnetic structure in $\mathrm{Mn}_{1-x}\mathrm{Fe}_x\mathrm{Si}$”, Phys. Rev. B **81**, 012408 (2010).

[111] V. Dmitriev, D. Chernyshov, S. Grigoriev, and V. Dyadkin, “A chiral link between structure and magnetism in MnSi”, J. Phys.: Condens. Matter **24**, 366005 (2012).

[112] T. Hoshino, R. Zeller, P. H. Dederichs, and M. Weinert, “Magnetic Energy Anomalies of 3d Systems”, Europhys. Lett. **24**, 495 (1993).

[113] L. Ortenzi, I. I. Mazin, P. Blaha, and L. Boeri, "Accounting for spin fluctuations beyond local spin density approximation in the density functional theory", Phys. Rev. B **86**, 064437 (2012).

[114] P. Mavropoulos, N. Stefanou, and N. Papanikolaou, "Magnetic impurity states in simple metals: A study of the spin-polarization energy", Phys. Rev. B **58**, 1096–1099 (1998).

[115] A. Bauer, A. Neubauer, C. Franz, W. Münzer, M. Garst, and C. Pfleiderer, "Quantum phase transitions in single-crystal $\mathrm{Mn}_{1-x}\mathrm{Fe}_x\mathrm{Si}$ and $\mathrm{Mn}_{1-x}\mathrm{Co}_x\mathrm{Si}$: Crystal growth, magnetization, ac susceptibility, and specific heat", Phys. Rev. B **82**, 064404 (2010).

[116] A. Oswald, R. Zeller, and P. H. Dederichs, "Giant Moments in Palladium", Phys. Rev. Lett. **56**, 1419–1422 (1986).

[117] J. Friedel, "Metallic alloys", Il Nuovo Cimento **7**, 287–311 (1958).

[118] C. Herschbach, D. V. Fedorov, I. Mertig, M. Gradhand, K. Chadova, H. Ebert, and D. Ködderitzsch, "Insight into the skew-scattering mechanism of the spin Hall effect: Potential scattering versus spin-orbit scattering", Phys. Rev. B **88**, 205102 (2013).

[119] S. Lowitzer, "Relativistic electronic transport theory – The spin Hall effect and related phenomena", PhD thesis (LMU München, 2011).

[120] S. Lowitzer, D. Ködderitzsch, and H. Ebert, "Coherent Description of the Intrinsic and Extrinsic Anomalous Hall Effect in Disordered Alloys on an *Ab Initio* Level", Phys. Rev. Lett. **105**, 266604 (2010).

[121] S. Frota-Pessôa, "Magnetic behavior of $3d$ impurities in Cu, Ag, and Au: First-principles calculations of orbital moments", Phys. Rev. B **69**, 104401 (2004).

[122] P. M. Levy, H. Yang, M. Chshiev, and A. Fert, "Spin Hall effect induced by Bi impurities in Cu: Skew scattering and side-jump", Phys. Rev. B **88**, 214432 (2013).

[123] F. Freimuth, S. Blügel, and Y. Mokrousov, "Anisotropic Spin Hall Effect from First Principles", Phys. Rev. Lett. **105**, 246602 (2010).

List of Publications

[B1] B. Zimmermann, P. Mavropoulos, S. Heers, N. H. Long, S. Blügel, and Y. Mokrousov, “Anisotropy of Spin Relaxation in Metals”, Phys. Rev. Lett. **109**, 236603 (2012).

[B2] Y. Mokrousov, H. Zhang, F. Freimuth, B. Zimmermann, N. H. Long, J. Weischenberg, I. Souza, P. Mavropoulos, and S. Blügel, “Anisotropy of spin relaxation and transverse transport in metals”, J. Phys.: Condens. Matter **25**, 163201 (2013).

[B3] N. H. Long, P. Mavropoulos, B. Zimmermann, S. Heers, D. S. G. Bauer, S. Blügel, and Y. Mokrousov, “Spin relaxation and the Elliott-Yafet parameter in W(001) ultrathin films: Surface states, anisotropy, and oscillation effects”, Phys. Rev. B **87**, 224420 (2013).

[B4] N. H. Long, P. Mavropoulos, S. Heers, B. Zimmermann, Y. Mokrousov, and S. Blügel, “Spin-flip hot spots in ultrathin films of monovalent metals: Enhancement and anisotropy of the Elliott-Yafet parameter”, Phys. Rev. B **88**, 144408 (2013).

[B5] V. Kashid, T. Schena, B. Zimmermann, Y. Mokrousov, S. Blügel, V. Shah, and H. G. Salunke, “Dzyaloshinskii-Moriya interaction and chiral magnetism in $3d$-$5d$ zigzag chains: Tight-binding model and ab initio calculations”, Phys. Rev. B **90**, 054412 (2014).

[B6] N. H. Long, P. Mavropoulos, B. Zimmermann, D. S. G. Bauer, S. Blügel, and Y. Mokrousov, “Spin relaxation and spin Hall transport in $5d$ transition-metal ultrathin films”, Phys. Rev. B **90**, 064406 (2014).

[B7] B. Zimmermann, M. Heide, G. Bihlmayer, and S. Blügel, “First-principles analysis of a homochiral cycloidal magnetic structure in a monolayer Cr on W(110)”, (accepted for publication in Phys. Rev. B), 2014.

[B8] M. Bouhassoune, B. Zimmermann, P. Mavropoulos, D. Wortmann, P. H. Dederichs, S. Blügel, and S. Lounis, “Amplified spin-dependent electron focusing through interference of scattered quantum well states”, (accepted for publication in Nat. Commun.), 2014.

[B9] B. Zimmermann, K. Chadova, D. Ködderitzsch, S. Blügel, H. Ebert, D. V. Fedorov, N. H. Long, P. Mavropoulos, I. Mertig, Y. Mokrousov, and M. Gradhand, “Skew scattering in dilute ferromagnetic alloys”, (submitted for publication), 2014.

List of Figures

Acknowledgements

First of all, I would like to thank Prof. Dr. Yuriy Mokrousov for supervising this thesis and providing guidance throughout my journey of the scientific world. I learned so much not only from his vast expertise in the field of transverse and topological transport, but also from the excellent research conditions he and his group “Topological Nanoelectronics” have provided me.

I am thankful to Prof. Dr. Carsten Honerkamp for his willingness to examine this thesis as a second referee.

I am also deeply indebted to Prof. Dr. Stefan Blügel, first for giving me the opportunity to conduct my research at the institute “Quantum Theory of Materials” at the Peter Grünberg Institute and Institute for Advanced Simulation, and also for the stimulating and – most importantly – motivating discussions, which we have had.

I am most grateful to Dr. Phivos Mavropoulos, for his constant support throughout the last three years, and for answering my many questions which ranged from general solid-state physics over the KKR formalism to minute numerical details.

I would also like to thank Dr. Nguyen H. Long for his close collaboration, countless suggestions, and for sharing his expertise on the KKR formalism.

Among the many people at the PGI-1/IAS-1 who have helped me through many discussions on physics and technical issues, I would like to mention a few explicitly: Dr. David Bauer for sharing his strong expertise in the KKR formalism and providing access to his impurity program, KKRimp; Dr. Swantje Heers for introducing me to the field of scattering properties of defects and making her code available to me, which strongly accelerated my work; Dr. Paul Baumeister for his invaluable help regarding parallel computing and coding; Dr. Frank Freimuth and Jürgen Weischenberg for many discussions regarding transverse transport properties; and Ute Winkler for all of her support concerning organizational and administrative issues.

I would also like to thank Dr. Martin Gradhand for the vivid exchange of ideas on the skew-scattering mechanism behind the AHE and SHE.

I am very grateful to Dr. Vaishali Shah and Dr. Vikas Kashid for their generous hospitality during my stay at the University of Pune / India, and to Dr. Hemant Salunke during my stay at BARC Mumbai / India, but most of all for our enjoyable collaboration.

I warmly thank Benedikt Schweflinghaus, Dr. Nguyen H. Long, Dr. Phivos Mavropoulos, Timo Schena and Dr. Martin Gradhand for carefully proofreading this thesis.

Furthermore, I am grateful to the PGI/IAS-1 “racket sport division”, led by Timo Schena, and the “parking-lot soccer team”, headed by Dr. Alexander Thieß, for the crucial sports distractions. Many thanks go to my office mates Benedikt Schweflinghaus and Philipp Rüßmann, as well as Dr. Markus Betzinger, Dr. Mohammed Bouhassoune, Dr. Gregor Michalicek and Dr. Felix Gunkel for their genius scientific and non-scientific distractions.

Last but not least, I thank my friends, my family and Noémie for their unlimited support, constant motivation and invaluable love.

Schriften des Forschungszentrums Jülich
Reihe Schlüsseltechnologien / Key Technologies

Band / Volume 76
Temperature-Induced Metamagnetic Transition and Domain Structures of Single-Crystalline FeRh Thin Films on MgO(100)
X. Zhou (2013), xi, 104 pp
ISBN: 978-3-89336-919-5

Band / Volume 77
Interplay between Magnetism and Superconductivity in Iron Based High Temperature Superconductors
S. Price (2013), 196 pp
ISBN: 978-3-89336-921-8

Band / Volume 78
Magnetoresistance and transport in carbon nanotube-based devices
C. Morgan (2013), viii, 131 pp
ISBN: 978-3-89336-926-3

Band / Volume 79
Development of a relativistic full-potential first-principles multiple scattering Green function method applied to complex magnetic textures of nano structures at surfaces
D. Bauer (2014), 193 pp
ISBN: 978-3-89336-934-8

Band / Volume 80
Identifizierung von artifiziellen Liganden eines in Nanodiscs inkorporierten integralen Membranproteins
M. Pavlidou (2014), 106 pp
ISBN: 978-3-89336-942-3

Band / Volume 81
Interdomain Functional Dynamics of Phosphoglycerate Kinase Studied by Single-Molecule FRET
M. Gabba (2014), v, 179 pp
ISBN: 978-3-89336-943-0

Band / Volume 82
Silizium Nanoribbon Feld-Effekt Transistoren zur Kopplung an elektroaktive Zellen
M. Jansen (2014), xvi, 181 pp
ISBN: 978-3-89336-944-7

Band / Volume 83
Microscopic description of the inverse Faraday effect at subpicosecond time scales
D. Popova (2014), 183 pp
ISBN: 978-3-89336-962-1

Band / Volume 84
Neutron Scattering
Lectures of the JCNS Laboratory Course held at Forschungszentrum Jülich and at the Heinz Maier-Leibnitz Zentrum Garching
edited by Th. Brückel, G. Heger, D. Richter, G. Roth and R. Zorn (2014), ca. 360 pp
ISBN: 978-3-89336-965-2

Band / Volume 85
Neutron Scattering
Experiment Manuals of the JCNS Laboratory Course held at Forschungszentrum Jülich and at the Heinz Maier-Leibnitz Zentrum Garching
edited by Th. Brückel, G. Heger, D. Richter, G. Roth and R. Zorn (2014), ca. 195 pp
ISBN: 978-3-89336-966-9

Band / Volume 86
Development and Characterization of a Microfluidic Magnetic Oscillation Reactor for Enzymes
D. Jussen (2014), xxi, 131 pp
ISBN: 978-3-89336-974-4

Band / Volume 87
Submolecular imaging with single particle atomic force sensors
G. Kichin (2014), 140 pp
ISBN: 978-3-89336-976-8

Band / Volume 88
Multiscale Multimodel Simulation of Micromagnetic Singularities
C. Andreas (2014), xix, 188 pp
ISBN: 978-3-89336-983-6

Band / Volume 89
***Ab initio* description of transverse transport due to impurity scattering in transition-metals**
B. Zimmermann (2014), 164 pp
ISBN: 978-3-89336-985-0

Weitere ***Schriften des Verlags im Forschungszentrum Jülich*** unter
http://wwwzb1.fz-juelich.de/verlagextern1/index.asp

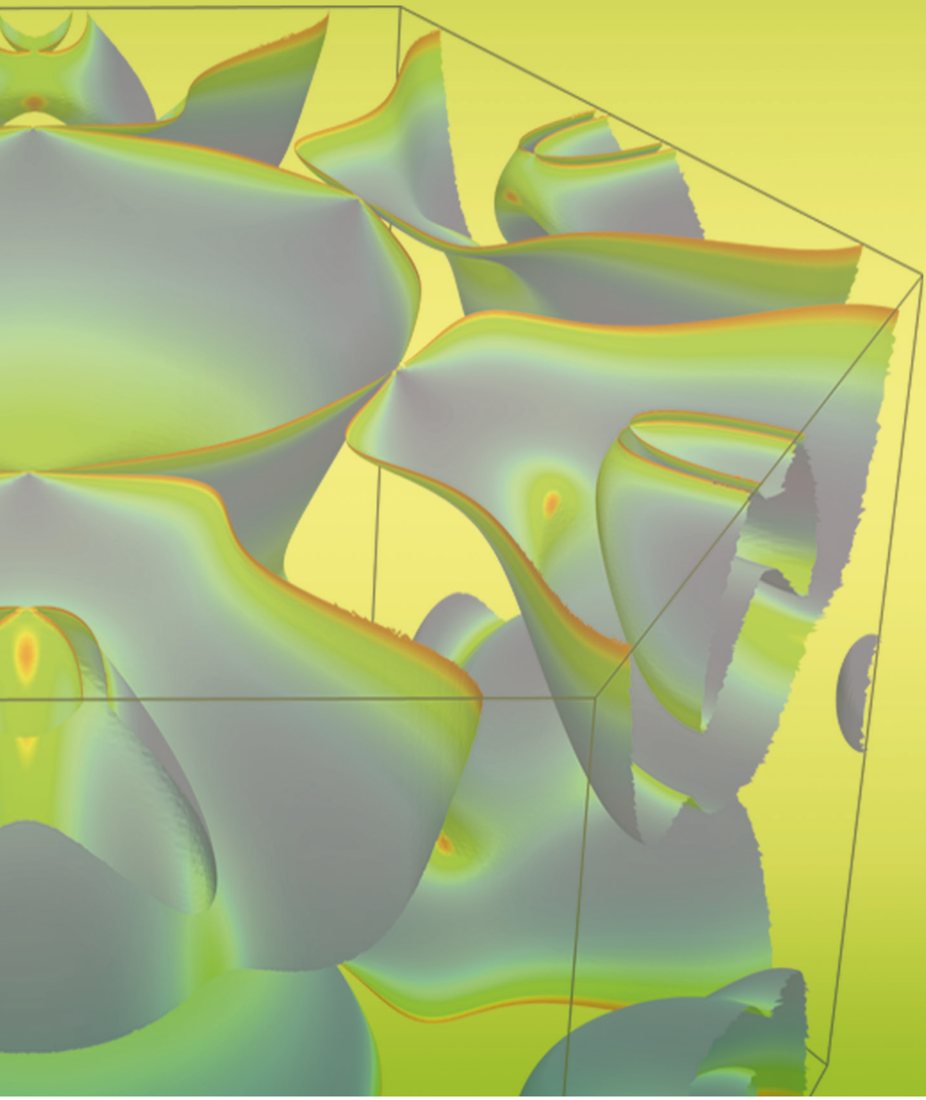

Schlüsseltechnologien / Key Technologies
Band / Volume 89
ISBN 978-3-89336-985-0